The University of Nottingham
UNITED KINGDOM · CHINA · MALAYSIA

Achamfuo-Yeboah, Samuel Osei (2012) Design and implementation of a CMOS Modulated Light Camera. PhD thesis, University of Nottingham.

Access from the University of Nottingham repository:
http://eprints.nottingham.ac.uk/12931/1/thesis.pdf

Copyright and reuse:

The Nottingham ePrints service makes this work by researchers of the University of Nottingham available open access under the following conditions.

- Copyright and all moral rights to the version of the paper presented here belong to the individual author(s) and/or other copyright owners.
- To the extent reasonable and practicable the material made available in Nottingham ePrints has been checked for eligibility before being made available.
- Copies of full items can be used for personal research or study, educational, or not-for-profit purposes without prior permission or charge provided that the authors, title and full bibliographic details are credited, a hyperlink and/or URL is given for the original metadata page and the content is not changed in any way.
- Quotations or similar reproductions must be sufficiently acknowledged.

Please see our full end user licence at:
http://eprints.nottingham.ac.uk/end_user_agreement.pdf

A note on versions:

The version presented here may differ from the published version or from the version of record. If you wish to cite this item you are advised to consult the publisher's version. Please see the repository url above for details on accessing the published version and note that access may require a subscription.

For more information, please contact eprints@nottingham.ac.uk

Design and Implementation of a CMOS Modulated Light Camera

Samuel Osei Achamfuo-Yeboah

Division of Electrical Systems and Optics

University of Nottingham

Thesis submitted to the University of Nottingham

for degree of Doctor of Philosophy

December 2012

Abstract

Modulated Light Cameras represent a breed of cameras designed specifically to capture intensity modulated light. This is because using coherent detection it is possible to lift a signal of interest out of the background noise and thus increase the precision of measurements.

This work presents a camera designed to detect the phase of amplitude modulated light. By implementing an in-pixel demodulation, wide-field detection of the phase of light is possible. The camera provides 32 by 32 pixels, each with a pitch of 115 μm with a fill factor of 16 %.

This pixel used in the camera introduces a novel tuning mechanism that matches the camera to the frequency of operation and light conditions. This enables the camera to work at high modulation depths, and increases the detection frequency to 50 MHz. The camera also provides an improved linear response without compromising on dynamic range and pixel size. The noise response of the camera is also improved as compared with previous work performed.

The camera has been demonstrated in wide-field range measurements of a scene (Imaging LIDAR). It has also been applied to wide-field heterodyne interforemetry and in ultra-stable interferometry.

Acknowledgements

I would like to thank my supervisors Prof Matt Clark and Dr Roger Light. They have been very patient and supportive in this work. I appreciate their great depth of skill and knowledge, and their guidance over the course of this project. I'm always amazed at the depth of knowledge, memory and ingenious ways of solving problems. I'm honoured to have worked with them.

I'd also like to thank Dr Ian Stockford who supervised the first year of the PhD, and all the people in SiOS and Applied Optics at the University of Nottingham, particularly Dr Steve Sharples, Dr Kuldip Modha, Rikesh Patel, Rob Ellwood, and others.

I also wish to acknowledge my wife Dr Sheila Achamfuo-Yeboah, who has been very supportive and patient with my unpredictable hours and quirks. I also acknowlodge the support of all the family home in Ghana.

I also wish to appreciate the support of Harvest Chapel International Ministries, which has provided spiritual and social support as well a place to forget the stress of PhD. My thanks go to my housemates over the years, Tanvir, Florent, and Eric, and my friends all over Nottingham particularly Felix and Daakpe.

Last but not at all least, I acknowledge God, thanking Him for grace, provision and sustenance.

I'd like to dedicate this honour to my father Rt. Rev'd. Samuel Achamfuo-Yeboah, who shared this vision with me in 1996. The award is dedicated to my baby boy, Nana Kwame.

Contents

Page

Abstract **i**

Acknowledgements **ii**

Table of Contents **iii**

List of Figures **xiii**

List of Tables **xiv**

1 Introduction **1**

1.1 Photography 1

1.2 Electronic Photodetection 2

1.2.1 Types of Photosensitive elements 3

1.2.2 Performance Parameters for a CMOS photodetector 5

1.3 Modulated Light cameras 6

1.4 Applications 7

1.4.1 Imaging LIDAR 7

1.4.2 Interferometry 10

1.5 Aims/Objectives 11

1.6 Thesis Layout 12

2 Literature Review **14**

2.1 Continuous-Time Cameras 14

2.1.1 Stenflo 14

2.1.2 Povel 15

2.1.3 Spirig 16

2.1.4 Lange 16

2.2 CMOS Integrating Cameras 17

2.2.1 Ando 17

2.2.2 Schwarte 18

2.2.3 Ohta 20

2.2.4 Oike 21

2.2.5 Stoppa 23

2.2.6 Light . . . 23
2.3 CMOS Continuous Time Cameras . . . 24
2.3.1 Benten . . . 25
2.3.2 Bourquin . . . 26
2.3.3 Lu . . . 27
2.3.4 Pitter 2003 . . . 28
2.3.5 Pitter 2004 . . . 29
2.3.6 Dmochowski 2004 . . . 29
2.3.7 Dmochowski 2006 . . . 31
2.4 Other Cameras . . . 31
2.4.1 Ma . . . 32
2.4.2 Kleinfelder . . . 32
2.4.3 Niclass . . . 33
2.4.4 Perelman . . . 35
2.4.5 Microsoft Kinect . . . 36
2.5 Summary . . . 37

3 Theory **41**
3.1 Modulation Theory . . . 41
3.2 Operating Principle . . . 43
3.3 Light Budget . . . 48
3.3.1 Sunlight and Solar Spectrum . . . 50
3.4 Noise and Uncertainty Sources . . . 52
3.4.1 Optical Sources . . . 52
3.4.2 Electronic Noise Sources . . . 53
3.4.3 Propagation of Uncertainty . . . 54
3.5 Electronic Implementation . . . 57
3.6 Transistor Operating Regions . . . 59
3.6.1 Triode/Linear Operation . . . 60
3.6.2 Saturation Region Operation . . . 60
3.6.3 Subthreshold Operation . . . 62
3.7 Logarithmic Pixel . . . 63
3.7.1 Low Frequency Response . . . 64
3.7.2 AC Small Signal Response . . . 66
3.7.3 Frequency Response . . . 67
3.7.4 Common Gate Amplifier . . . 71
3.7.5 Regulated Cascode input stage . . . 73
3.8 Tunebias (Source Degeneration) . . . 76
3.8.1 Noise . . . 78

3.9 Design Decisions 78

4 Test Designs **80**
4.1 MLCv6FE 80
4.1.1 Design Details 80
4.1.2 Experiment 82
4.1.3 Experimental Results 83
4.1.4 Discussion of Results 83
4.1.5 Discussion 85
4.2 MLCv6 88
4.2.1 Pixel 88
4.2.2 Chip 102
4.2.3 Design differences v5 and v6 104
4.2.4 Corners Analysis 106
4.2.5 Characterization of MLCv6 107
4.2.6 Experiment Procedure 111
4.2.7 Addressing Problem 112
4.2.8 Experiment Results 121
4.2.9 Discussion of results 125
4.2.10 Experimental Comparison of MLCv5 and MLCv6 126
4.2.11 Discussion 129

5 Final Design **131**
5.1 Design Motivation 131
5.2 Design Details 133
5.2.1 Pixel 134
5.2.2 Chip 150
5.2.3 Corners Analysis 153
5.3 Characterisation 155
5.3.1 Hardware 155
5.3.2 Acquisition Software 157
5.3.3 Local (reference) oscillator generation and DC offsets . . . 157
5.4 Experimental Results 160
5.4.1 Single Pixel 160
5.4.2 Multiple pixel phase response 172
5.4.3 Widefield Images 172
5.4.4 Output filter response 173
5.5 Phase/DC light Dependence 176
5.6 Conclusion 178

6 Applications **179**
6.1 Widefield Time of Flight Imaging 179
6.1.1 Experiment Setup 179
6.1.2 Results and Discussion 180
6.2 Heterodyne Interferometry 182
6.2.1 Experiment Setup 186
6.2.2 Results and Discussion 186
6.3 Ultrastable Heterodyne Interferometry 188
6.3.1 Experimental Setup 188
6.3.2 Results and Discussion 189
6.4 Practical Considerations 191

7 Discussion and Conclusion **196**
7.1 Thesis Summary 196
7.2 Conclusions 198
7.3 Future Research 199

A C35 Wafer cross-section **201**

B Bias currents **202**
B.1 MLCv6 202
B.2 LIDAR1 202

C Photomicrographs **204**

Bibliography **206**

List of Figures

Page

Chapter 1: Introduction **1**

1.1 Three (3) Transistor Active Pixel Sensor 4
1.2 MLC Imaging LIDAR setup 8

Chapter 2: Literature Review **14**

2.1 Povel Pixel 15
(a) Povel detection setup 15
(b) Slit mask on the CCD 15
2.2 Ando's CIS Pixel 18
2.3 PMD Pixel Cross-section 19
2.4 Ohta Pixel Schematic 21
2.5 Oike Pixel 22
2.6 Oike Pixel Schematic 22
2.7 Stoppa Range Sensor Schematic 24
2.8 Roger Light's integrating pixel 25
2.9 Schematic for Bourquin Pixel 27
2.10 Pitter Pixel Schematic 28
2.11 Pitter 64 × 64 camera layout 30
2.12 Dmochowski's Test Pixel 30
2.13 Dmochowski's Camera Pixel 31
2.14 Kleinfelder pixel schematic 33
2.15 Niclass SPAD Pixel Photomicrograph 34
2.16 Niclass 3D camera 35
(a) Niclass SPAD Pixel Schematic 35
(b) Photomicrograph of sensor array 35
2.17 Perelman pixel sensor architecture 35
2.18 Kinect Patent 36
2.19 Kinect Ranging 37
2.20 Kinect Image 38

Chapter 3: Theory **41**

3.1 Modulation Characteristics 42
3.2 MLC Block Diagram 45
3.3 Solar Radiation Spectrum 51
3.4 Photodiode with Resistive Load 57
(a) Simple Resistive Load Front-end 57
(b) Simple Resistive Load Front-end Small signal model 57
3.5 An NMOS Transistor 59
(a) A CMOS N-type transistor 59
(b) Cross-section of an NMOS transistor 59
3.6 NMOS transistor in triode region 60
3.7 An NMOS Transistor in Saturation 61
(a) NMOS at pinch-off 61
(b) NMOS in saturation 61
3.8 Diode-Connected transistor 62
3.9 Subthreshold Current 62
3.10 Simplified Front End 63
(a) Logarithmic Pixel 63
(b) Small signal model for log pixel 63
3.11 Front-end SS circuit with g_m circuit 66
3.12 $1/g_m$ with varying current 68
3.13 Simulated capacitance of photodiode 69
3.14 Phase response of simplified front end 70
3.15 Common Gate Amplifier 72
3.16 RGC TIA 74
(a) RGC Amplifier 74
(b) RGC Amplifier - Small Signal 74
3.17 Front end with resistor to sink current 74
3.18 Completed front-end circuit 78
3.19 Simplified noise equivalent circuit for Noise analysis 79

Chapter 4: Test Designs **80**

4.1 MLCv6FE Front End Schematic 81
4.2 MLCv6FE Front-End layout 82
(a) Layout 82
(b) Schematic 82
4.3 MLCv6FE PCB Board 83
(a) PCB Layout Gerber 83

(b) PCB Schematic 83
4.4 Experimental Results 1 - MLCv6FE 84
4.5 Experimental Results 2 - MLCv6FE 85
4.6 Experimental Results 3 - MLCv6FE 86
4.7 Experimental Results 4 - MLCv6FE 86
4.8 Layout and schematic of MLCv6 pixel 89
(a) Layout 89
(b) Schematic 89
4.9 MLCv6 Front-end schematic 90
4.10 Front-end AC Amplitude Response 90
4.11 Front-end AC Bandwidth Response 91
4.12 Front-end AC Phase Response 91
4.13 Front-end Noise Response 92
4.14 MLCv6 Simulated Response 92
4.15 MLCv6 Amplifier AC amplitude response 93
4.16 MLCv6 Amplifier AC phase response 94
4.17 MLCv6 Amplifier Noise response 94
4.18 MLCv6 Amplifier DC response 95
4.19 MLCv6 mixer schematic 96
4.20 MLCv6 mixer layout 96
4.21 MLCv6 mixer characteristics 97
4.22 MLCv6 Low pass filter AC amplitude response 98
4.23 MLCv6 Low pass filter Phase respons 98
4.24 MLCv6 Low pass filter Bandwidth response 99
4.25 MLCv6 Low pass filter Noise respons 99
4.26 MLCv6 Low pass filter DC response 100
4.27 Acceptance Window Diagram for MLCv6 101
4.28 MLCv6 Bonding Diagram 103
4.29 MLCv6 Chip Schematic 104
4.30 MLCv6 AVDD3 pixel IR drop and Ground Bounce 105
(a) MLCv6 3.3V IR Drop 105
(b) MLCv6 Ground Bounce 105
4.31 Periodic Noise performance of MLCv5 compared with MLCv6 . . 107
4.32 Experiment Setup - MLCv6 108
4.33 MLCv6 PCB Schematic 110
4.34 Comedi Acquisition System 111
4.35 MLCv6 Response to light variation - Image 112
4.36 Simulation to investigate addressing problem - results 1 114
4.37 Simulation to investigate addressing problem - results 2 115

4.38 Column simulation results 117
4.39 Matlab Simulation of MLCv6 scrambling /reconstruction 120
4.40 Experiment results - Single Spots reconstructed 121
4.41 MLCv6 Single Pixel DC response 123
4.42 MLCv6 Single Pixel RF response 124
4.43 MLCv6 DC Image 124
4.44 MLCv6 IQ image with Phase = -180° 126
4.45 MLCv6 IQ images with Phase variation: -135° to 0° 127
(a) Phase = -135° 127
(b) Phase = -90° 127
(c) Phase = -45° 127
(d) Phase = 0° 127
4.46 MLCv6 IQ images with Phase variation 45° to 180° 128
(a) Phase = 45° 128
(b) Phase = 90° 128
(c) Phase = 135° 128
(d) Phase = 180° 128

Chapter 5: Final Design **131**

5.1 LIDAR1 Chip Projection 132
5.2 LIDAR1 pixel schematic 133
5.3 LIDAR1 front end schematic 134
5.4 Front-end AC Amplitude Response 135
5.5 Front-end AC Bandwidth Response 135
5.6 Front-end AC Phase Response 136
5.7 Front-end AC Phase Response 136
5.8 Front-end Noise Response 137
5.9 Front-end AC Phase Gradient 137
5.10 Front-end AC Phase Gradient 138
5.11 LIDAR1 amplifier schematic 139
5.12 LIDAR1 Amplifier AC amplitude response 140
5.13 LIDAR1 Amplifier AC phase response 140
5.14 LIDAR1 Amplifier Noise response 141
5.15 LIDAR1 Amplifier DC response 141
5.16 LIDAR1 output buffer 142
5.17 LIDAR1 Low Pass Filter schematic 143
5.18 LIDAR1 Low pass filter AC amplitude response 143
5.19 LIDAR1 Low pass filter Phase response 144

5.20 LIDAR1 Low pass filter Bandwidth response 144
5.21 LIDAR1 Low pass filter Noise response 145
5.22 LIDAR1 Low pass filter DC response 145
5.23 LIDAR1 multiplexer 145
5.24 LIDAR1 output buffer 146
5.25 LIDAR1 output buffer 146
5.26 LIDAR1 simulated offsets on DC and IQ outputs 147
5.27 LIDAR1 simulated offsets and DC Gain 148
5.28 LIDAR1 Acceptance Window Diagram 149
5.29 LIDAR1 Bonding Diagram 150
5.30 LIDAR1 Chip Schematic Diagram 151
5.31 LIDAR1 LO buffer outputs 152
5.32 LIDAR1 AVDD3 pixel IR drop 153
5.33 Experiment setup - LIDAR1 155
5.34 LIDAR1 PCB schematic 156
5.35 LO spectrum 158
5.36 Determination of phase - DC offset 159
5.37 LIDAR1 IQ outputs, phase, and phase error 161
(a) LIDAR1 IQ response 161
(b) LIDAR1 IQ polar response 161
(c) LIDAR1 IQ phase 161
(d) LIDAR1 IQ phase error 161
5.38 LIDAR Transimpedance Gain with tunebias 162
5.39 LIDAR1 Amplitude response 163
5.40 LIDAR Amplitude/Phase response 164
5.41 LIDAR Amplitude/Phase response 164
5.42 LIDAR Amplitude/Phase response 165
5.43 LIDAR Amplitude/Phase response 165
5.44 LIDAR Amplitude/Phase response 166
5.45 LIDAR1 amplitude response - transient simulation 167
5.46 LIDAR1 phase response at 1, 2 and 5 MHz 169
(a) Phase response at 1 MHz 169
(b) Phase error at 1 MHz 169
(c) Phase response at 2 MHz 169
(d) Phase error at 2 MHz 169
(e) Phase response at 5 MHz 169
(f) Phase error at 5 MHz 169
5.47 LIDAR1 phase response at 10.2, 15.2 and 33.1 Mhz 170
(a) Phase response at 10.2 MHz 170

(b) Phase error at 10.2 MHz 170
(c) Phase response at 15.2 MHz 170
(d) Phase error at 15.2 MHz 170
(e) Phase response at 33.1 MHz 170
(f) Phase error at 33.1 MHz 170
5.48 LIDAR1 phase response at 47.5 MHz 171
(a) Phase response at 47.5 MHz 171
(b) Phase error at 47.5 MHz 171
5.49 LIDAR1 phase error 171
(a) Phase error with frequency 171
(b) Phase error with frequency (subset) 171
5.50 LIDAR pixel array: phase response and error 173
(a) Phase response 173
(b) Phase error 173
5.51 LIDAR1 Amplitude Image 174
5.52 LIDAR1 DC Image 174
5.53 LIDAR1 Filter Bandwidth 175
5.54 LIDAR1 dark noise 175
5.55 LIDAR1 FPN image 176
5.56 LIDAR1 Phase/DC Relationship 177

Chapter 6: Applications **179**

6.1 LIDAR1 imaging lidar 179
6.2 LIDAR1 LIDAR experiment results 181
(a) DC (mV) 181
(b) Amplitude (mV) 181
(c) Phase (degrees) 181
6.3 LIDAR1 imaging lidar 182
(a) Threshold map 182
(b) Phase (degrees) - thresholded 182
(c) Distance (m) - thresholded 182
6.4 Michelson Interferometer 183
6.5 Acousto - Optical Frequency Shifter 186
6.6 Experiment Setup - Optical Heterodyne Interferometer 187
6.7 Heterodyne interferometer phase image 187
6.8 Experiment Setup - Ultrastable Interferometer 189
6.9 Mirror mount vibration velocity 190
(a) No vibration 190

(b) 1 Hz vibration 190
(c) 62 Hz vibration 190
6.10 Standard heterodyne interferometry fringe 190
(a) No vibration 190
(b) 1 Hz vibration 190
(c) 62 Hz vibration 190
6.11 Ultrastable Experiment fringes 190
(a) No vibration 190
(b) 1 Hz vibration 190
(c) 62 Hz vibration 190
6.12 Imaging LIDAR practical scenario 192
6.13 64×64 pixel image 194

Chapter 7: Discussion and Conclusion **196**

Chapter A: C35 Wafer cross-section **201**

A.1 CMOS C35 wafer cross-section 201

Chapter B: Bias currents **202**

B.1 LIDAR1 bias resistances 203

Chapter C: Photomicrographs **204**

C.1 MLCv6 photomicrograph 204
C.2 LIDAR1 photomicrograph 205

List of Tables

Page

2.1 Summary of reviewed devices 38

4.1 MLCv6 corners analsis 108

5.1 LIDAR1 corners analysis 154

B.1 LIDAR1 bias currents 202

B.2 LIDAR1 bias currents 203

1 | Introduction

This chapter introduces detection of light and presents the rationale for this thesis.

1.1 Photography

Photography refers to the science as well as the art and practice of capturing electromagnetic radiation (both visible and invisible) present in a scene and saving it as an image. The word photography is based on the greek words $\phi\omega\eta$ and $\gamma\rho\alpha\phi\eta$ which means “drawing with light". Long before the first photographs were made, Chinese philosopher Mo Di and Greek mathematicians Aristotle and Euclid described a pinhole camera in the 5th and 4th centuries BC. In modern times photography is done electronically using an image sensor or chemically using a light-sensitive material.

Louis Daguerre invented the first practical process for image capture in the 1830s, leading to a great impact in information processing and entertainment. In 1881, the first film negatives were designed, simplifying the process of photography. James Clark Maxwell took the first colour picture in 1907, but it was only after that that plates became commercially available.

Pictures can be taken via wholly analogue means, as with film cameras, or with electronic means such as digital cameras. Digital cameras use a photosensitive array to to detect light, whereas film photography uses silver halide crystals.

Cameras are not limited to taking still images. By taking several consecutive images, i.e. a whole frame at a time, at a rapid enough rate, videos can be taken.

Most videos run at about 30 frames per second (fps), but a higher frame rate gives a higher quality video, and is necessary for high-speed photography, often desirable in sport and science. It also allows time-lapse photography, in which the frame rate is quite low, used for example in the study of plant growth.

It is immediately obvious that in all these cases the property of light under observation is its intensity. This is a measure of the energy contained in the light wave. Dark spots in the image are formed from areas reflecting little light, and bright spots in the image corresponding to objects in the scene reflecting more light to the sensor. In order to get colour images, the light from the scene can be filtered with red, green and blue optical filters (Bayer Filter), giving a palette of colours that can be used to reconstruct a colour image.

1.2 Electronic Photodetection

Modern detection of light involves the detection of light photons either by Charge Coupled Devices (CCD), or by Complementary Metal Oxide Semiconductor Devices. To make a camera, a uniform array of (usually square) light sensitive devices (pixels or photo-sites) are used.

Choosing the most appropriate pixel is one of the most important design decisions. It will set the limits of sensitivity and bandwidth of the system. The size of the photo-sensitive part of each pixel also affects the noise performance. This is often parametrised by characterising the pixel with a parameter known as *fill factor*, defined in Equation 1.1.

$$\text{fill factor} = \frac{\text{photo} - \text{sensitive area}}{\text{pixel area}} \tag{1.1}$$

A high fill factor is desirable because it means most of the pixel is used for

photon detection. There is often a trade-off because in-pixel processing circuits contribute to the area used by the pixel. Small pixels are desirable because they make it possible to fit more pixels in a given area. However they usually have a poorer noise performance due to the smaller photo-sites and tighter space usage.

1.2.1 Types of Photosensitive elements

Photodiodes are a most basic photosensitive element. They are basically the same as a diode, formed as a PN semiconductor junction. Photodiodes often use a P-I-N junction in order to improve the speed of response. They are operated in reverse-bias. Photodiodes exhibit excellent linearity of output current as a function of input light, and can receive light with wavelength from 190 nm to 1100 nm (Silicon). They have relatively low cost and can be very rugged in build. They usually however have no internal gain (except for avalanche photodiodes).

Active pixel sensors (APS) are image sensors consisting of an integrated circuit that contains an array of pixel sensors. Each pixel contains both a light sensor and an active amplifier. There are many types of active pixel sensors including the CMOS APS commonly used in cell phone cameras, web cameras, and some DSLRs. An image sensor produced by a CMOS process is also known as a CMOS sensor, and has emerged as an alternative to Charge-coupled device (CCD) sensors. The schematic of an APS is shown in Figure 1.1.

Charge-coupled devices (CCD), which are used to record images in astronomy, digital photography, and digital cinematography. CCDs were developed in 1969 at AT&T labs [1]. They are made by using p-doped MOS capacitors to convert photons into electrical charge, and shift them from one photo-site to the next to the reading terminal. Each site acts as a storage bin, and by appropriate manipulation of electrode potential highly efficient transfer of the charge occurs.

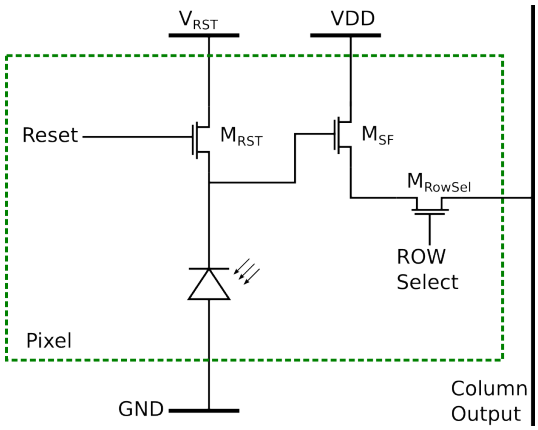

Figure 1.1: Three (3) Transistor Active Pixel Sensor

At the reading terminal, the charge may be amplified, digitised and processed further. They are highly efficient devices, with up to 95% quantum efficiency.

Chemical detectors, such as photographic plates, in which a silver halide molecule is split into an atom of metallic silver and a halogen atom. The photographic developer causes adjacent molecules to split similarly. Cryogenic detectors are sufficiently sensitive to measure the energy of single x-ray, visible and infrared photons. Although before the 1990s photographic plates were the most common in astronomy. Glass-backed plates were used rather than film, because they do not shrink or deform in going between wet and dry condition, or under other disturbances.

Photo-resistors or light dependent resistors (LDR) which change resistance according to light intensity. Photovoltaic cells or solar cells which produce a voltage and supply an electric current when illuminated Photodiodes which can operate in photovoltaic mode or photo-conductive mode.

Photomultiplier tubes contain a photo-cathode which emits electrons when illuminated, the electrons are then amplified by a chain of dynodes such that the tube conducts a current proportional to the light intensity.

Photo-transistors act like amplifying photodiodes. Normal CMOS transistors usually have a poly-silicon gate, meaning that photon-conversion can occur in the transistor.

Quantum dot photo-conductors or photodiodes, which can handle wavelengths in the visible and infrared spectral regions.

1.2.2 Performance Parameters for a CMOS photodetector

Concentrating on CMOS photodetectors - particularly photodiodes - critical performance parameters of a CMOS photodetector include, but are not limited to the following:

Responsivity/Quantum Efficiency (R/η): This is the ratio of generated photocurrent to incident light power, typically expressed in Amps/Watt when used in photoconductive mode. The responsivity may also be expressed as a Quantum efficiency (at a specific wavelength) or the ratio of the number of photo-generated carriers to incident photons and thus a unit-less quantity.

$$Q_E = \frac{N_{electron}}{N_{photons}} \tag{1.2}$$

$$R(\lambda) = \frac{Q_E e}{hf} \tag{1.3}$$

Photographic film typically has a QE of much less than 10%, while CCDs can have a QE of well over 90% at some wavelengths.

Dark current: This is the current flowing through the photodiode in the absence of light. For integrating devices, it represents the charge present in the absent of light. The dark current includes photocurrent generated by background radiation and the saturation current of the semiconductor junction. Dark current must be accounted for by calibration if a photodiode is used to make an accurate optical

measurement, and it is also a source of noise.

Noise-equivalent power (NEP): This is the minimum input optical power to generate detectable photocurrent. It is equal to the RMS noise current in a 1 Hz bandwidth. The related characteristic detectivity (D) is the inverse of NEP, 1/NEP; and the specific detectivity (D^*) is the detectivity normalised to the area (A) of the photo-detector, $D^*=D\sqrt{A}$. The NEP is roughly the minimum detectable input power of a photodiode. It is often quoted in $W/Hz^{\frac{1}{2}}$.

1.3 Modulated Light cameras

Measuring intensity provides information about the nature and state of the scene or environment under consideration, but sometimes this does not convey enough information, and the use of modulated light is required. A very simple explanation is that the light is "tagged", and we need a camera capable of locking into that tag and retrieving the information is required.

The light can be at source by a characteristic of the scene itself or it is possible to introduce the modulated light into the scene. For example, in fluorescence imaging, dyes can be added to an experiment. These dyes have the property of fluorescing when illuminated with light at the right wavelength. For example, if illuminated with ultra-violet right, they absorb the energy and release it as heat and light with a different wavelength. This light is released for a few nanoseconds, and this period corresponds to square wave modulation with a frequency inversely related to the light period [2].

The light may be modulated in several ways, but in most cases it is amplitude modulated sinusoidally, and the phase and amplitude is measured by a camera that is designed to detect and demodulate the light. Smart pixels are capable

of performing this operation at the pixel level, so that they provide phase and amplitude information at the outputs of each pixel. This camera is then called a modulated light camera (MLC).

1.4 Applications

There are several applications of modulated light cameras. This section presents two applications (specific but not exclusive) which were intended as targets to utilise the MLC.

1.4.1 Imaging LIDAR

Under some conditions, detecting the intensity of light in a scene does not provide sufficient information about the characters in the scene. Applying some modulated components of light to the scene (by structured illumination or intensity modulation) can provide further information.

The scene can contain modulated light components of itself, or modulated light may be introduced to make it easier to characterise the scene, or identify a particular object/specimen. The scene characteristics affect the modulated light, and correlating the received light with a reference can give extra information about the scene or specimen.

RAdio **D**etection and **R**anging (RADAR) is implemented by projecting a modulated radio wave from an antenna, and the wave reflected from the scene is compared with a reference wave (usually same frequency or waveshape) to calculate the ranges to objects in the scene. This method of range determination is a kind of **Time-Of-Flight Ranging** technique.

Imaging **LI**ght **D**etection **A**nd **R**anging (LIDAR) using CMOS Modulated Light Cameras works on the same principle as RADAR. Intensity modulated light is projected onto a target, and the phase of the return light used to determine the range to the target. This setup is shown in Figure 1.2.

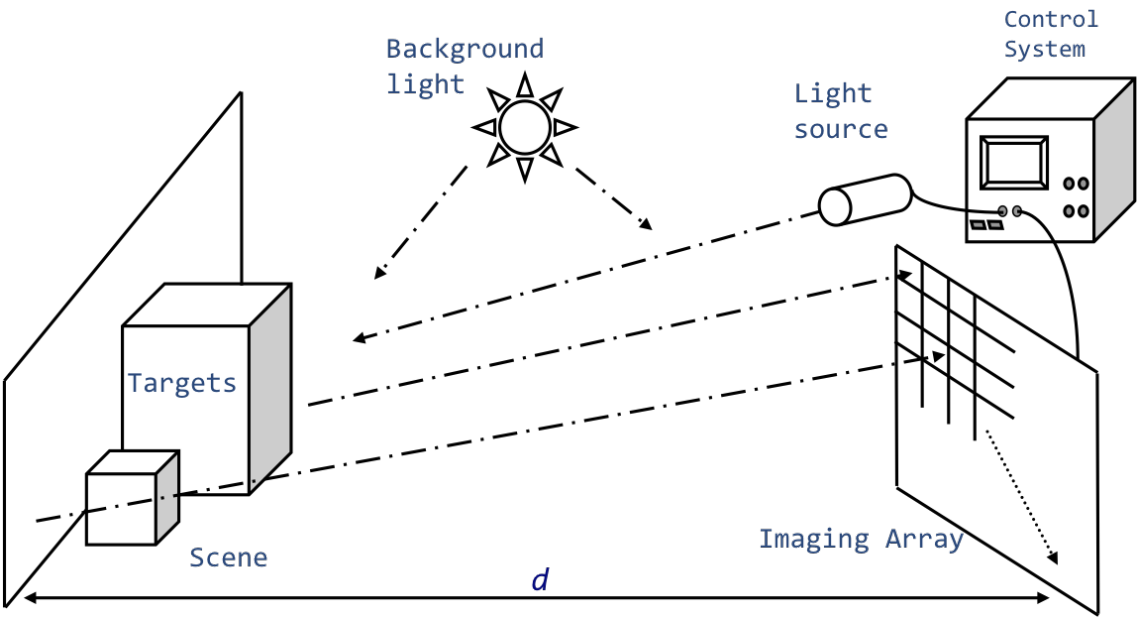

Figure 1.2: The diagram shows a typical setup for an Imaging LIDAR measurement using a Modulated Light Camera.

There exist ranging systems that typically contain a single photo-sensor, and by projecting some light, the range to a single point in the scene can be measured. An example of this is the Bosch PLR 25 [3]. It has a Class 2 laser with a wavelength of 625 nm, and can measure from 0.05 to 25m with an accuracy of 2mm. There also exist systems that are capable of scanning a scene and determining the nature of the scene.

An application for the MLC is a LIDAR system capable of rapid full wide-field imaging using a full custom CMOS photo-sensor. An array of pixels independently computes range by measuring phase information. By combining

the range information with the 2D spatial picture, a 3D picture can be composed, giving more information about the nature and placement of objects in the scene. It is also possible to place modulated light sources in the scene itself, so that they act as markers for object detection, identification and range determination.

The extension to widefield imaging demands small pixels capable of independent light detection and demodulation, and also requires that these are fabricated in a high enough density to provide good spatial resolution.

The range information received is subject to error from shadowing, noise and variations in electronics both on and off-chip. In order to improve the range/depth resolution, three options are available.

1. The first is to increase the modulation frequency. If the phase measurement accuracy can be taken as constant (for example 1% from 1 to 100 MHz), then it means that a 1% absolute accuracy at 100 MHz translates to a resolution of 3 cm.

2. The second option is to improve the phase and amplitude measurement accuracy. This can be through any of the following:

   - Noise reduction. This noise may be optical or electronic. This includes thermal noise, background illumination, optical shot noise and shadowing.
   - Through increased linearity in the demodulation stage. Demodulation from the high frequency to the low frequency is done using a non-linear element such as a diode. Carefully design of the demodulation circuit is required for the best phase accuracy under many conditions.
   - Higher conversion gain. This makes sure that the desired signal dominates the signal chain, ensuring a good signal to noise ratio.
   - An ADC on-chip generally means that the signal is digitised even

before leaving the chip, making it more resilient to off-chip noise sources.

- Using differential outputs means that the noise picked up from off-chip components is much reduced.

3. The third option is to design the chip with pixel-to-pixel variation in mind. Because of the fabrication process variations, it is necessary to design the pixel, and lay out the electronics so that any variation (for example, transistor width to length ratio, especially for differential pairs) causes as little change as possible to the operation of the device as a whole. It is also possible to use various techniques such as correlated double sampling to correct for errors.

1.4.2 Interferometry

Interferometry is the superposition of electromagnetic radiation. It was intended that the MLC should provide extra features that would make it useful for mitigating some of the common problems associated with interferometers such as temporal phase shift due to changes in optical path length and vibrations. This makes it useful in the inspection of samples in industrial systems as well as other instrumentation systems.

An interferometer offers a highly accurate method of optical path-length measurement. Riza [4] reports an instrument with the potential to measure optical path length at angstrom resolution over continuous thickness in the micrometer range. This optical path length could be used to calculate the thickness of any material if the refractive index is known or to measure the refractive index of the material if the thickness is known.

The use of modulated light camera in an interferometer could greatly reduce some of the noise sources that challenge their effective use in all environments. A

particular noise source is mechanical vibration. An objective is therefore to make the modulated light suitable for use in such an interferometer.

The modulated light camera also improves on some existing technology because by offering a wide-field image, there is no need for any scanning.

1.5 Aims/Objectives

Overall aims for this research can be briefly summarised as follows. These are motivated by the applications listed above. The following objectives were therefore set.

- A high frame rate that allows quick acquisition of wide-field depth information is desirable. This is relevant for time-of-flight purposes, so that fast travelling objects can be imaged with depth information at video frame rates. A target of at least 30 frames per second is desired, since this will closely approximate commercially available video cameras.

- Design a photosensitive pixel with a very high Gain Bandwidth response. For example. An AC photocurrent of 1 pA at 100 MHz needs a transimpedance gain-bandwidth product of 1 TΩ (340 dBΩ) to be converted to a 1 mV electrical signal. This will allow good signal detection even under low light conditions.

- Small pixel size, so that more pixels can be fabricated per chip. This will increase the spatial resolution of the sensor. A design objective is a pixel pitch of 100 μm or less.

- Design the entire device to use as little current as possible, as it may be used in low power environments, such as mobile devices. A design objective is to have a power consumption of less than 1 W.

- Characterise the device providing sufficient information for a number of applications.
- RF output. This is particularly important for the interferometry applications. A bandwidth of 100 MHz was set as an objective.
- It is desired that the camera will be able to operate at light levels comparable to background radiation or even lower, so that it does not require excessively complex light sources. This will make it easy to build and setup, and also available in a wide area of applications were low light is required such as bio-medical imaging environments. An objective of 1 nA was set based on review of previous work.

1.6 Thesis Layout

Various implementations of modulated light cameras or other detectors which can be configured to operate as such are presented in Chapter 2. Their properties are summarised in Table 2.1.

Chapter 3 presents the mathematical theory necessary for the implementation of modulated cameras. It investigates the light budgets and noise concerns. It goes on to present an electronic implementation of a modulated light detector. This design serves as the masthead front-end for this thesis.

Chapter 4 introduces the two devices that were designed and fabricated as test designs. The first was a single front-end with amplification. The second is a complete camera, but its effectiveness was crippled by a design flaw. These devices led the way to the final device.

The final device is presented in Chapter 5. The chapter presents the design, simulation results and layout of some key parts. The experimental results from

characterising the device are also shown, and this leads to a discussion on the phase error.

In Chapter 6, the design presented in Chapter 5 is applied to a number of scenarios and the results are presented. These include an imaging LIDAR experiment and a heterodyne interferometer experiment.

Chapter 7 discusses the project and draws conclusions on the knowledge acquired. It then suggests some research that could be carried out to further improve the operation of the devices in this thesis.

Photomicrographs of the devices and some other information is provided at the end in the appendices.

2 | Literature Review

This chapter presents a review of pixels or cameras that have been demonstrated for use as modulated light detectors. There is also a brief discussion of devices which are not designed primarily as modulated light detectors, but may be configured for use as such. A few time-of-flight cameras are also presented in this chapter.

2.1 Continuous-Time Cameras

2.1.1 Stenflo

Lock In Cameras were first mentioned by Stenflo and Povel in 1985 [5], when they wrote about a camera that could be used in polarimetry, using the lock-in technique. They note that it is possible to attach a lock-in amplifier to a single pixel system, but this becomes very cumbersome for a multi-pixel system. They suggest reading the pixel array at a very high frame rate, and using the pixel values to perform off-chip demodulation. This would work, but since CCDs were then limited to a readout rate of about 5 MHz, this means the frame would have been limited to about 32×32 pixels, or else low modulation frequencies. With an array of 128×128 pixels, taking 4 samples per modulation cycle per pixel, the maximum modulation frequency detectable would work out to about 1 kHz.

2.1.2 Povel

A better alternative to the system suggested by Stenflo [5] is the device suggested by Povel [6]. This design improves on Stenflo's by using a slit mask with a commercially available CCD camera. The slit mask shields alternative rows from light. In the first half cycle of the modulation period, the light is integrated onto the exposed rows, and the charge is quickly shifted down to the covered rows, just as a CCD normally functions. This means the charge from the first half is now in the shielded rows, and exposed rows are empty. During the second half-period, the light is once again integrated onto the exposed pixels, and the charges are quickly shifted up one row. The charge now on the exposed row is from the first half-cycle. The cycle is then repeated. At this point the signal may be read, or it is possible to integrate for more cycles to increase the signal level. This technique was successfully used to measure frequencies of 50 kHz and 100 kHz. A schematic of the design is shown in Figure 2.1.

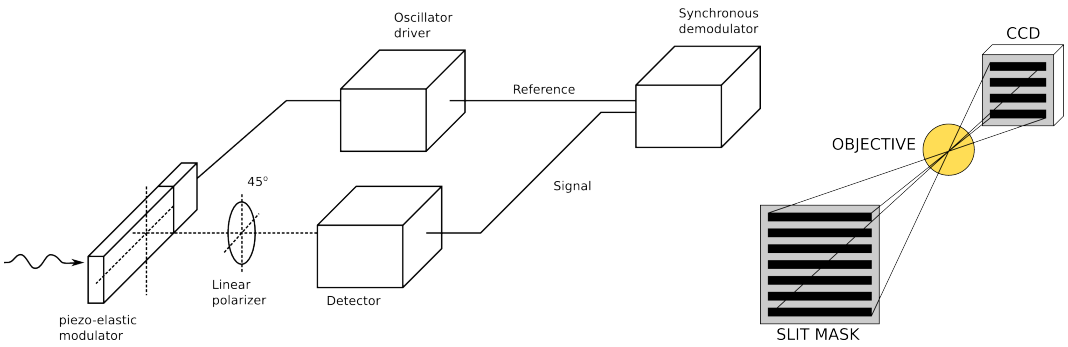

(a) Povel detection setup **(b)** Slit mask on the CCD

Figure 2.1: Povel's modulated light sensor

This implementation suffers from the fact that using a slit mask to cover some pixels is difficult to set up and is prone to misalignment. This problem may be solved by using a custom design in which a metal layer covers the rows which are never exposed. The real disadvantage is the fact that half of the available light sensitive area is not used. This corresponds to a loss of spatial resolution. Again this may be alleviated by using a custom solution with smaller storage

cells. Another problem with this implementation is that during charge shifting, a finite charge will add to the transferred signal from the light currently exposed to the CCD.

2.1.3 Spirig

Since Povel's system only takes 2 samples per modulation period, it is only capable of detecting the amplitude and offset of the light signal, and this is correct only if the phase difference between the signal and charge transfer cycle is known and kept constant. Spirig [7] improves Povel's design by increasing the samples per period from 2 to 4. This makes measurement of phase, amplitude and offset possible.

This design uses a custom fabricated 3×3 array with each pixel consisting of a single photosensitive area (a photogate) with four storage gates. This new device was christened as a lock-in CCD camera. Transmission gates between the photogate and storage gates control the integrated charge to the correct storage gate. However with a fill factor of 17 % and a pixel size of 87.5 μm × 80 μm, the pixel may be considered rather large since it does not implement quadrature demodulation. The authors postulate a maximum modulation frequency of 30 MHz using the process, and measure frequencies up to 100 kHz. In later work, Spirig investigates multi-tap lock-in CCDs with eight storage bins, allowing the determination of phase, amplitude and offset with greater certainty [8].

2.1.4 Lange

Range finding is a major application of modulated light cameras. Suggested by Spirig [8], ranging using modulated light was first implemented in a full-field camera in 2001 by Robert Lange, as reported in [9]. Using the speed of light as

a constant, it is possible to measure distance by measuring the time of flight for a pulse of light to travel from a reference point to the point of interest and back. A similar principle uses a continuous wave modulated source instead of a pulsed wave. This method measures range by measuring the phase of the signal relative to the source signal. When the phase difference is known the range to the object can be calculated as Equation 2.1, [10]

$$d = \frac{c}{2} \cdot \tau_{\text{ToF}} = \frac{c}{2} \cdot \frac{\Delta\phi_{\text{ToF}}}{2\pi \cdot f_{mod}} \tag{2.1}$$

The maximum range measurable with this system depends on the frequency of modulation, and is half of the wavelength corresponding to the modulation frequency. Thus a 10° phase measurement would be same as a 370° measurement. To get around this problem, multiple modulation frequencies can be used. Lange uses a single modulation frequency, employing a CCD that integrates four samples per second. He uses a modulation frequency of about 20 MHz, allowing for some relatively high resolution imaging.

2.2 CMOS Integrating Cameras

2.2.1 Ando

Ando claims the first CMOS implementation of a lock-in camera [11]. This is based on the model suggested earlier by Povel [6], in that two storage capacitors are used to store the integrated charge, one for each half of the cycle. The schematic for the pixel is shown in Figure 2.2. This was implemented in a 100×100 pixel single phase correlation image sensor (CIS), and a 64×64 pixel three-phase CIS [12]. In both of the devices, basic functionality is the same, but the three-phase system allows the measurement of the phase of the modulated signal to be measured as well as the amplitude.

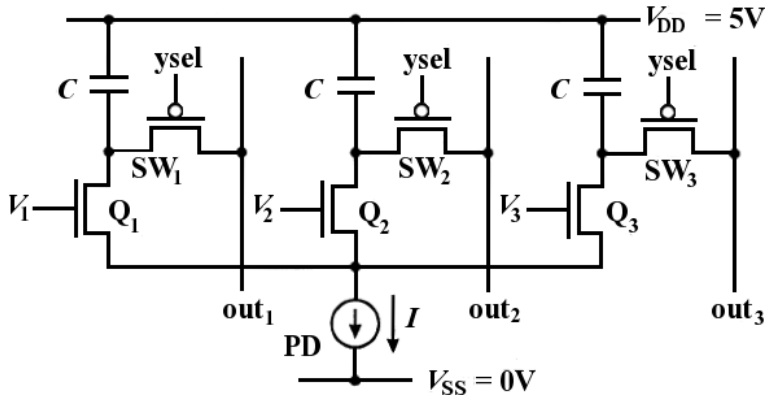

Figure 2.2: 3-phase Correlation Image Sensor (CIS) pixel designed by Ando. [11]

The pixels operate in 2 modes, the first being a mode similar to the CCD implementation by Spirig [7]. The integration capacitor C is reset with switch SW_i to V_{DD}. SW_i is then opened until next reset. Control voltages V_i are then operated as non-overlapping pulses so that only one of the phases is in operation at any one time. The capacitor is discharged to give 3 results. These results are then used to calculate the DC offset, amplitude and phase difference.

The second mode makes more efficient use of the light by integrating with all capacitors at once. Readout still requires a dead-time. The V_i control signals are identical, but have a 120° phase difference between them. The difference with the first mode is that continuous signals can be used. Using a sine wave is advantageous as the mixing is done at a single frequency, as opposed to the square-wave mixing which requires an infinite bandwidth.

2.2.2 Schwarte

The Photonic Mixer Device (PMD) implemented by Schwarte as described in [13] performs the demodulation on the sensing device. This is a kind of electro-optical mixer. This is achieved by using two reverse biased photodiodes (formed from p-type substrate and an n+ diffusion. The junction is not exposed, but the substrate region between the diodes is left exposed through transparent electrodes. A cross-

sectional view is shown in Figure 2.3.

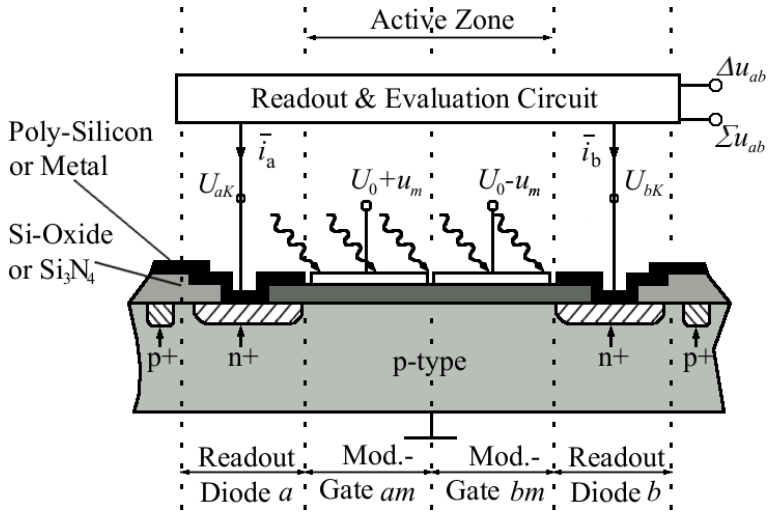

Figure 2.3: The diagram shows the cross-section for the PMD pixel. [13]

As shown in the figure above, each of the photodiodes can be read as a normal single photodiode pixel. When the control voltages applied to the transparent gates are equal, the photocurrent is split equally between the two diodes. By using different voltages on each photodiode, it is possible to sweep the photo-electrons towards the more negative gate. By applying periodic signals 180° out of phase with each other ($V_{AB} = V_A$ - V_B), a push pull effect can be generated, creating the same result as that seen in a differential mixer. However in practice, not all the photocurrent-electrons flows towards the more positive gate, but some of the electrons drift to the more negative gate.

To detect the current, each diode is connected to a current readout circuit. This integrates the current onto a storage capacitor and provides a voltage output. A reset transistor is used to set the integration period. This is very similar to the technique used in the CCD domain by Povel [6] and Spirig [7, 8].

In a later device, Schwarte proposes another device with 3 transparent control gates instead of two, but still using two diodes [14]. With this method, the two

outer gates operate in push-pull mode as before, and the middle gate is held at a voltage midway between those two. This extra control gate has the effect of making the potential V_{AB} more uniform, thus resulting in more efficient charge transfer. This results in a more linear response, higher modulation frequency capability, and the device works with a smaller gate voltage range.

The inventors of the PMD designed it primarily for range-finding, and that is the use for which it is most discussed. In [10, 15] and similar literature, it's implementation for optical level gauging and 3D imaging is discussed. Sinusoidal signals are used rather than square waves, resulting in cleaner mixing, analogous to continuous wave mixing.

Gulden uses a technique known as Frequency Stepped Continuous Wave, which works by taking distance measurements over a stepped range of frequencies, and then using spectral analysis to find the distances. He manages to determine the range to two objects at the same time to an accuracy of 2.5 cm. Further discussion of FSCW may be found in Wu [16].

2.2.3 Ohta

The idea of two phase integration is taken further by Ohta [17]. A camera with 64×64 pixels is implemented, with each pixel containing a photogate and two independent floating diffusions (used to accumulate the charge - FD1 and FD2). The schematic is shown in Figure 2.4.

This pixel is designed for detection of square-wave modulation, in which the modulation is either totally present or not, ie. **ON** or **OFF**. TX1 and TX2 are used to integrate the photocurrent from PG onto FD1 and FD2 respectively, and then the voltages can be read out non-destructively through OUT1 and OUT2.

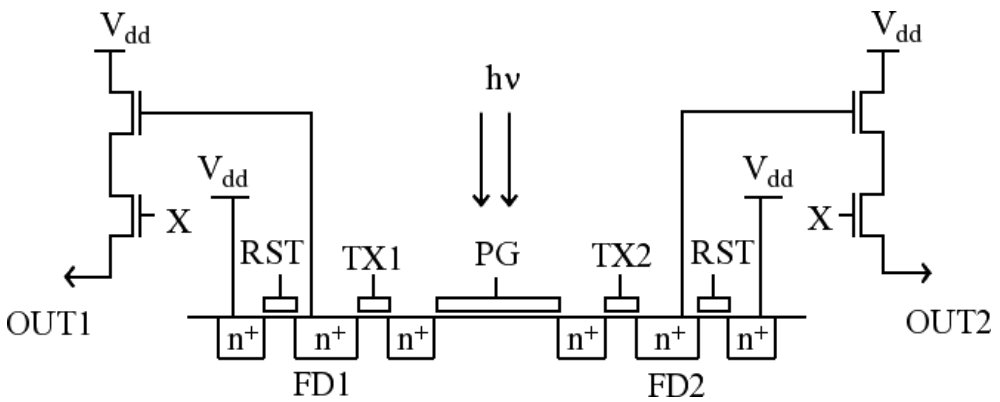

Figure 2.4: The figure shows the schematic of the pixel designed by Ohta in his 64×64 pixel camera implemented in Ohta [17].

The difference of these two readings can be used to determine the intensity of the modulated signal. By choosing the integration period, ie the number of times the signal is integrated onto the diffusions, it is possible to trade between frame rate and sensitivity.

2.2.4 Oike

Oike's pixel addresses the problem that is present in most modulated light applications, namely that the modulation depth is quite low. Their design [18] uses a series of current mirrors and a low pass filter to seperate the DC current from the AC current. The schematic for the pixel layout is shown in Figure 2.5, and Figure 2.6 shows the circuit for the front end.

The circuit uses a photodiode as a detector, and the detected photocurrent (I_{pd}) is mirrored using a cascode current mirror. This current is mirrored twice more (αI_{pd}), resulting in a current sink. One channel is mirrored a final time, creating a current source. This is low pass filtered using a capacitor, and the difference between source and sink currents gives the modulation component. The modulation component is then converted to a voltage using a logarithmic load.

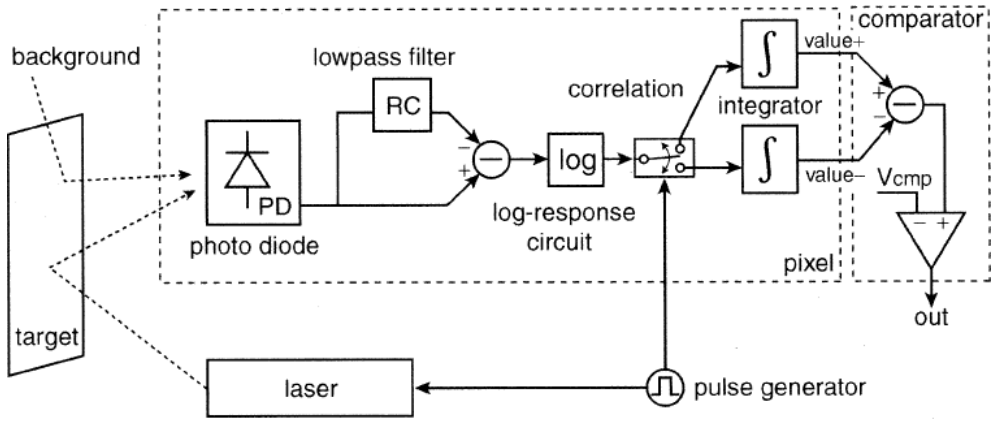

Figure 2.5: Pixel schematic for Oike's Pixel

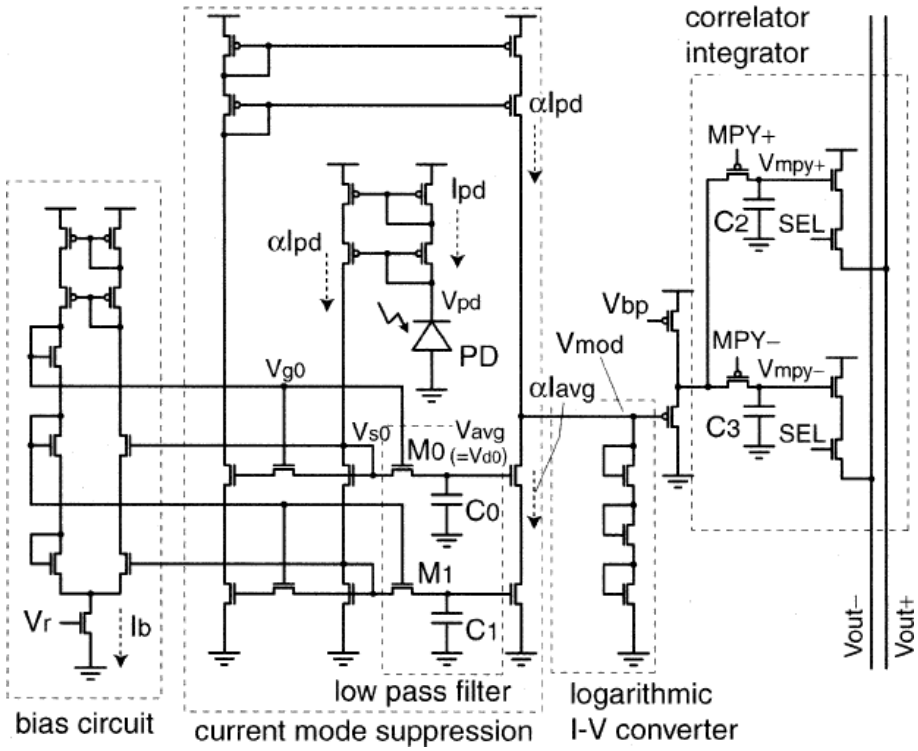

Figure 2.6: Current Suppression and front-end circuit

This may be illustrated simply as follows:

$$\begin{aligned} I_1 &= DC + AC \\ &= \alpha I_{pd} \\ I_2 &= DC \\ &= \alpha I_{avg} \\ I_1 - I_2 &= (DC + AC) - DC \\ &= AC \end{aligned}$$

2.2.5 Stoppa

This is a design demonstrated by David Stoppa in [19]. This design is implemented in 0.18 μm CMOS process. It uses a buried channel photo-detector. Each pixel has a fill factor of 24%, and the pitch is 10 μm. It is reported to have a maximum demodulation frequency of 50 MHz, with a contrast of 29.5 %. There are 80 $\times$ 60 pixels in the camera. It operates very similarly to the PMD device discussed earlier, but differs in that it uses a surface channel instead of a buried channel. A schematic is shown in Figure 2.7.

The camera is designed for time-of-flight imaging, can produce images at a rate of 5-20 frames per second over a range of 3 to 6 metres, with a precision of 2.7 cm at 50 MHz.

2.2.6 Light

Roger Light implements a custom integrated circuit in 0.35 μm CMOS process. The circuit consists of an integrating type pixel whose output is connected to a comparator. The amount of time taken for the photodiode to reach a particular voltage can be measured by coupling a counter to the output of the comparator.

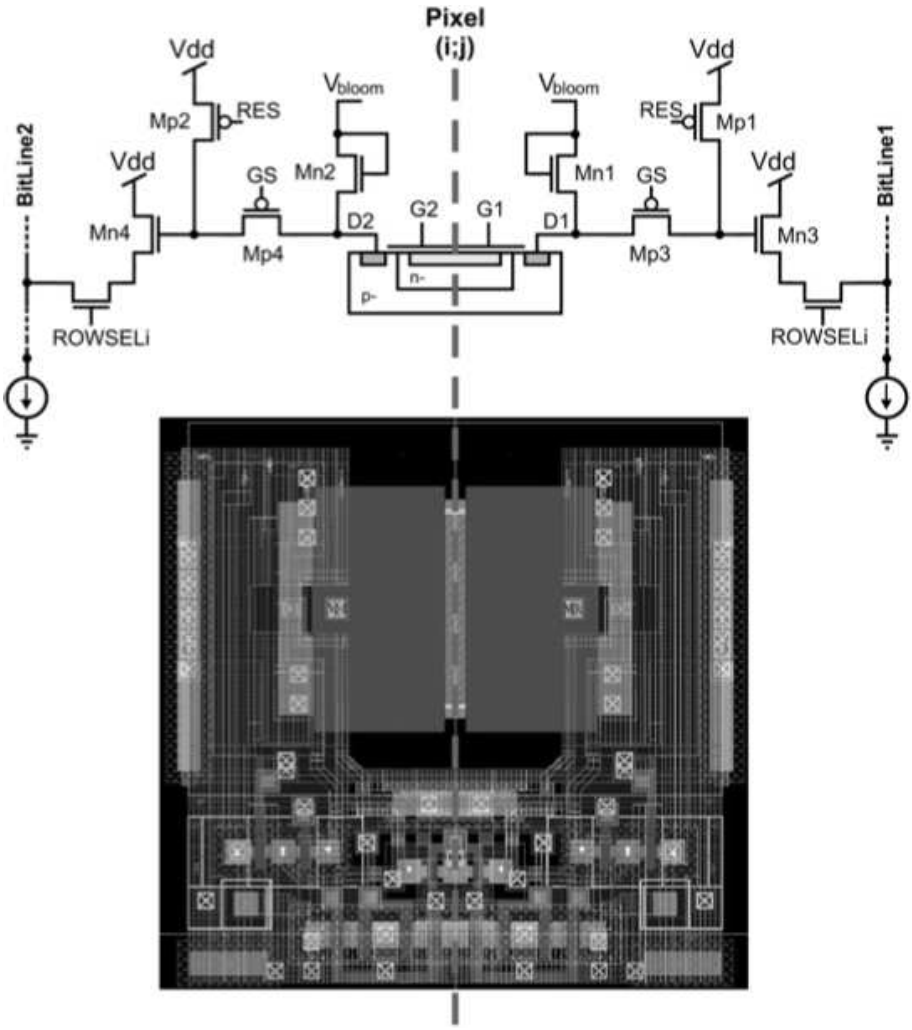

Figure 2.7: The Stoppa Range Sensor. [19]

The camera has 128 × 128 pixels, and is reported [20] to detect modulated light signals at a modulation depth of 1.39% and a modulation frequency of 420 Hz. It has been operated at modulation frequencies up to 2.5 kHz. The layout for a single pixel is shown in Figure 2.8.

2.3 CMOS Continuous Time Cameras

This section discusses a number of CMOS pixels and cameras which are capable of continuous detection of modulated without integration on the photodiode or a capacitor. It includes pixels that are designed for optical communication systems, since these are often capable of Gigahertz modulation frequencies.

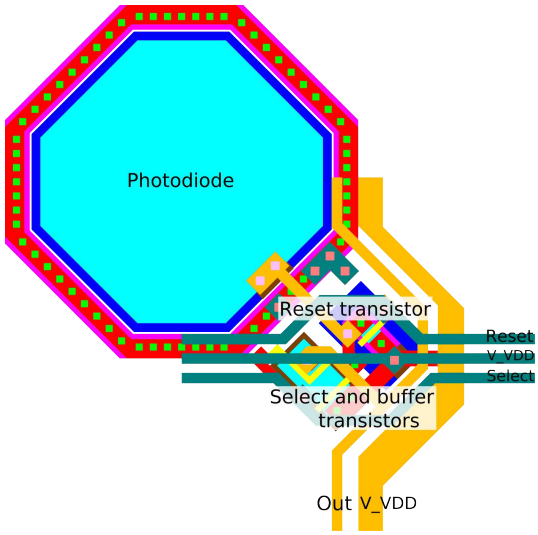

Figure 2.8: Layout for Roger Light's integrating pixel design. [20]

2.3.1 Benten

The authors in [21] apply the concept of traditional electronic lock-in techniques to an optical system. They propose the system as an instrumentation solution for measuring low frequency signals for use in measuring oxygen saturation in arteries, and dental pulp vitality. This application involves measurements inside the buccal cavity, and therefore a compact sensor is required. An optical fibre system is used to deliver and sense the signals in the mouth.

An innovation with this particular design is that it allows the simultaneous detection of light signals of two different modulation frequencies. The sensor consists of two detection paths, one for each modulation frequency. Each path comprises a switching multiplexer or square wave mixer. The input signal is switched between two amplifiers. The next stage in the path is low pass filter, shared by both amplifiers. The amplitude of the low pass filter is proportional to the amplitude of the input signal. By using a square wave mixer, it is possible to use the modulation frequencies f_s and $2f_s$, because odd-order harmonics are created by the mixing which do not contaminate with the demodulation of each path.

In summary, the input reduced noise current spectral density is between 0.20 and $0.30\,\mathrm{pA}/\sqrt{\mathrm{Hz}}$ at all relevant frequencies, and the total programmable channel transimpedance is between $7\,\mathrm{M\Omega}$ and $500\,\mathrm{M\Omega}$, with a low -3 dB bandwidth frequency of at least 50 Hz, and an upper -3 dB bandwidth frequency of 40 kHz, maximum voltage swing at the demodulator output of 2.4 V.

The use of optical fibres limits the number of pixels that this system can serve, meaning that they only present a single-pixel system. It however has the advantage that it is optimised for low noise and high sensitivity, having a transimpedance amplifier with a gain of $2\,\mathrm{M\Omega}$. It is implemented in a BiCMOS process chosen to reduce noise (specifically 1/f noise). The full device uses an area of 2.9 mm $\times$ 0.45 mm.

2.3.2 Bourquin

[22] present a continuous wave detector similar to the detector presented by [21]. It is implemented as a 58 $\times$ 58 pixel camera. Each pixel consists of a photodiode, a voltage controlled current source, an amplifier, a square-wave mixer and a low-pass filter. The photodiode occupies an area of $35\,\mu$m $\times$ $35\,\mu$m, and the pixel pitch is $110\,\mu$m. The whole chip occupies an area of 7.2 mm $\times$ 7.2 mm. The schematic is shown in Figure 2.9.

Each pixel uses a feedback loop between the filter and the amplifier to ensure that the amplifier is operating under optimum conditions, and also regulates the frequency response. This camera is capable of detecting signals from 1 kHz to 1 MHz, and a pixel rate of 3 MHz.

The authors report that the AC gain is 8.5 MV/W, and the RMS noise is given as

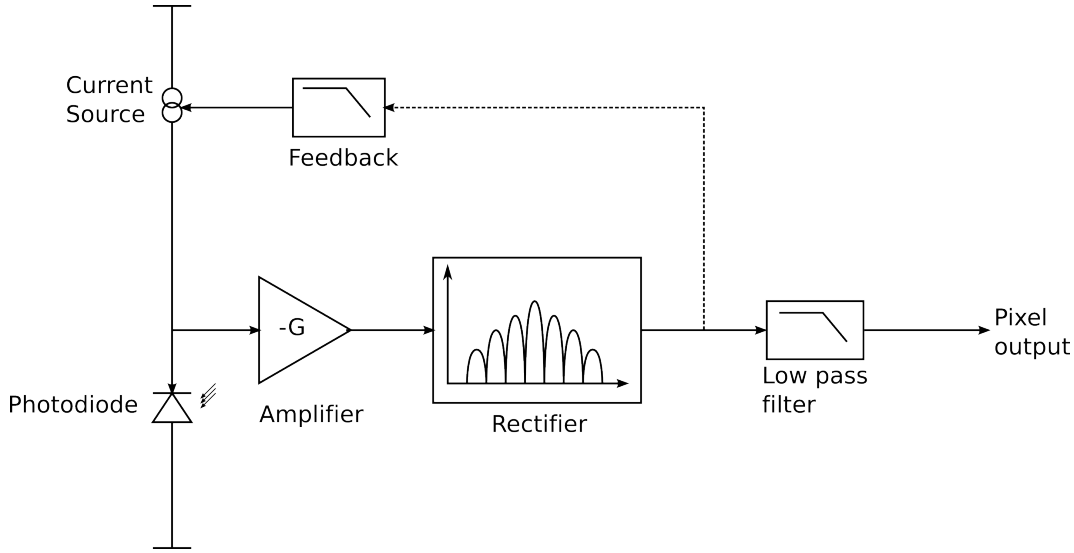

Figure 2.9: Schematic for Bourquin Pixel

1.2 mV, corresponding to an input referred noise of 142 pW with a filter bandwidth of 35 kHz.

2.3.3 Lu

This design presented in [23,24] uses a buried double p-n junction (BDJ) detector, a transimpedance amplifier, differential amplifier, mixer and finally a low pass filter. The BDJ has outputs that are sensitive to differnet ranges of wavelengths because of the differing junction depths. Each output is demodulated using an identical channel.

The amplifiers in this work consume an area of 0.2 mm^2 and consume 1.3 mW, which is substantial quantity. The photodectector is 1 mm^2, and each mixer is 0.15 mm^2 and consumes 6 mW. It may be estimated considering the 10 pF capacitors used in the filters that the area per pixel is at least 2.5 mm^2, and the power consumption is about 20 mW per pixel, making it not particularly suitable for a full-field camera array.

This camera shines brightest in that it is optimised for sensitivity and low noise. The ability to measure suitably separate wavelengths allows an application to

flourescence imaging. It can be used where two dyes with different emission wavelengths are in use.

2.3.4 Pitter 2003

This work [25] is a 4×4 pixel array that is fabricated for measuring modulated thermo-reflectance. Each pixel has a logarithmic front-end, amplification, bandpass filtering and mixing via two channels of a switched capacitor and integrating capacitor demodulation systems, with different channels for the I and Q phases. Each pixel is $200\,\mu$m by $200\,\mu$m with a 9% fill factor.

As shown in Figure 2.10, C_1 is the switched capacitor and C_2 is the integrating capacitor. Φ_1 and Φ_2 are non-overlapping clocks at the same frequency as the modulated light signal. The signal is switched onto C_1 by Φ_1 and integrated by ϕ_2 on C_2. This happens for both the I and the Q channels, with the clock signals being 90° out of phase.

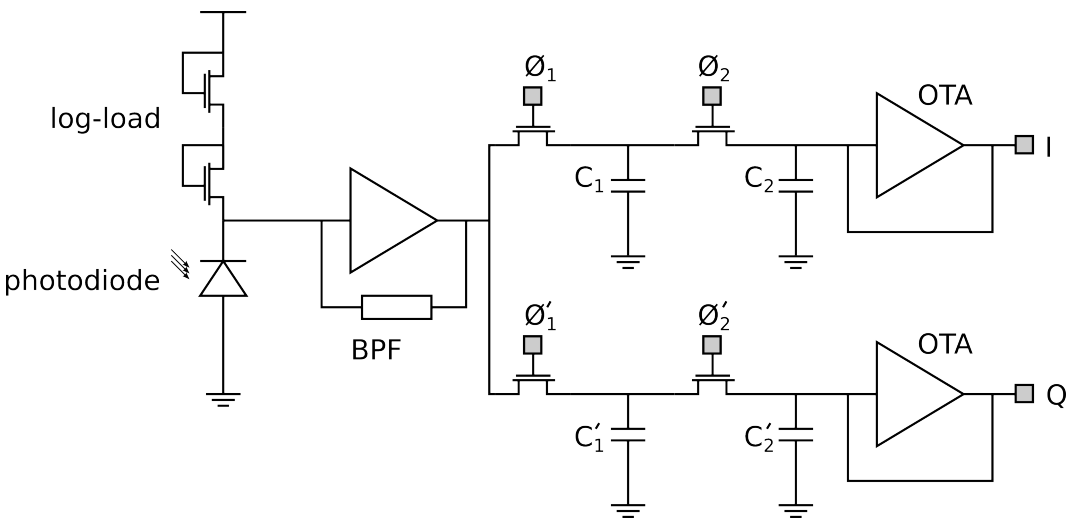

Figure 2.10: Circuit schematic for Pitter's Modulated Thermoreflectance pixel

2.3.5 Pitter 2004

This represents a follow-up on the design reviewed in section 2.3.4, and is implemented as a 64 by 64 array [26]. The processing is performed at the column level, rather than at the pixel level. Thus the pixel contains only an IV converter, a buffer and a selection switch. The remainder of the signal processing: amplification and demodulation is performed with circuits shared at the pixel level. Each pixel has a pitch of 25 μm, with a fill factor of 56 %. The total area is 3.3 $\times$ 2.5 mm, with each column laid out in a strup of 25 $\times$ 1200 μm.

Each pixel in this design contains a deep photodiode implemented in NTUB to P-Substrate with a size of 22 $\times$ 16 μm, the AC signal is highpass filtered and amplified with a hysteritic differentiator circuit (HD). This is an amplifier with a lowpass feedback network and has a gain of 40 dB. The demodulators are clocked independently , the most useful being a 90° phase difference for IQ demodulation of sinusoidally modulated light. It is also possible to clock them as a pair of boxcar averaging circuits. The layout is shown in Figure 2.11

This implementation is not particularly efficient because only one row can be used at a time. Whilst this is better than scanning methods, at any time 63 of 64 rows are not in use, and it represents a rather low frame rate.

2.3.6 Dmochowski 2004

This design is similar to [24], in that Dmochowski [27] uses a pixel that has continuous wave mixer with two channels. The channels are for in-phase and quadrature mixing, instead of differing wavelengths. The emphasis is on higher frequency demodulation. The schematic showing the detail of the front-end as well as the remainder of the pixel is shown in Figure 2.12.

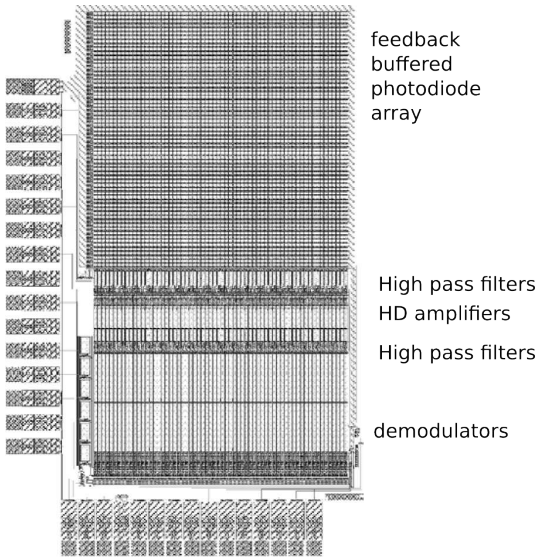

Figure 2.11: Layout of the modulated camera showing the photodiode array and synchronous detection circuitry. [26]

The pixel uses a logarithmic front-end with a regulated cascode circuit, allowing its use from 500 kHz to 25 MHz. Each pixel is completely independent, containing the amplification, mixing and low pass filtering circuits. The fill factor is 4 %, with a pixel pitch of 250 μm. It also uses 180 μA per pixel, making it a power hungry device when scaled up.

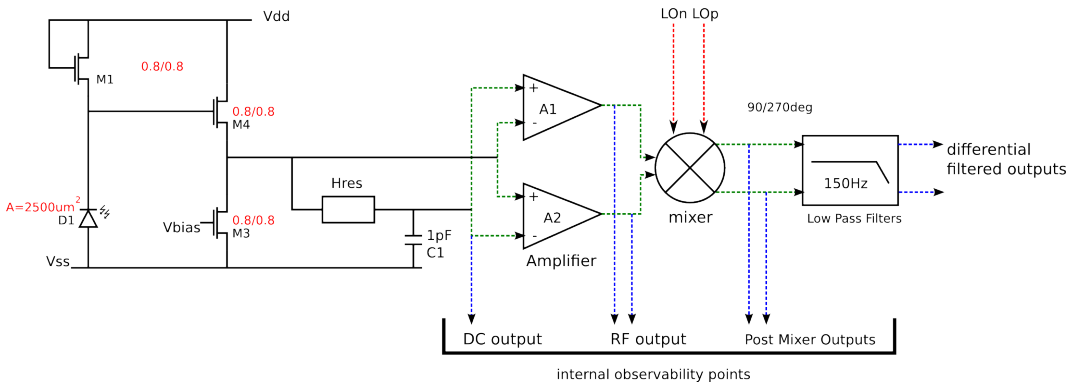

Figure 2.12: Dmochowski's test pixel of 2004

2.3.7 Dmochowski 2006

The pixel described in section 2.3.6 is refined and tiled into a camera with 24 by 32 pixels. The pixels are implemented with a pitch of 130 μm, but the photodiode shrinks, resulting in a fill factor of only 5.4 %. It is reported to operate from 10 kHz to 30 MHz at the cost of consuming 200 μA per pixel. The camera is christened MLCv5 [28].

The use of the logarithmic front-end poses severe problems including non-linearity in the response, and a variation in gain and phase response with incident DC light per pixel. Figure 2.13 shows a 3D projection of the layout of a single pixel.

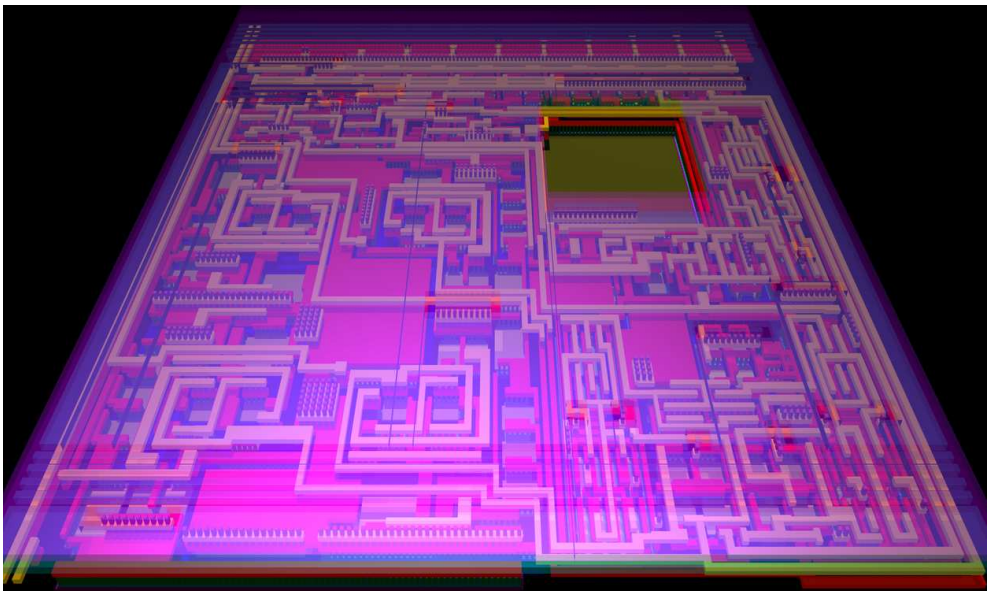

Figure 2.13: A 3D projection of Dmochowski's pixel implemented in his 24 by 32 pixel camera.

2.4 Other Cameras

This section discusses cameras that have been designed with other intentions, but may be, or have been demonstrated to act as modulated light detectors.

2.4.1 Ma

This work presents a CMOS active pixel sensor camera [29]. It is a 128 × 96 camera fabricated on a 0.5 μm CMOS process.

The camera operates by taking two and storing consecutive samples, and outputting the difference. It is intended for use as a motion detector, as only changes to the recorded illumination are recorded. By choosing the reset and sampling frequency to be twice the modulation frequency, it is possible to demodulate a signal. The camera offers a second mode of operation in which it outputs normal intensity images.

The camera contains an ADC with a sampling speed of 3 MSpS, limiting the frame rate to about 250 fps, suggesting that it could work with modulation frequencies up to 250 Hz. The ADC occupies 1 mm^2 of silicon space.

2.4.2 Kleinfelder

This work [30] is a CMOS camera originally designed to be a very fast frame camera, with 10 000 frames per second. This makes it fast enough to detect 2.5 kHz signals if amplitude, phase and DC intensity are considered. It has 352×288 pixels implemented as a digital pixel sensor (DPS). Each pixel has an ADC and allows massively parallel conversion and high spead readout. It is therefore capable of achieving over 1.33 giga pixels/second read rates over a 64-bit (8 pixeles) wide readout bus operating at 167 MHz.

This camera uses pixels with a pitch of 9.4 μm with a fill factor of 15% in a 0.18 μm, 5-metal CMOS process. Each pixel has 37 transistors, allowing a fill factor of sensor conversion gain is 13.1 μV/e-. At 1000 frames/s, measured integral nonlinearity is 0.22% over a 1 V range, rms temporal noise with digital

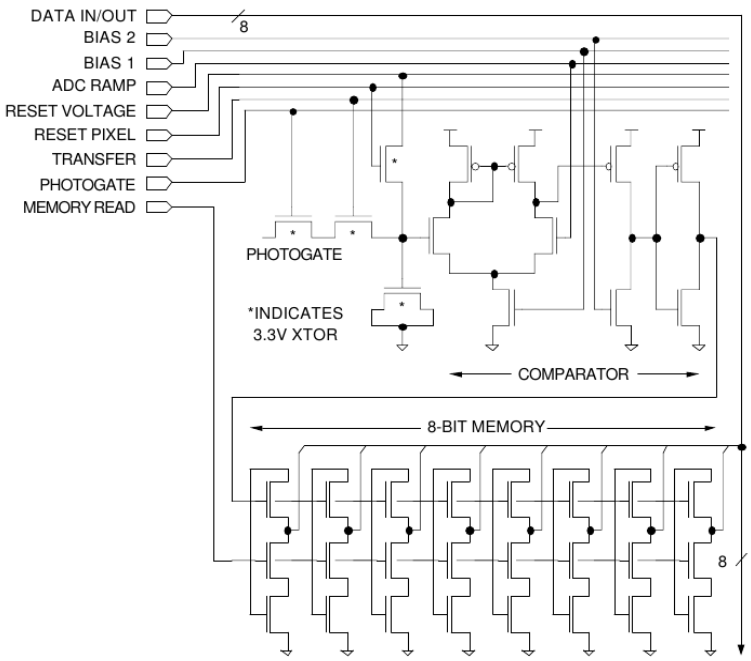

Figure 2.14: Kleinfleder pixel schematic. [30]

CDS is 0.15%, and rms FPN with digital CDS is 0.027%. Figure 2.14 shows the schematic for the DPS pixel.

2.4.3 Niclass

This design centers around the use of single photon avalanche diodes (SPAD). In this paper [31], a SPAD operating in Geiger mode is used to accurately detect the arrival of a single photon. SPADs are quite effective in computing range because they simply detect the arrival time of a synchronised pulse of light when they are synchronised with the light source.

This paper presents a system for evaluation of ToF with an 8×4 array of pixels fabricated in 0.8 μm CMOS process. As shown in Figure 2.15, the pixel consists of a circular SPAD, a quenching resistor (implemented in R-poly) and a comparator that transforms the geiger voltage pulse into a digital signal. The anode of the diode is biased at -18.5 V, with the breakdown voltage of the SPAD being 21 V. The comparator is a simple inverter with a threshold voltage of 3V.

When a photon impinges upon the avalanche region, a pulse is generated, creating an avalanche current. This current causes a voltage drop across the resistor of VDD - V, which is sufficient to switch the invertor and to stop the avalanche (quenching), within a time of 32 nS (known as dead time). The quantum efficiency is reported to be 10% at 635 nm. Since the output is digital, no amplification or analogue signal processing is required. The power dissipation is reported to be 1 mW.

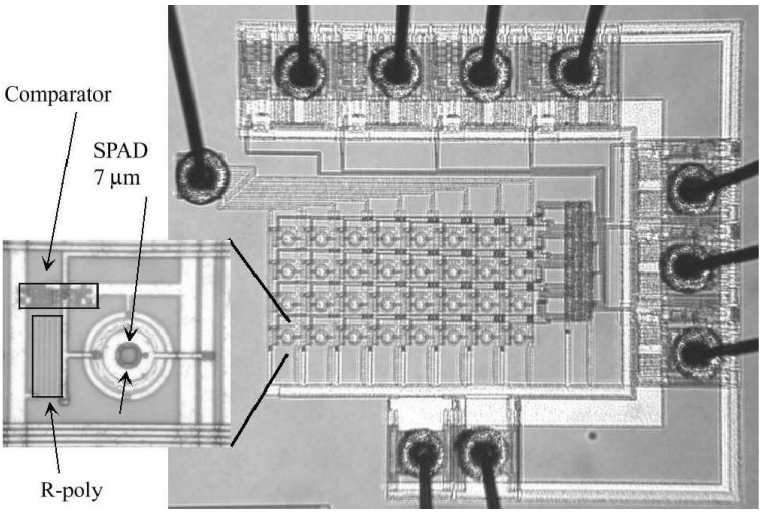

Figure 2.15: Schematic of a single pixel of Niclass 3D SPAD Camera [31]

Niclass follows this camera up [32] with another with 32 by 32 pixels. It is powered by VDD = 5 V, and V_{p+} = -25.5 V. The schematic for this is shown in Figure 2.16. Each pixel has a pitch of 58 μm, and the chip size is 7 mm^2.

By averaging over 10000 measurements the camera is capable of achieving submillimetric precision. The light source laser with peak power of 50 mW pulsed at 50 MHz.

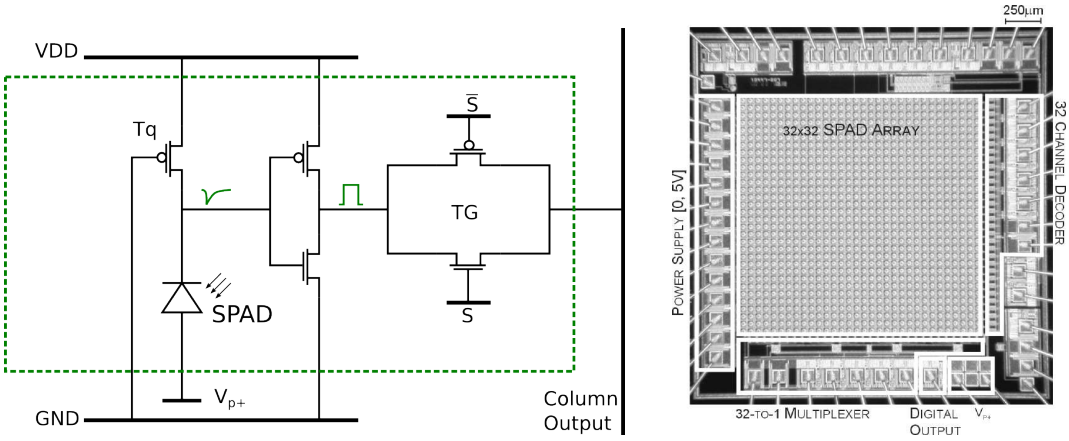

(a) Niclass SPAD Pixel Schematic **(b)** Photomicrograph of sensor array

Figure 2.16: Niclass second 3D SPAD Camera [32]

2.4.4 Perelman

This work presents a low-light-level sensor for medical diagnostic applications. It is designed to be a single-use disposable probe. The authors [33] measure the light intensity emitted by a chemoluminant reaction in a biological sample. This allows the identification of a specific virus (such as HIV) by the presence of antibodies.

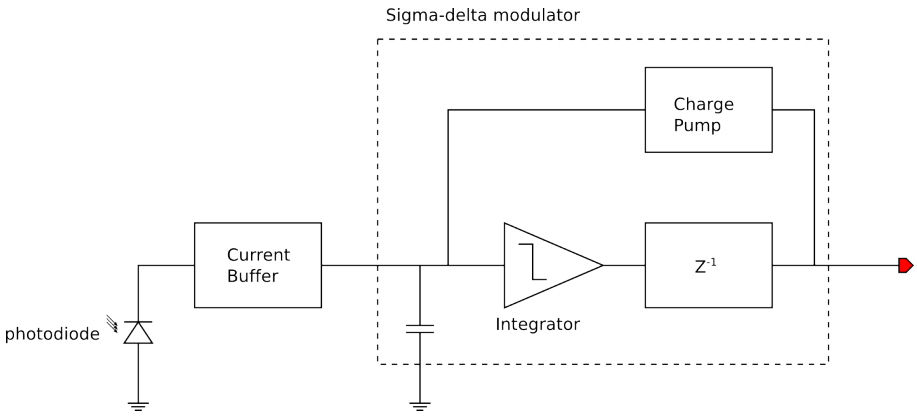

Figure 2.17: Perelman sensor architecture

Implemented in an HP 0.5 μm IP3M process, this design has a photodiode with a size of 500 × 500 μm^2, and the remainder of the circuit covers an area of 160 × 110 μm^2. The sensor includes a detecting element, an analogue to digital converter (ADC), digital signal processing and a serial bus interface. It is implemented

using a photodiode, a current buffer and sigma-delta modulater. The detected photo-current is buffered by the current buffer onto an integrating capacitor. A first order single-bit sigma-delta modulation loop is formed which is modulated by the input photocurrent. The sensor was designed for maximal incident optical power density of approximately 5 to 10 μW/cm^2 in the visible light spectrum. The input bandwidth is 10 Hz. The schematic is shown in Figure 2.17.

2.4.5 Microsoft Kinect

The Microsoft Kinect [34] was initially designed as an extension to Microsoft's XBox game system. It is based on technology developed by Microsoft Game Studios Rage (software) and Primesense (hardware). It works by employing light-coding methods. The Kinect has a laser diode, a monochrome VGA (640 × 480 pixels) detector, and a second monochrome image sensor with 1200 × 960 pixels.

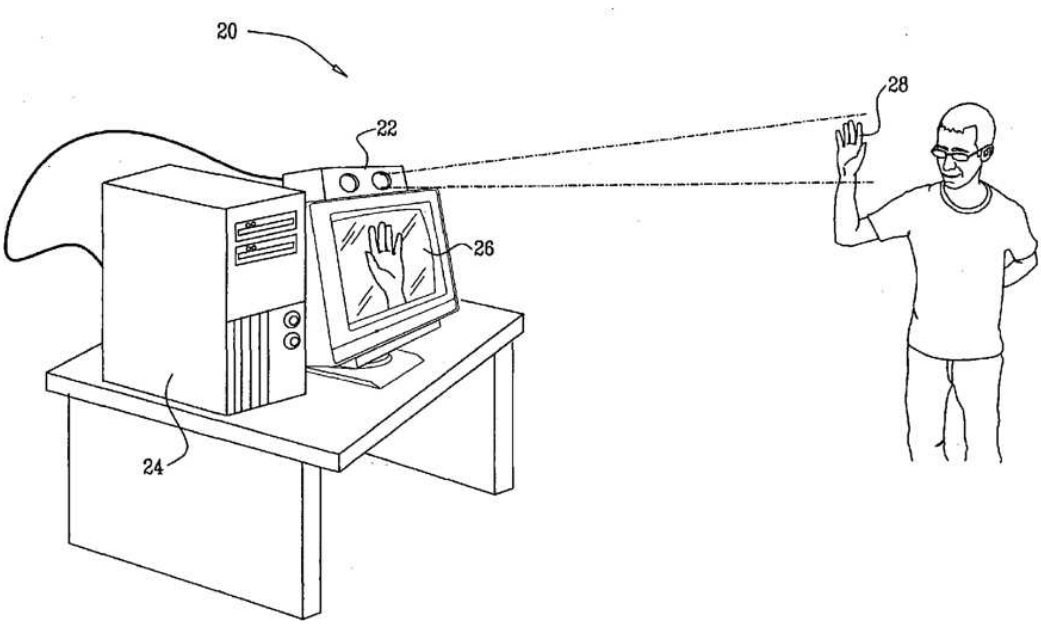

Figure 2.18: Kinect Patent graphic - Patent number US20100118123 - Depth mapping using projected patterns

Figure 2.18 shows a graphic from the Patent held by Microsoft for the Kinect (US Patent number US20100118123 - Depth mapping using projected patterns)

published in March 2010. An image acquired using the range detection is shown in Figure 2.19.

Illumination is provided by the 830 nm laser diode. It does not modulate the light, but has a constant power output of approximately 60 mW. A temperature sensor and peltier are used to stabilize the laser. The laser output is structured by pattern generating optics. This pattern is projected onto the scene, and the first detector captures a frame and compares it with the originally projected pattern. The distortion in the captured image is used to determine the range to different parts of the scene. The depth sensor has an infra-red filter at the laser wavelength. All the depth processing is performed on the Kinect using a system-on-chip. This reportedly reduces the processing load on the game console to less than 10%.

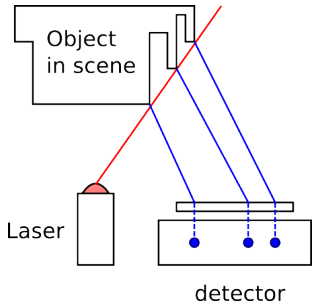

Figure 2.19: Kinect Ranging schematic

The second detector captures a normal (but higher resolution) intensity image. The kinect can acquire images within an area of about 6 m^2, within a range of 1.2 to 3 m in front of the sensor. An example of such an image is shown in Figure 2.20. This figure shows a depth image as well as a normal intensity image.

2.5 Summary

Table 2.1 shows provides a summary of the devices reviewed in this chapter.

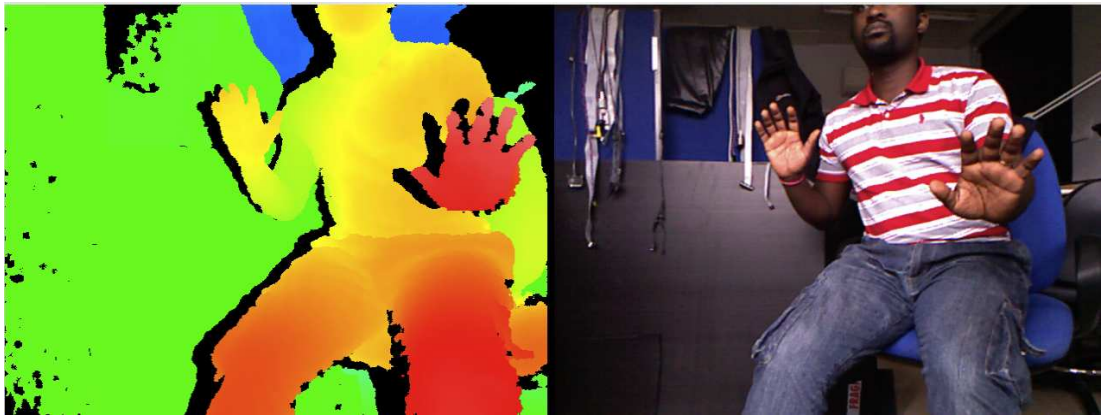

Figure 2.20: Picture acquired using the Kinect.

Table 2.1: Summary of devices reviewed in this chapter

Author	Year	Ref	Notes
Stenflo	1985	[5]	CCD. 32×32. 5 MHz demodulation off-chip
Povel	1990	[6]	CCD, slit mask synchronised to modulated light. 100 kHz. 2 storage bins
Spirig	1997	[7, 8]	CCD, as Povel but 4 bins. Bandwidth 100kHz×3 pixels, 87.5μm×80μm. 17% fill factor
Lange	2001	[9]	CCD, Bandwidth of 20MHz. 4 Storage bins
Ando	2002	[11]	CMOS, 2 storage bins. 100×100 pixels
Schwarte (PMD)	1999	[13]	Electro-optical mixing. Uses a buried channel
Ohta	2003	[17]	64×64 pixels. 2 storage bins
Oike	2001	[18]	DC Current suppression circuit. Log load. 2 integration bins
Stoppa	2011	[19]	0.18μm CMOS. 24% fill factor with 10μm pitch. Maximum frequency 50MHz. Similar to PMD with surface channel. Up to 20fps, 2.7 cm precision at 50 MHz

Continued on next page

Table 2.1 – continued from previous page

Author	Year	Ref	Notes
Light	2008	[20]	0.35 μm CMOS. 128×128. Operated up to 2.5 kHz.
Benten	1997	[21]	BiCMOS process, bandwidth of 40 kHz. 2.9 mm×0.45 mm
Bourquin	2001	[22]	58×58 pixels. Square wave mixer and low pass filter (35 kHz). 10% fill factor with 110 μm pitch. Feedback loop controls operating conditions. 1 kHz to 1 MHz bandwidth. RMS Noise at input is 142 pW.
Lu	2000	[23]	Buried double PN junction. Low noise device. 1 mm^2 photodiode. Multiple demodulation paths.
Pitter	2003	[25]	4×4 pixels. Log front-end. Integration onto 2 capacitors. 200μm pixel pitch with 9% fill factor.
Pitter	2004	[26]	64×64 pixels with pitch of 25μm with fill of 56% fill factor. Column level amplification, demodulation and filtering
Dmochowski (MLCv1)	2004	[28]	1 pixel, 4% fill factor with 250 μm. Bandwidth 500 kHz to 25 MHz.
Dmochowski (MLCv5)	2006	[28]	24×32 pixel, 5.4% fill factor with 130 μm pixel pitch. Bandwidth 10 kHz to 30 MHz.
Ma	1999	[29]	128×96 pixels. 0.5μm process. Records changes in consecutive frames. Frame synchronised, up to 250 Hz (250 fps).
Kleinfelder	2001	[30]	Up to 10000fps, or 2.5 kHz bandwidth. 9.4 μm with 15% fill factor. 0.18μm 5M process. 1.33 GbS^{-1} throughput. Pixel-level ADC.

Continued on next page

Table 2.1 – continued from previous page

Author	Year	Ref	Notes
Niclass	2004	[31]	SPAD ToF Ranger. 8×4 pixels in 0.8 μm process. Dead time of 32nS.
Niclass	2004	[32]	SPAD ToF Ranger. 32×32 pixels. 58 μm pitch, 7 mm^2 chip.
Perelman	2001	[33]	10 Hz bandwidth. HP 0.5 μ 1P3M process. RMS input referred noise 0.82 pA
Kinect	2010	[34]	Pattern projected from 60 mW 830 nm laser. VGA camera uses distortion in pattern to determine range.
LIDAR1	2010	Chap 5	0.35 μm 2P4M CMOS process, 16% fill factor with 115 μm pitch. 32×32 pixels. Continuous-time (non-integrating), quadrature demodulation and differential filtering. Bandwidth 50MHz. RF output available.

3 | Theory

This chapter introduces some modulation concepts pertinent to the understanding of the operation and characterisation of modulated light cameras, and discusses the ways in which they may be implemented electronically.

3.1 Modulation Theory

Modulation is very simply varying any one or more properties of a signal based on a second signal. This definition applies to scenarios such as the modulation of pitch and volume in a voice during speech in a crowded (and noisy room) in order to make one-self heard, to modulation of radio waves in communication systems.

There are three main types of analogue modulation: amplitude modulation, frequency modulation, and phase modulation, collectively known as continuous wave modulation. Given any two signals $\mathrm{S}_M(t)$ and $\mathrm{S}_C(t)$, these three ways are presented in Equation 3.1 to Equation 3.3. In each case S_M (the modulating signal) modulates S_C (the carrier signal).

$$\begin{aligned}
\text{taking } S_M &= A_M \cos(2\pi f_M t + \phi_M) \\
\text{and } S_C &= A_C \cos(2\pi f_C t + \phi_C)
\end{aligned}$$

it is possible to write

$$S_{AM} = A_C \cdot A_M \cos(2\pi f_C t + \phi_M) \cos(2\pi f_M t + \phi_C) \quad (3.1)$$

$$S_{FM} = A_C \cos(2\pi f_C \cdot A_M \cos(2\pi f_M t + \phi_M) t + \phi_C) \quad (3.2)$$

$$S_{PM} = A_C \cos(2\pi f_C t + \phi_C \cdot A_M \cos(2\pi f_C t + \phi_M)) \quad (3.3)$$

where f is the frequency, ϕ is the phase, t is time and $S_{AM}(t)$, $S_{FM}(t)$ and $S_{PM}(t)$ are the results of amplitude, frequency and phase modulation respectively. DC components are ignored in this example.

We start by observing some of the most basic properties of a modulated wave. In Figure 3.1, the period and amplitude of two waves are shown. It is also possible to see the phase difference between the two waves and the offset DC level, labelled background.

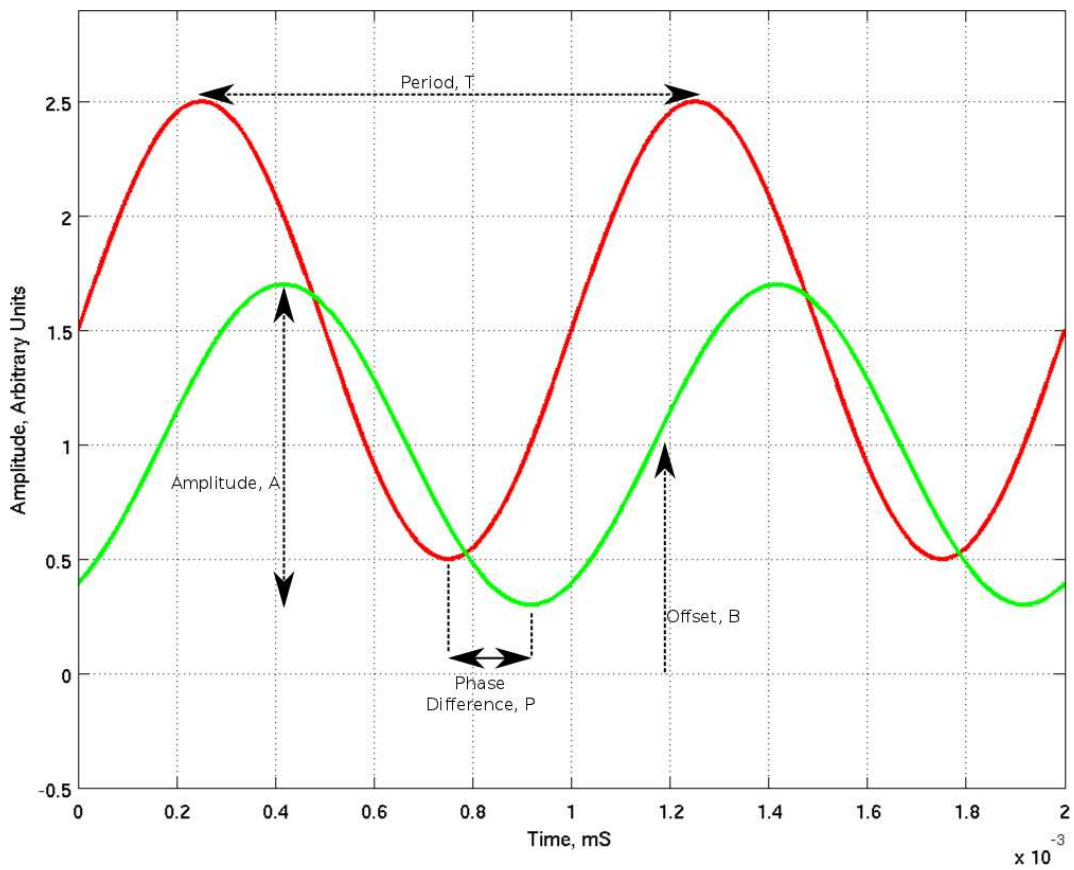

Figure 3.1: Sinusoidal waveforms showing general characteristics

Modulation can be found naturally in evocation, music (vibrato and tremolo), and sound synthesis (oscillators and filters). It is important to realise that noise can also be considered a modulation source. Radio stations employ modulation to carry baseband signals (the information content) to higher frequency bands and at the receiving home radio, demodulation (to extract the information content)

is performed.

Modulation can also be observed in optical systems. This includes optical communication systems, in which digital modulation techniques are applied to some information and transmitted over optical fibre links. This allows several information streams to share the same transmission medium.

Some scientific and medical applications use the measurement of the frequency content of signals, as in the case of blood flow imaging [35]. In ultrasound testing, the amplitude, frequency shift, and phase are measured to provide insight into material properties and state, whether it is for non-destructive testing of mechanical parts or scans of body parts in-vivo.

3.2 Operating Principle

Since this work uses amplitude modulation, this discussion will focus on that kind of modulation theory. We consider light to be the carrier wave $S_C(t)$, with a wavelength that gives it a frequency in the Terahertz region (red light with a wavelength of 625 nm has a frequency of 400 THz). Light is often considered to be DC, with the RMS value used instead of amplitude because the carrier frequency is very high relative to the modulation frequency.

After detection of the modulated signal the modulation information must be extracted. The bandwidth-limited information content is shifted across the frequency spectrum from the carrier frequency to an easily measurable frequency range. This is often carried out by determining the correlation with a reference signal. This can be thought of as a matched filter, or more simply as a multiplication or mixing technique.

The CMOS MLC works by receiving a modulated light wave and converting to an electrical current in a photosensitive element, amplifying it and mixing it with a reference oscillator. By using the same modulation frequency for the modulated light and the local oscillator, the signal of interest is down-converted to the baseband, and can be easily measured for calculation of the phase and intensity of the received light. The up-converted signal and other harmonics are often filtered out. A schematic for the MLC is shown in Figure 3.2.

For example, in time of flight imaging (Figure 1.2) the location of the camera is chosen as a reference point, and a point in the scene under observation is at a distance **d** metres away. If a modulation frequency **f** Hz is chosen (corresponds to $\omega = 2\pi f$), then the objects may be determined by the phase θ of the modulation component in a reflected wave as:

$$2 \cdot d = \left(2\pi m + \frac{\theta}{2\pi}\right) \cdot \frac{c}{f} \tag{3.4}$$

where **c** is the speed of light in m/s, and **m** is zero or a positive whole number.

This shows how detecting the phase can be used as a time of flight measurement technique, allowing ranging, and shows that the modulation frequency must be chosen such that there is no ambiguity due to the phase wrapping, i.e. always **m** = **0**. The $2 \cdot d$ on the left hand side of Equation 3.4 shows the flight from the camera to the scene and back.

By using a quadrature oscillator, the amplitude and phase of the returned wave can be measured at the same time. If the reference oscillator at the camera works in quadrature, and is taken to have a phase of $\theta_{LO_0} = 0°$ and $\theta_{LO_90} = 90°$, then the reference signals may be written as Equation 3.5 and Equation 3.6:

$$V_{LO_0} = V_{LO_DC} + V_{LO_AC} \sin(\omega_{LO} \cdot t) \tag{3.5}$$

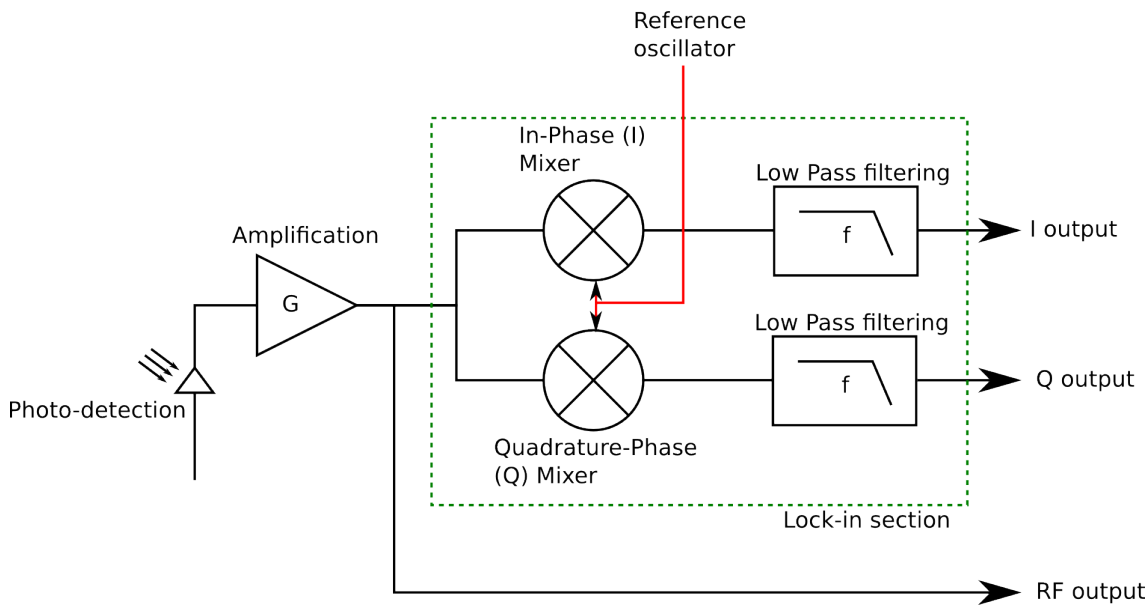

Figure 3.2: The internals of a Modulated Light camera.

$$V_{LO_90} = V_{LO_DC} + V_{LO_AC} \sin(\omega_{LO} \cdot t + \frac{\pi}{2}) \tag{3.6}$$

The light signal received by the photosensitive element is converted to an electrical signal which contains the background illumination and modulation component of the light wave, and is amplified and input to the mixer. This may be written as Equation 3.7

$$V_{RF} = V_{RF_DC} + V_{RF_AC} \sin(\omega_{RF} \cdot t + \theta_{RF}) \tag{3.7}$$

where V_{RF_DC} is the DC voltage due to background illumination and the DC component of the light beam itself. These equations do not include noise sources.

The mixed signal is (ideally) the result of the multiplication of Equation 3.5 and Equation 3.6 with Equation 3.7. The two results are called the **I** and **Q** results respectively. This gives the following results:

$$
\begin{aligned}
V_I = V_{LO_DC} \cdot V_{RF_DC} &+ V_{RF_AC} \sin(\omega_{RF} \cdot t) \\
&+ V_{LO_DC} \cdot V_{RF_AC} \sin(\omega_{RF} \cdot t + \theta_{RF}) \\
&+ V_{RF_DC} \cdot V_{LO_AC} \sin(\omega_{LO} \cdot t) \\
&+ V_{RF_AC} \cdot V_{LO_AC} \sin(\omega_{LO}) \cdot \sin(\omega_{RF} + \theta_{RF}) \\
= V_{LO_DC} \cdot V_{RF_DC} &+ V_{RF_AC} \sin(\omega_{RF} \cdot t) \\
&+ V_{LO_DC} \cdot V_{RF_AC} \sin(\omega_{RF} \cdot t + \theta_{RF}) \\
&+ V_{RF_DC} \cdot V_{LO_AC} \sin(\omega_{LO} \cdot t) \\
&+ \frac{V_{RF_AC} \cdot V_{LO_AC}}{2} \cos\left[(\omega_{RF} - \omega_{LO}) \cdot t + \theta_{RF}\right] \\
&- \frac{V_{RF_AC} \cdot V_{LO_AC}}{2} \cos\left[(\omega_{RF} + \omega_{LO}) \cdot t + \theta_{RF}\right]
\end{aligned} \tag{3.8}
$$

$$
\begin{aligned}
V_Q = V_{LO_DC} \cdot V_{RF_DC} &+ V_{RF_AC} \sin(\omega_{RF} \cdot t) \\
&+ V_{LO_DC} \cdot V_{RF_AC} \sin(\omega_{RF} \cdot t + \theta_{RF}) \\
&+ V_{RF_DC} \cdot V_{LO_AC} \sin(\omega_{LO} \cdot t + \frac{\pi}{2}) \\
&+ V_{RF_AC} \cdot V_{LO_AC} \sin(\omega_{LO} + \frac{\pi}{2}) \cdot \sin(\omega_{RF} + \theta_{RF}) \\
= V_{LO_DC} \cdot V_{RF_DC} &+ V_{RF_AC} \sin(\omega_{RF} \cdot t) \\
&+ V_{LO_DC} \cdot V_{RF_AC} \sin(\omega_{RF} \cdot t + \theta_{RF}) \\
&+ V_{RF_DC} \cdot V_{LO_AC} \sin(\omega_{LO} \cdot t + \frac{\pi}{2}) \\
&+ \frac{V_{RF_AC} \cdot V_{LO_AC}}{2} \cos\left[(\omega_{RF} - \omega_{LO}) \cdot t + \theta_{RF} - \frac{\pi}{2}\right] \\
&- \frac{V_{RF_AC} \cdot V_{LO_AC}}{2} \cos\left[(\omega_{RF} + \omega_{LO}) \cdot t + \theta_{RF} + \frac{\pi}{2}\right]
\end{aligned} \tag{3.9}
$$

Equation 3.9 can be simplified further with the trigonometric identity

$$
\cos\left(\alpha \pm \frac{\pi}{2}\right) = \mp \sin(\alpha)
$$

giving Equation 3.10

$$\begin{aligned} V_Q = V_{LO_DC} \cdot V_{RF_DC} &+ V_{RF_AC} \sin(\omega_{RF} \cdot t) \\ &+ V_{LO_DC} \cdot V_{RF_AC} \sin(\omega_{RF} \cdot t + \theta_{RF}) \\ &+ V_{RF_DC} \cdot V_{LO_AC} \sin(\omega_{LO} \cdot t + \frac{\pi}{2}) \\ &- \frac{V_{RF_AC} \cdot V_{LO_AC}}{2} \sin\left[(\omega_{RF} - \omega_{LO}) \cdot t + \theta_{RF}\right] \\ &+ \frac{V_{RF_AC} \cdot V_{LO_AC}}{2} \sin\left[(\omega_{RF} + \omega_{LO}) \cdot t + \theta_{RF}\right] \end{aligned} \quad (3.10)$$

The equations above show that the mixer outputs contain frequencies at baseband, ω_{RF} and ω_{LO} and $\omega_{RF} \pm \omega_{LO}$. By setting $\omega_{RF} = \omega_{LO} = \omega$, the frequencies present will be at DC, ω and 2ω.

Since the phase element is mixed to baseband the outputs of the mixer can be low pass filtered to eliminate the high frequency components produced as a by-product of the mixing process. In an ideal scenario, only the harmonics mentioned above are present, but in an electronic mixer, a non-linear device is used. This introduces spurious components into the outputs.

A non-linear mixer produces an output that can be expressed as Equation 3.11. The second order product term represents the desired product.

$$V_{out} = a_0 + a_1 v_{in}(t) + a_2 v_{in}^2(t) + a_3 v_{in}^3(t) + ... \quad (3.11)$$

Using a sharp cutoff low pass filter reduces the high frequency components and sets the noise bandwidth of the system. It also sets the integration time of the mixer, since if the 3dB bandwidth of the filter is $\mathbf{f}_{LPF}$, a period of $\mathbf{T} = \frac{1}{f_{LPF}}$ is needed for the filter to settle to an acceptable level.

Using an ideal low pass filter with a cutoff below ω, the outputs can be written

as

$$V_{If} = V_{LO_DC} \cdot V_{RF_DC} + \frac{V_{RF_AC} \cdot V_{LO_AC}}{2} \sin(\theta_{RF}) \tag{3.12}$$

and

$$V_{Qf} = V_{LO_DC} \cdot V_{RF_DC} + \frac{V_{RF_AC} \cdot V_{LO_AC}}{2} \cos(\theta_{RF}) \tag{3.13}$$

Using a low f_{LPF} creates a good selectivity, but reduces the frame rate. Reading frames faster than the filter cutoff is still possible, but will only result in over-sampled data.

From the V_{If} and V_{Qf} obtained, the DC offset is subtracted. This subtraction is easily performed if differential circuits are used, i.e. V_{If+} and V_{If-}, and V_{Qf+} and V_{Qf-}. The range **d** is determined by using the Equation 3.14 below:

$$d = \frac{\lambda}{4\pi} \tan^{-1}\left(\frac{V_{Qf+} - V_{Qf-}}{V_{If+} - V_{If-}}\right) \tag{3.14}$$

By performing this operation pixel by pixel, it becomes possible to determine the range at different points in the scene. The higher the pixel density and count (limited by pixel pitch and total chip area), the better the spatial resolution.

3.3 Light Budget

Modulated light sent from the light source must get back to the camera system with enough intensity to make sure that a good mixing product is obtained. This sets the dynamic ratio, and background rejection ratio of the device. The modulation depth (m) is the ratio of modulation component amplitude (AC) to the un-modulated component (DC).

Light may be sent in a diverging or focused beam. A focused beam allows the scene to be illuminated with lower light loss. Depending on the reflection profile of the objects in the scene, the light coming to the camera may reduce with

the inverse square law (**Lambertian** reflector), may completely miss the camera (misaligned mirror), or may fall perfectly on the camera (aligned mirror).

The number of electrons generated is related to the optical power by the responsivity. Consider light with frequency $f = c/\lambda$ where c is the speed of light and λ is the frequency. The energy (E) is $E = hf = \frac{h \cdot c}{\lambda}$, where h is the Planck constant. Given the integration time or frame rate f_{int}, the size of the photo-sensitive element (A_{pixel}) and the size of the image in the sensor plane(A_{image}), it is possible to determine the total amount of optical power that must arrive at the sensor. It is also possible to consider the losses due to the optics, P_{lens}.

Given a Lambertian reflector, the optical power in the scene has to be a factor of $(\frac{D}{2 \cdot R})^2$ higher than the power at the lens, where R is the distance to the target and D is the diameter of the aperture of the lens. This factor is obtained from the following integration in Equation 3.18:

$$P_{lens} = P_{obj} \cdot \frac{\int_0^{2\pi} \int_0^{\theta_c} \cos\theta \sin\theta d\phi}{\int_0^{2\pi} \int_0^{\frac{\pi}{2}} cos\theta \sin\theta d\theta d\phi} \tag{3.15}$$

$$= P_{obj} \left(\sin\theta_c\right)^2 \tag{3.16}$$

$$= P_{obj} \left(\frac{D}{2R}\right)^2 \tag{3.17}$$

$$= P_{obj} \left(\frac{f}{R}\right)^2 \cdot \left(\frac{1}{2 \cdot F/\#}\right) \tag{3.18}$$

where $F/\#$ is a measure of the aperture.

When the reflection coefficient ρ of the object is taken into consideration, the required power from the light source can be calculated. This may be summarised as follows:

Optical power per pixel P_{pixel}, with a light sensitive area per pixel of A_{pixel}, is given by:

$$P_{pixel} = \frac{P_{source} \cdot \rho \left(\frac{D}{2R}\right)^2 \cdot k_{lens}}{\frac{A_{image}}{A_{pixel}}} \tag{3.19}$$

and this may be expressed in terms of power density P_i as

$$P'_{pixel} = P'_{obj} \left(\frac{1}{2 \cdot F/\#}\right)^2 \cdot k_{lens}$$

Where k_{lens} is a loss factor due to the lenses used in the optics. Thus the optical energy required per pixel is $E_{pixel} = P_{pixel} \cdot T_{int}$, and the number of electrons generated per pixel, with N_p photons per pixel is

$$N_e = N_p \cdot \eta(\lambda) = P_{pixel} \cdot T_{int} \cdot \frac{1}{h \cdot c/\lambda} \cdot \eta(\lambda)$$

where $\eta(\lambda)$ is the quantum efficiency of photo-conversion at that wavelength. The required optical power of a uni-directional source is then given by Equation 3.20:

$$P_{source} = \frac{N_e \cdot \frac{A_{image}}{A_{pixel}} \cdot h \cdot c}{\rho \left(\frac{D}{2R}\right)^2 \cdot k_{lens} \cdot \eta(\lambda) \cdot \lambda \cdot T_{int}} \tag{3.20}$$

This derivation assumes that the target is a Lambertian reflector, with the intensity distribution of the back-scattered light does not depend on the illumination angle. The reflected intensity decreases with the cosine of the observation angle with respect to the surface normal. The reflection coefficient varies between zero and one for Lambertian reflectors, with paper having $\rho = 1$.

3.3.1 Sunlight and Solar Spectrum

An idea of typical radiation intensity is important, since this gives an idea of the background light that is present in a typical time-of-flight scene. A graph showing the typical radiation spectrum at the exosphere (uppermost atmospheric layer) and at sea-level is presented in Figure 3.3.

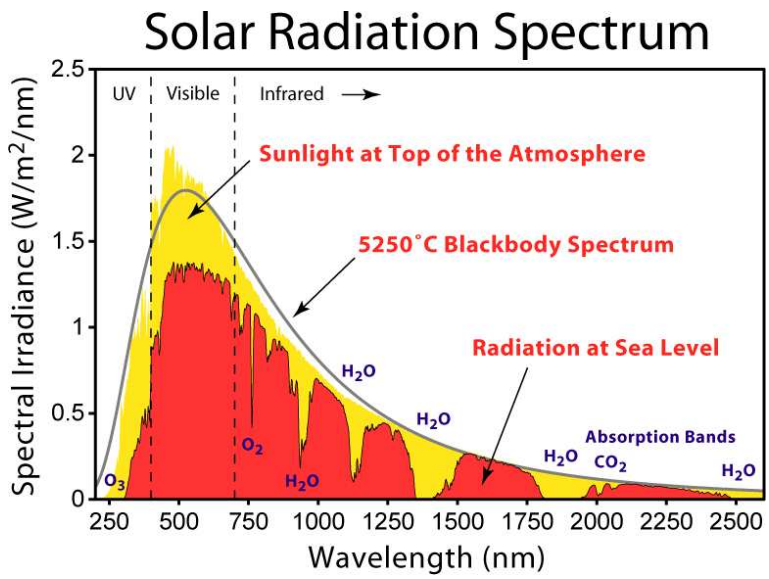

Figure 3.3: Solar radiation spectrum. The figure shows the solar radiation spectrum for direct light at both the top of the Earth's atmosphere and at sea level. The sun produces light with a distribution similar to what would be expected from a 5525 K (5250 °C) blackbody, which is approximately the sun's surface temperature. As light passes through the atmosphere, some is absorbed by gases with specific absorption bands. Light is additionally redistributed by Rayleigh scattering, which is responsible for the atmosphere's blue color. These curves are based on the American Society for Testing and Materials (ASTM) Terrestrial Reference Spectra. Regions for ultraviolet, visible and infrared light are indicated. [36]

Normal room lighting is about $1.3\,\mathrm{Wm}^{-2}$ [37]. Thus a camera system with a photo-sensitive area of $1.6\,\mu\mathrm{m}^2$ would receive $5\,\mathrm{nW}$ per pixel. Given that silicon has a responsivity of about $0.3\,\mathrm{A/W}$ in the wavelengths of interest (visible spectrum), the photo-current from background light is approximately $1.5\,\mathrm{nA}$.

This information is used to determine that generally for an SNR of 1, at least $1.5\,\mathrm{nA}$ of photocurrent is required per pixel. Because we use a lock-in technique, the SNR is greatly improved.

3.4 Noise and Uncertainty Sources

In an ideal case, all the light sent to the scene would be reflected, and depending on the shape of the reflection profile and albedo of the objects in the scene, some of it would get back to the camera. The camera would then demodulate the signal, adding no noise of its own and so it would be possible to use even the least amount of light to make a perfectly accurate/precise measurement.

However, in a real opto-electronic system, there are a number of sources of noise that contribute to errors in measurement.

3.4.1 Optical Sources

Light may be modelled as photons, which exhibit a Poisson distribution when detected. This means that the time of arrival of each photon at the detector can vary according to a Poisson Distribution. Poisson distribution describes the occurrence of independent random events. This leads to uncertainty in the detected signal. This is called shot noise, and is dominant when the number of photons (i.e. photo-current) is small. The shot noise $\mathrm{N_{shot}}$ is given by the square root of the number of photo-electrons $\mathrm{N_{photons}}$, as given by Equation 3.21.

$$N_{\text{shot}} = \sqrt{N_{\text{photons}}} \tag{3.21}$$

Another optical noise source is the light-generation stage. For example, if an LED or laser is used for light generation, and this is biased outside its rated region, it can contain significant distortion. This will manifest as out of band distortion, and will contribute to measurement uncertainty.

3.4.2 Electronic Noise Sources

Similar to optical shot noise, electronic current is modelled as the flow of electrons, which means it is subject to shot noise. This is likely to be a dominant noise source at the point of detection because of the low photocurrents involved. The detector used can also introduce significant noise by way of non-linear demodulation. This often manifests as a distorted sine-wave non-linearity (wiggle shape) in a phase-in, phase-out plot.

In the case of multiple detectors, or in this case of a wide-field camera, the components used in each pixel have to be exactly the same, or there can be significant variation in the performance of different pixels. The variation in pixels are caused by many factors such as the specific layout of the design and fabrication process parameters. This noise source is often referred to as Fixed Pattern Noise (FPN).

Johnson-Nyquist or Thermal Noise also presents a problem. As presented by [38], it is the electronic noise generated by the agitation of charge carriers (usually the electrons) inside any electrical conductor at equilibrium, at a temperature above 0 K, which happens regardless of any applied voltage. The one-sided power spectral density, or voltage variance (mean square) per hertz of bandwidth (Δf), is given by Equation 3.22.

$$v_n^2 = 4K_B T R \Delta f \tag{3.22}$$

where K_B is the Boltzmann constant, T is the absolute temperature, and R is the resistance of the conductor being considered.

Significant power supply noise reduction is also required, because of the sensitive nature of the measurement. This is relevant at light generation, detection and demodulation stages.

All of these noise sources may be eliminated, compensated for or reduced by cooling or signal processing techniques, with the exception of shot noise. Shot or quantum noise represents the fundamental limit to detection, as it cannot be eliminated. It is therefore best to have as much light as possible.

3.4.3 Propagation of Uncertainty

To determine the limitation of noise on range accuracy, from Equation 3.14, with slight modifications to consider phase:

$$\phi = tan^{-1}\left(\frac{V_{Qf+} - V_{Qf-}}{V_{If+} - V_{If-}}\right) \tag{3.23}$$

From the rules of error propagation, a function $f(x_1, x_2, ..., x_n)$ of n variables has uncertainty Δf obtained from the uncertainties Δx_i in x_i. This is given by Equation 3.24

$$\begin{aligned}\Delta f &= \Delta f(x_1, x_2, ...x_n, \Delta x_1, \Delta x_2, ...\Delta x_n) \\ &= \left(\sum_{i=1}^{n}\left(\frac{\delta f}{\delta x_i}\Delta x_i\right)^2\right)^{\frac{1}{2}}\end{aligned} \tag{3.24}$$

and the function has value $f+\Delta f$. In particular, for $\phi = f(V_i) = \tan^{-1}\left(\frac{V_{Qf+}-V_{Qf-}}{V_{If+}-V_{If-}}\right)$, the uncertainty is given by

$$\frac{\delta f}{\delta V_i} = \frac{1}{1+V_i^2}$$

Thus starting from Equation 3.23 and taking partial differentials:

$$\begin{aligned}(\Delta\phi)^2 = &\left(\frac{\delta\phi}{\delta V_{If+}}\right)^2 \Delta^2(V_{If+}) + \left(\frac{\delta\phi}{\delta V_{If-}}\right)^2 \Delta^2(V_{If-}) \\ &+ \left(\frac{\delta\phi}{\delta V_{Qf+}}\right)^2 \Delta^2(V_{Qf+}) + \left(\frac{\delta\phi}{\delta V_{Qf-}}\right)^2 \Delta^2(V_{Qf-})\end{aligned} \tag{3.25}$$

and considering that each of the values V_* has a standard deviation of $\Delta(A_*) =$

$\sqrt{A_*}$, where each A_* is the number of electrons corresponding to the voltage, the shot noise limited phase error $\Delta\phi$ is given by:

$$(\Delta\phi)^2 = \left(\frac{\delta\phi}{\delta V_{If+}}\right)^2 (V_{If+}) + \left(\frac{\delta\phi}{\delta V_{If-}}\right)^2 (V_{If-}) + \left(\frac{\delta\phi}{\delta V_{Qf+}}\right)^2 (V_{Qf+}) + \left(\frac{\delta\phi}{\delta V_{Qf-}}\right)^2 (V_{Qf-}) \tag{3.26}$$

The range resolution can then be determined for special phase values (0°, 45°, 90°, 135°, ...) as:

$$\Delta L = \frac{L}{360^\circ} \cdot \Delta\phi = \frac{L}{\sqrt{8}} \cdot \frac{\sqrt{B}}{2 \cdot A} \tag{3.27}$$

where L is the non-ambiguous range $= \frac{\lambda_{mod}}{2}$, and A is the amplitude of the light signal, and B the offset, with these 2 measurements are in discrete photo-electron counts. This can be improved by averaging, which effectively increases the integration or mixing time. Equation 3.27 shows that a large background level ($B \gg A$) restricts the quantization levels available, and increases the quantum noise of the system. Thus a slower frame rate increases the range resolution. This is a problem for most of the devices reviewed in section 2.2. By using a continuous time camera that uses no integration, the offset B may be easily eliminated with a high pass filter so that it does not contribute much in Equation 3.27.

Background illumination may be reduced by using spectral filters or taking measurements under special illumination conditions. For the sake of generalization, this discussion will continue to include the background offset B.

Other sources of noise, like $1/F$, reset and thermal noise may be included by adding additional electrons N to the background term. They do not correlate with the modulation signal, and hence contribute to B rather than A. Thus

Equation 3.27 may be modified to Equation 3.28:

$$\Delta L = \frac{L}{\sqrt{8}} \cdot \frac{\sqrt{B+N}}{2 \cdot A} \tag{3.28}$$

with N being obtained simply by squaring the noise-equivalent number of Noise electrons:

$$N = (\text{No of dark noise electrons})^2 = \left(\frac{V_{\text{dark-noise}} \cdot C_{conv}}{q \cdot A_{sf}} \right)^2 \tag{3.29}$$

where q is the charge on an electron, $V_{\text{dark-noise}}$ is the dark noise measurement, which contains all noise sources except photon shot noise, and A_{sf} is the off-chip amplification, and C_{conv} is the conversion capacitance. Thus, for example, for $V_{\text{dark-noise}} = 0.63\,\text{mV}$ rms, $A_{sf} = 0.9$, $C_{conv} \approx 40\,\text{fF}$, N is $(175)^2 \approx 30{,}000$.

3.5 Electronic Implementation

A photodiode acts a transducer that receives light and converts it to electrical current. This current is converted to a voltage by passing it through a load device such as a resistor. The photodiode may be analysed as a current source in parallel with a capacitance C_{pd}.

A high resistance is necessary to provide a high current-to-voltage (transimpedance) gain, since V = IR. For example, to convert a photocurrent of about 1 nA to 1 mV would require a resistance of 1MΩ. This circuit is shown in Figure 3.4.

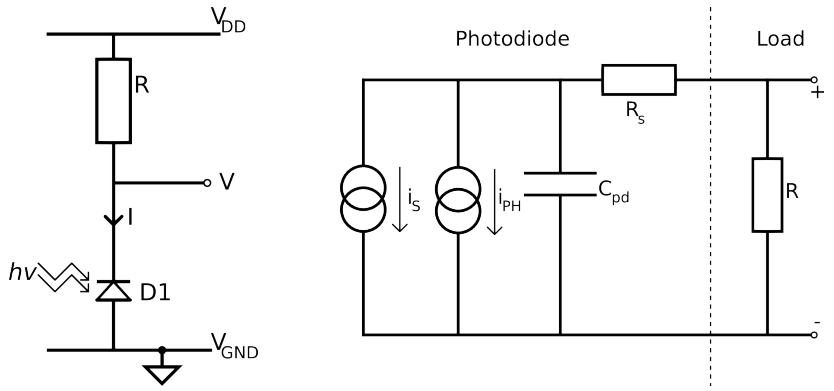

(a) Simple front-end with an ideal resistive load.

(b) Small signal model with a resistive load.

Figure 3.4: A photodiode with a resistive Load, and its small signal model. The resistance R_S is the substrate resistance between the diode and the ground constant, and is ignored in the remaining discussion.

The photodiode capacitance (C) and the resistance (R) of the load device act together to place a limit on the bandwidth of this system, acting as a low pass RC filter. The -3 dB bandwidth may be written as:

$$f_{-3dB} = \frac{1}{2\pi R C_{pd}} \tag{3.30}$$

This means that a trade-off between the bandwidth and the transimpedance gain

exists.

Resistance: Using a resistor has the advantage of a simple linear relationship between voltage and photocurrent: V = IR. It however presents some issues:

1. A high resistance is costly in terms of silicon area. The 0.35μm CMOS C35 design kit offers a high-resistance polysilicon layer (RPOLYH) with a typical sheet resistance $R_{\text{square}} = 1.2k\Omega/\square$. The minimum width allowed is 0.8 μm. To create a minimum width 1MΩ resistor using RPOLYH, a length of 291.65 μm is required. If bends were used placed in the resistor to make a minimum area device, the area used would be about 35 μm by 35 μm. Fabricating these in an array is impractical because of the area requirements per pixel. Since this is a minimum width device, there would also be significant pixel-to-pixel variation, contributing to fixed pattern noise as discussed in section 3.8.1. Increasing the width to 1 μm would require a length of 833.35 μm!

2. The large silicon area of this resistor also contributes a significant capacitance which must be considered in calculating the bandwidth. The capacitance of the 1M Ω resistor would be 93 fF, which results in an RC filter by itself (even without the photodiode) with a bandwidth of only 1.7 MHz. A wider device (widened to mitigate variation from pixel to pixel) would have an even bigger capacitance and hence a lower bandwidth.

3. The resistance of the load device may be reduced to increase the bandwidth of the system, but this comes at the cost of the transimpedance gain.

Capacitance: The capacitance varies with the area of the photodiode. A larger area is needed for greater light capture, but reduces the bandwidth of the system.

It is also important to realise that the voltage across the photodiode affects the capacitance of the photodiode. This means that even for the idealized photodiode-resistor circuit, the bandwidth will vary with the DC light content.

To solve these problems, a diode-connected transistor is used as the load device, and a Regulated Cascode stage as an input stage. The diode-connected transistor offers a good impedance (high resistance, small capacitance), and the regulated cascode stage reduces the effect of the photodiode capacitance on the bandwidth determination. These two circuits allow a practical pixel to be constructed but they both contribute significant non-linearity to the system.

3.6 Transistor Operating Regions

Figure 3.5 shows an enhancement mode transistor as often used in CMOS circuit design. It shows the Drain, Source and Gate terminals. The drain current is also shown. W is the width of the device, L is the length of it. The size of the transistor is usually written simply as W/L, eg. 2/2 means the gate is 2 μm wide and 2 μm long.

Depending on the voltages at the terminals, the transistor is said to operating in certain regions, and these regions are discussed next.

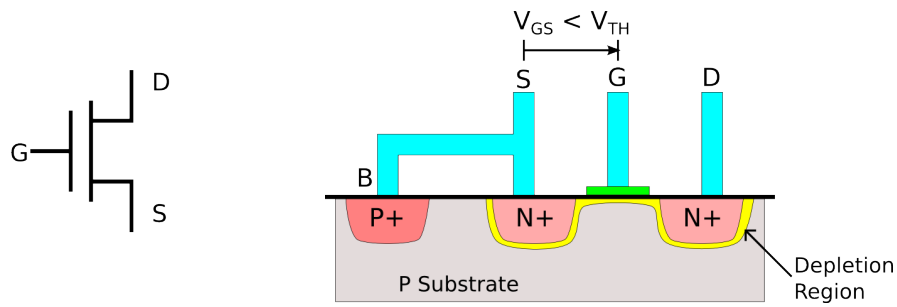

(a) An NMOS transistor symbol

(b) Cross-section of an NMOS transistor.

Figure 3.5: The symbol for an NMOS transistor (figure 3.5a), and a cross-section of an NMOS showing the depletion region (figure 3.5b)

3.6.1 Triode/Linear Operation

In this region of operation, the transistor is turned on, and a channel allows the flow of current between the drain and source. The transistor operates like a voltage controlled resistor, and so this mode is also referred to as the Ohmic mode. The current through the channel may be written as:

$$I_D = KP_N \times \frac{W}{L} \times \left((V_{GS} - V_{THN}) \cdot V_{DS} - \frac{V_{DS}^2}{2} \right) \tag{3.31}$$

In this region (for an NMOS transistor): $V_{GS} > V_{THN}$ and $V_{DS} < (V_{GS} - V_{THN})$. FigureFigure 3.6 shows a cross-section of an NMOS transistor in the triode region of operation.

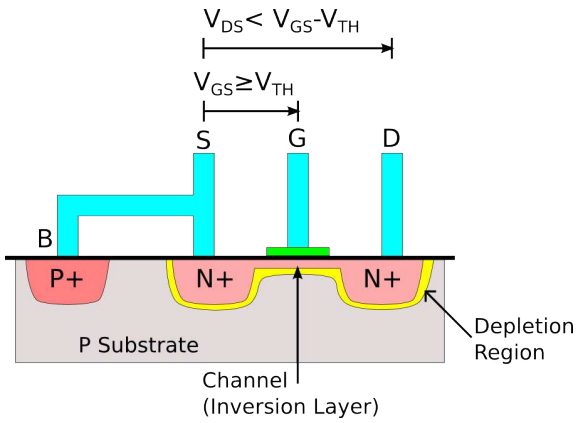

Figure 3.6: NMOS transistor in triode region

3.6.2 Saturation Region Operation

Figure 3.7a shows an NMOS transistor at pinch-off, when $V_{DS} = V_{GS} - V_{THN}$. Figure 3.7b shows it in saturation. An NMOS transistor can be said to be in saturation if $V_{DS} \geq V_{GS} - V_{THN}$ and $V_{GS} \geq V_{THN}$. The gate overdrive voltage $V_{DS,sat}$ is given by $V_{DS,sat} = V_{GS} - V_{THN}$ and gives the voltage at pinch-off. The

drain current at $V_{DS} = V_{DS,sat}$ is given by

$$\begin{aligned} I_D &= \frac{KP_n}{2}\frac{W}{L}(V_{GS} - V_{THN})^2(1 + \lambda(V_{DS} - V_{DSsat})) \\ &= \frac{KP_n}{2}\frac{W}{L}(V_{DS,sat})^2 \end{aligned} \tag{3.32}$$

where λ is the channel length modulation parameter (CLM). CLM is also known as the Early effect and it is observed as a shortening in the length of the channel with increase in drain bias for large drain biases. This results in an increased current (or a reduction in output resistance).

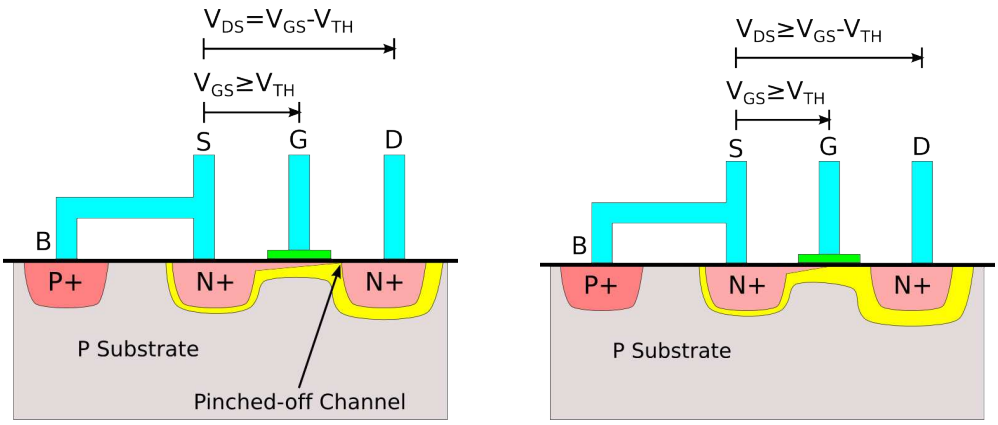

(a) An NMOS transistor at pinch-off

(b) An NMOS transistor in saturation mode

Figure 3.7: An NMOS transistor at pinch-off (figure 3.7a) and in saturation (figure 3.7b), showing channel length modulation.

In saturation (also known as active mode),

$$I_D = I_{D,sat} + I_{D,sat}\lambda(V_{DS} - V_{DS,sat}) \tag{3.33}$$

Thus this may be compared with a current source $I_{D,sat}$ in parallel with a resistor of value $R_{on} = \frac{1}{\lambda I_{D,sat}}$.

For the gate-drain connected MOSFET, shown in Figure 3.8, $V_{GS} = V_{DS}$ (NMOS). From Equation 3.32, if $V_{GS} \geq V_{THN}$ then the MOSFET is in the

saturation region of operation because $V_{DS} \geq V_{GS} - V_{THN}$, which will always be true. This confirms that it is operating in the saturation region.

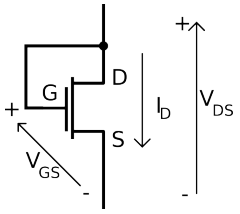

Figure 3.8: A diode connected NMOS transistor.

3.6.3 Subthreshold Operation

The diffusion current that flows in a transistor when $V_{GS} < V_{THN}$ (cutoff/weak inversion) is referred to as the subthreshold current. In digital circuits this is unwanted, but this region of operation is very useful in analogue circuits because it gives the highest possible transconductance (g_m) to current ratio ($g_m/I_D = 1/(nV_T)$), where $V_T = kT/q$ is the thermal voltage. This current is given by Equation 3.35,

$$I_S(V_{DS}) = I_{SO}(V_{DS})\frac{W}{L}e^{\left(\frac{V_{GS}-V_{THN}}{nV_T}\right)} \tag{3.34}$$

The subthreshold current is shown in Figure 3.9.

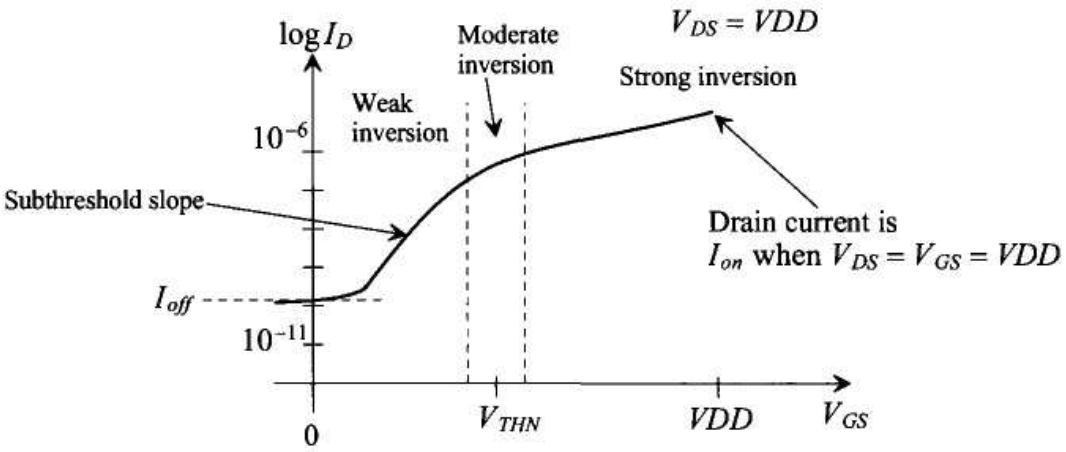

Figure 3.9: Variation with subthreshold current with gate-source voltage for a NMOS transistor. This is discussed in Equation 3.35 of section 3.6.3 [39].

For the PMOS transistor, $V_{SG} < V_{THP}$, and since $V_S = V_{DD}$, and $V_D = V_G$

$$I_S = I_{DO}(V_{DS})\frac{W}{L}e^{\left(\frac{V_{DD}-V_D-V_{THP}}{nV_T}\right)} \tag{3.35}$$

where n is given by

$$n = 1 + \frac{C_D}{C_{OX}}$$

and I_{D0} is the scaled current through the PMOS transistor at the onset of subthreshold operation.

3.7 Logarithmic Pixel

The logarithmic pixel was originally designed by Chamberlain [40] to act as a high dynamic range pixel.

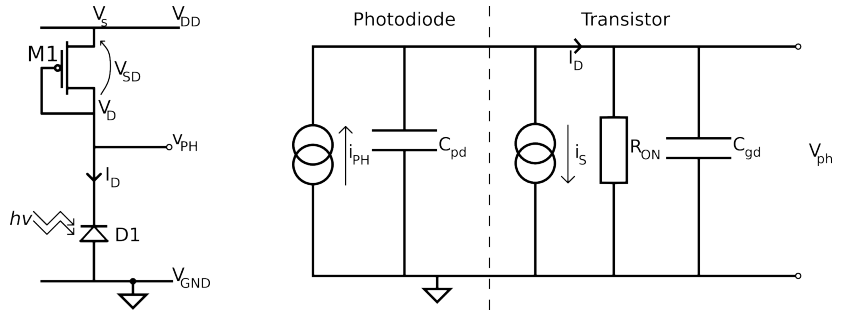

(a) Logarithmic pixel front-end

(b) Small signal model for log pixel front end shown in subfigure 3.10a

Figure 3.10: A logarithmic pixel circuit (a) and small signal model (b)

Figure 3.10a shows a simple front end circuit. It shows an n-well diode with a diode-connected PMOS transistor load. Under normal operating conditions, this transistor operates in the subthreshold region, and the relationship between the drain current and the voltage (V_{DS}) across the transistor M1 is given by Equation 3.35. The small signal model is shown in figure 3.10b.

Let $i_D = I_S + i_{PH}$, where illumination $i_{PH} = I_{PH} + i_{ph}$. The current becomes

$$\begin{aligned} I_D(V_{SD}) &= I_S(V_{SD}) + i_{PH} \\ &= I_{DO}(V_{SD})\frac{W}{L}e^{\left(\frac{V_{DD}-V_D-V_{THP}-v_{PH}}{nV_T}\right)} \end{aligned} \tag{3.36}$$

where v_{PH} is the voltage change at V_D due to the i_{PH}. Subtracting Equation 3.36 from Equation 3.35, we get:

$$\begin{aligned} i_{PH} &= i_D - I_S \\ &= I_{D0}(V_{SD})\frac{W}{L}e^{\left(\frac{V_{DD}-V_D-v_{PH}-V_{THP}}{nV_T}\right)} - I_{D0}(V_{DS})\frac{W}{L}e^{\left(\frac{V_{DD}-V_D-V_{THP}}{nV_T}\right)} \\ &= I_{D0}(V_{DS})\frac{W}{L}\left[e^{\left(\frac{V_{DD}-V_D-v_{PH}-V_{THP}}{nV_T}\right)} - e^{\left(\frac{V_{DD}-V_D-V_{THP}}{nV_T}\right)}\right] \\ &= \left[I_{D0}(V_{DS})\frac{W}{L}e^{\left(\frac{V_{DD}-V_D-V_{THP}}{nV_T}\right)}\right]\left[e^{\frac{-v_{PH}}{nV_T}} - 1\right] \\ i_{PH} &= I_S[e^{(\frac{v_{PH}}{nV_T})} - 1] \end{aligned} \tag{3.37}$$

Considering the small signal model in figure 3.10b, and using the Laplace transform ($s = j\omega$),

$$v_{PH}(s) = [i_{PH}(s) - I_S(s)]\left[\frac{R_{on}}{1 + s(C_{pd} + C_{gd})R_{on}}\right] \tag{3.38}$$

3.7.1 Low Frequency Response

At low frequencies, $s \approx 0$, and Equation 3.38 gives the result:

$$v_{PH}(s) = [i_{PH}(s) - I_s(s)]R_{on}$$

Noting that because of the I_S component, v_{PH} is a function of V_{DS}, the inverse transform gives:

$$\begin{aligned} v_{PH}(V_{DS}) &= \big(i_{PH} - I_S(V_{DS})\big[e^{(\frac{v_{PH}(V_{DS})}{nV_T})} - 1\big]\big)R_{on} \\ \frac{v_{PH}(V_{DS})}{R_{on}} &= i_{PH} - I_S(V_{DS})\big[e^{(\frac{v_{PH}(V_{DS})}{nV_T})} - 1\big] \\ i_{PH} &= I_S(V_{DS})\big[e^{(\frac{v_{PH}(V_{DS})}{nV_T})} - 1\big] + \frac{v_{PH}(V_{DS})}{R_{on}} \end{aligned} \tag{3.39}$$

Case 1: If $\frac{v_{PH}(V_{SD})}{R_{on}} \ll I_S(V_{SD})e^{(\frac{v_{PH}}{nV_T})}$, then

$$\begin{aligned} i_{PH} &= I_S(V_{SD})[e^{(\frac{v_{PH}}{nV_T})} - 1] \\ v_{PH}(V_{SD}) &= nV_T \ln\left(\frac{i_{PH} + I_S(V_{SD})}{I_S(V_{SD})}\right) \end{aligned} \tag{3.40}$$

Thus for $i_{PH} \gg I_S$, then Equation 3.40 shows that voltage v_{PH} varies with the natural logarithm of the photocurrent. The signal voltage varies logarithmically with the intensity of the illumination source.

If $i_{PH} \ll I_S$, then $v_{PH} = V_T \ln(1 + i_{PH}/I_S)$. Taking the Taylor Series of $\ln(1+x), x = i_{PH}/I_S$ and ignoring second order and higher terms, we observe v_{PH} varies linearly with i_{ph}/I_S, and $v_{PH} \approx V_T \frac{i_{ph}}{I_S(V_{SD})}$.

Case 2: If $\frac{v_{PH}}{R_{on}} \gg I_S(V_{SD})e^{(\frac{v_{PH}}{nV_T})}$, then

$$v_{PH}(V_{SD}) = (i_{PH} + I_S(V_{SD}))R_{on} \tag{3.41}$$

Equation 3.41 shows that at low light levels, when the quiescent subthreshold current dominates, the voltage at the signal voltage of the photo-detector is quasi-linearly proportional to the photocurrent i_{ph}.

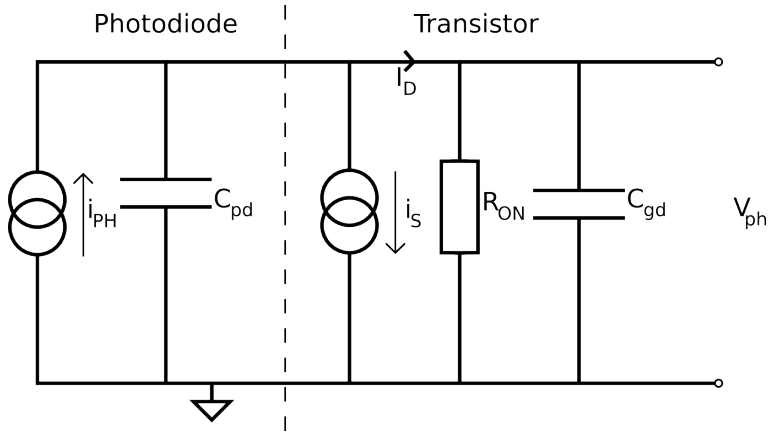

Figure 3.11: This circuit shows the ac small signal circuit. The small signal gain due to g_m is shown, and the output signal voltage due to the AC photocurrent is given as v_{ph}.

3.7.2 AC Small Signal Response

The ac small signal gain of the transistor is given by

$$g_m = \left[\frac{\partial i_{ph}}{\partial v_{DS}}\right]_{V_{SD}=V_D+V_{PH}=constant}^{I_D=I_S+I_{PH}=constant}$$

From the ac small signal model shown in Figure 3.11

$$\begin{aligned} i_{ph} &= I_S + \frac{1}{R_{on}} v_{ph} \\ &= g_m v_{ph} + \frac{1}{R_{on}} v_{ph} \end{aligned}$$

Using Equation 3.32, and briefly ignoring channel-length modulation ($\lambda = 0$, $R_{on} = \infty$), and letting $|v_{DS}| \ll V_{SD}$

$$\begin{aligned} I_D &= I_S + i_{PH} \\ &= I_S + I_{PH} + i_{ph} \\ &= \frac{KP_p}{2}\frac{W}{L}(v_{PH} + V_{SD} - V_{THP})^2 \\ g_m &= KP_p\frac{W}{L}(v_{PH} + V_{SD} - V_{THP}) \\ g_m &= \sqrt{2\left(KP_p\frac{W}{L}\right) I_D} \end{aligned} \tag{3.42}$$

$$
\begin{aligned}
i_{ph} &\approx v_{ph} g_m \\
i_{ph} &= v_{ph}\sqrt{2\left(KP_p\frac{W}{L}\right)I_D} \\
v_{ph} &= i_{ph}\frac{1}{\sqrt{2\left(KP_p\frac{W}{L}\right)I_D}}
\end{aligned}
\tag{3.43}
$$

Equation 3.42 shows that transconductance varies with the square-root of the drain current. The gain due to the transconductance is equivalent to a small signal resistance of $\frac{1}{g_m} = \frac{v_{ph}}{i_{ph}}$, which is shown in the small signal model in Figure 3.10b. Equation 3.43 gives the ac small signal voltage of the front-end, showing that it varies with $\frac{1}{\sqrt{I_D}}$.

This simulated variation in ac small signal gain $(1/g_m)$ with DC photocurrent is shown in Figure 3.12.

3.7.3 Frequency Response

The frequency response of the front-end can then be modelled from Figure 3.10b. This model is the Norton equivalent to an RC series circuit with a voltage source. We treat the transconductance g_m as a resistor of value $1/g_m$, and use $R_D = R_{on}\|g_m$ in Equation 3.38. The transfer function for the system is given by:

$$
\begin{aligned}
H(s) &= \frac{v_{PH}(s)}{i_{PH}(s)} \\
\frac{v_{PH}(s)}{i_{PH}(s)} &= \frac{(1/g_m)\|R_{on}}{1 + s(C_{pd} + C_{gd})((1/g_m)\|R_{on})} && (3.44) \\
&= H(s, I_D) && (3.45)
\end{aligned}
$$

Note that since g_m is strongly dependent on I_D, the transfer function is also a function of I_D. We write this as $R(I_D)$ Lumping the resistances and capacitance

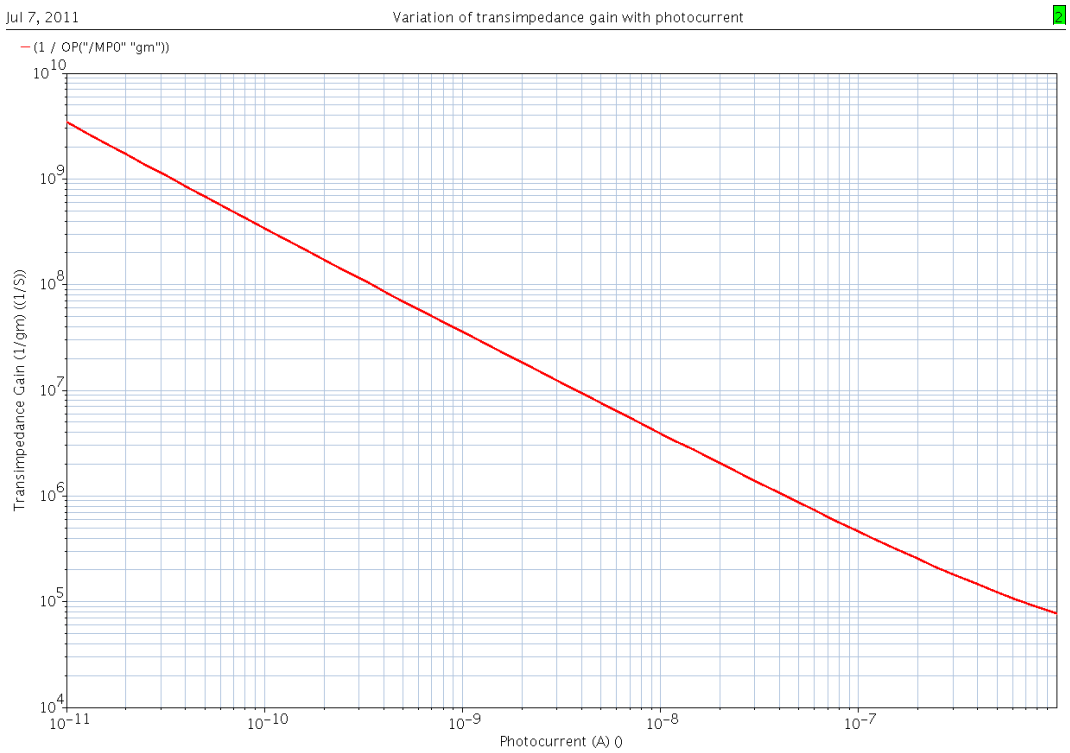

Figure 3.12: Simulated variation in ac transimpedance gain $(1/g_m)$ with increasing photocurrent for a 2/2 transistor. The departure from the straight line is due to departure from subthreshold operation at high drain current. Figure 3.9 shows where a device enters strong inversion.

together, the amplitude and phase response is given by

$$\begin{aligned} |H(j\omega, I_D)| &= \frac{1}{\sqrt{1+(\omega CR(I_D))^2}} \\ \angle H(j\omega, I_D) &= \tan^{-1}(\omega CR(I_D)) \end{aligned}$$

Practical Case: The photodiode in LIDAR1 (section 5.2.1) has an area (A) of $2137\,\mu m^2$ and a perimeter(P) of $263\,\mu$m. From the C35 process parameters, for the voltage V = 2.7 (varies with I_D), and junction potential (PB) $\approx 0.53\,$V, the capacitance of the photodiode may be calculated from Equation 3.46.

$$C = \frac{A \times C_{\mathrm{J}}}{\left(1+\frac{V}{\mathrm{PB}}\right)^{\mathrm{MJ}}} + \frac{P \times C_{\mathrm{JSW}}}{\left(1+\frac{V}{\mathrm{PB}}\right)^{\mathrm{MJSW}}} \tag{3.46}$$

as

$$
\begin{aligned}
C &= \frac{21370.08f}{\left(1+\frac{2.7}{0.53}\right)^{0.39}} + \frac{2630.51f}{\left(1+\frac{2.7}{0.53}\right)^{0.27}} \\
&= 84.45 + 82.34 \\
&= 166.82\,\mathrm{fF} \qquad (3.47)
\end{aligned}
$$

where C_{J} is the junction capacitances, C_{JSW} is the junction capacitance per drawn perimeter, MJ is the area junction grading coefficient, and MJSW is the sidewall junction grading coefficient.

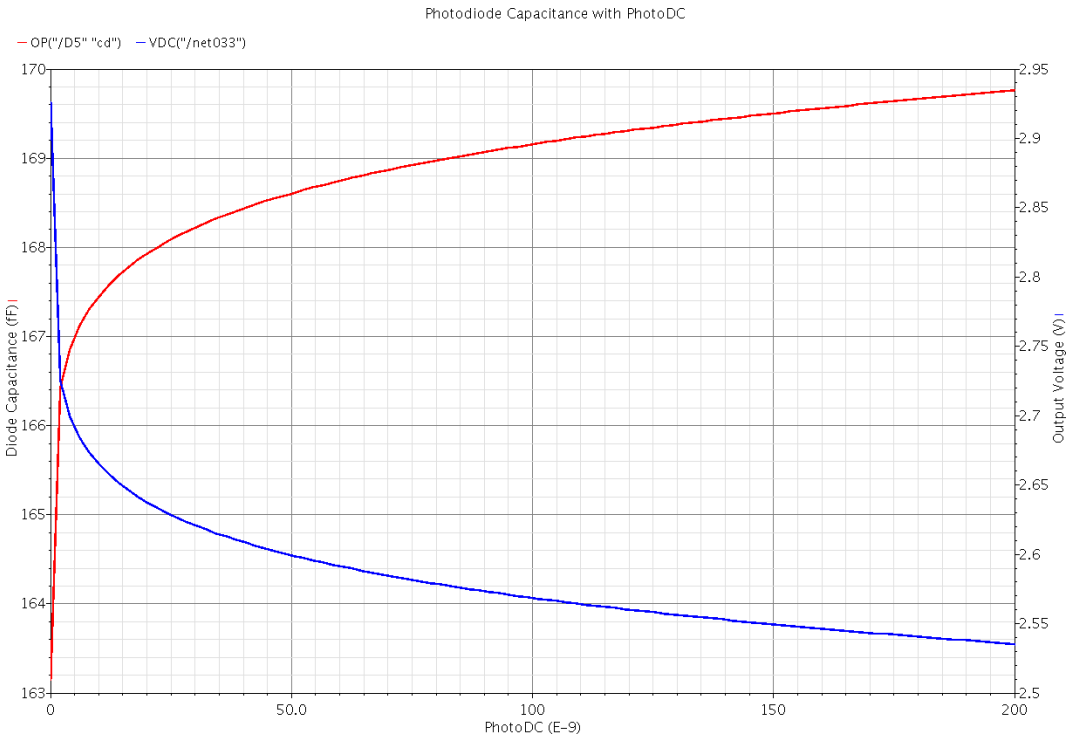

Figure 3.13: Simulated variation of capacitance of the photodiode with the drain current. The blue trace is the capacitance, and the red trace shows the DC output voltage.

The simulated variation of the capacitance and output voltage with changing DC photocurrent is shown in Figure 3.13. Ignoring all other capacitance, and using $C_{ph} = 166\,\mathrm{fF}$, the bandwidth may be approximated using the formula for an RC

circuit as:

$$
\begin{aligned}
f_{-3dB} &\approx \frac{1}{2\pi RC} \\
&= \frac{1}{2\pi \left(\frac{g_m R_{on}}{g_m + R_{on}}\right) C_{pd}}
\end{aligned}
\tag{3.48}
$$

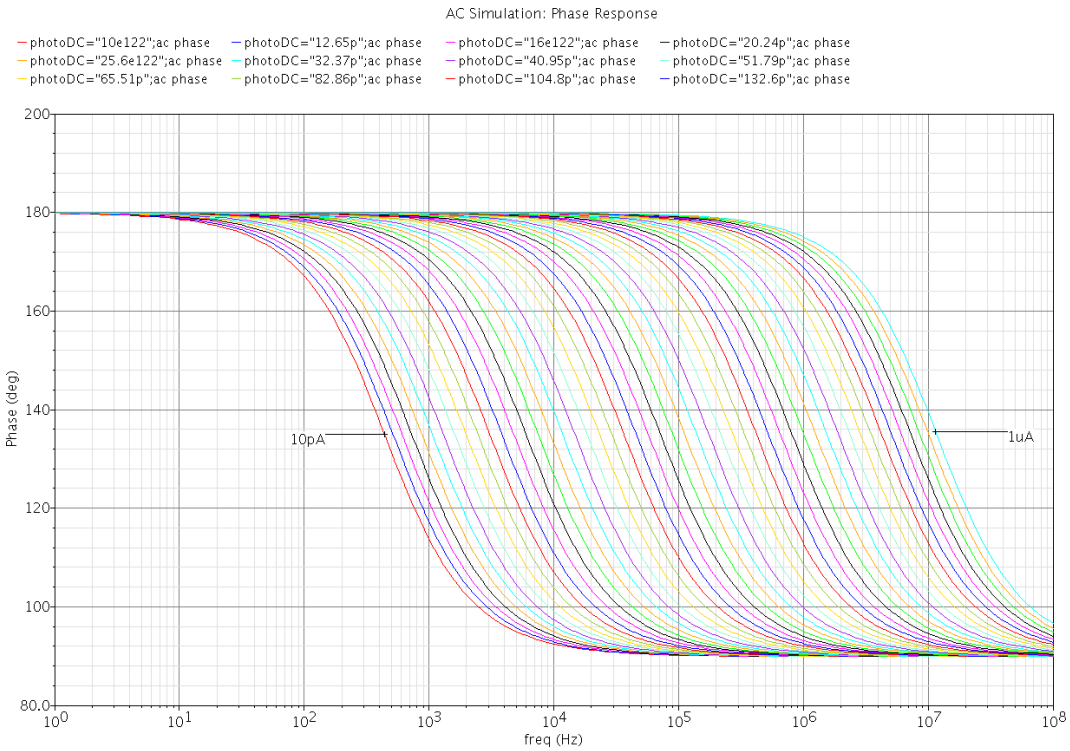

Figure 3.14: Simulated variation of the phase response with the drain current. These results are from an AC simulation. The markers show the phase response for the extremes of the I_D variation: 10 pA and 1 μA.

As Equation 3.43 shows, the voltage output due to ac illumination varies non-linearly with the DC photocurrent (I_{PH}). This is a problem because with varying DC photocurrent, the bandwidth of the system varies. Also, the capacitance across the diode is a function of the voltage across it, and this voltage (V_D), varies with the photocurrent. However this variation is relatively small and is ignored in this discussion.

In an array of pixels with this front end, different DC lighting conditions at each

pixel will lead to different gain and bandwidth conditions, making it difficult or near impossible to correctly measure i_{ph}. If the modulation frequency is close to the bandwidth, different pixels (with identical AC photocurrent but different DC photocurrent) would return a different amplitude and phase because the small signal response is (non-linearly) dependent on the DC conditions, and this is shown in Figure 3.14.

The analysis suggests sinking some current through the load transistor, M1, to fix the operating point and linearise the response. This may be done electronically or with the use of DC photocurrent.

It should also be noted that the bandwidth of this front-end is very low. This is due to the high input capacitance of the photodiode. In section 3.7.5 we discuss how this is mitigated. To mitigate the effect of the high input impedance, an input stage is needed to decouple the source (photodiode) from the load (resistor).

3.7.4 Common Gate Amplifier

The common gate (CG) amplifier is an input stage that is used because it decouples the source from the load. It is a current mode device, accepting a current I_D and passing the same current out. As shown in Figure 3.15, the current supplied by V_{in} is converted to a voltage at the drain of M1. The gate voltage V_b is used to bias M1 in saturation. The output voltage can be written as

$$\begin{aligned} V_{out} &= V_{DD} - \frac{KP_n}{2}\frac{W}{L}(V_b - V_{in} - V_{TH})^2 R_D \\ A_v &= \frac{\partial V_{out}}{\partial V_{in}} \\ &= KP_n\frac{W}{L}(V_b - V_{in} - V_{TH})\left(-1 - \frac{\partial V_{TH}}{\partial V_{in}}\right) R_D \\ &= g_m\left(1 + \frac{g_{mb}}{g_m}\right) R_D \end{aligned} \tag{3.49}$$

using $\frac{\partial V_{TH}}{\partial V_{in}} = \frac{g_{mb}}{g_m}$.

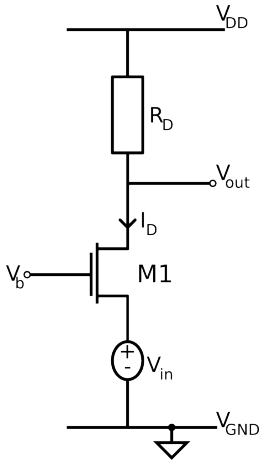

Figure 3.15: A Common gate amplifier, with a voltage source.

It is important to note the importance of body effect, since the source of M1 is not at the same potential as the base. The body effect decreases the input impedance of the common-gate stage. It is also important to note that the drain current sets the operating conditions, because the transconductance (g_m) depends on the current.

Therefore the capacitance of the photodiode is reduced by the transconductance $\approx g_m$. The bandwidth equation (Equation 3.30) may then be written as

$$f_{-3dB} \approx \frac{g_m}{2\pi C_{pd}}$$

Thus by putting the common gate amplifier between the source and load, the bandwidth increases by a factor of $1/g_m$. The common gate amplifier must be in saturation for proper operation, and this means that the dynamic range is reduced by the overdrive voltage of M1.

3.7.5 Regulated Cascode input stage

The cascade of a common-source and a common-gate stage is called a *cascode* topology. The name is believed to be an acronym for "cascaded triodes", from vacuum tube terminology.

The regulated cascode (RGC) stage is a feedback system comprising a common source and a common gate amplifier. It is equivalent to a common-gate amplifier with a large transconductance (G_m). Two advantages of the RGC are the high output and low input impedance as well as a wide voltage swing. The theory in this section is discussed in more detail in [41–43].

Short channel devices exhibit noticeable channel length modulation (CLM or λ). This reduces the maximum achievable gain, since the intrinsic gain of a transistor is given by $g_m R_o$ and R_o is inversely proportional to λ. To achieve high gain and accuracy with low power consumption requires longer and wider transistors, but these are slower. The regulated cascode amplifier is a transimpedance amplifier (TIA) that can be used to achieve high speed, high gain, wide dynamic range and low power consumption.

Figure 3.16 shows the RGC amplifier with a photodiode input source and the small signal circuit. The bias current for M1 is provided by the Resistor R_1. The voltage output is drawn at the drain of M1. The feedback stage (M2 and R_2) provide the bias for the input transistor M1 and thus the input node (1) sits at virtual ground.

The operation of the TIA is thus as follows: When the current through M1 increases, the voltage at (1) increases and the drain current of M2/R_2 increases. Due to the increasing voltage drop over R_2, the voltage at (2) reduces, and reduces the drain current of M1. Thus the voltage at node (2) varies less with current than

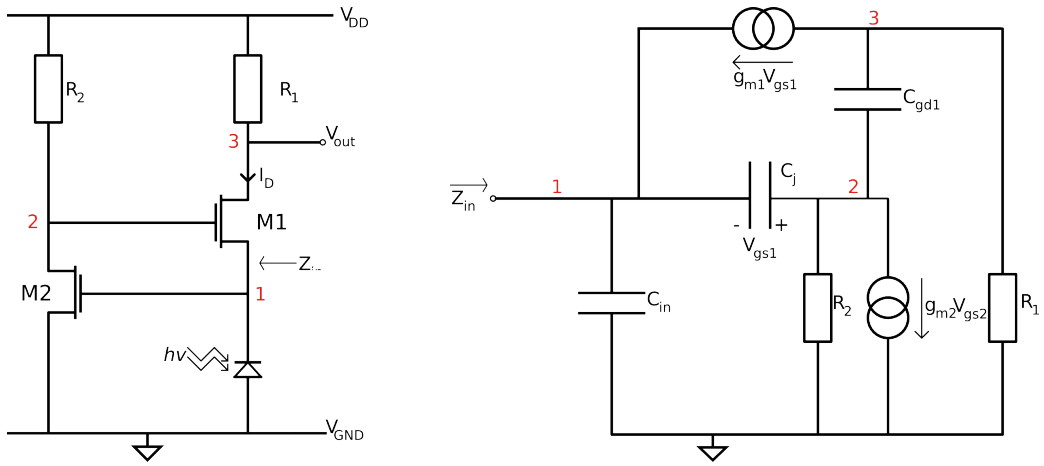

(a) RGC TIA (b) RGC TIA SSM

Figure 3.16: A regulated cascode TIA in a front end, and its small signal model. C_{in} is the sum of all the parasitic capacitance at the input node, and $C_j \approx C_{gs1} + C_{gd2}$

it would without the feedback. Since this happens with M1 in saturation, the effect is to reduce the effect of channel-length modulation. (Thus the contribution of R_{on1} can henceforth be ignored). This is the source of the *regulation* (in the name), and the source of the transistor M1 is regulated by M2.

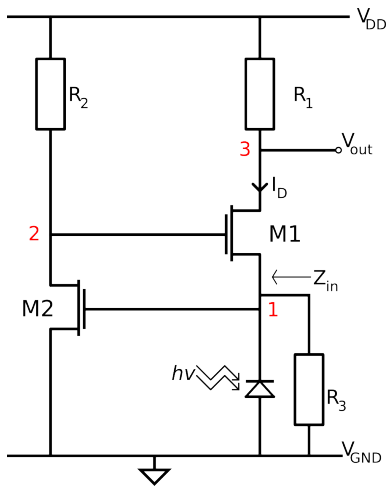

Figure 3.17: Front-end with resistor R_3 to sink current

The input impedance is the impedance seen by the signal source at node 1, using

the Laplacian variable $s = j\omega$:

$$Z_{in}(s) = \frac{\frac{1}{R_2} + s(C_{gs1} + C_{gd2})}{\mathbf{X} + \mathbf{Y}} \tag{3.50}$$

where $\mathbf{X}$ and $\mathbf{Y}$ are used here only for type-setting purposes, and are

$$\mathbf{X} = \left(g_{m2} + \frac{1}{R_2}\right)(g_{m1} + s(C_{gs1} + C_{gd2}))$$
$$\mathbf{Y} = \left(\frac{1}{R_2} + s(C_{gs1} + C_{gd2})\right)\left(\frac{1}{R_3} + s(C_{pd} + C_{gs2} + C_{gs1})\right)$$

The input resistance of the RGC stage is the inverse of the combination of the voltage gain of the feedback stage $(1 + g_{m2}R_2)$, and that of the common gate stage g_{m1}. This is given from Equation 3.50, using $s = 0$.

$$R_{in} = Z_{in}(0) \approx \frac{1}{g_{m1}(1 + g_{m2}R_2)}$$

Comparing this with the gain of the CG stage, the effective transconductance has increased by a factor of $(1 + g_{m2}R_2)$. The RGC is therefore more effective at isolating the large input parasitics that are associated with photodiodes, providing a greater input bandwidth. Even at high frequencies, the dependence of the response on the photodiode capacitance (C_{pd}) is reduced by the voltage gain, reducing its effect on bandwidth determination. It is possible to conclude that the RGC circuit behaves as a common-gate transistor with a effective transconductance $G_m = g_{m1}(1 + g_{m2}R_2)$.

Due to the virtual ground in the feedback stage, a pole appears at node (2) and causes a peaking in the frequency response. This is internal to the feedback stage, and the peaking occurs at f_{peak} as shown in Equation 3.51

$$f_{peak} = \frac{1}{2\pi R_2(C_{gs1} + C_{gd2})} \tag{3.51}$$

The peak can be shifted by varying R_2 or the sizes of the transistors. It is also possible to use a transistor as a current source, and by varying the current, move the pole as required.

The -3dB bandwidth point is determined by the dominant pole, which is given by the impedance seen in the output. This occurs at

$$f_{-3db_RGC} \approx \frac{1}{2\pi R_1 C_{d1}} \tag{3.52}$$

where $C_{d1} \approx C_{gd1} + C_{gd2}$. The effect of the photodiode capacitance is effectively removed from the analysis by the RGC input stage.

3.8 Tunebias (Source Degeneration)

Besides pushing the dominant pole to higher frequencies to increase the bandwidth, it is possible to compensate the pole with a zero, and this can be achieved by capacitive degeneration. This works by degenerating the transistor M1 at the source so that with increasing frequency, the effective transconductance also increases to counter the gain roll-off due to the pole at node (3) in Figure 3.17. The voltage gain due can be written as

$$A_v = \frac{v_{out}}{v_{in}} = \frac{g_{m1}R_1}{1 + g_{m1}R_3} \frac{1 + sR_3C_3}{1 + s\frac{R_3C_3}{1+g_{m1}R_3}} \tag{3.53}$$

This contributes a zero at $(R_3C_3)^{-1}$ and a pole at $\frac{R_3C_3}{1+g_{m1}R_3}$.

A major innovation in this project is to insert a current source that linearises the load transistor (M3) response, sets the operating point for the RGC transistor M1, and degenerates M1. The circuit is shown in Figure 3.18.

The current that M4 sinks is henceforth referred to as *tunebias* (I_T). M4 (which replaces R_3 in Figure 3.17) is referred to as the tuning transistor. Figure 3.18 shows the schematic of the front-end with tunebias and tuning transistor M4. Transistor M5 is common to all pixels in the array, ensuring that operating conditions are the same across all the pixels, and that phase and amplitude response are the same, given that $I_T \gg I_{PH}$.

It is possible to write I_T as the current that flows through M4, M1 and M3, and we write this as

$$I_T \approx \frac{V_{DD}}{R_{on4} + R_{on1} + R_{on3}} \tag{3.54}$$

where we assume that $I_T \gg I_{PH}$.

Tunebias performs the additional task of determining the slew rate of the TIA. For a load capacitance C_L the slew rate may be calculated as

$$\begin{aligned} I &= C_L \frac{\mathrm{d}V_{out}}{\mathrm{d}t} \\ \frac{\mathrm{d}V_{out}}{\mathrm{d}t} &= \frac{I}{C_L} \end{aligned} \tag{3.55}$$

For a current of 100 nA, and a capacitance of 1 pF, the slew rate is 100 kV/μS. This circuit allows a 2-mode system.

1. **DC mode:** With tunebias = 0 nA, the system can be used as a normal DC camera. The gain is very high at low I_D, and this gives a good DC image.

2. **AC mode:** For high frequency measurements, tunebias can fixed to give a trade between gain and frequency. This reduces the DC dynamic range but linearises the response across the pixels, giving a linear phase and amplitude response, even at high modulation depths.

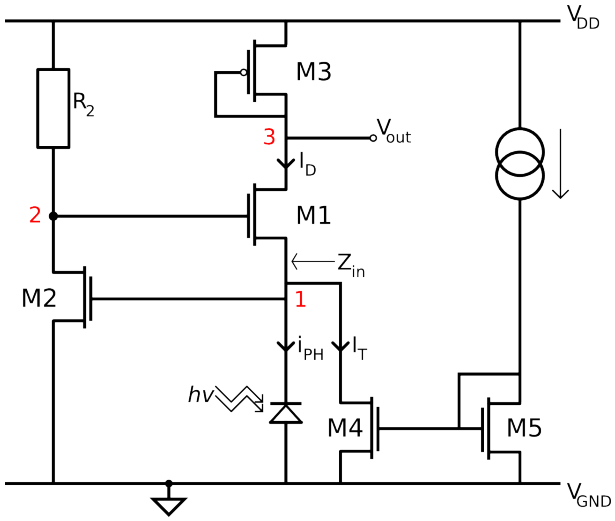

Figure 3.18: Front-end circuit showing the tuning transistor (M4 replaces R_3 in Figure 3.17) and tunebias (I_T).

3.8.1 Noise

Assuming that all noise sources are uncorrelated, the equivalent noise current spectral density is given by

$$\begin{aligned} \bar{i_{eq}^2} \approx & \frac{4kT}{R_S} + \frac{4kT}{R_1} + \frac{4kT(\frac{1}{g_m})}{g_{m2} + \frac{1}{R_2}} \left[\frac{1}{R_2^2} + \omega^2 \left(C_{total}\right)^2 \right] \\ & + \frac{4kT\omega^2 \left(C_{gs1} + C_{gd2}\right)^2}{g_{m1}^2} \left(\frac{1}{R_1} \right) \end{aligned} \tag{3.56}$$

where k is the Boltzmann Constant, and T is the absolute temperature. The total input capacitance is written as $C_{total} = C_{pd} + C_{gs2} + C_{sb1} + C_{gd4} + C_{gs4}$.

Figure 3.19 shows the simplified noise equivalent circuit.

3.9 Design Decisions

For all these reasons, the approach taken in the devices presented in this thesis is to electronically sink a fixed amount of current through M1 by the use of the current source M4, as shown in Figure 3.18. This current may be varied externally (off-chip) in accordance with operating conditions. The following results are

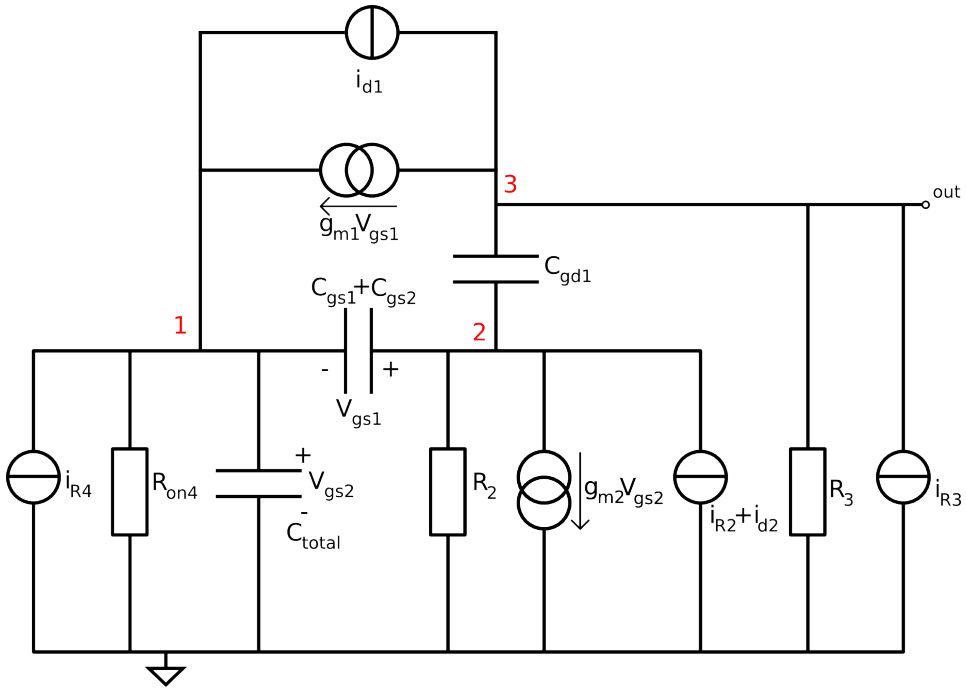

Figure 3.19: Noise Equivalent Circuit for the schematic shown in Figure 3.18.

observed:

1. From Case 2 of section 3.7.1, the response to low frequency photocurrent is linearised, ie Equation 3.41 holds true.

2. From Equation 3.42 the g_m is set by the I_D. Using a high I_D linearises the result.

3. With the operating point set by the DC reference current, it is possible to use a consistent bandwidth and gain profile for all pixels. This is particularly important because without this, at high modulation depths different pixels would have different amplitude/phase responses and it exhibits a high non-linearity.

4. The transimpedance gain reduces with current, thus the gain of the system reduces as the inverse square root of the DC drain current (which comprises leakage, DC photocurrent and tunebias).

5. The dimensions of M1 and M2 must be chosen carefully to ensure optimal noise, bandwidth and gain response.

4 | Test Designs

Two chips were fabricated in the process of designing the full modulated camera. There first was a single pixel circuit christened MLCv6FE, and the second had a full array of 32 by 32 pixels, and that was christened MLCv6. This chapter discusses those two designs which leads to the final design, LIDAR1, presented in Chapter 5.

4.1 MLCv6FE

This design was a test of the front-end proposed for MLCv6, and it was based loosely on Perelman's pixel, as discussed in [33]. The design was submitted for fabrication in June 2008, and was received in September 2008. It was a minor part of a multi-project chip, and due to limited pad (connection points) availability, it comprised only a single pixel, an amplifier and an output buffer.

4.1.1 Design Details

As shown in Figure 4.1, the front end is similar to the front end used in MLCv5 [28], with the inclusion of a bias transistor. This transistor acts as a current sink for the log load transistor, and the regulated cascode circuit, effectively fixing its bias point and transimpedance. This transimpedance is determined by the current through the so-called *tuning* transistor.

As shown in the diagram in Figure 4.1, the front end has a 40 μm by 40 μm photo-active area, using an n-well for the photo-electron conversion. A trans-impedance (TIA) feedback arrangement of the transistors MN1 and MN2 provide 42 dB gain, and increase the bandwidth by isolating the impedance of the load transistor from

the capacitance of the photodiode. As a measure of the isolation, the capacitance of the photodiode was simulated to be 90 fF, and that of the drain-gate junction of MN1 was calculated as 5 fF. The tuning transistor MN3 is simulated to have a capacitance of 13 fF. The load transistor MP2 has a capacitance of 25 fF. The resistance $r_{on} = 681\,k\Omega$ (dependent on light/bias conditions, simulated at 100 nA). This suggests a bandwidth in the region of 30 MHz.

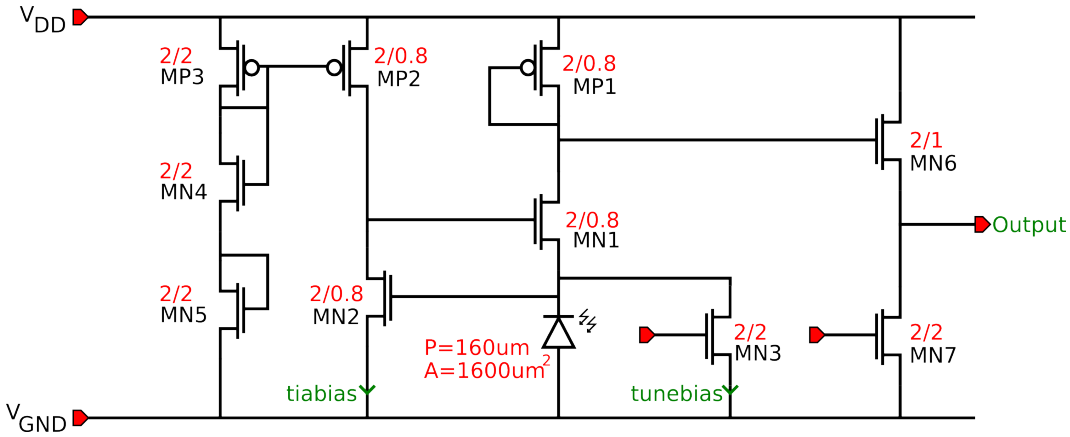

Figure 4.1: Schematic detailing MLCv6FE front end

The main amplification is from two cascaded Output Transconductance Amplifiers (OTAs), each biased to provide 34 dB of gain. The bandwidth is about 30MHz with this bias current.

The signal is then buffered using the same buffer designs from MLCv5 to drive the signals off the chip. This is a 3.3 V buffer rated for operation from DC to 30 MHz with a bias current of 10 μA.

Figure 4.2 shows the layout for the MLCv6FE design, as well as a schematic that gives the overview of it.

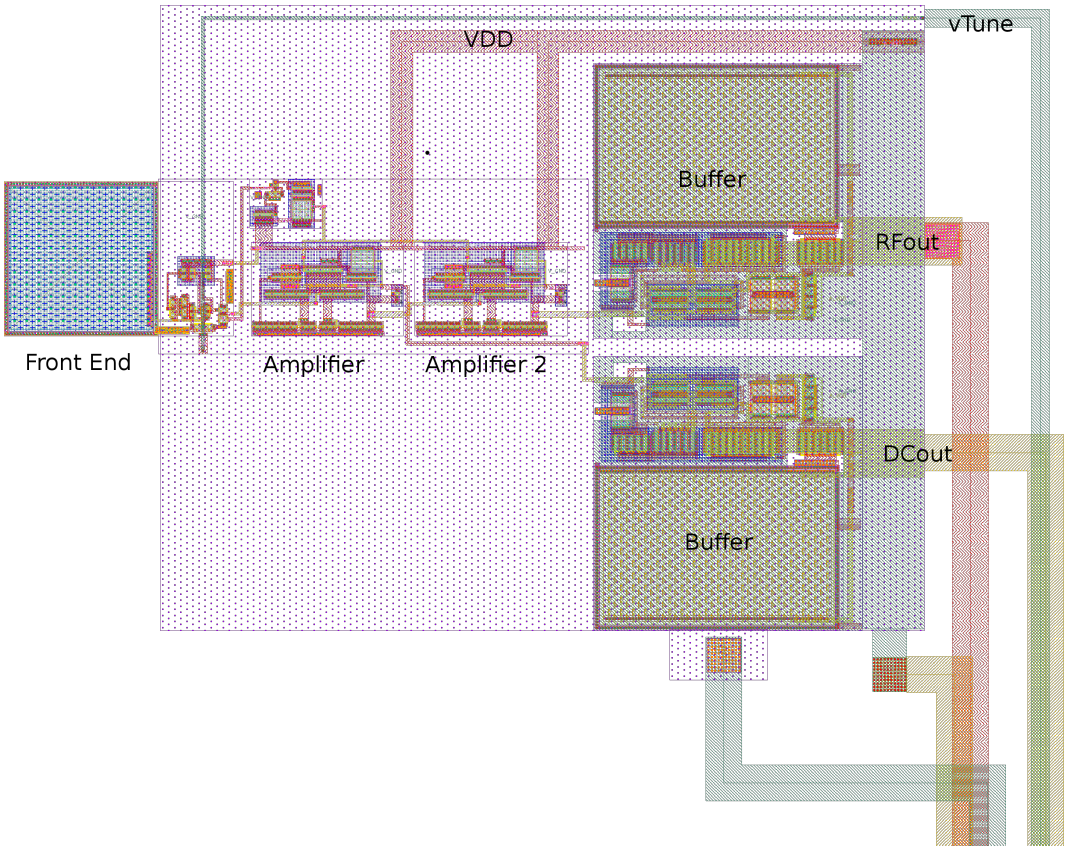

(a) Layout

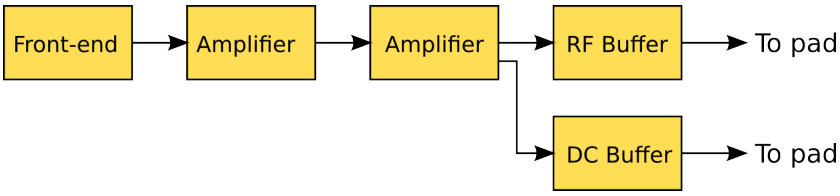

(b) Schematic

Figure 4.2: The layout and schematic for MLCv6FE.

4.1.2 Experiment

The PCB shown in Figure 4.3 was designed and fabricated to test MLCv6FE.

The experimental setup comprised a line of sight system. A 635 nm laser with bandwidth from DC to 14 MHz and 6mW of light power was used to characterise the system. The Thorlabs PDA63A-EC was used as a reference photodiode, with gain set to 0 dB.

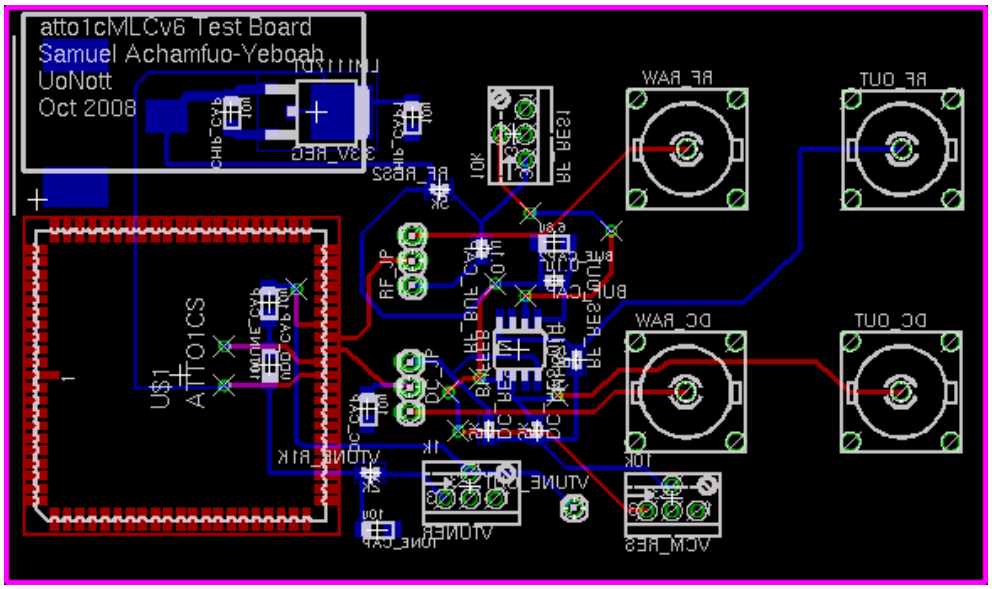

(a) PCB Layout Gerber

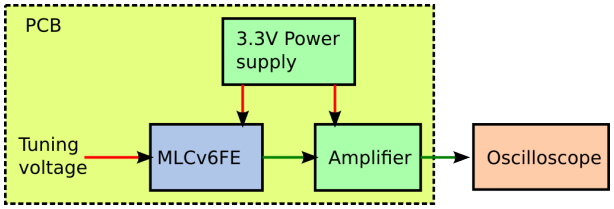

(b) PCB Schematic

Figure 4.3: The PCB used to characterise MLCv6FE

4.1.3 Experimental Results

Due to some design weaknesses discussed in section 4.1.5 and the fact that the laser used in characterising MLCv6FE was limited to a bandwidth of 14MHz, most of the tests were constrained to this bandwidth.

The graphs from Figure 4.4 to Figure 4.7 show the results of a characterisation experiment. The modulating signal is increased from 100 mV to 500 mV in steps of 10 mV. The frequency is swept from 2 MHz to 14 MHz.

4.1.4 Discussion of Results

As shown in Figure 4.4, the amplitude response of MLCv6FE was as expected. Reading from the first subfigure, when the signal generator amplitude is 500 mV,

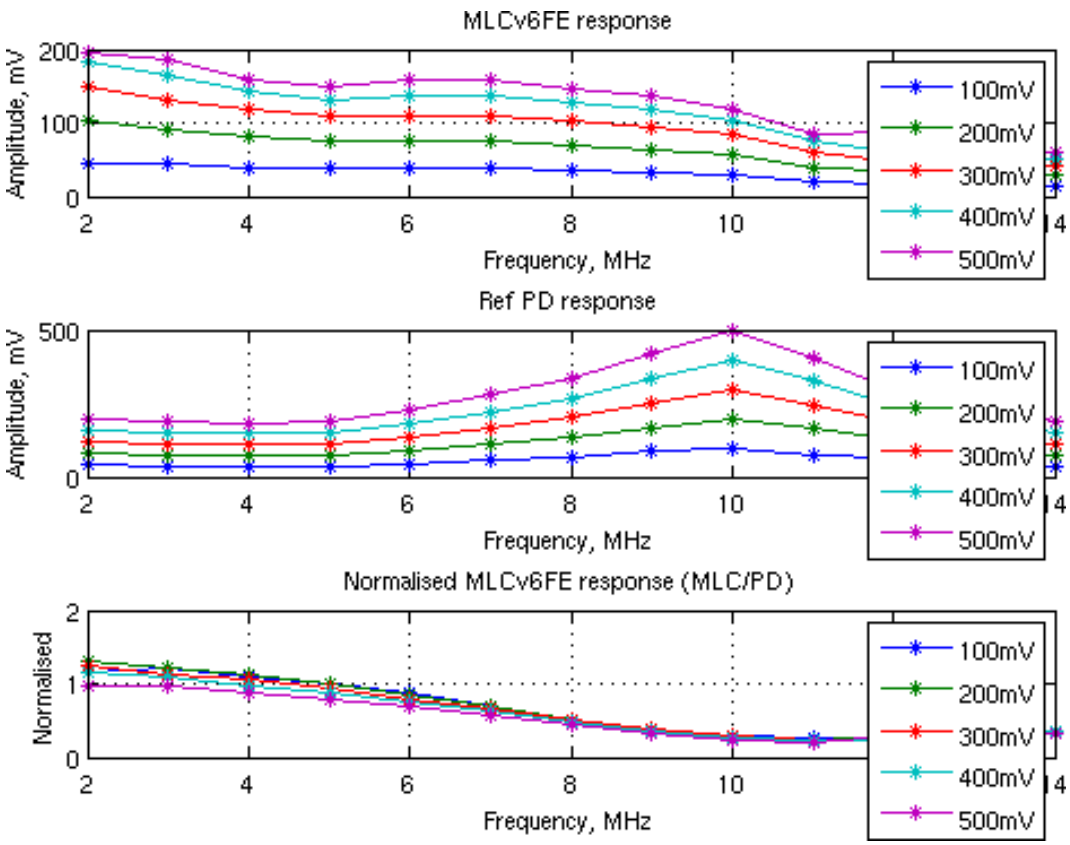

Figure 4.4: Frequency response from the characterisation of MLCv6FE. Details are discussed in section 4.1.3. The first subfigure shows the signal on MLCv6FE RFout, the second is for the reference photodiode, and the third is a ratio of the two, providing a means of normalisation.

the output voltage is 200 mV at 2 MHz. The measured AC light is 12 nW. This suggests a transimpedance gain of $\frac{200\,mV}{4nA}$ =5 MΩ. The second subfigure shows the response of the Thorlabs photodiode to the same stimulus. This allows elimination of the contribution or the response of the light source to the response of MLCv6FE. The third subfigure is a normalised ratio of the two responses. This allows a more correct interpretation of the response of the test device.

Figure 4.5 shows a similar response to that in Figure 4.4, but the emphasis is on the amplitude response with frequency. The measured amplitude of the test device and the photodiode are shown, and a normalised ration is also shown, with varying signal-generator amplitudes and frequencies.

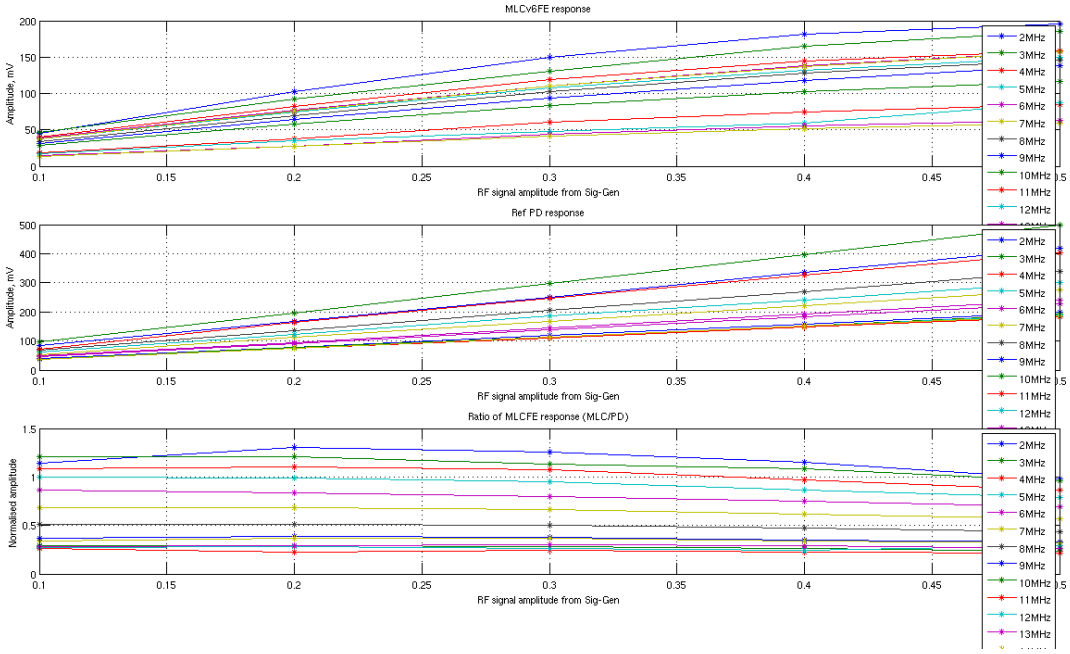

Figure 4.5: The graph shows the amplitude response with different frequencies for MLcv6FE. It also shows the response of the reference photodiode, and a ratio of the two.

Figure 4.6 shows the normalised frequency response. In this case the frequency at which the peak amplitude occurs is used to normalise the characteristic.

Figure 4.7 shows the standard deviation of the measured amplitude from MLCv6FE, the reference photodiode with varying signal amplitude. This gives an indication of the error in measurement. It can be seen that with increasing signal to the laser, both reference photodiode and MLCv6FE record an increase in standard deviation. The third subfigure shows that the ratio of $\delta(\mathrm{V_{MLCv6FE}})$ to $\delta(\mathrm{V_{Ref}})$ is almost constant about 0.36.

4.1.5 Discussion

This being the first chip, it was not as test-worthy as it could have been. A number of design weaknesses came to the fore in the process of testing.

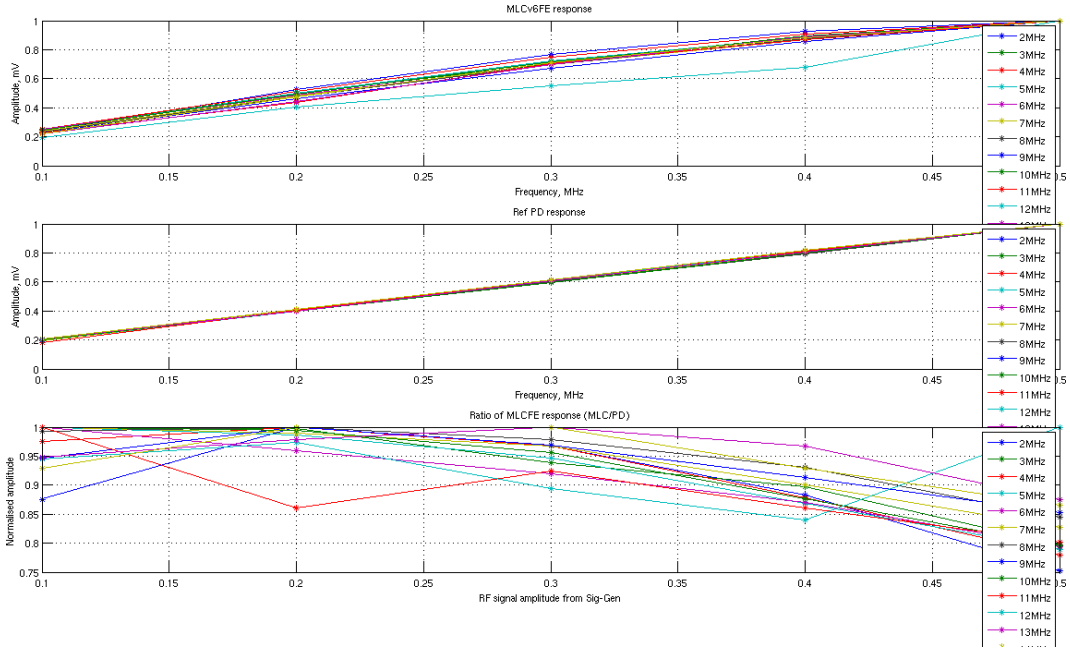

Figure 4.6: The graphs show the normalised results from the first experiment on MLCv6F.E The curves are normalised to the peak amplitude for each frequency.

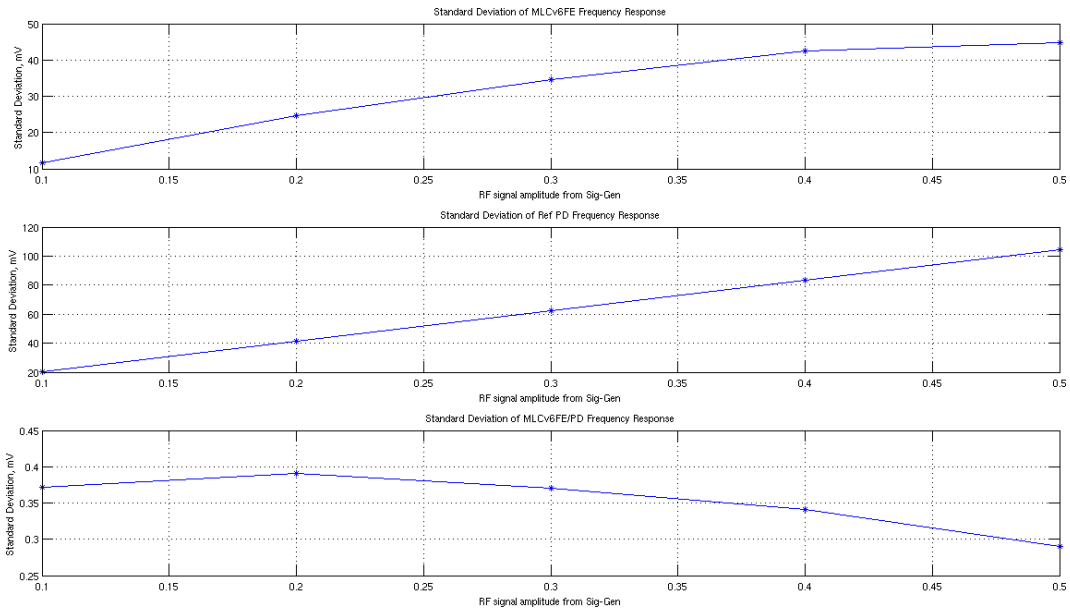

Figure 4.7: Standard deviation in measured amplitude from MLCv6FE

One weakness is that the tuning resistor was set up as a voltage controlled current source, instead of as a current controlled current source. This led to an inability to correctly set the bias current in the pixel.

Another weakness was that because there was only one pixel, there was no way

of checking the crosstalk between pixels. For example, in a full array, the tuning current would be shared across several pixels. Since these are so close to the photodiode, a signal from one pixel could easily be seen in another. The effect could not be checked on MLCv6FE.

Another problem was that the buffer had a very low slew rate, with a rise time of about 5 seconds. Since the bias current was fixed internally, there was no way of increasing the drive and increasing the slew rate.

As seen from the results, the dynamic range of the pixel is very small, only being able to detect within 200 pA to 10 nA of light (equivalent to approximately 30 W/m^2 at peak) before saturating. This is due to the use of the cascaded amplifiers. Since the gain of the amplifiers is set internally, it is not possible to change the gain. It is also not possible to bypass the second amplifier.

Overall, the pixel showed the promise of being able to detect light from 0 Hz to 13 MHz, with the caveat of a very small dynamic range. This suggested it would be better to work with a single amplifier.

4.2 MLCv6

This was a complete camera, built around the MLCv6FE design.

Working further from the results and conclusions seen in MLCv6FE, MLCv6 was developed from November to March 2009. It was submitted in March 2009 to Fraunhoffer for fabrication at a cost of Euro 15,800.

MLCv6 is based on the MLCv6FE concept. It is optimised for high bandwidth, and comprises a single OTA amplifier, two fully differential gilbert-cell mixer, and 4 filters. All components are designed so that their bias points can be set externally, allowing much greater control over the operation of the chip.

4.2.1 Pixel

The MLCv6 pixel is based loosely on the MLCv5 pixel. The layout view for a single pixel is shown in Figure 4.8a. A schematic showing the whole pixel is shown in Figure 4.8b.

Front-end: One of the changes from MLCv5 in MLCv6 is that the front-end uses a cascoded current mirror to bias the transimpedance amplifier. The schematic is shown in Figure 4.9.

An initial design objective was to maximise the space used by the photodiode. To this end, a fill factor of 23 % was achieved. This however greatly worsened the noise performance and reduced the bandwidth due to the extra capacitance of the larger photodiode. The photodiode size was therefore reduced to $50\,\mu\text{m}\times20\,\mu\text{m}$. This results in a fill factor of 7.56 %. This smaller fill factor was acceptable because a lenslet array may be used to increase the light collection efficiency.

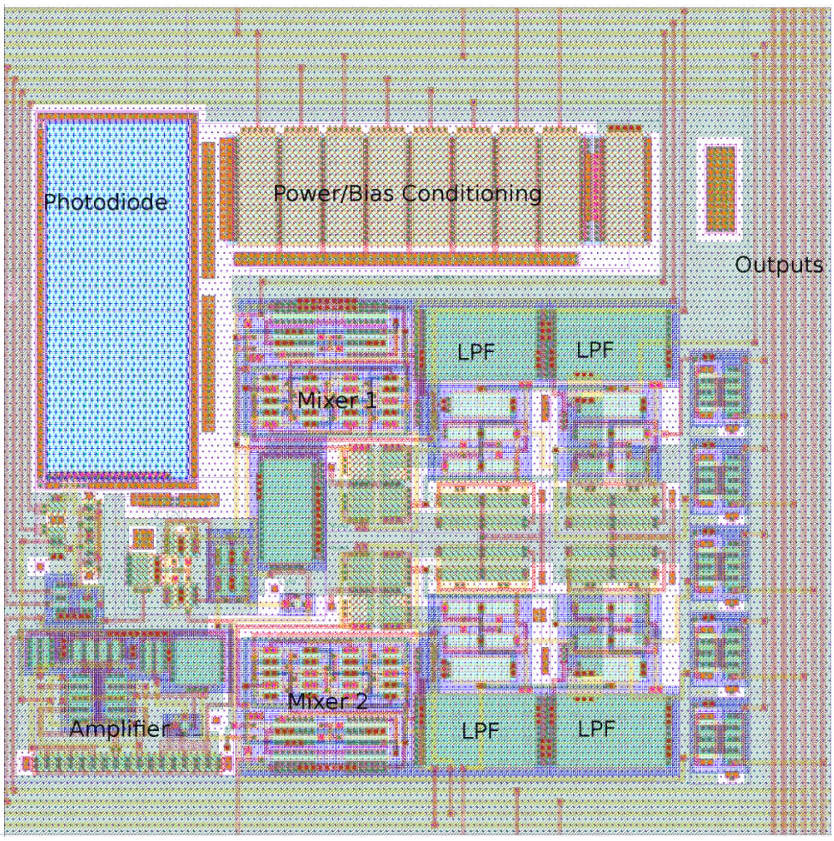

(a) Layout

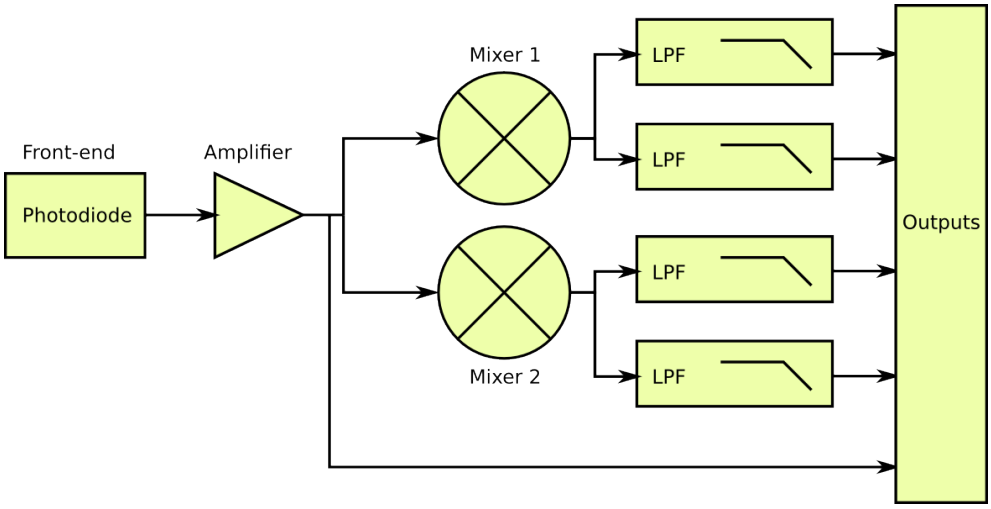

(b) Schematic

Figure 4.8: Layout and schematic of MLCv6 pixel

A lenslet array is an external optical array placed in front of the chip after manufacture.

Figure 4.10 shows the amplitude response of the front-end with varying tunebias currents. It shows that the bandwidth increases with increasing current. The

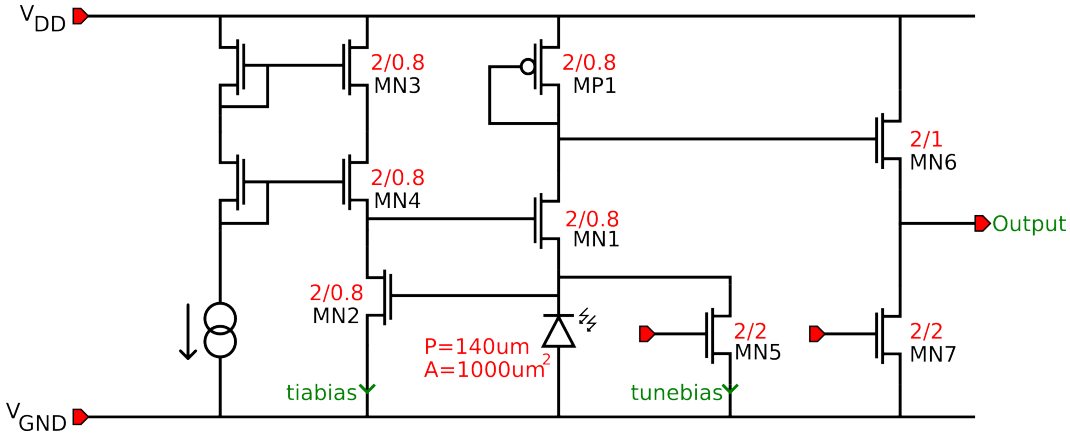

Figure 4.9: The schematic shows the front end implemented on MLCv6

.

bandwidth response is shown more clearly in Figure 4.11. This is simulated using an ideal source of 1nA AC current and 1nA DC current. The circuit is simulated post-layout using conditions of 25°C, with a 10 fF capacitive load.

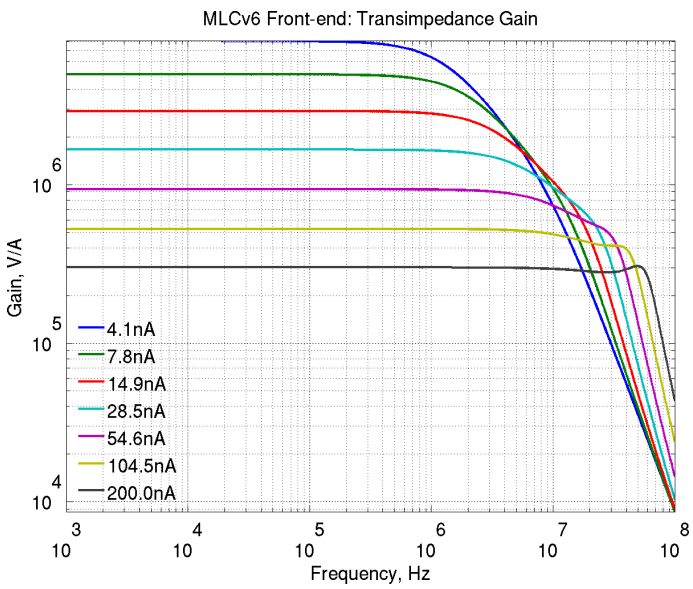

Figure 4.10: AC Amplitude response, showing gain and frequency response with various tunebias currents.

Figure 4.12 shows the phase response of the front-end. This is important because we are very interested in using the device to measure phase. It shows a rapid change in phase for lower tunebias currents. As tunebias is increased the phase margin improves and the change in response is lower at higher frequencies.

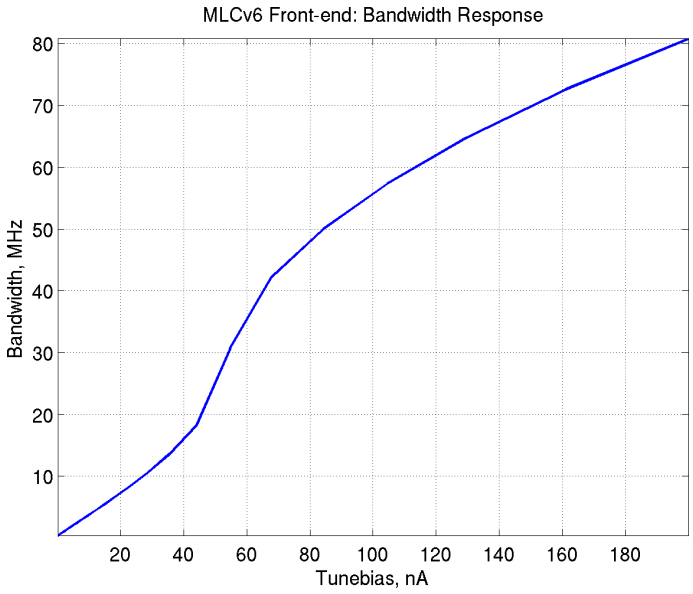

Figure 4.11: Simulated MLCv6 front-end bandwidth response.

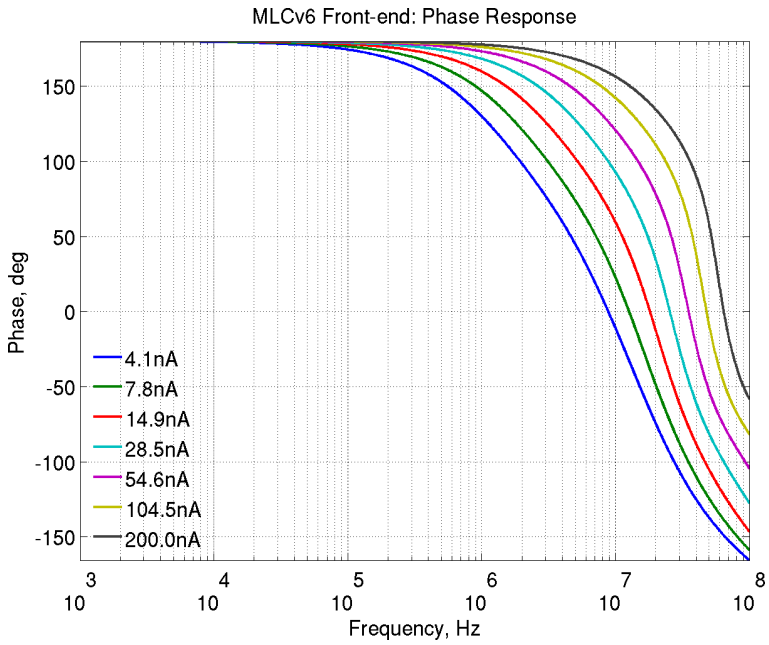

Figure 4.12: MLCv6 front-end phase response with varying tunebias current.

Figure 4.13 shows the input referred noise response. Although it suggests that increasing tunebias makes the sensor more noisy, combining this figure with Figure 4.10 shows that the SNR actually improves at high frequencies with increasing tunebias.

The DC response is shown in Figure 4.14. It confirms the log response at low values of current, and that it is quasilinear at higher values of current. Not

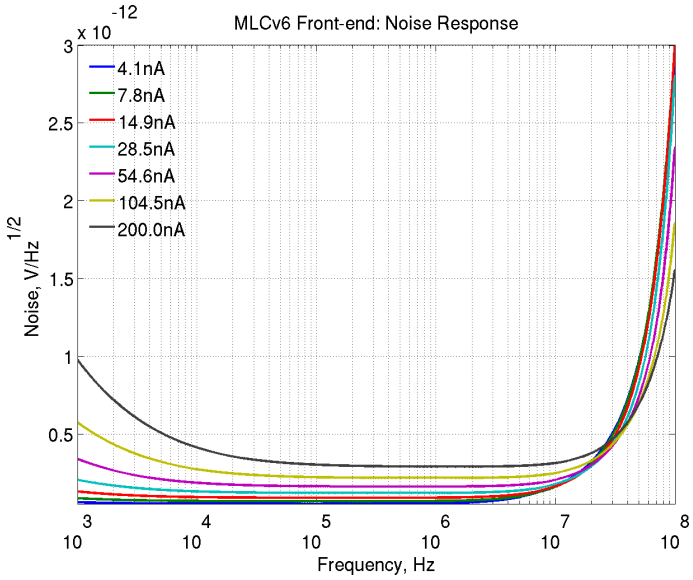

Figure 4.13: MLCv6 front-end input referred noise with varying tunebias current.

that whilst the graph is for photocurrent, the response is similar for variation in tunebias.

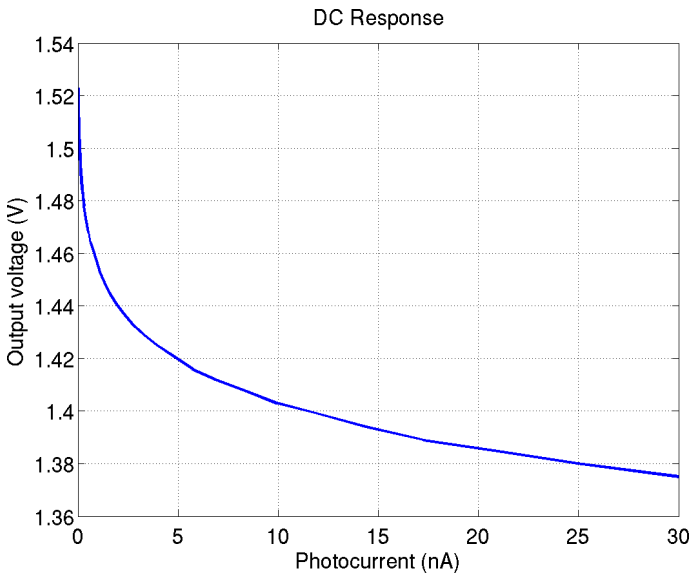

Figure 4.14: Simulated DC response of the MLCv6 front-end.

The **amplifier** is designed to offer about 32 dB to 38 dB of gain, with a bandwidth from 17 MHz to 40 MHz, depending on bias conditions. It's operating charateristics are shown in from Figure 4.15 to Figure 4.18 with varying bias current. The results are from a testbench using an ideal voltage source 1 mV

AC on a 1.5 V DC voltage at the input. Simulated post-layout using typical conditions of 25°C, with a 10 fF capacitive load

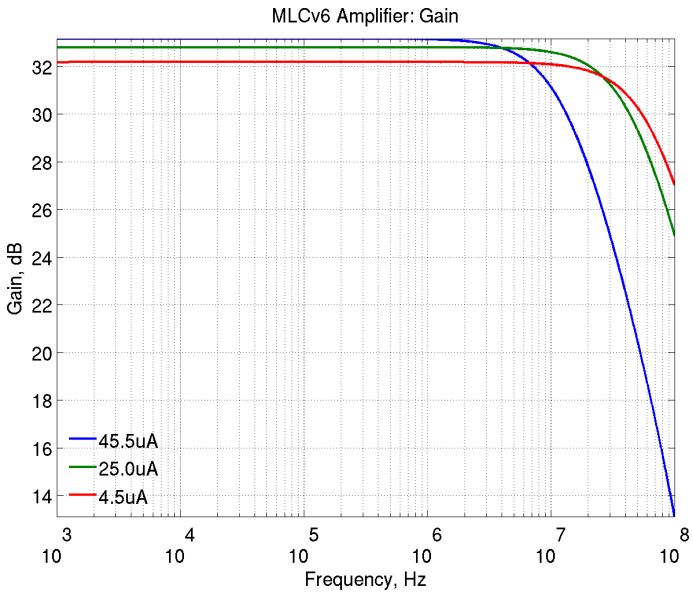

Figure 4.15: MLCv6 pixel amplifier amplitude response.

The amplitude response is considered with various values of bias current. It is important to consider bias current because using 1024 of these amplifiers places a demand on the power supply to the chip. Thermal dissipation information for the chip package was not available, so it was important to keep power consumption as low as possible, without compromising performance. The graphs show that higher bias currents provide more gain at the expense of bandwidth.

The phase response is also considered, because as a phase measurement sensor, it is important to know how much phase shift is introduced by the electronics, especially when working close to their bandwidth limits. Figure 4.16 shows that higher bias currents introduce greater phase shift at a particular frequency.

The noise response in Figure 4.17 shows that higher current introduces more noise. This is correlated to the gain curves shown in Figure 4.15. The trade-off between gain and bandwidth becomes the determining factor in choosing the

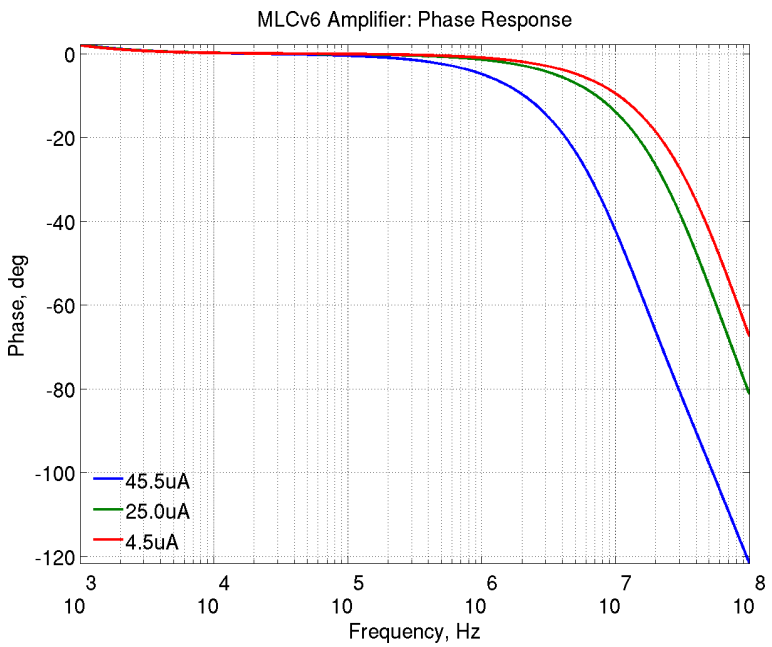

Figure 4.16: MLCv6 pixel amplifier AC phase response with various bias currents

bias current. By making the bias current externally controllable, it is possible to modify the performance to meet the experiment.

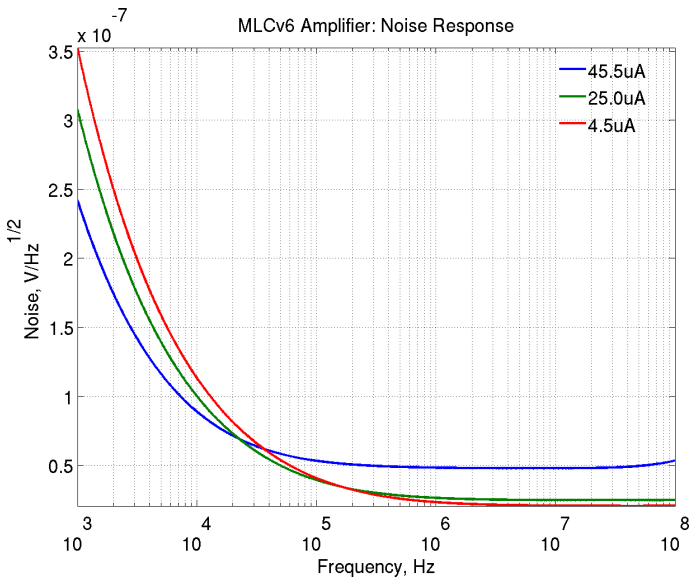

Figure 4.17: MLCv6 pixel amplifier input-referred noise response with various bias currents.

The **mixers** perform the demodulation of the input signal. Mixing is achieved with two fully differential Gilbert cell mixers, one for the in-phase mixing, and

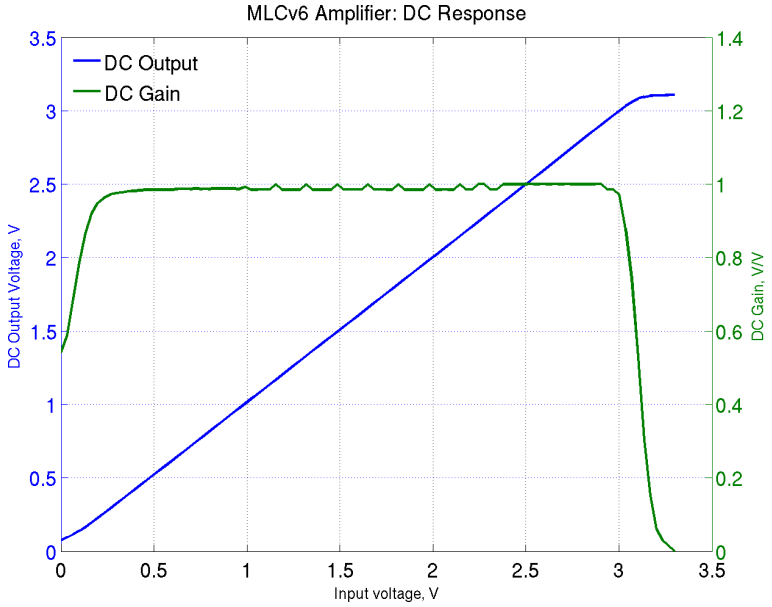

Figure 4.18: MLCv6 pixel amplifier DC response.

another for the quadrature phase mixing. To investigate the operation of the mixers, they are simulated using periodic steady-state (PSS) simulations. These are analoguous to AC simulations except that they compensate for the frequency shifting nature of mixer operation. PSS simulations make it possible to quickly compute the steady state nature of circuits with long time constants.

PSS Simulations suggest a conversion gain from RF to IF (or in normal use from RF to DC) of -1dB. A number of structures were investigated to increase the gain, including the use of bleeding transistors and bias current variation. These worked out to cost more in silicon space or pixel current consumption. To this end, the best possible wide-band mixer was designed. The schematic of the mixer is shown in Figure 4.19 and layout is shown in Figure 4.20.

The simulation results for the MLCv6 mixer are shown in Figure 4.21. The figure shows that increasing the bias current increases the bandwidth of the system at the cost of current consumption. The gain also improves as the size of the differential pair is increased. The -3 dB compression point was also determined to be 60 mV.

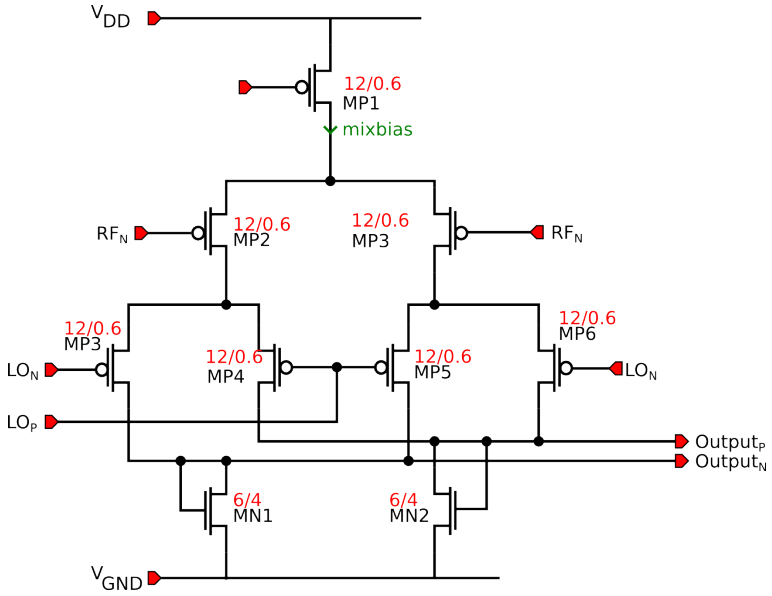

Figure 4.19: MLCv6 mixer schematic

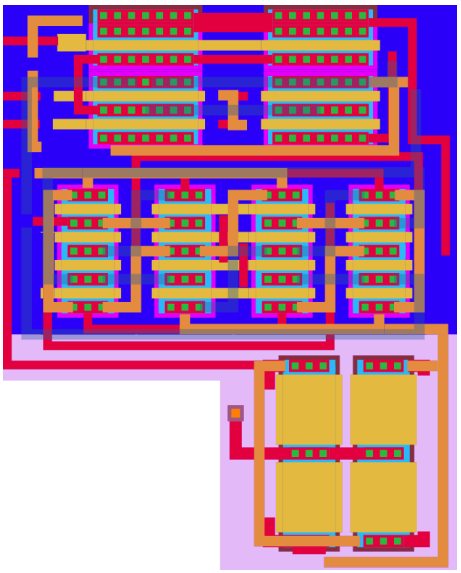

Figure 4.20: MLCv6 mixer layout utilizing a common-centroid layout

The use of differential to single ended convertors was investigated. The use of fully differential quadrature mixing requires 4 low pass filters, requiring a big area of silicon space. Careful analysis however showed that the amplitude of the upconverted signal would greatly affect the bias point of the filters, rendering them ineffective.

The **filters** are output transconductance amplifiers set up with very low bias

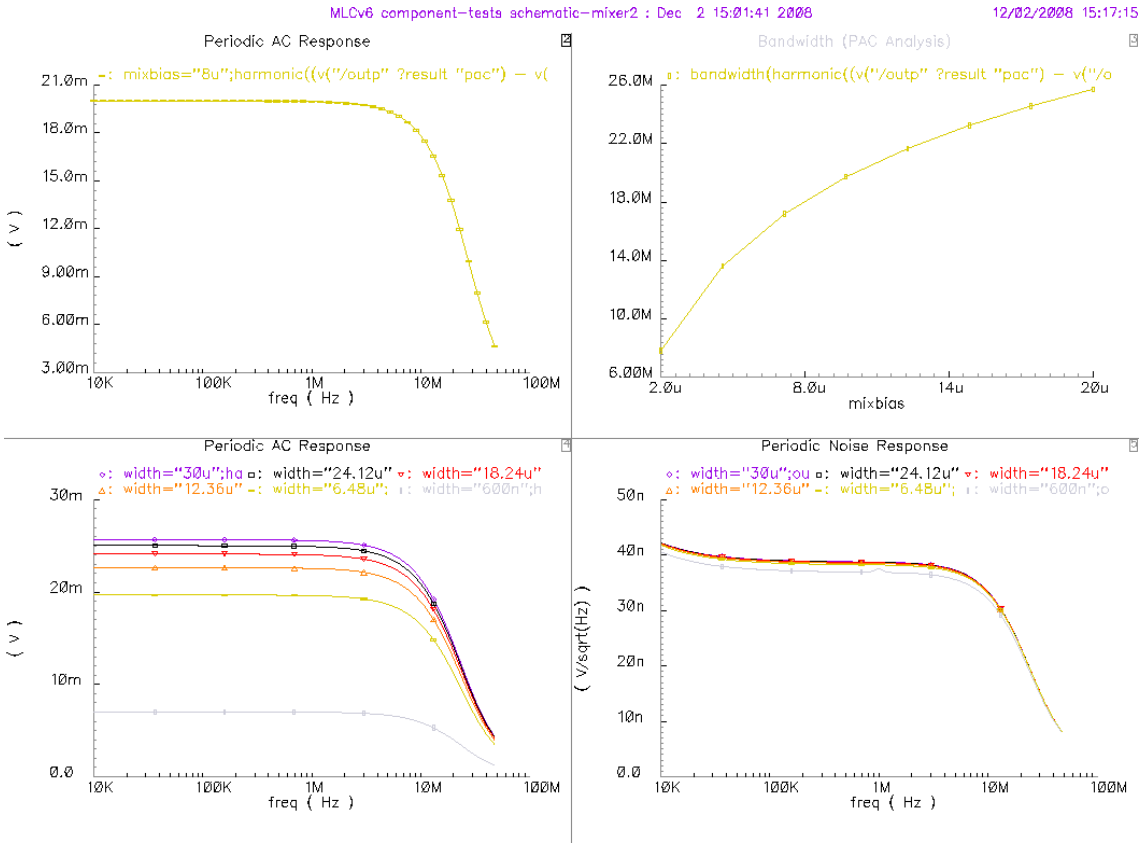

Figure 4.21: MLCv6 mixer frequency response. The bias current is increased from 600 nA to 30 μA. The figure also shows that the gain increases as the transistor width of the differential pair increasing.

currents. This means they have unity gain, but very low bandwidth. By using an externally variable bias current, it is possible to vary the bandwidth from 1 kHz to 5 kHz.

The graphs from Figure 4.22 to Figure 4.26 show the variation in filter bandwidth and noise performance with varying bias current. The filter testbench is simulated using an ideal voltage source of 1 mV AC on a 1.5 V DC voltage input. The circuit is simulated post-layout using typical conditions of 25°C, with a 10 fF capacitive load.

The filters determine the selectivity of the camera. By varying the bias current their bandwidth may be varied, making it possible to modify the camera to the

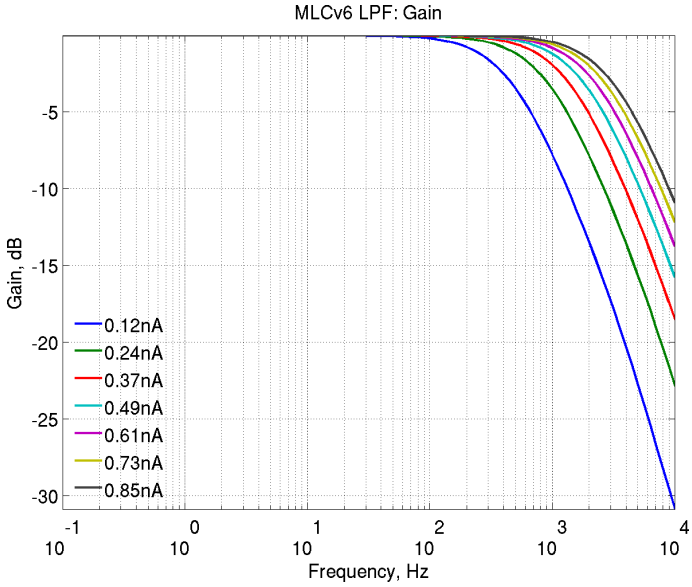

Figure 4.22: MLCv6 low pass filter amplitude response for various bias current.

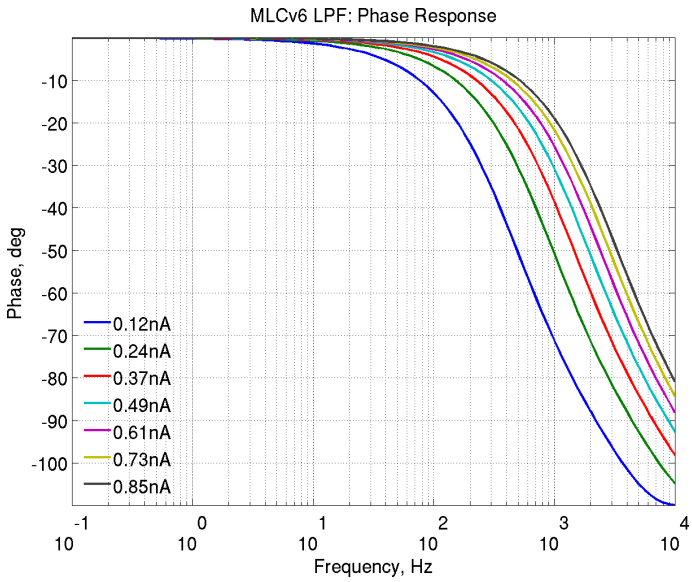

Figure 4.23: MLCv6 low pass filter input referred noise response for various bias current.

experiment under consideration. The default is to set it to bandwidth of 2 kHz.

Figure 4.27 shows a summary of the working conditions and acceptance windows for a single pixel of MLCv6.

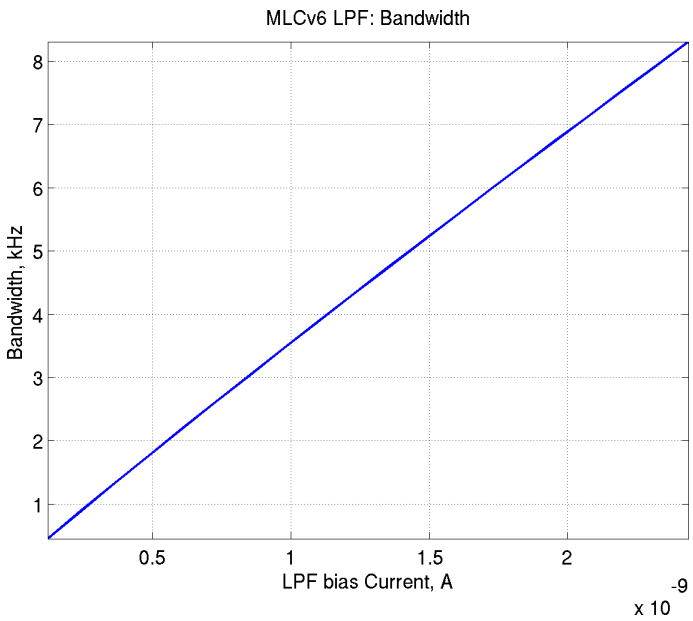

Figure 4.24: MLCv6 low pass filter Bandwidth response for various bias currents.

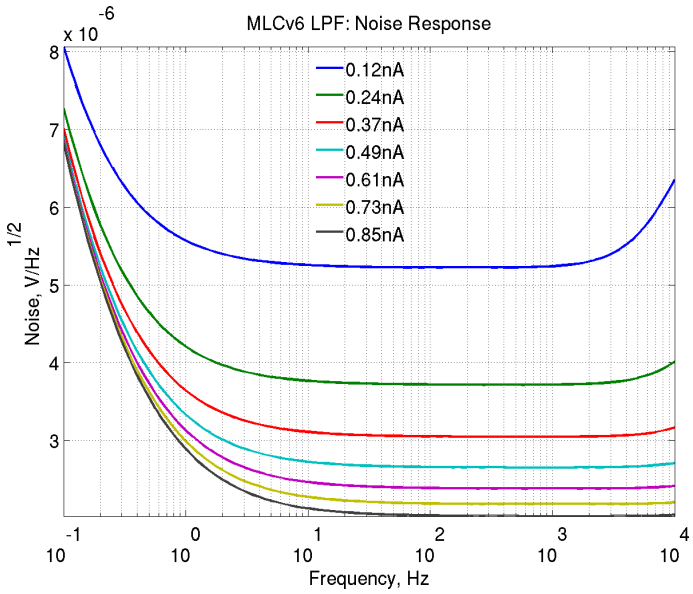

Figure 4.25: MLCv6 low pass filter input referred noise response.

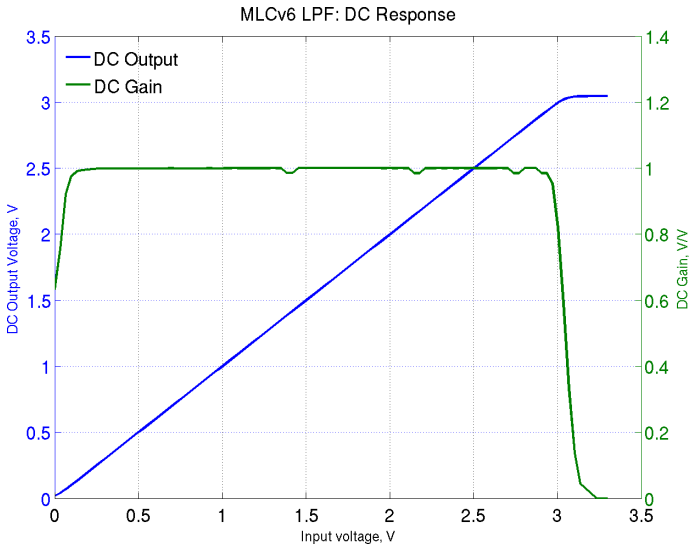

Figure 4.26: MLCv6 low pass filter DC response.

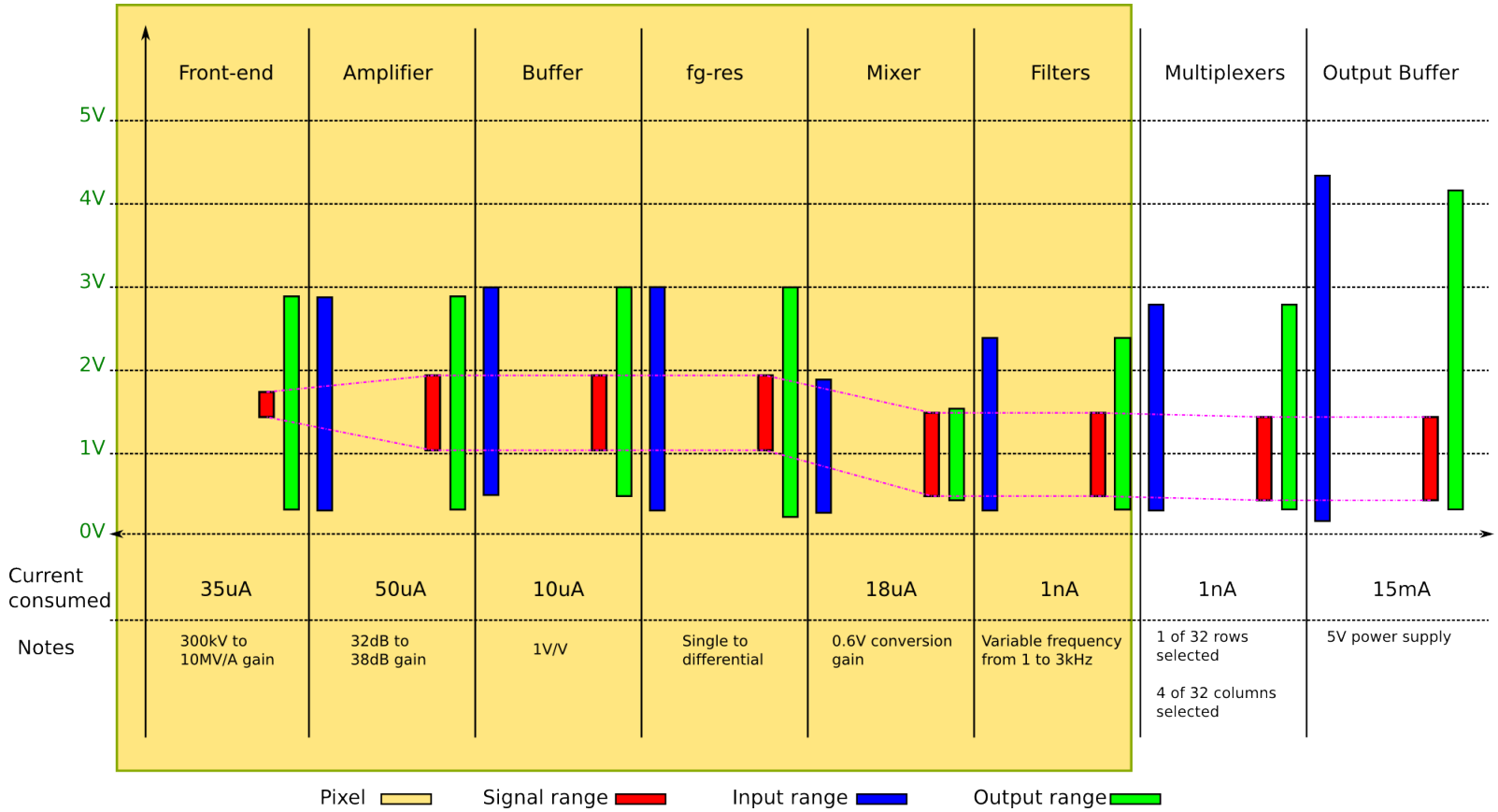

Figure 4.27: The diagram shows the windows of acceptance and output for various components of MLCv6, as well as a brief summary of their performance.

The remainder of the components in MLCv6 were re-used later in the final design and are discussed in section 5.2.

4.2.2 Chip

MLCv6 has 32 by 32 pixels, set up in 8 banks of 4 columns. Each pixel has 5 outputs: DC, In, Ip, Qn, Qp. In addition, 4 pixels in the centre of the pixel array have RF outputs, with any two selectable at a time. These four pixels are referred to as master pixels.

The bonding diagram for MLCv6 is shown in Figure 4.28. The plan for the layout of the chip is shown in Figure 4.29. It shows the main parts of the chip, and how they connect to each other. A photomicrograph of the fabricated device is shown in Figure C.1

An important part of the design flow is to determine the power supply requirements and make sure there is sufficient power for all the circuits on the chip. The current consumption causes a voltage drop, causing the pixels farthest from the supply points to have a voltage below 3.3 V. There are 4 metal layers in this CMOS fabrication process. The first two layers are used for signal connections from transistor to transistor. The third layer is used for 3.3 V power supply (VDD), and the fourth (highest) layer is used for ground (GND). These 2 top layers almost appear as a sheet across the entire chip, except where holes are made for light to reach the photodiode.

Even though there is a sheet of metal for supply, there is a drop in the supply from source pads to the pixels. There is also a rise in the ground potential at the pixels furthest from the ground pads. The design tool Voltage Storm is used to determine the voltage drop using the basic ohmic relationship V = IR. To

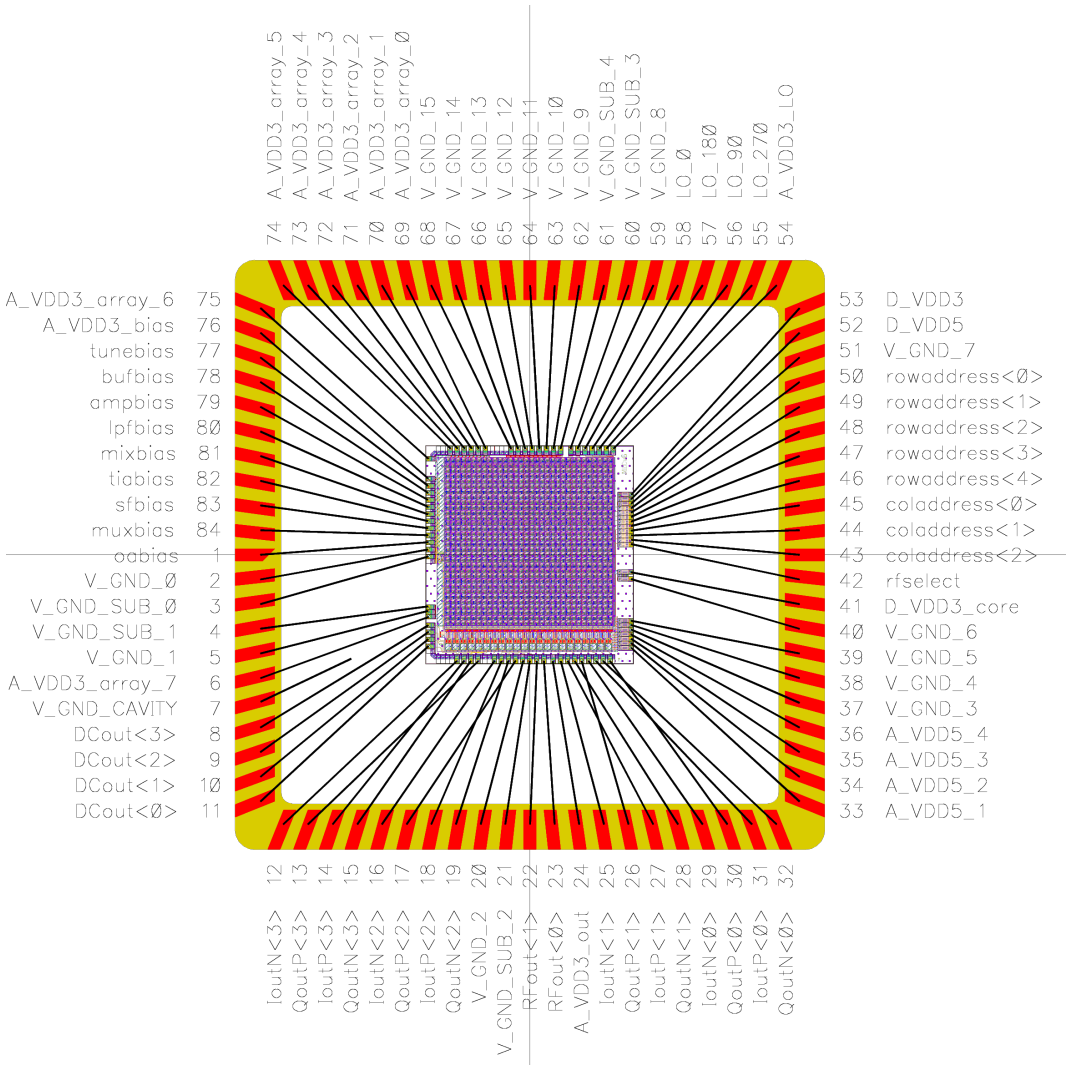

Figure 4.28: The diagram shows the bonding diagram for the MLCv6 chip

reduce computation time, a resistive element that consumes 200 μA (pessimistic current consumption estimate) was used in the power consumption moduel. 1024 of these resisters are arranged in an array similar to the pixels, and the same supply points and metal layers are used in the simulation.

Figure 4.30 gives a summary of the IR analysis of the chip. It shows the variation in the 3.3V supply to the array (Figure 4.30a), as well as the ground bounce across the entire array (Figure 4.30b).

The graphs show that MLCv6 has a drop of 66 mV at the pixel farthest from the supply. The ground bounce is 16 mV at the same pixel, indicating that this

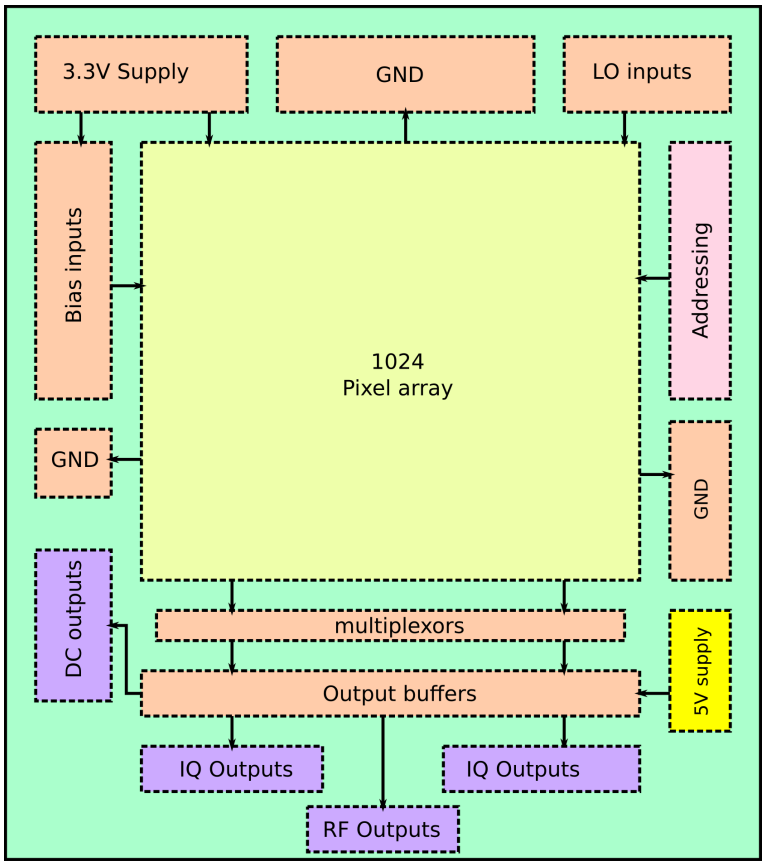

Figure 4.29: The diagram shows a schematic for main parts of the MLCv6 chip

pixel will have a voltage rail of approximately 3.2 V. Given this information, the operation of the pixels was resimulated to make sure they would operate normally.

4.2.3 Design differences v5 and v6

Learning from the experiences of MLCv5 and MLCv6FE a number of structures were introduced in MLCv6. Some of these changes are discussed in section 4.2.1.

The tuning transistor is the most important change. As explained in section 3.5, this has the job of electronically introducing the current that sets the bias point of the load transistor and the regulated cascode circuit. This increases the bandwidth and linearises the response of the front-end.

Another important difference is that the current mirrors used to set up the bias

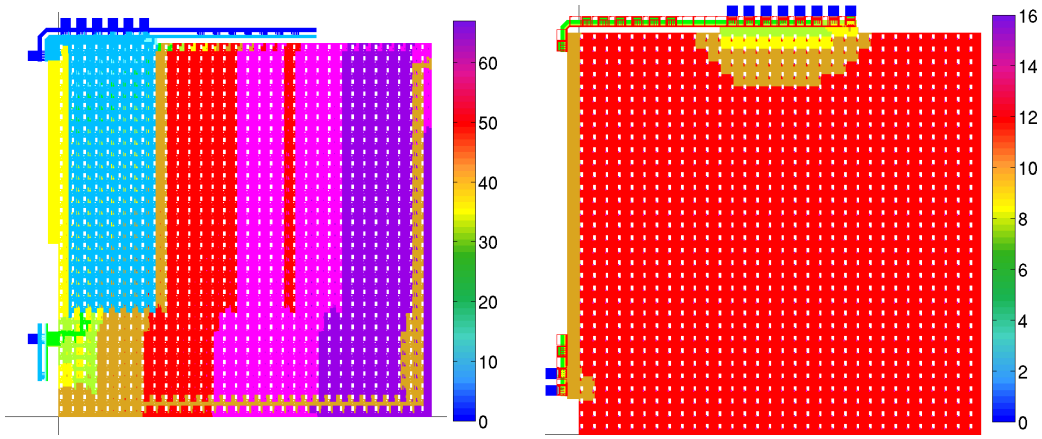

(a) MLCv6 3.3V IR Drop **(b)** MLCv6 Ground Bounce

Figure 4.30: Voltage Storm Analyses on MLCv6. Subfigure 4.30a shows the IR drop in VDD accross 1024 pixels. The supply is from the 7 pads on the top left, as well as a single pad on the left side. Subfigure 4.30b shows the Ground bounce across the 1024 pixels. The supply is from the 7 pads on the top, as well as a 2 pads on the left side. Simulated with 16 kΩ resistors per pixel. The voltages are shown in mV, so there is a peak drop of 66 mV, and a peak bounce of 16 mV

currents are shared across the array. This has the advantage of reducing the number of transistors per pixel, allowing the more compact pixel (with a pixel pitch of 115 μm as compared with 130 μm for v5). It also allows v6 to have a bigger photodiode. (1000 μm^2 as compared with 900 μm^2 for v5). The fill factors are thus 7.6% for v6, and 5.3% for v5. To mitigate the cross-pixel interaction through the bias lines, Bypass capacitances are set-up on all pixels, using the gate capacitance of diode connected PMOSes. These supply about 100 fF per bias-line per pixel.

Another difference in design is that wherever possible in v6, longer transistors have been used instead of minimum-sized transistors. For example, the load transistors in MLCv5 are 12/0.6, but in v6, this is changed to 12/0.8. This reduces fixed pattern noise since the mismatch between the transistors is less due to the increased size.

As an addition, all these bias points can be set externally, making it possible to fine tune the operation of the device across different operating conditions.

Another difference between MLCv6 and v5 is that the amplifier, mixer and other devices which contain differential or matched pairs have been laid out using a common-centroid pattern. This has the propensity to reduce mismatch in the fabrication process. This technique and others suggested in [44] were used to improve the transistor to transistor matching (where applicable) and pixel to pixel matching (where possible). For example, each of the four transistors in the mixer M_A to M_D was split width-wise as $M_A \equiv (M_{A1}{:}M_{A4})$ were laid out thus:

M_{A1}	M_{B1}	M_{C1}	M_{D1}
M_{B2}	M_{A2}	M_{D2}	M_{C2}
M_{D3}	M_{C3}	M_{B3}	M_{A3}
M_{C4}	M_{D3}	M_{A4}	M_{B4}

The graphs shown in Figure 4.31 show the difference in noise performance per pixel. It shows the performance for MLCv6 pre-layout (Blue), MLCv6 post-layout (Purple), and MLCv5 pre-layout (Red).

Figure 4.31 shows that the similuted input referred noise of MLCv6 of

4.2.4 Corners Analysis

It is important to model the response of the circuit accounting for process variations. This is performed using Corners Analysis. A process corner represents the extremes of variation within which a circuit will work properly. The analysis is combined with Monte Carlo experiment to repeatedly generate random samples. Thus a probalistic result of the performance of the chip may be determined.

Worst speed and worst power corners were simulated on a single pixel of MLCv6. The results are presented in Table 4.1. 100 points were specified for a Monte Carlo

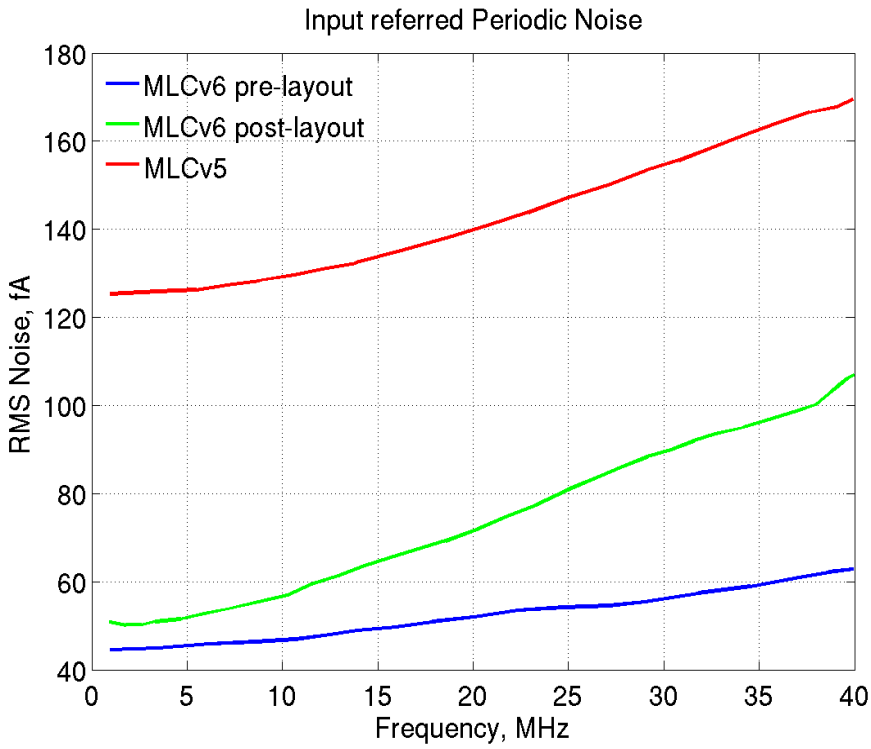

Figure 4.31: The graphs show the simulated periodic noise (post mixers and filters) of MLCv5 post layout, MLCv6 pre-layout and post-layout.

run and the conditions observed were Bandwidth, Gain and RMS Input Noise at 10MHz. The yield estimate is 34% with the given conditions. The simulation temperature is 90 °C.

4.2.5 Characterization of MLCv6

This section discusses the experimental characterization of MLCv6. The picture in Figure 4.32 shows the experimental setup that is used in initial characterisation of MLCv6.

4.2.5.1 Hardware

A printed circuit board was designed for testing MLCv6. It is made up of 5 boards:

Table 4.1: MLCv6 Corners analysis

Test Name	Yield(%)	Min	Target	Max	Mean	σ(STD)
Bandwidth (Hz)	38	28.3M		50.14M	38.25M	522.3k
*Nominal	100	35.27M	>30M	39.19M	37.35M	740.8k
*Worst Power	100	44.39M	>30M	50.14M	47.58M	1.05M
*Worst Speed	38	28.3M	>30M	31.1M	29.81M	522.3k
Gain (V/A)	98	3.925M		5.679M	4.572M	217.4k
*Nominal	100	4.03M	>4M	5.314M	4.549M	237.5k
*Worst Power	100	4.187M	>4M	5.679M	4.769M	272.5k
*Worst Speed	98	3.925M	>4M	5.075M	4.399M	217.4k
RMS Noise (A)	90	39.81p		65.46p	51.16p	2.512p
*Nominal	100	41.27p	less60p	55.76p	49.01p	2.512p
*Worst Power	100	39.81p	<60p	58.99p	49.1p	3.731p
*Worst Speed	90	46.64p	<60p	65.46p	55.37p	3.669p

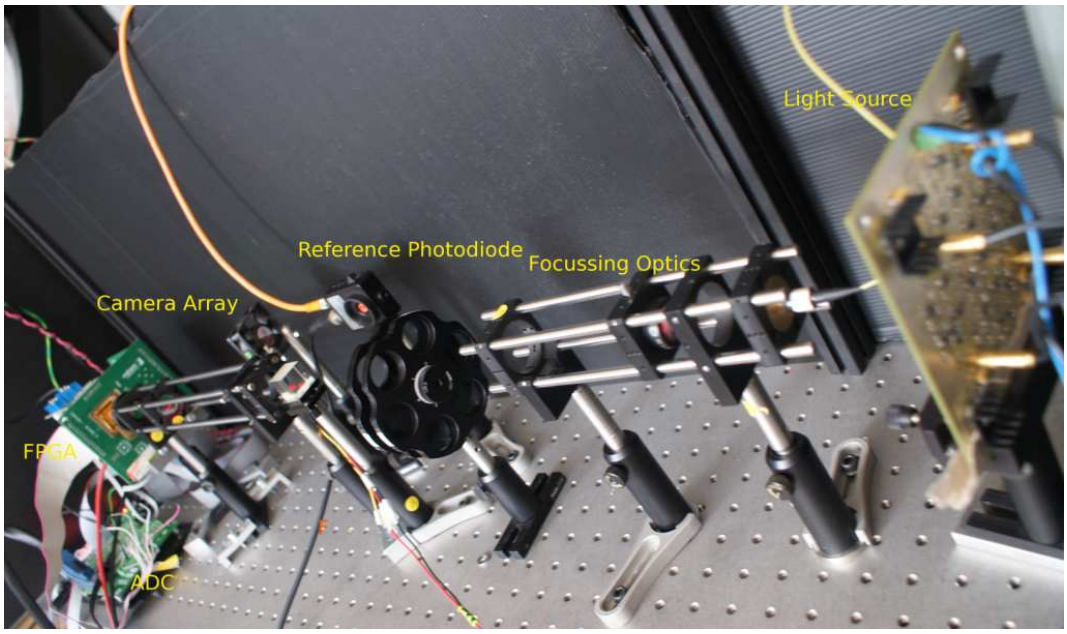

Figure 4.32: This picture shows the experimental setup used in characterising MLCv6. A DC laser, Modulated LEDs, focussing optics, Neutral Density Filters, Camera, ADC breakout board are shown in the picture.

- **The Main Board:** This has bypass capacitors, LO generation circuits, and an RF driver. This makes sure the RF signals travel only a short distance without amplification, reducing signal degradation and interference. It also

houses the PLCC84 socket for MLCv6. Power supply conditioning circuits for both 3.3 and 5V circuits are also implemented.

- **Power Board:** This board generates the 3.3V and 5V supplies used for various parts of the circuit. It uses fixed power regulators (LM317) and an input is at about 8.5V will generate the required output voltages. The board used for experiments uses fixed regulators, but is designed so that it can be used with adjustable regulators.

- **Amplification Board:** This board has the differential amplifiers used to amplify the signals from MLCv6. All amplifiers are fully differential (THS4052). 8 amplifiers are available for the I and Q signals from the 4 banks, and 4 more for the DC channels. It has its own power supply, needing both positive and negative supply ($\pm 6\,\mathrm{V}$).

- **Multiplex Board:** This board contains a multiplexing structure that allows the 20 amplified channels to be multiplexed for reading by the 16 channel ADC available (NI PCI 6251).

- **Bias Board:** This receives power from the power board. It has fixed and variable resistors that set the bias points necessary for correct operation of MLCv6. The rheostats allow up to $\pm 40\%$ variation about the set points for normal operation found in simulations. The default resistances are listed in Table B.1:

After the initial tests had been conducted, the 5 boards were replaced by a single board containing all the needed circuits, and utilising fixed bias resistances. The schematic for the PCB is shown in Figure 4.33.

With bias resistances set to their optimum values, the chip consumes about 600 mA, as expected. This excludes the main (off-chip) amplifiers. Most of this consumption is from the pixel array (180 μA per pixel), and the buffers (20 mA

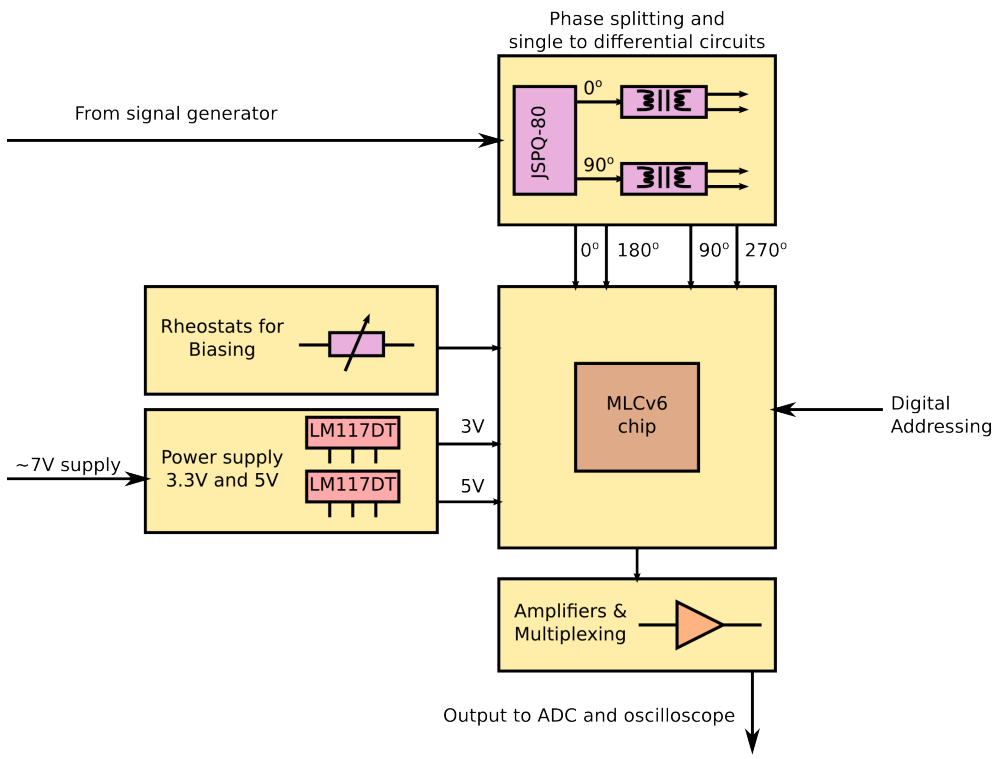

Figure 4.33: MLCv6 PCB schematic

per buffer, 22 buffers).

The data from the camera is captured by a 16-bit, 16 channel NI PCI 6251 in the experimental PC. The ADC is capable of 1Ms/S (multichannel) acquisition rate.

4.2.5.2 Software

The software for acquisition is written in VHDL, C and C++. Comedi v0.8 [45] is used for the acquisition system. The camera addressing, clock and acquisition trigger is provided by an FPGA. Figure 4.34 shows some of the important timing points required in the acquisition process. The acquisition signal, scan and conversion signals are need for correct sampling process. The software was version-controlled using svn.

Two versions of the acquisition software were written. The first was a console based application. This grabbed a complete frame of data at a time and saved it

in a binary file for post-processing.

The second version utilized the same driver as the console application, but used a separate thread to read in the captured data and display it on screen. The DC, I and Q channels were shown. Later the Amplitude and Phase images were also shown.

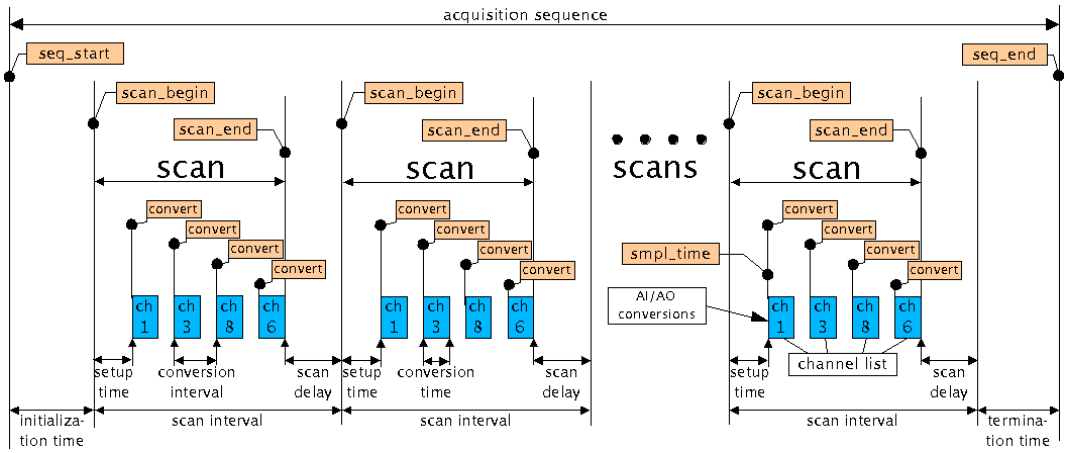

Figure 4.34: The diagram shows the acquisition system and terminology used by Comedi [45]

4.2.6 Experiment Procedure

With the experiment set up as described above, several attempts were made at taking a complete image. The first experiment was to determine the returned voltage with varying DC light. The results obtained are shown below in Figure 4.35.

The next experiment was to create a more complex image. The first step was by covering half the chip, illuminate only a corner etc etc. Whilst differences could be seen in the voltages returned, they did not directly correspond with the expected results. This suggested a problem with addressing.

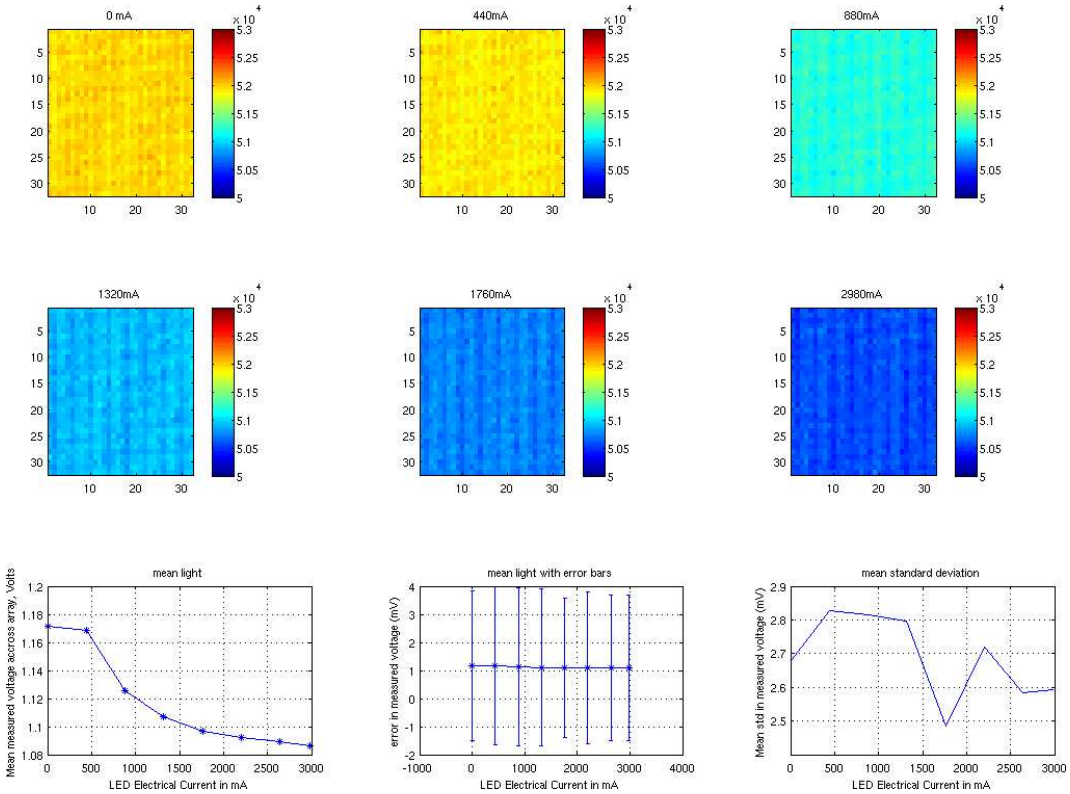

Figure 4.35: The figures show the response to light from MLCv6. The titles in the subplots correspond to the current supplied to the illumination (LED bank). Since this is a DC experiment, tunebias is set to 0 nA. ADC Range = 16-bit from ±2V

4.2.7 Addressing Problem

The FPGA was reprogrammed to allow manual addressing using the pixels. The chip outputs were examined on the scope, concentrating on DC. A light beam was focussed onto the top-right corner of the chip (about 0.5 mm), and that address set using the switches on the FPGA. When the column switches were switched (from 000 to 111), the intensity reduced gradually, until it disappeared completely, as expected. It was however observed that switching through the rows produced no noticeable effect.

The beam was moved to the opposite corner of the array, ie. the bottom left. The addressing was adjusted once again, and it was noticed that it was possible to address the relevant column and changing the set address (from 111 to 000)

caused the intensity to reduce. However once again, changing the row addressing (from 00000 to 11111) produced no observable effect.

The pins on the chip, in socket on PCB were probed to ensure all voltages were being correctly received. Having checked and ensured that the addressing was set up correctly, the schematic was observed once again in Cadence. It was observed that the selection switches in pixel are active low (PMOSs), but the address decoders are active high. This suggested that selecting a pixel<0>in a column of 32 rows would actually deselect that pixel<0>and select all the others, tying their output together.

4.2.7.1 Addressing Problem Simulations

With this problem in mind, a simulation was set up to verify the problem and recreate the experiment. The simulation uses the voltage sources as pixels, going through the selection switches, through the column multiplexing, buffers and pads.

The simulation runs by putting a signal on pixel<0>, selecting it and observing the output. The signal was a DC signal varying between 500 mV and 1500 mV. These values were chosen since I, Q are at about 700 mV (increasing with light), and DC is at about 1.45V (decreasing with increasing light) under normal operating conditions. No signal was seen at the output for this simulation.

The next simulation was to select/address pixel<1> and observe the output. A signal was seen on the output this time. Pixel<2>was then selected, and the output was seen once again.

To confirm the simulation, a 1 MHz signal was put on pixel<0>, a 3 MHz signal

on pixel<1>and none on pixel<2>and pixel<3>. Pixel<2>was selected, and a transient simulation was run. The output showed the sum of the two waves, confirming the problem.

The next step in the simulation was to vary the 3 sources (pixel<1>, pixel<2>, pixel<3>) from 500 mV to 1500 mV in various combinations. Pixel<0>was selected. Some of the results are shown in Figure 4.36 and Figure 4.37. It also suggests that the since the circuit was designed to work linearly under normal operating conditions, the circuit may be linearised into combinations of resistors and current sources, and the use of the superposition theorem may help in reconstructing an image from the array. This is written in the form of Equation 4.2.

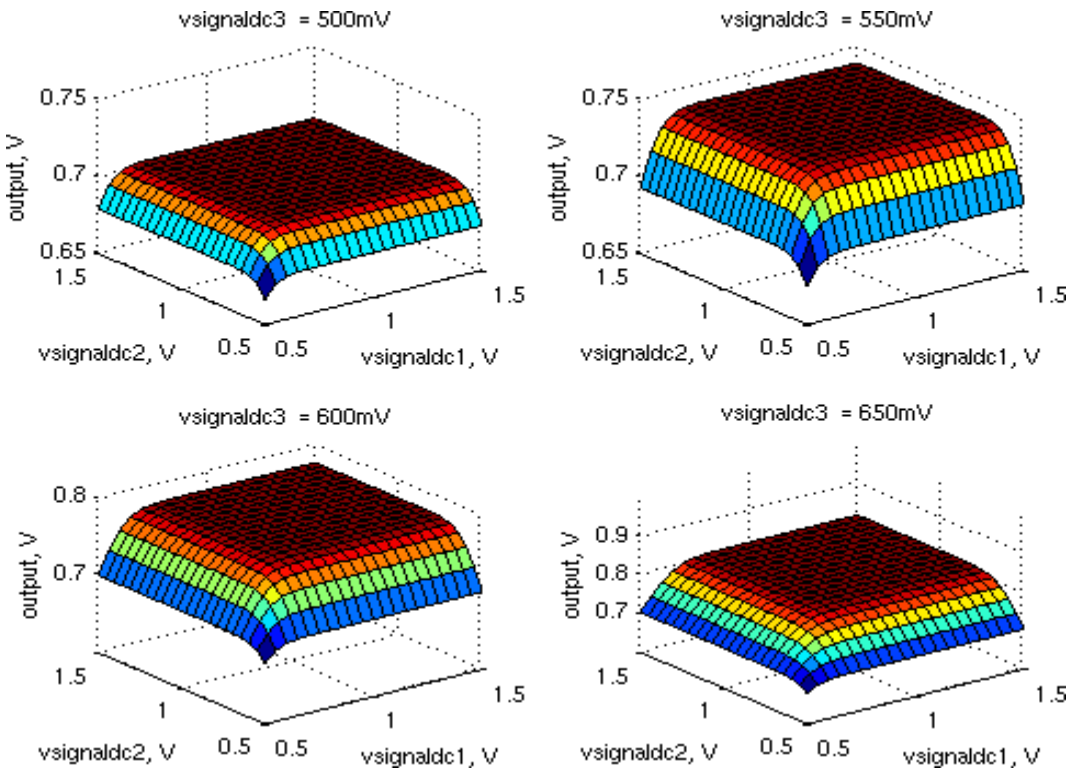

Figure 4.36: The graphs show the results of the simulations described in section 4.2.7.1. The different subplots correspond to the different values of signal<3>from 500 to 650 mV

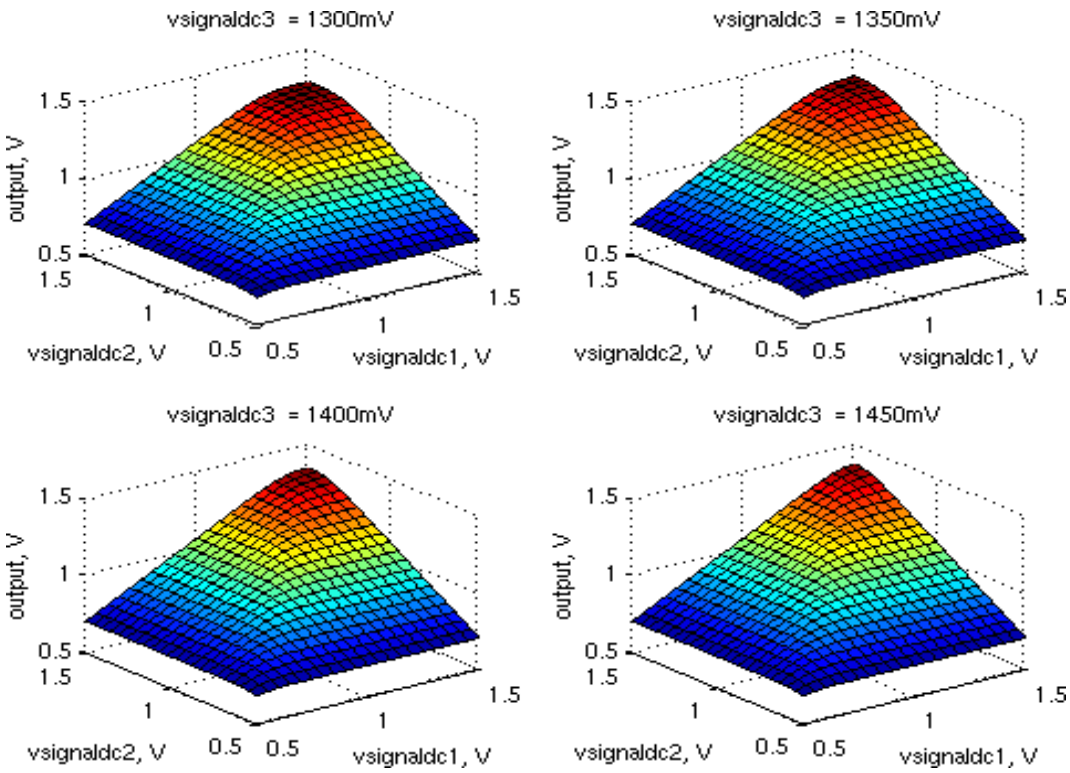

Figure 4.37: The graphs show the results of the simulations described in section 4.2.7.1. The different subplots correspond to the different values of signal<3> from 1300 mV to 1450 mV

$$V_{out} = c_{<0>} \cdot V_{<0>} + c_{<1>} \cdot V_{<1>} + ...c_{<3>} \cdot V_{<3>} \tag{4.1}$$

$$= \sum_{i=0}^{3} c_{<i>} \cdot V_i \tag{4.2}$$

where $c_{<i>} = f(V_{<0>}; V_{<1>}; ....V_{<3>}) \forall$ i $\neq$ j), $c_{<j>} = 0$, and pixel<j>is the selected pixel.

A second simulation was set up that used real pixels. This was a column of 32 pixels (giving 32 rows). It was set up exactly as on fabricated chip. With a signal on pixel<0>, no signal is observed at the output. However with address set to (00001) to select pixel<1>, a signal is observed at the output. This simulation was run once again using various values of muxBias from 5 μA to 1 mA, and sweeping the photocurrent from 0 nA to 100 nA. The results are seen

in Figure 4.38. Subwindow 3 gives an indication of the signal loss due to the addressing problem. The curve is given by Equation 4.3. It must be noted that the loss is due both to the addressing problem and the loss due to passing through 2 source followers.

$$\left[\frac{\Delta V_{pixel<0>}}{\Delta V_{output}}\right]_{I_{photo<0>}} = \frac{\Delta V_{pixel<0>}}{\Delta I_{photo<0>}} \div \frac{\Delta V_{output}}{\Delta I_{photo<0>}} \tag{4.3}$$

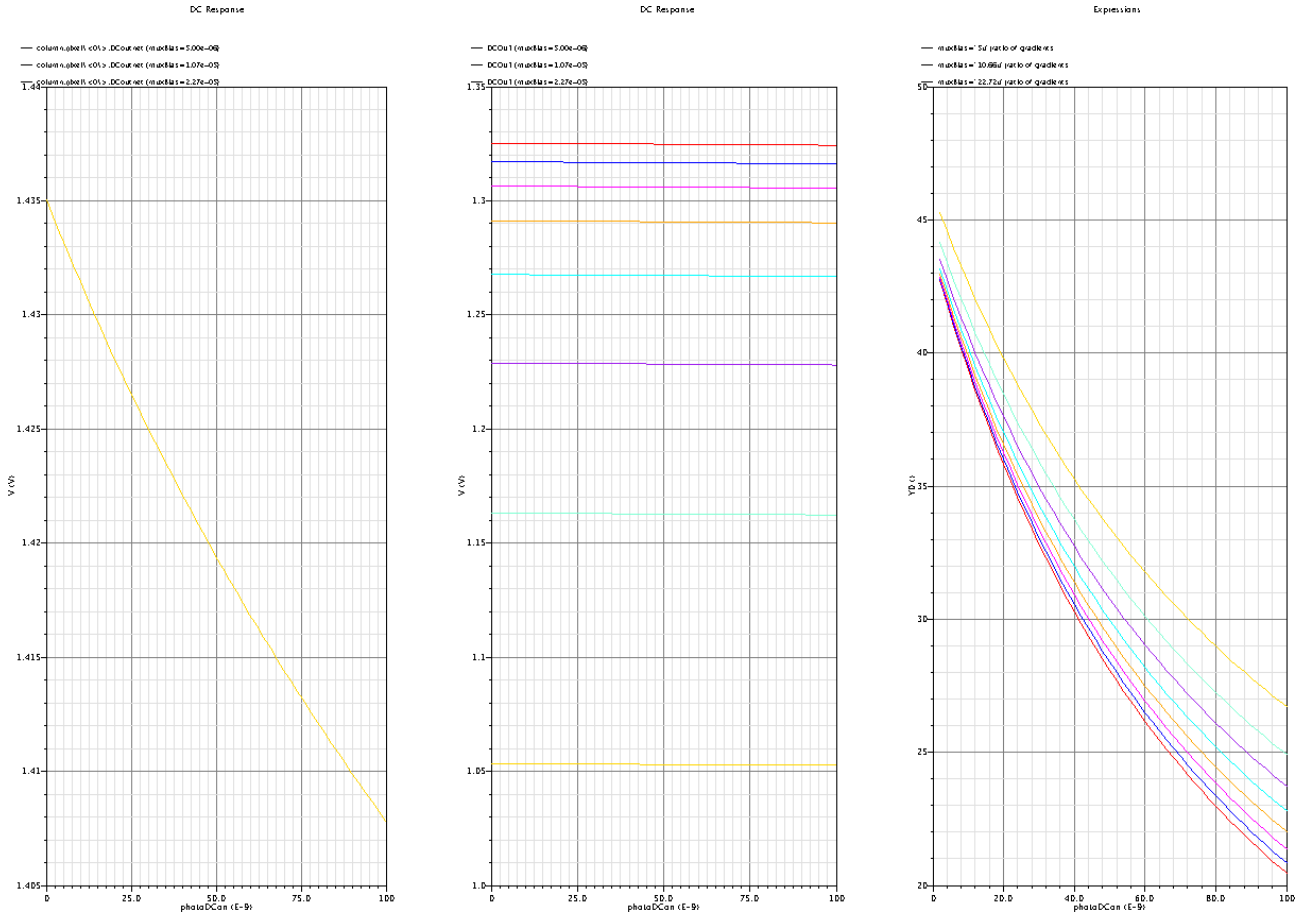

Figure 4.38: The graphs show the results of a simulation to determine the effect of flawed addressing on a column of 32 rows. Light current is varied on pixel<0>from 0 to 100nA, and pixel<1>is selected. Subwindow 1 shows the pre-select switch output of the pixel. Subwindow 2 shows the results observed post-pad, with varying multiplexer bias current. Subwindow 3 shows the ratio of the gradients of subwindows 1 and 2. Tunebias = 100nA.

The results in Figure 4.38 suggest that a loss between 40 and 20 should be expected, depending on light level. In order to make the best of the situation, 2 possible solutions were proposed.

4.2.7.2 Addressing problem resolution - Single Row Operation

The first solution involves using the camera as a linear array of 32 ×1 pixels. This could be optically by spreading the light of one row onto 31 rows, effectively forcing them to the same output. The unexposed row would be addressed, and the output would be average of the other 31 exposed pixels.

Another alternative is to cover 31 rows, blocking them from receiving light. This would mean that any signal seen on the exposed row is the only contributor to the output. This has the disadvantage that the gain at output would be reduced between 20 and 40, as discussed above in section 4.2.7.1.

4.2.7.3 Addressing problem resolution - Reconstruction

Continuing in this line of thinking, it may be deduced that the the superposition theorem may be applied to this problem, allowing the reconstruction of the image, albeit with a distortion in quality. If the problem is compared to a circuit of current sources in parralel with resistors, and connected to a common current controlled load resistor, it is immediately obvious that the solution may be found using a system of equations:

$$[V_{out<0:31>}] = [C_{<32\times32>}] \times [V_{pixel<0:31>}] \tag{4.4}$$

where the coefficient matrix C may be written as shown in Equation 4.5

$$C = \begin{bmatrix} 0 & c_{<1>} & c_{<2>} & \cdots & c_{<31>} \\ c_{<0>} & 0 & c_{<2>} & \cdots & c_{<31>} \\ c_{<0>} & c_{<1>} & 0 & \cdots & c_{<31>} \\ \vdots & \vdots & \vdots & \ddots & \vdots \\ c_{<0>} & c_{<1>} & c_{<2>} & \cdots & 0 \end{bmatrix} \tag{4.5}$$

The zero diagonal is a result of the non-contribution of the addressed pixel to the output voltage. The image may be reconstructed by solving Equation 4.6

$$\begin{bmatrix} V_{out<0>} \\ V_{out<1>} \\ V_{out<2>} \\ \vdots \\ V_{out<31>} \end{bmatrix} = \begin{bmatrix} 0 & c_{<1>} & c_{<2>} & \cdots & c_{<31>} \\ c_{<0>} & 0 & c_{<2>} & \cdots & c_{<31>} \\ c_{<0>} & c_{<1>} & 0 & \cdots & c_{<31>} \\ \vdots & \vdots & \vdots & \ddots & \vdots \\ c_{<0>} & c_{<1>} & c_{<2>} & \cdots & 0 \end{bmatrix} \times \begin{bmatrix} V_{pixel<0>} \\ V_{pixel<1>} \\ V_{pixel<2>} \\ \vdots \\ V_{pixel<31>} \end{bmatrix} \tag{4.6}$$

Thus given any column of 32 rows, the corrected outputs may be found from Equation 4.4 as

$$[V_{pixel<0:31>}] = [C_{<32\times32>}]^{-1} \times [V_{out<0:31>}] \tag{4.7}$$

It is assumed in this derivation that the coefficient matrix includes any loss factors from multiplexing through to pad.

The code below is a Matlab script that gives an example of how a triangular shape on an array may be deconstructed and reconstructed. The results of running the code above are shown in Figure 4.39.

As a result of the above algorithm, the image shown in Figure 4.40 was obtained. It shows the results obtained from focusing a spot of light onto a single pixel.

Program 1 Matlab program showing an example of the averaging problem, and the reconstruction programs.

```
% Create the original image
lightImage = zeros(32);
lightImage(10:20,16) = 1;
lightImage(11:19) = 1;
lightImage(12:18) = 1;
lightImage(13:17) = 1;
lightImage(14:16) = 1;
lightImage(15) = 1;

avgImage = repmat(sum(lightImage),32,1);
recImage = avgImage - lightImage/32;

% Now we've got the received image, lets try and reconstruct it
avgImage2 = repmat(sum(recImage),32,1)/31;
reconImage = (avgImage 0 recImage)*32;
x = [0:31]; % for the axis
subplot(3, 1, 1)
imagesc(x, x, recImage); colorbar;
title('Received Image');
subplot(3, 1, 2);
imagesc(x, x, avgImage2); colorbar;
title('Average of received image);
subplot(3, 1, 3);
imagesc(x, x, reconImage); colorbar;
title('Reconstructed Image');
```

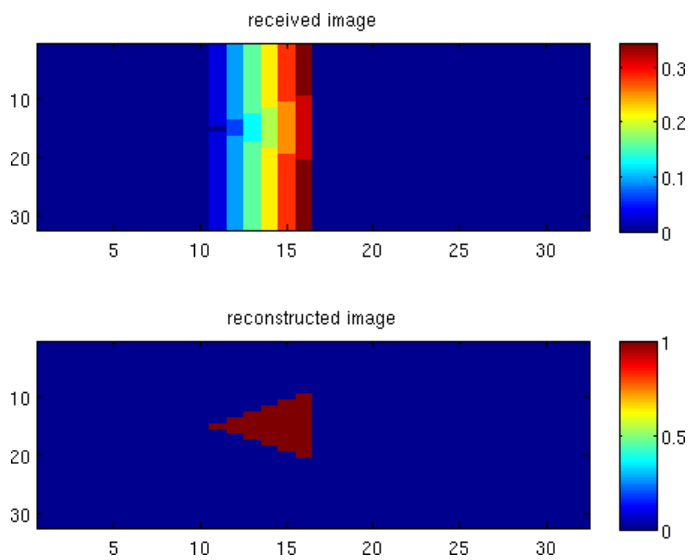

Figure 4.39: The graphs show a matlab simulation showing how an image of a triangle would appear at the output of MLCv6, and how the reconstruction image would appear.

The experiment is repeated for 2 other pixels. The image is reconstructed and shown on the RHS of the graph. It can be easily seen that this agrees closely with the matlab simulation results.

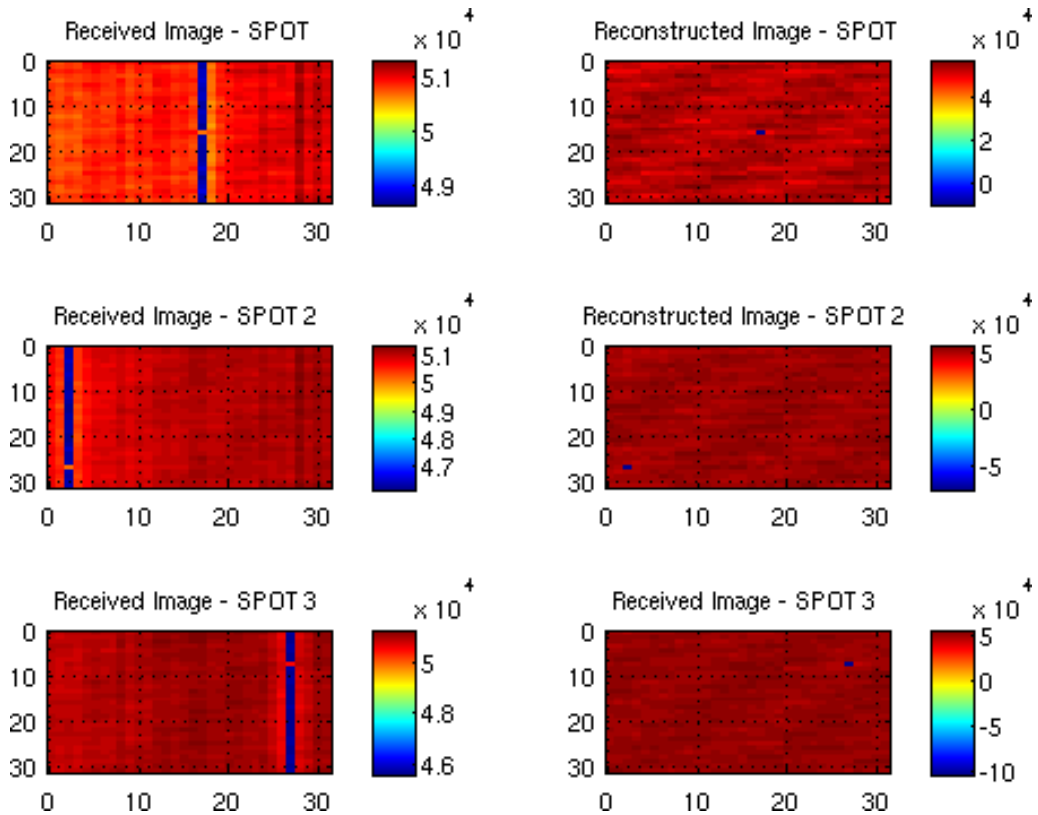

Figure 4.40: The image shows 3 MLCv6 images, showing the experimental results obtained when a beam is focussed onto 3 randomly chosen pixels on the left hand side, and then the reconstructed images on the right hand side.

4.2.8 Experiment Results

This section presents some of the results obtained from experiments performed using MLCv6.

4.2.8.1 Single Pixel

The first experiment conducted was to determine the response of a single pixel to light. To this end, the DC and RFout channels of pixel (0, 0) were probed.

The DC response was probed with tunebias = 100 nA. The result is shown in Figure 4.41. This shows the response of pixel (0,0) to a 2 Hz ramp modulated light. It shows that even though tunebias = 100 nA, the response is still not completely linear. This can be compared with the response of the reference photodiode. This may be explained by the fact that the response was getting into saturation at this point. It also shows the response to a rapid change in light. Since this output is DC-coupled, the measured slew rate is relatively slow at about 60 ms.

With tunebias = 0 nA (ie MLCv5 equivalent mode), the RF output was probed. The laser light was modulated at 1 MHz, and the output is shown in Figure 4.42. It shows the RFout directly from chip, the response of the photodiode, and the frequency content (FFT) of the RFout signal. This shows that there is some harmonic distortion especially in the second and third order components (2 MHz and 3 MHz).

The RF response was then probed with tunebias = 100 nA. The response was very similar to the response with tunebias = 0nA, as expected at this freqency from the Cadence AC simulations. The only difference was that the output was amplitude modulated by a 50 MHz oscillation (modulation depth about 10%). The oscillation was traced to the power supply, and to solve the problem bypass capicitors were added to the power supply circuit and the oscillation was suppressed.

4.2.8.2 Multiple Pixel

Multiple pixels have also been sampled to build up a complete image. Using the nomencleture in Figure 4.34, The I, Q and DC channels are sampled, interleaved

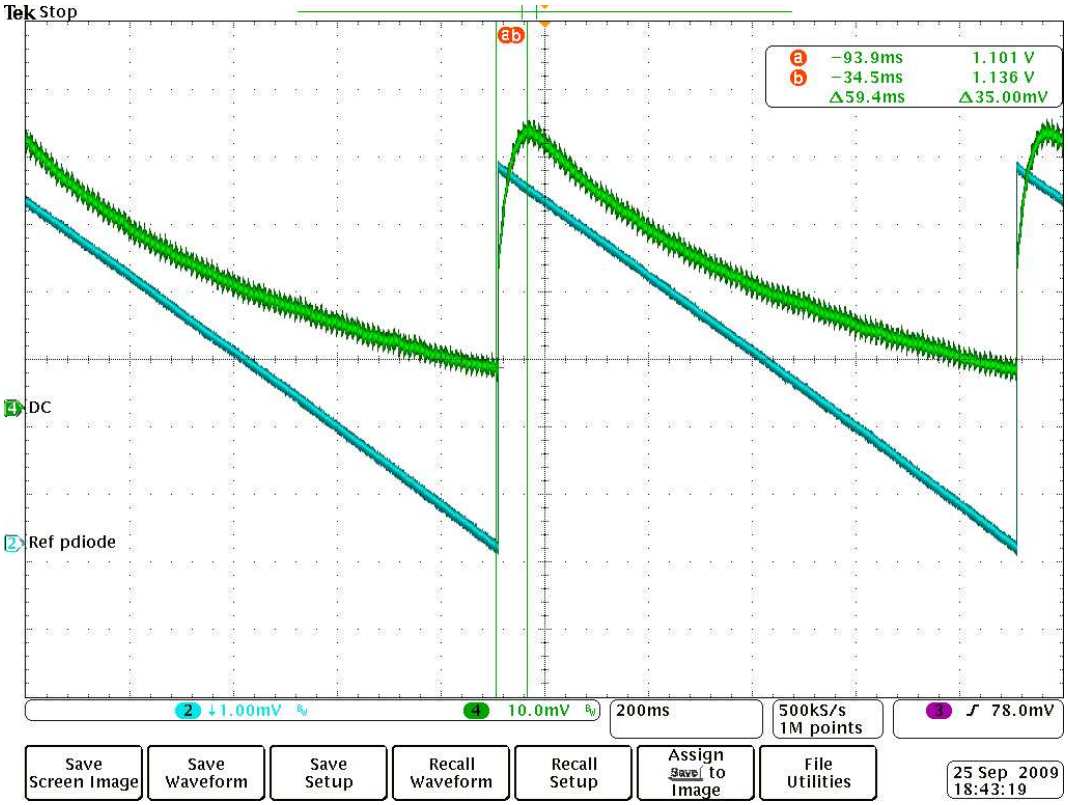

Figure 4.41: Response to DC light. Tunebias = 100nA in this case. A 2Hz ramp is used for this experiment. The reference PD-36A photodiode response is inverted to match better with the MLCv6 response.

or sorted out correctly, and presented on screen as an image using a C++ program written using wxWidgets v2.8 [46].

4.2.8.3 DC Image

As shown in Figure 4.43, the DC image of a cross was obtained by shining a laser through a crosshair. It is inclined at an angle to show avoid the possibiity of symmetry contributing to the seen image. The total light as detected using the Newport 842-PE light power meter was 320 μW at 635 nm. Since this has a detector with a diameter of 1cm, and the pixel has a photodiode area of 50 μm$\times$20 μm, this works out to 4 nA per pixel.

The image was taken by averaging over 20 frames. Since the signal to noise ratio is now $\sqrt{32}$ times worse given the row addressing problem, the averaging serves

Figure 4.42: Response of MLCv6 to a 1MHz RF signal. Tunebias = 0nA in this case. This is compared with the LO signal, the signal from the reference PD-36A photodiode. The FFT of the RF signal is also shown.

to revert to the expected conditions. The signal is taken directly off-chip, with no amplification or buffering.

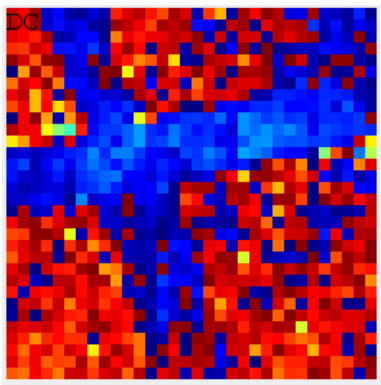

Figure 4.43: The image shows the DC images obtained from MLCv6. Tunebias = 0 nA. Light per pixel = 5 nA

4.2.8.4 IQ Image

The image shown below in Figure 4.44 and Figure 4.46 was obtained by using a 635 nm laser. It is modulated at 1 MHz, and tunebias = 0 nA. The DC channel acquisition is disabled for this experiment. The power meter measured a total power of 400 μW (20% modulated) of light at the image plane, translating from $\frac{50\mu m \times 20\mu m}{\pi \times 0.5cm^2} \times 80\mu W \times 0.3W/A = 1\,\text{nA}$ per pixel. The results are shown scaled to 65536/200mV (which is the conversion ratio of the analog to digital converters).

The figures below show the IQ response with varying phase from -180° to 180°. This is at 1 MHz, tunebias = 0 nA. Total photocurrent is about 380 μA/cm^2. The modulation depth is about 20%, giving about 3 nA/pixel. The DC channel is disabled. The results are shown in Figure 4.44 to Figure 4.46. Each figure shows the I and Q channel in the first column, then Amplitude and Phase in the second column. They show the response for input light phase from -180° to 180° in 45°.

4.2.9 Discussion of results

As seen in the results section 4.2.8, DC light is correctly detected with tunebias = 0nA (logarithmic response) and with tunebias = 100 nA (linear mode). The response in the log mode has more gain. The log response is shown in Figure 4.35.

It is also possible to see a streak of noisy pixels in the camera when RF light falls in the middle 4 pixels. This is clearly seen in the 4 rows in the middle of the In-Phase (I) image (the top left subfigure). Investigation led to the conclusion that since there are RF outputs on those four pixels, there must be cross-talk with the **IN** and **IP** channels, which are adjacent to the RF path. MLCv5 overcomes the RF problem by making the RF outputs selectable at the pixel level.

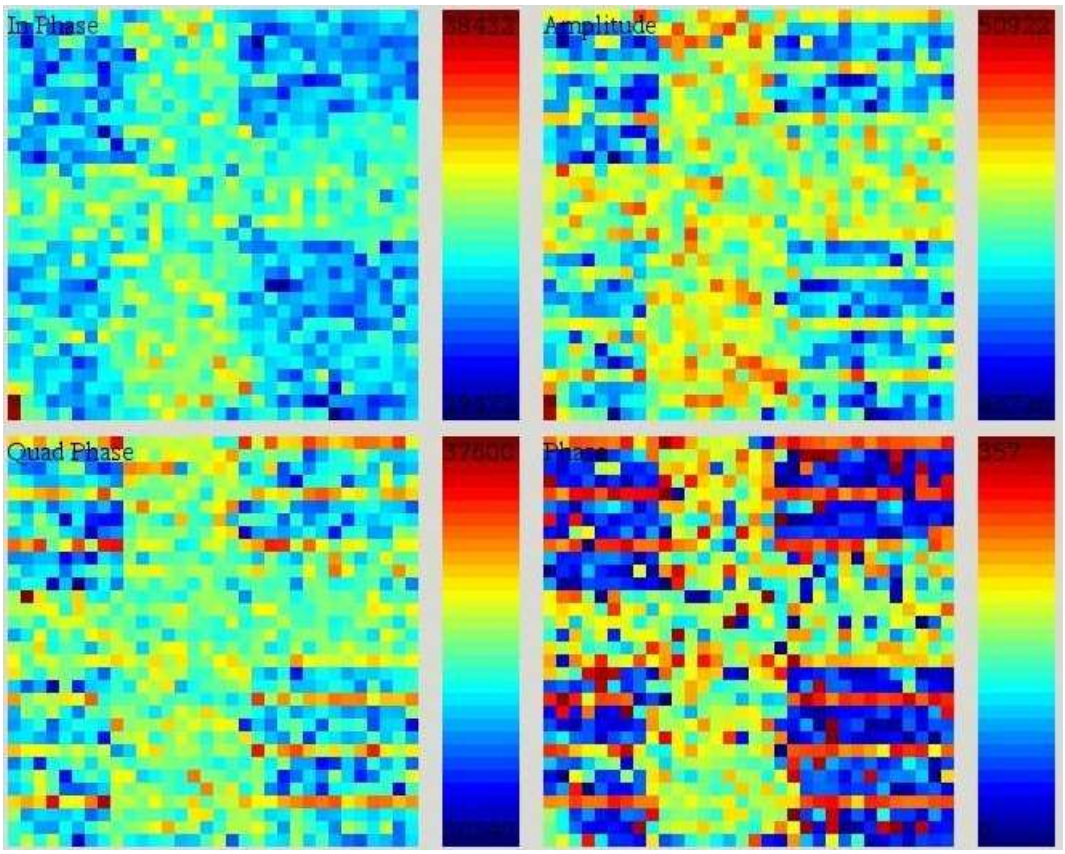

Figure 4.44: The figure shows the IQ image for phase = -180°. All images are scaled, and no averaging is performed. Tunebias = 0 nA.

IQ imagery is shown in Figure 4.45 and Figure 4.46. The total light power is about 350 μW/cm^2. This works out to about 4 nA, 20% modulated. It shows that there is some phase-amplitude dependency at this light level. This is heightened by the fact tunebias = 0 nA. The RFout signal is about 200 mV with the light focussed to a single pixel, suggesting a conversion gain of 100 mV/20nA = 5MV/A at this frequency.

4.2.10 Experimental Comparison of MLCv5 and MLCv6

MLCv5 [28] is the previous generation of modulated light camera. As reviewed in section 2.3.7, MLCv6 was designed to be an improvement upon it. A brief comparison is presented as a benchmark of the improvements gained in MLCv6 over MLCv5.

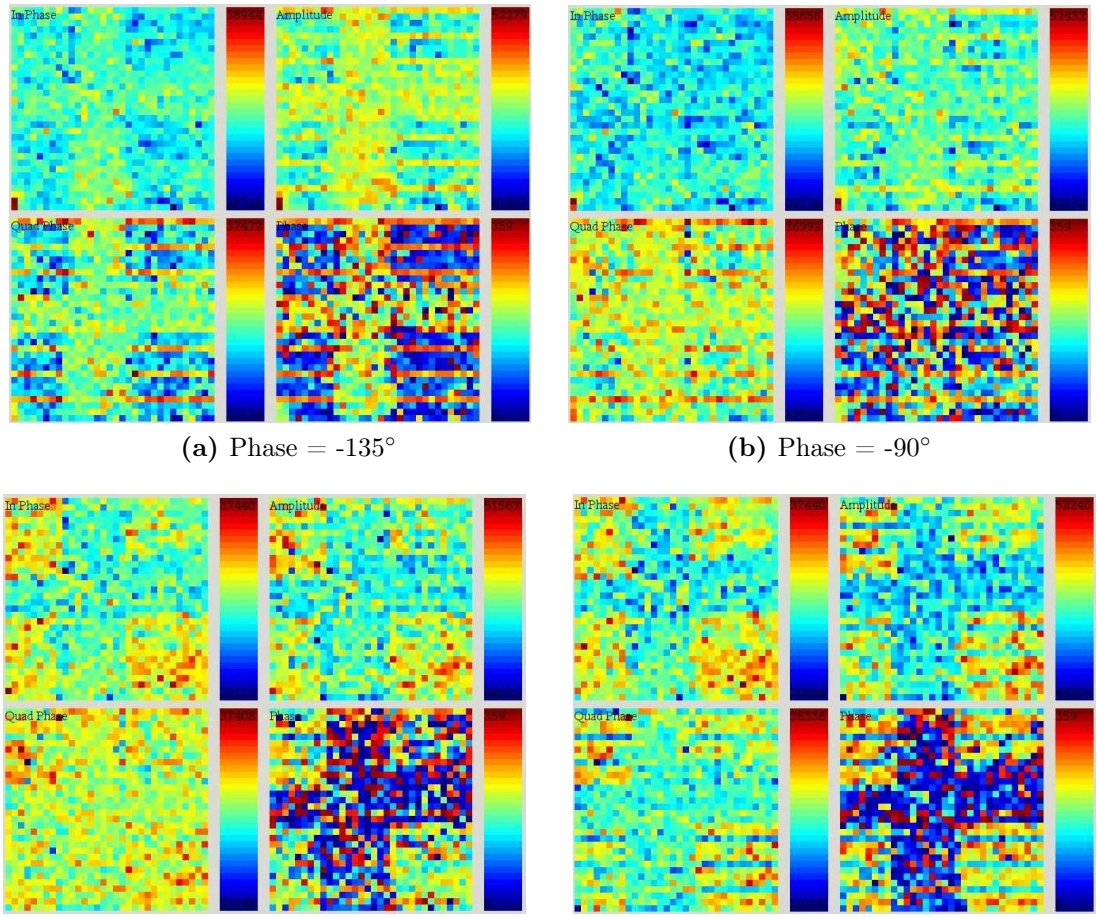

(a) Phase = -135°

(b) Phase = -90°

(c) Phase = -45°

(d) Phase = 0°

Figure 4.45: The figures show the response of MLCv6 to varying phases. Total light is about 380μW/cm^2. All images are scaled, no averaging is performed. Tunebias = 0nA.

- **Pixels**: MLCv6 has smaller and more pixels (256 more). This provides a greater imaging resolution, given the same optical system as MLCv5.

- **Noise/Sensitivity**: The few images gather suggest that MLCv6 is less noisy than MLCv5. Even granted the averaging problem, the image is quite easily seen. The results are also taken using a light source that has lower power than the LEDs used to characterise MLCv5. A quick calculation suggested an input noise floor of 0.5 nA at 1 MHz.

- **Bandwidth/Gain:** MLCv6 has a bandwidth that can be made independent of received light by the use of the tuning bias current. This also eliminates the gain-light dependence and provides a linear response.

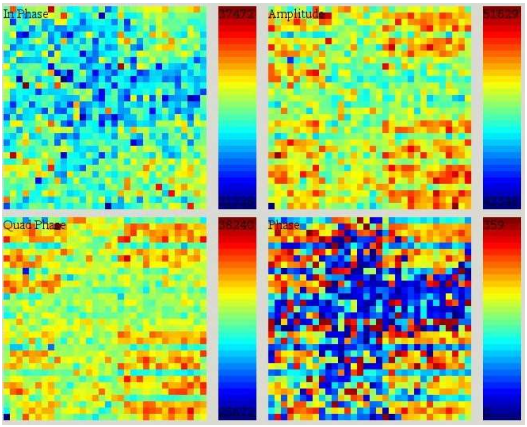

(a) Phase = 45°

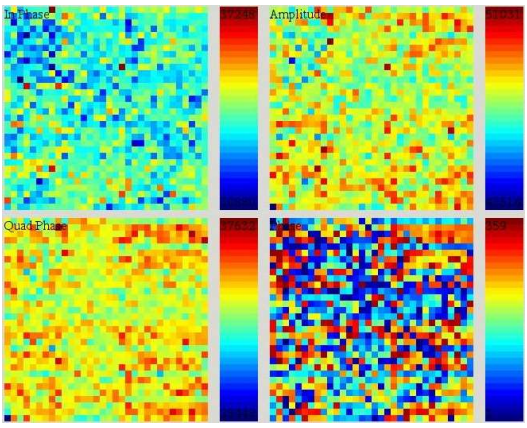

(b) Phase = 90°

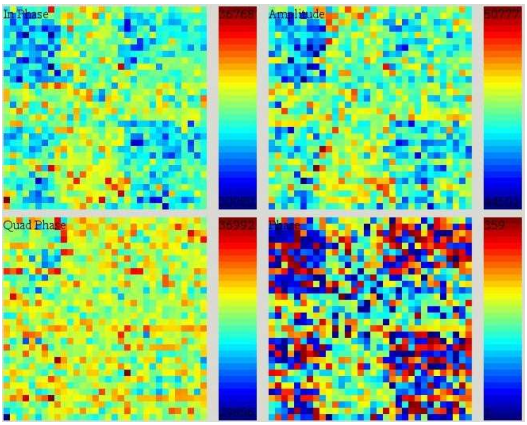

(c) Phase = 135°

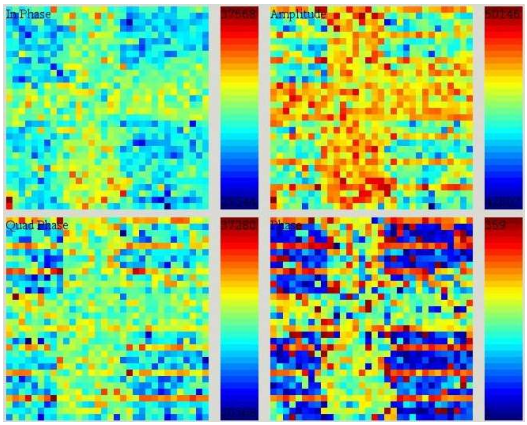

(d) Phase = 180°

Figure 4.46: The figures show the response of MLCv6 to varying phases. Total light is about 380μW/cm^2. All images are scaled, no averaging is performed. Tunebias = 0nA.

- **Ease of use:** MLCv6 is much easier to use, granted that an extra step is required to perform the reconstruction algorithm discussed in section 4.2.7. It is possible to control bias points quite easily.

- **Features:**

  – The presence of the RFout pixels can be taken both positively and negatively on MLCv6. This is because it makes it relatively easy to compare the received light with the reference light before it is even mixed and low pass filtered. Unfortunately, due to imperfect layout, there is significant cross-talk with some signal lines.

  – MLCv6 also uses smaller pixels (115μm as compared with 130μm).

This creates the oppportunity for higher pixel density and greater resolution given the same optics.

- MLCv6 however uses more current on the whole. Most of this current consumption is in the buffers used to drive the signals off the chip. This means that the chip gets warm during operation, reaching temperatures as high as 60°C. Simulations (DC, AC and Noise) show that performance is acceptable between -20°C to 130°C. The change in phase is about 1×10^{-6} degree per degree Celcius.

- **Step Response:** MLCv6 is ready to provide an image within 1 second of switch-on. This is much better than MLCv5, which took about 5 seconds to reach steady state and provide . This may be attributed to the 5 V buffers used. These have a drive bias of 18 mA, as opposed to the ones on MLCv5 which use a bias of 10 μA. Another observation is that rapid changes in light (step response) is much better on MLCv6.

4.2.11 Discussion

As shown in the results in section 4.2.9, it is possible to image a scene on MLCv6 in both DC and modulated light.

The results show that even though it is possible to image with MLCv6, in a real-world LIDAR scenario, a lot of light would be needed in order to make reflected light measurements. This suggests that the noise floor of 400pA (simulated) must be reduced even more.

The results also show that even with the superimposed signals worsening the noise outcomes, it is still possible to make line of sight measurements.

Adjustments have to be made for the phase measurement process. This will help mitigate the noise situation. Careful subtraction of the offsets (pixel by pixel)

will help correct for the very noisy phase signals seen.

5 | Final Design

This chapter presents the main modulated light camera, LIDAR1. The simulation results are presented, and the results from the characterisation of the fabricated device are presented and discussed.

LIDAR1 has 1024 pixels. The pixel array is arranged in a square array of 32 by 32 pixels, which are set up in 8 banks of 4 columns. Each pixel has 5 outputs: DC, In, Ip, Qn, Qp. In addition, 2 pixels in the centre of the pixel array have additional RF outputs. These will be referred to as the master pixels. There is a digital switch which can be used to turn the RF signals on or off.

A 3D projection of the chip as laid out is shown in Figure 5.1, and a photomicrograph is shown in Figure C.2.

5.1 Design Motivation

Working further from the results and conclusions seen in MLCv6, LIDAR1 was developed from November 2009 to March 2010. It was submitted in April 2010 to Fraunhofer for fabrication at a cost of 15,800 Euro.

The main motivation for the fabrication of LIDAR1 was the correction of the errors made on the MLCv6 chip. The first problem was with row addressing. The row address lines should select which one of the 32 rows is connected to the output bus. In the case of MLCv6, the sense of logic in the address decoder was accidentally inverted due to a missing logic inverter. Because of this change, instead of a single row being selected at a time, the output of every

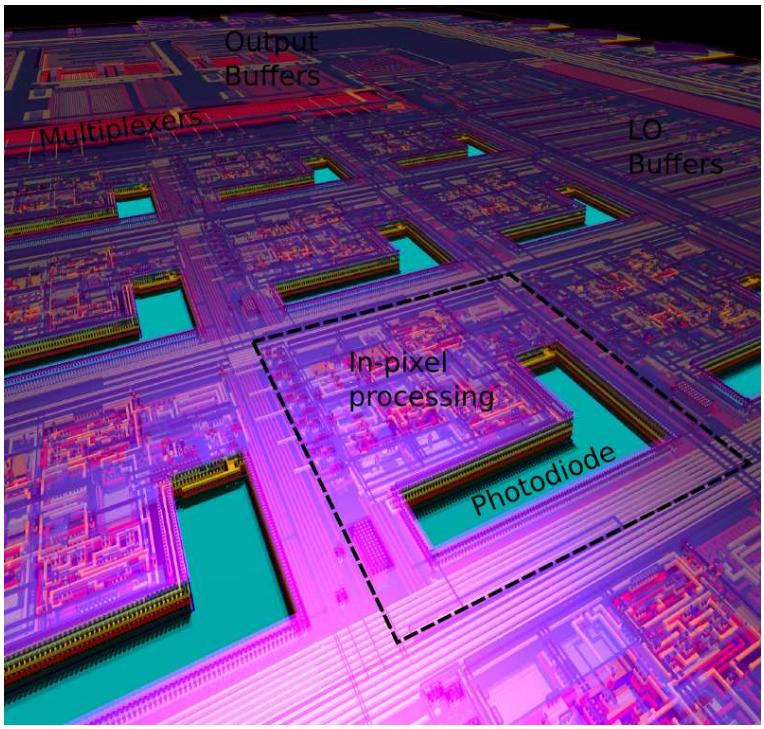

Figure 5.1: LIDAR1 chip rendered using POVRAY [47], showing an outlined pixel, the main output buffers and buffers for driving off-chip signals into the pixels.

row but the selected row is connected to the output bus. A custom algorithm for reconstructing the image is presented in section 4.2.7. Whilst this made it possible to use the device, it suffered a noisy response because several outputs were tied together post-filter.

A second improvement with LIDAR1 was the reduction in noise. This mainly refers to the high frequency noise observed along the middle of the MLCv6 chip in bank 3-4. This noise was attributed to the fact that the RF pixels had their output lines running close to the I, Q and DC lines, leading to signal crosstalk.

Some other improvements are also included in the new design. These include improvements in fill-factor, the supply voltage distribution over the chip, as well as the distribution of the local oscillator signal over the pixel array.

5.2 Design Details

LIDAR1 is based on the MLCv6 concept. Each pixel comprises a logarithmic front-end, a single OTA amplifier, two fully differential Gilbert-cell mixer, and 4 filters. All components are designed so that their bias points can be set externally, allowing much greater control over the operation of the chip. The schematic for a single pixel is shown in Figure 5.2.

The following sections presents some results from the simulations of designs. The designs are simulated using post-layout circuits. Post-layout circuits are created by capturing the schematic, laying out the circuit in silicon and metal layers, then parasitic components such as mutual capacitance, resistance of metal wiring, vias, and stray inductance are extracted, and these can be used in evaluating the circuit response. This results in more realistic results than using only schematic capture, which does not include these parasitic components.

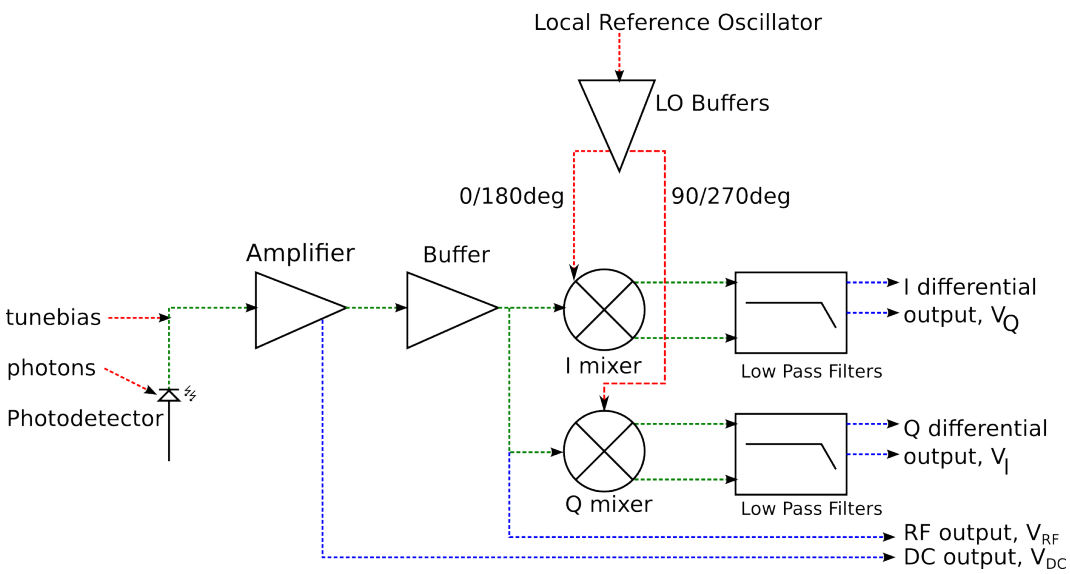

Figure 5.2: Schematic for the LIDAR1 pixel. Red lines show external inputs, green shows internal analogue signals, and blue lines show outputs.

5.2.1 Pixel

Front-end: The front-end, shown in Figure 5.3 uses a cascoded current mirror to bias the transimpedance amplifier. This has the advantage of increased output resistance, $R_o \approx g_m r_o^2$.

An initial design objective was to increase the space used by the photodiode. The photodiode size was increased to an area of 2138 μm^2. This results in a fill factor of 16 %.

The theory is discussed in section 3.5. Figure 5.4 to Figure 5.10 show the response of the front-end with a 1 nA AC on 1 nA DC photocurrent simulated with an ideal current source. Tunebias is provided separately with an ideal current source. The simulation is on a circuit with parasitics considered (post-layout/extracted cell) using a 10 fF capacitive load at 25°C. Figure 5.5 shows the increase in bandwidth with increasing tunebias current.

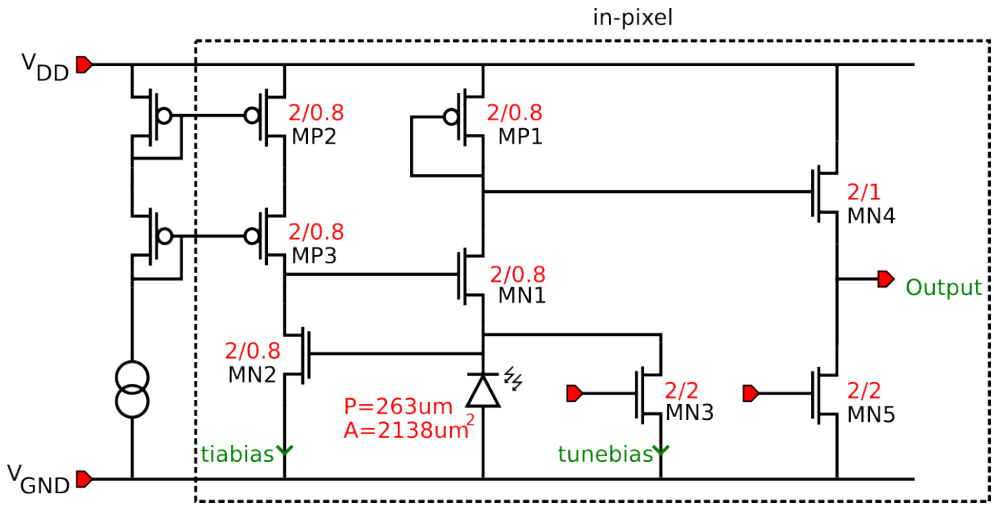

Figure 5.3: LIDAR1 front-end schematic

Figure 5.8 shows the simulated noise response of the front-end. It is shown input referred in units of photocurrent. This gives a measure of the minimum detectable signal. Using a noise equivalent bandwidth (NEB), it is possible work out the

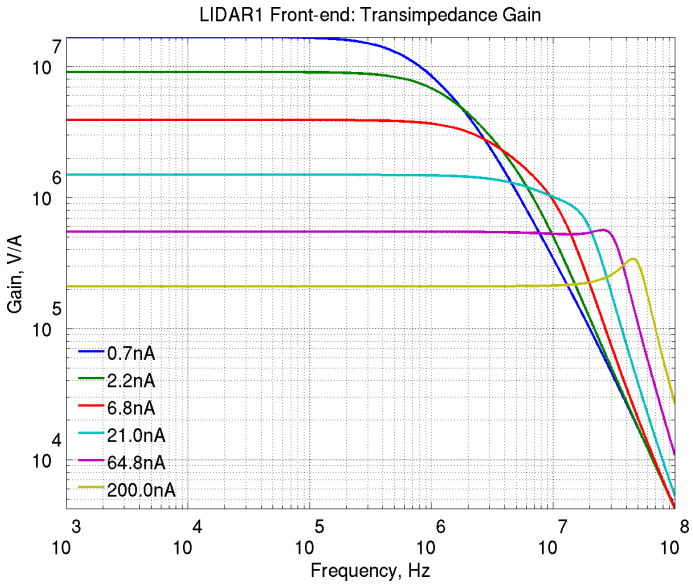

Figure 5.4: AC Amplitude response, showing gain and frequency response with various tune currents.

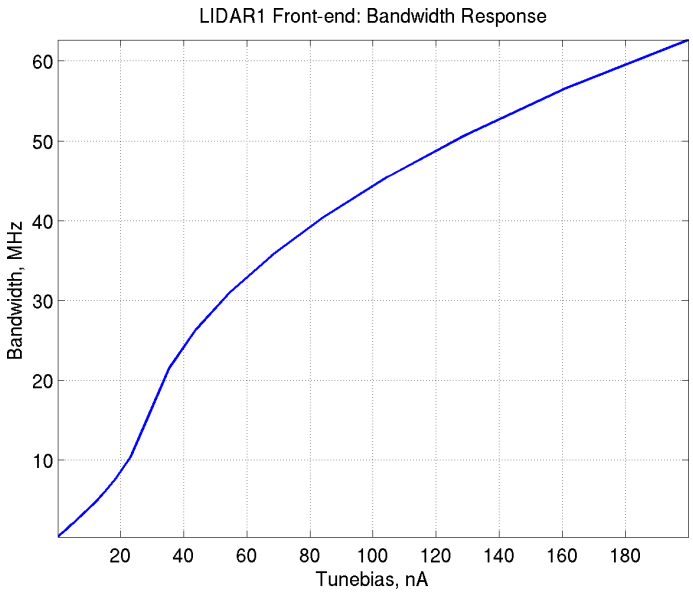

Figure 5.5: LIDAR1 front-end bandwidth response.

RMS noise at any given frequency. For example, at 10 MHz, with a NEB of 10 kHz, the minimum detectable signal is 50 fA. Later stages contribute noise, and their contribution will be referred backwards later.

The use of tunebias flattens the phase response, which is important when ensuring a minimum phase dependence on the photocurrent. This variation in the phase response with increasing tunebias is shown in Figure 5.9, and the gradient is taken

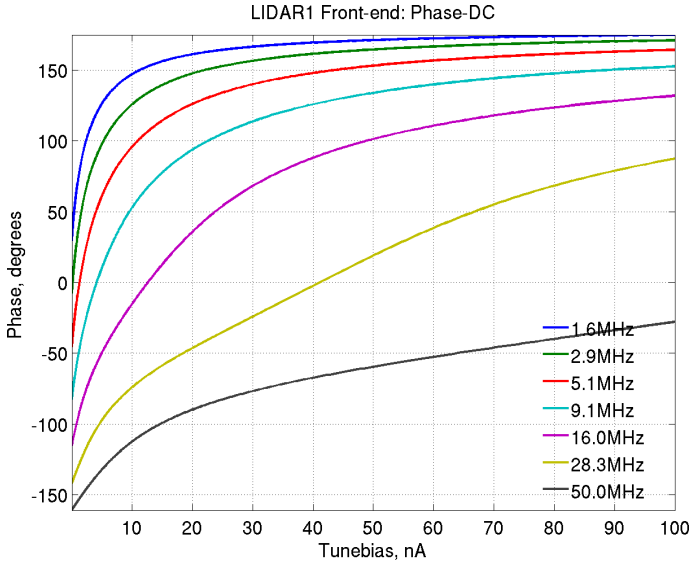

Figure 5.6: LIDAR1 front-end Phase response with varying photocurrent.

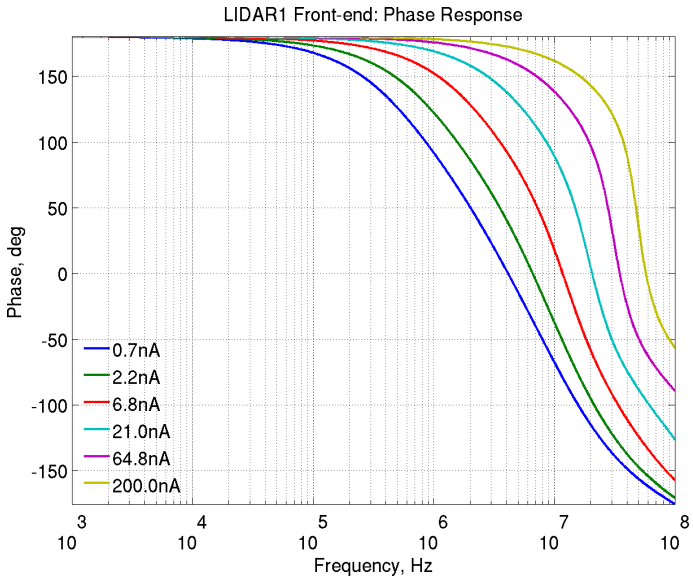

Figure 5.7: LIDAR1 front-end Phase response.

to be a measure of the flatness. This is shown in Figure 5.10.

A major improvement in the LIDAR1 front-end over MLCv6 is that it has a higher gain-bandwidth product. Using the larger photodiode also improves the fill factor.

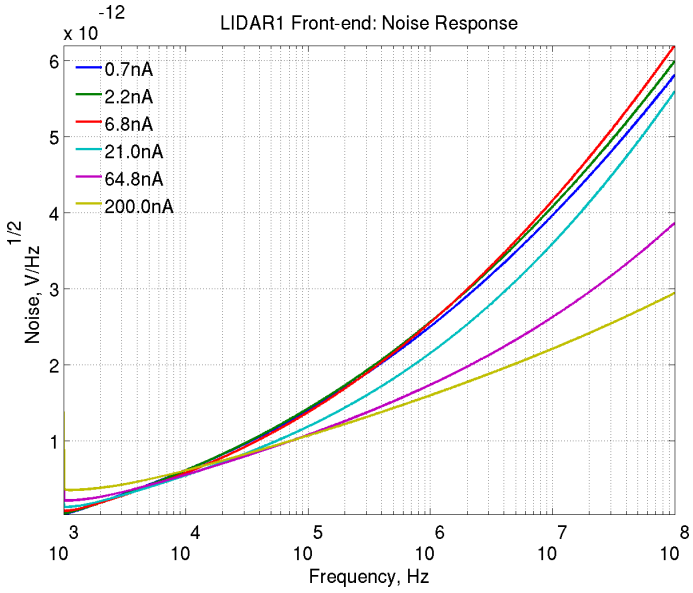

Figure 5.8: LIDAR1 front-end Noise response.

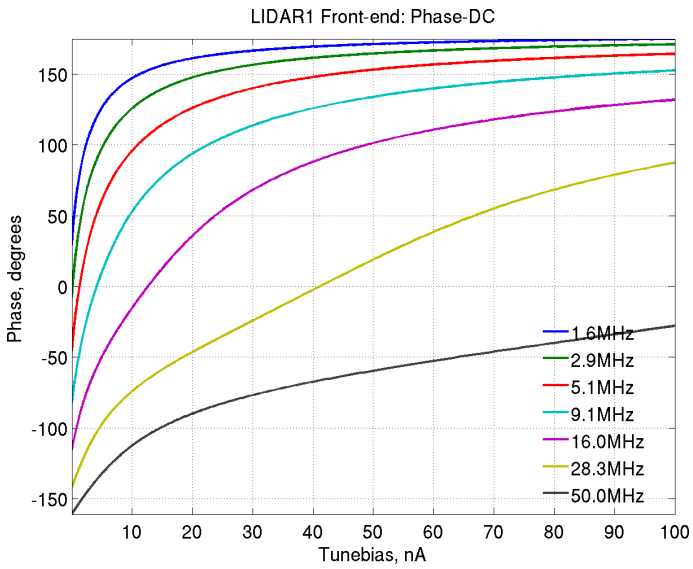

Figure 5.9: LIDAR1 front-end phase response.

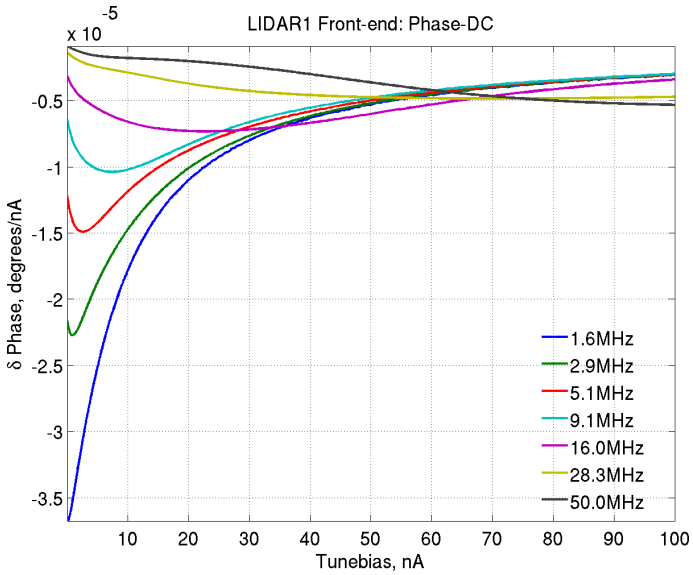

Figure 5.10: LIDAR1 front-end phase response.

Amplifier: The schematic of the in-pixel amplifier is shown in Figure 5.11. It is an operational amplifier. It is also designed to offer about 32 dB to 38 dB of gain, trading off with a bandwidth from 40 MHz to 17 MHz, depending on bias conditions. It's operating characteristics are shown from Figure 5.12 to Figure 5.15. The AC response shows a very flat response over a wide frequency region.

The testbench used for simulating the operation of the amplifier uses a 1.5 V voltage source, and is simulated post-layout at 25°C, with a 10 fF capacitive load.

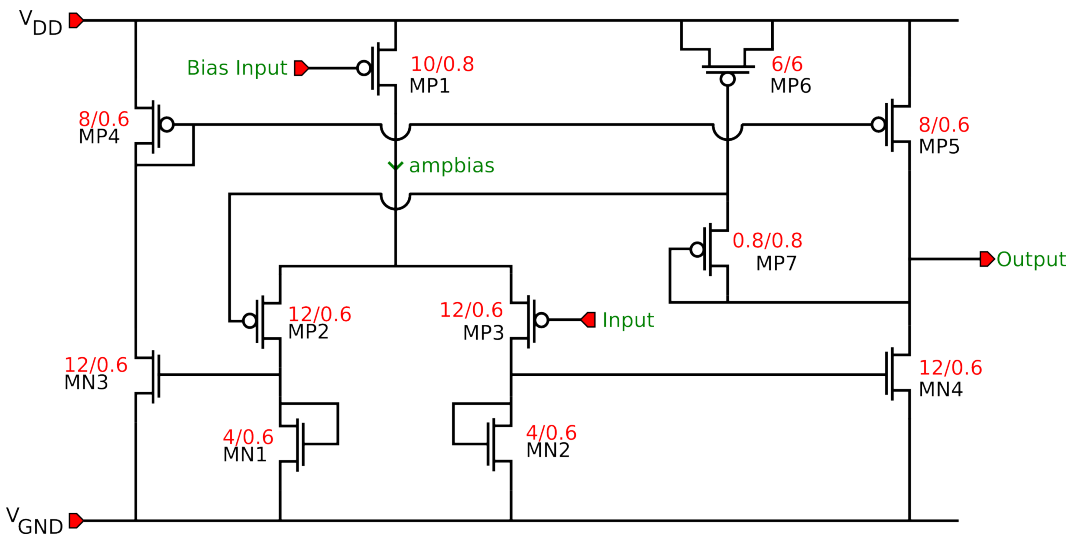

Figure 5.11: LIDAR1 in-pixel amplifier

The choice of the bias current is made to trade between gain and bandwidth. For low bandwidth requirements, below 1 MHz, a higher gain be configured by the use of higher bias current. The converse is applied for higher frequency experiments. The majority of results presented use a 10 μA bias current.

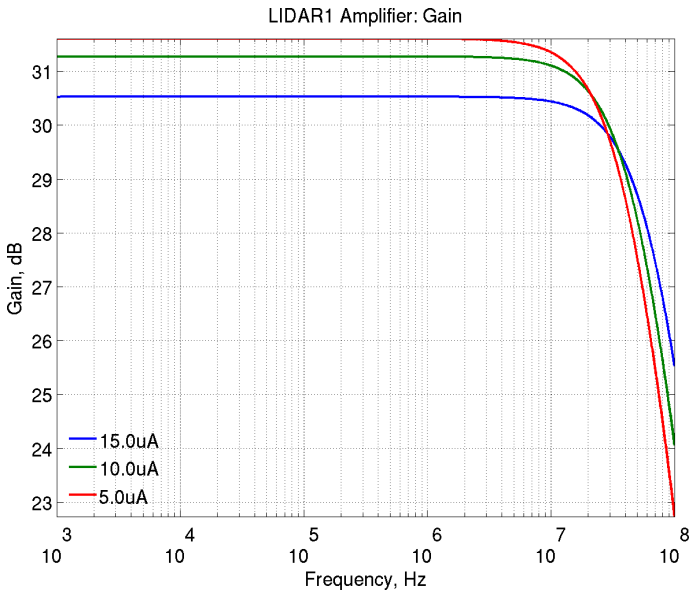

Figure 5.12: LIDAR1 pixel amplifier amplitude response.

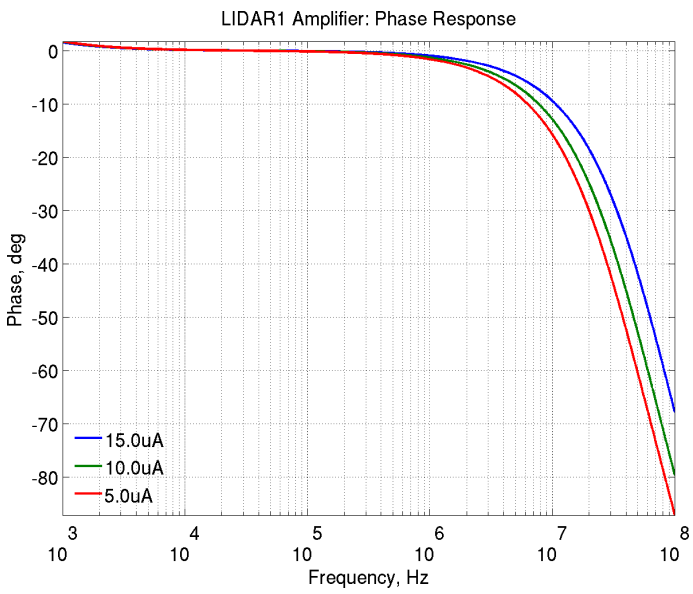

Figure 5.13: LIDAR1 pixel amplifier AC phase response.

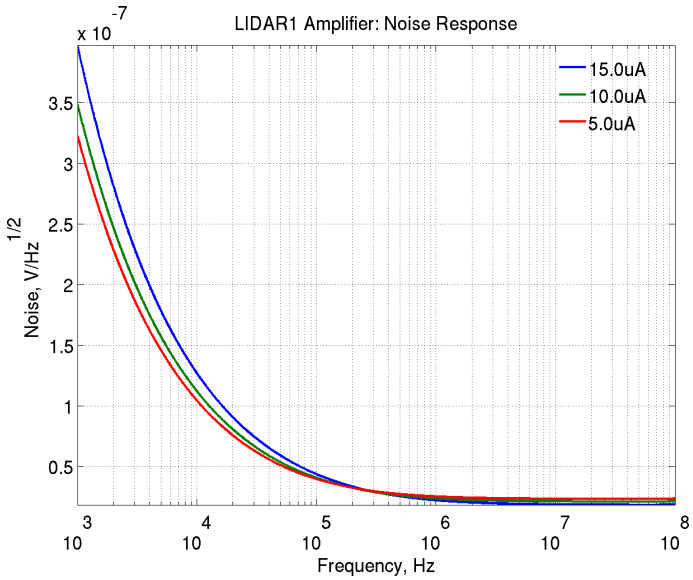

Figure 5.14: LIDAR1 pixel amplifier input-referred noise response.

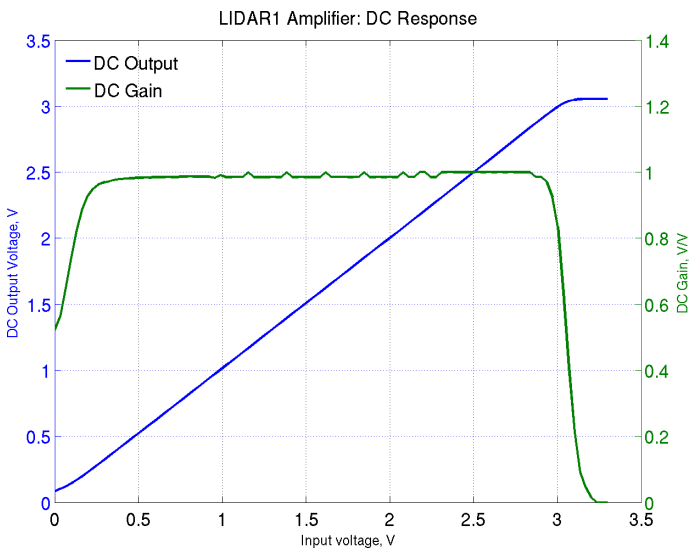

Figure 5.15: LIDAR1 pixel amplifier DC response.

Inter-stage buffer: This is a unity gain buffer that separates the amplifier from the mixer stage. It consumes 10 μA of current and has a bandwidth of 40 MHz. The schematic is shown in Figure 5.16

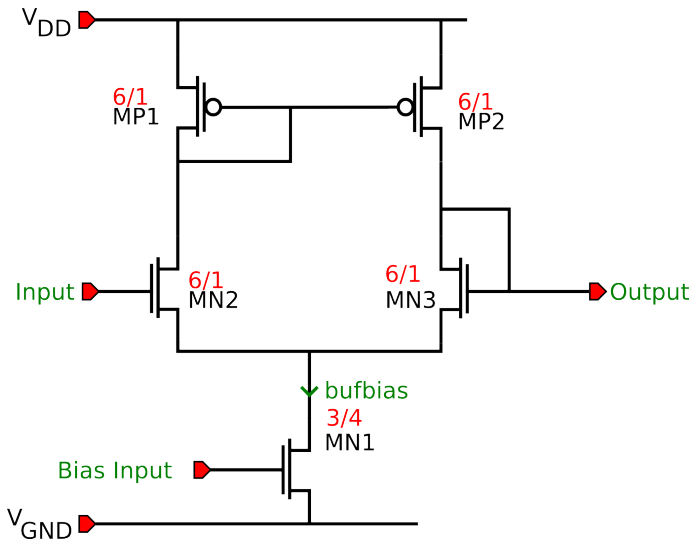

Figure 5.16: LIDAR1 inter-stage in-pixel buffer

Mixer: The mixing is achieved with two fully differential Gilbert cell mixers, one for in-phase mixing, and another for quadrature phase mixing. To simulate the operation of mixers, Periodic Steady State (PSS) simulations are required. PSS simulations are required for the simulation of mixers and oscillators because of the harmonic nature of the simulations. The simulations suggest a conversion gain from RF to IF (or in normal use from RF to DC) of -1 dB. A number of circuits were investigated to increase the gain, including the use of bleed transistors, bias current variation. However these worked out to cost more in silicon space or pixel current consumption. To this end, the best possible wide-band mixer was designed. This mixer is identical to the mixer in MLCv6, and the simulation characteristics are shown in Figure 4.21.

Filters: The output filters are operational transconductance amplifiers configured with very low bias currents. This low bias current gives a very high $g_m||r_o$, resulting in very low bandwidth [48]. By using an externally tunable bias current, it is possible to vary the bandwidth from 1 kHz to 5 kHz.

A schematic is shown in Figure 5.17. Figure 5.18 to Figure 5.22 show the simulated variation in filter bandwidth and noise performance with varying bias current. The testbench for the simulation uses an ideal voltage source of 1 mV AC on a 1.5 V DC voltage at the input. The circuit is simulated post-layout using typical conditions of 25°C, with a 10 fF capacitive load.

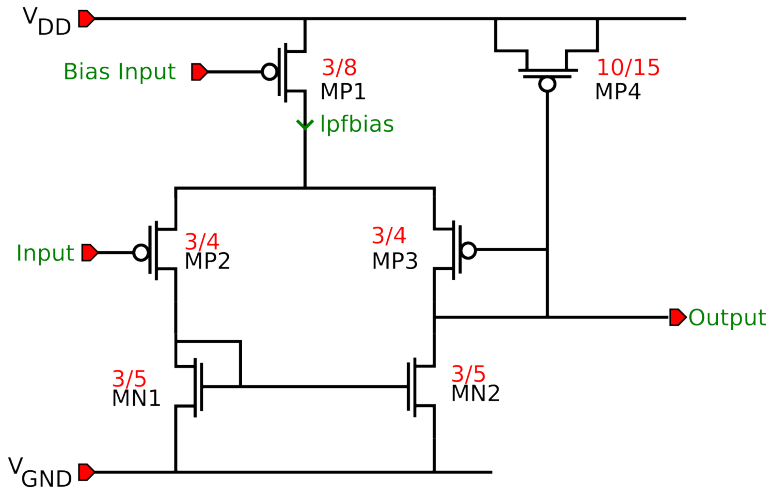

Figure 5.17: LIDAR1 in-pixel low pass filter.

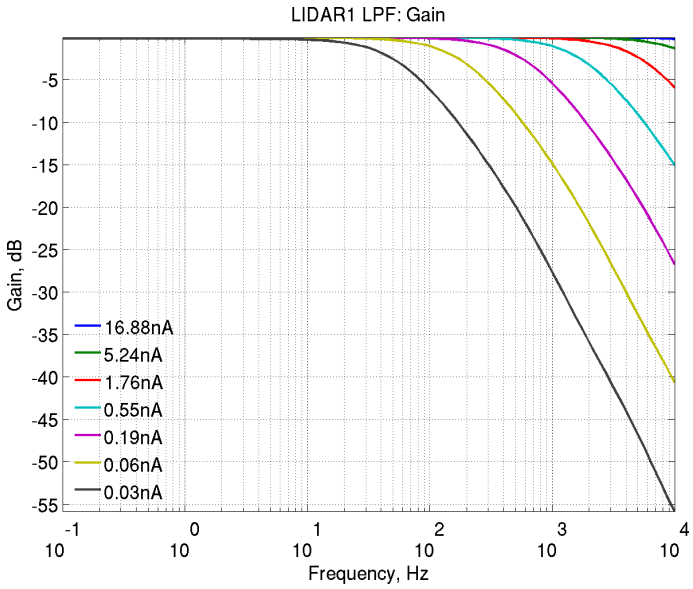

Figure 5.18: LIDAR1 low pass filter amplitude response.

Multiplexers: These are made up of a series of source followers. The column level selection uses PMOS transistors and thus needs an inverter to provide the

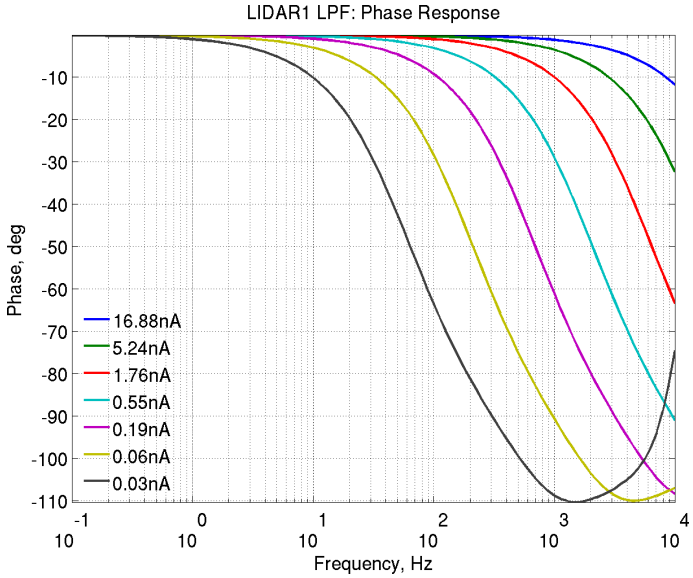

Figure 5.19: LIDAR1 low pass filter phase response.

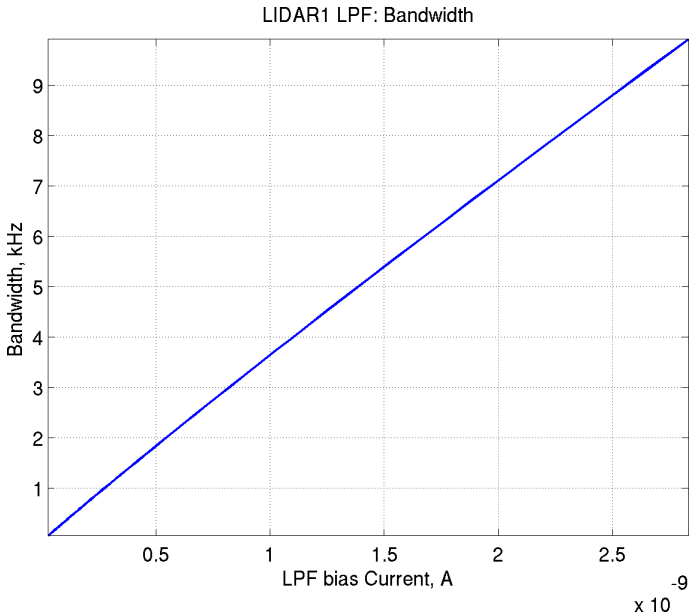

Figure 5.20: LIDAR1 low pass filter bandwidth response.

correct digital signal (active low). A separate 3.3 V power supply is provided for the digital circuits. The multiplexers are characterised to operate up to 1 Msps. They are selected (addressed) using address decoders based on Roger Light's work [20]. Given this speed, it is possible to acquire a frame in 1 ms. This speed also ties in well with the bandwidth of the filters (2 kHz).

The multiplexers group the array into 8 banks of 4 columns each. Thus only 3

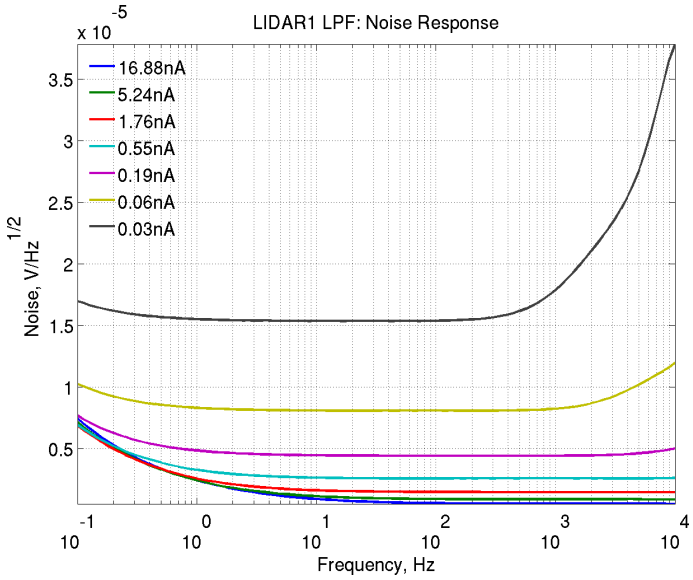

Figure 5.21: LIDAR1 low pass filter input referred noise response.

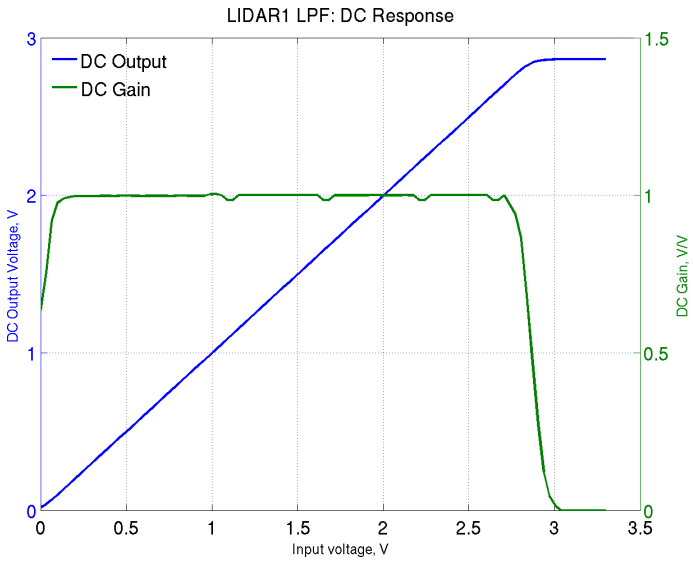

Figure 5.22: LIDAR1 low pass filter DC response.

bits are required for selecting any bank. The outputs of all four pixels selected in this scheme are available simultaneously. Figure 5.23 shows the layout of the multiplexer.

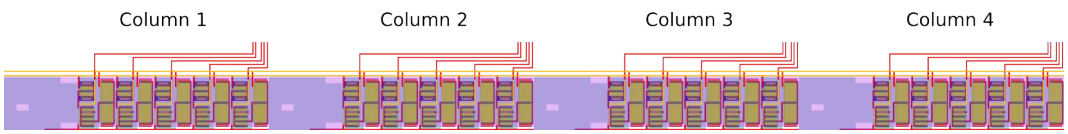

Figure 5.23: Layout of LIDAR1 multiplexer, showing four column level multiplexers (corresponds to one bank)

Output Buffers: LIDAR1 uses 5 V buffers to drive the signals off the chip to the pads. The buffers are unity gain opamps with a capacitance of 1 pF for stability. They are capable of a slew rate of 1 V/μs when biased with 5 mA of current. They are based on a design by Roger Light [20]. The schematic design is identical, but a new layout was drawn to allow it to fit with the array. Figure 5.24 shows the layout and Figure 5.25 shows the schematic of the buffer. A 16 pF is included in the output path for stability.

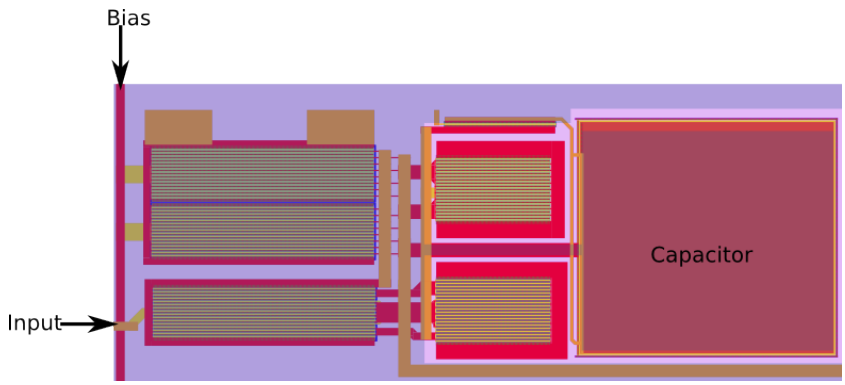

Figure 5.24: Layout showing LIDAR1's output buffer

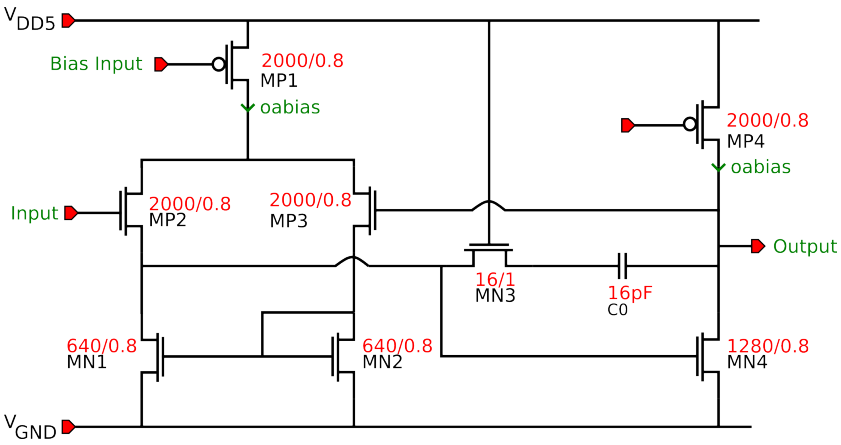

Figure 5.25: Schematic of LIDAR1's output buffer

At the end of the signal chain, it is possible to determine the noise performance of the pixel, and the contribution of each part. It was determined that the RMS noise at 10 MHz was approximately 60 pA, and the majority of this noise was from the front-end (specifically the TIA circuits - 10%), the filters (35%) and the

log load (2%).

Figure 5.26 shows the variation of the outputs of a single pixel at the pad (connection off-chip to the outside world) with increasing photocurrent. It shows a logarithmic response (the horizontal scale is log) for the DC channel (shown in blue). The IQ channels show a much smaller variation with photocurrent.

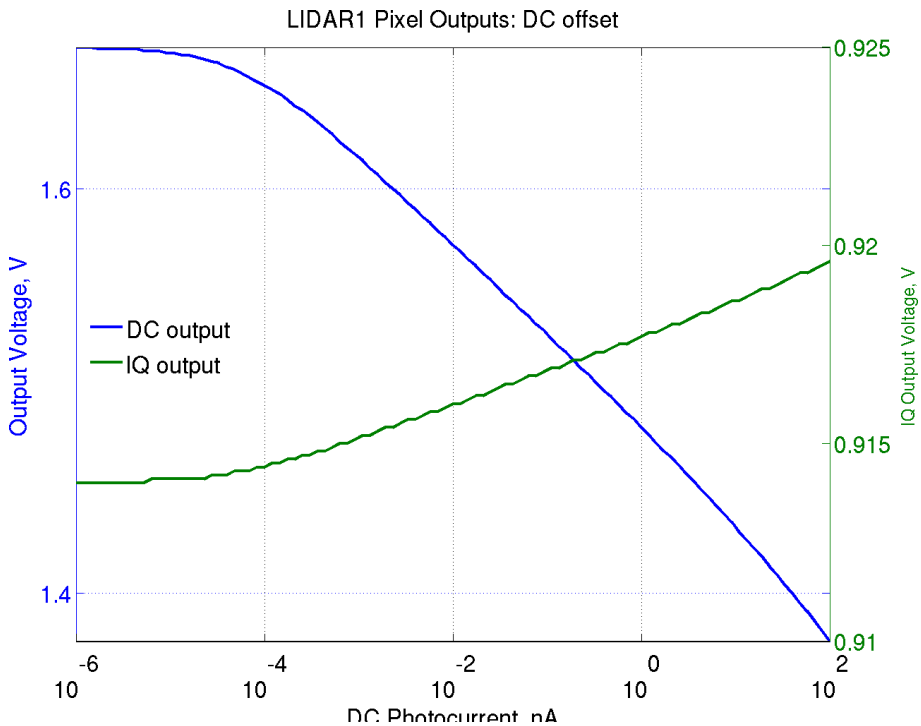

Figure 5.26: Simulated pixel DC and IQ output offset voltages. The logarithmic response is shown, and the conversion gain is shown in Figure 5.27. Output voltages is measured post-pad. Simulated post-layout, at 25°C.

The transimpedance gain for the pixel is shown in Figure 5.27. It provides the conversion gain from the beginning of the electronic chain through to the pad. It also shows the noise floor (outlined in red), and the operating region of interest in most experiments (outlined in green).

LIDAR1 was designed in stages, with each component designed at a time. It is important to make sure that each component has an output range that could/

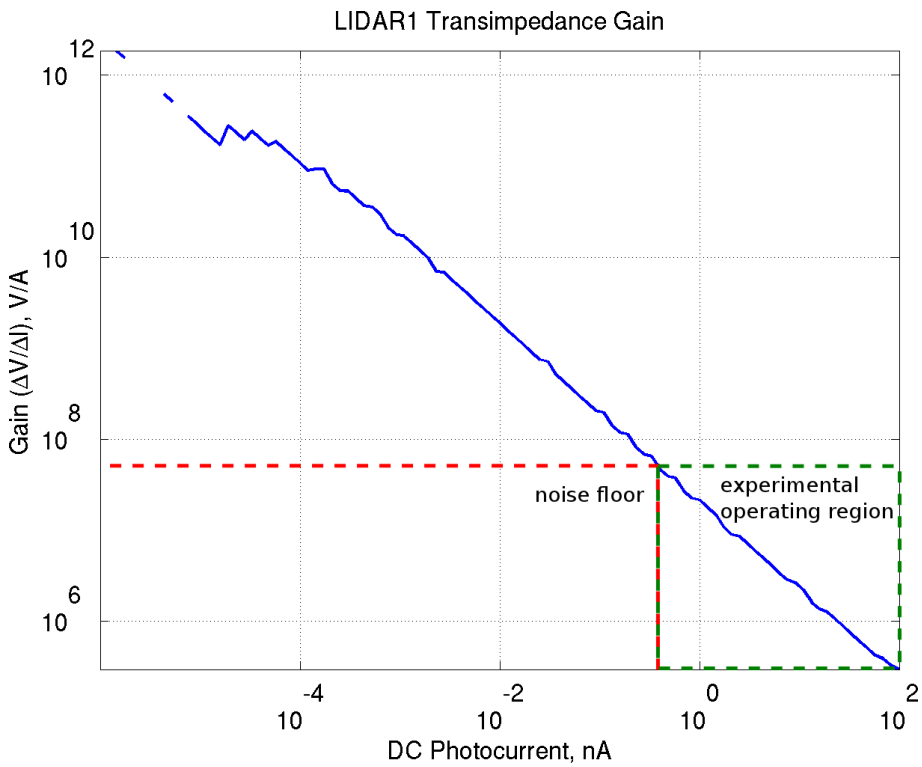

Figure 5.27: Simulated conversion gain of the LIDAR1 pixel. Output voltage is measured post-pad. Simulated post-layout, at 25°C.

would work within the input range of the next stage. This is shown as a signal flow diagram the shows the flow and expected range of the signals from one component to the next. Figure 5.28 shows the operation windows for the LIDAR in blue and green, and typical expected signal range in red. A brief note is also provided.

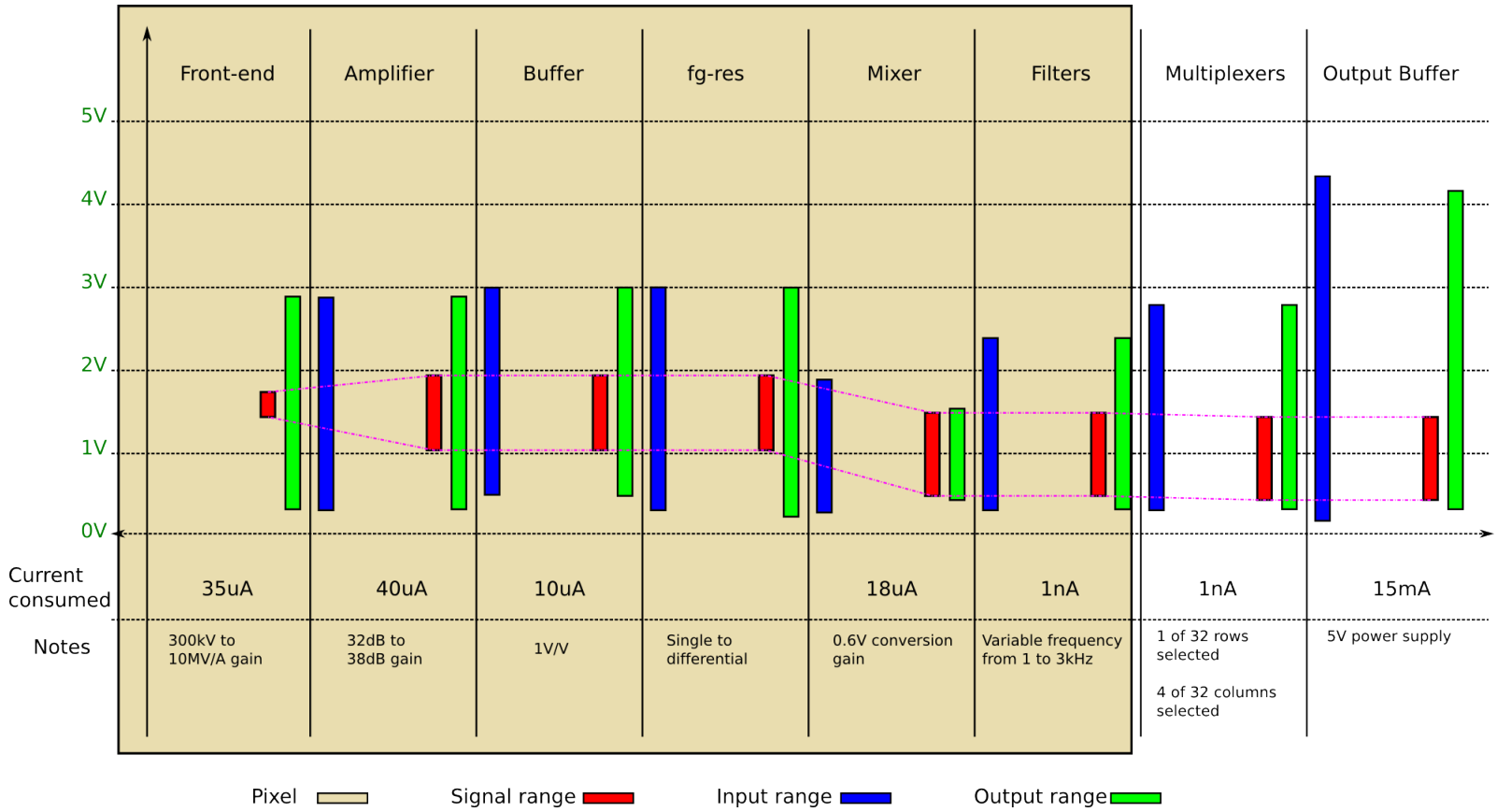

Figure 5.28: The diagram shows the windows of acceptance and output for various components of LIDAR1, as well as a brief summary of their performance.

5.2.2 Chip

The pixels are tiled into an array of 3.68 mm by 3.68 mm. This area includes the area for bias current mirrors, buffers and multiplexing. The bonding diagram that shows the pin connections is shown in Figure 5.29, and the layout plan is shown in Figure 5.30. A photomicrograph of the fabricated device is shown in Figure C.2

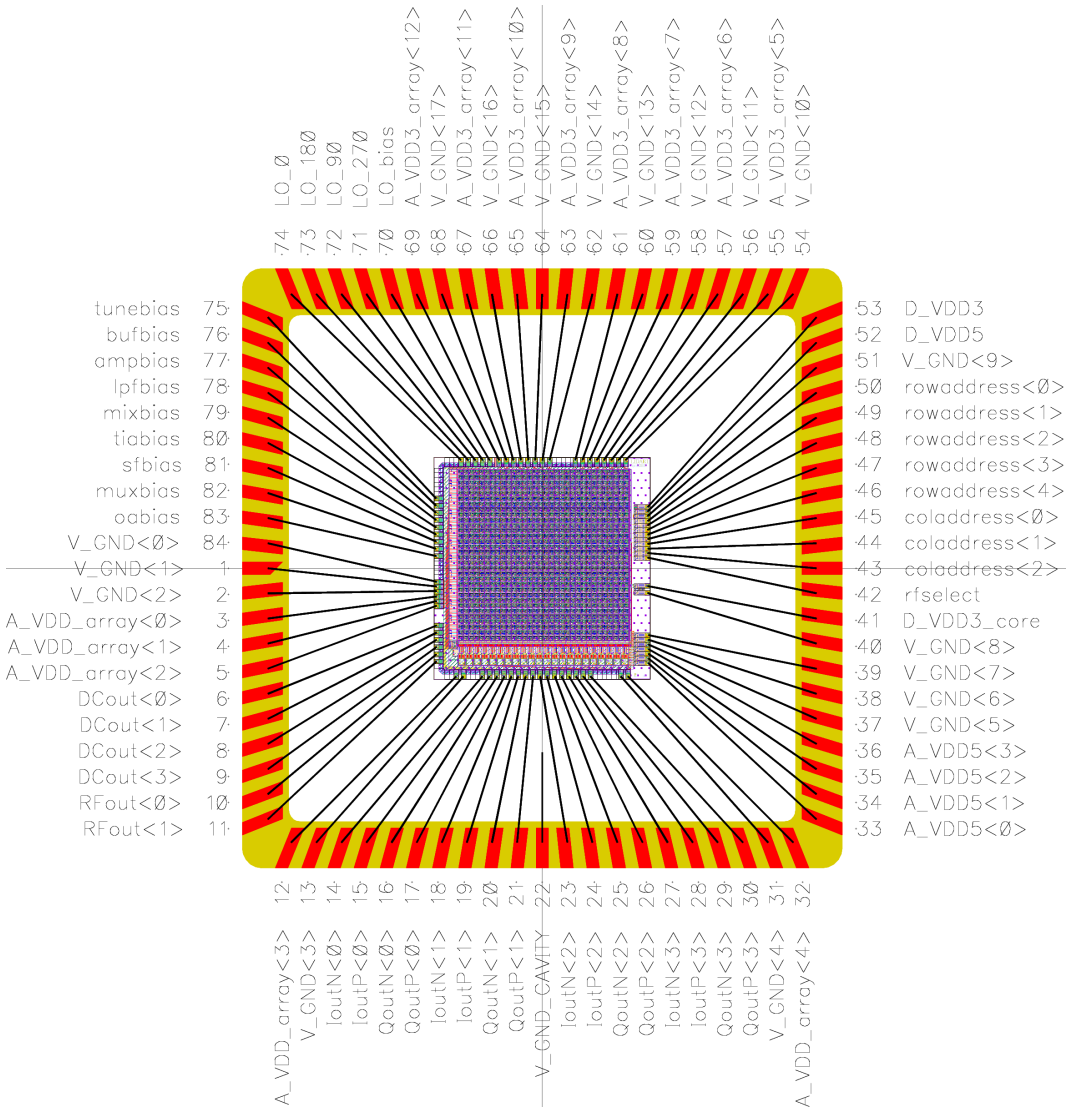

Figure 5.29: Bonding diagram for the LIDAR1 chip

It was observed during the testing of MLCv6 that the bandwidth of the reference oscillators (LOs) varied depending on the pixel which was under observation. The LOs on MLCv6 are introduced at one corner of the pixel array. The bandwidth at

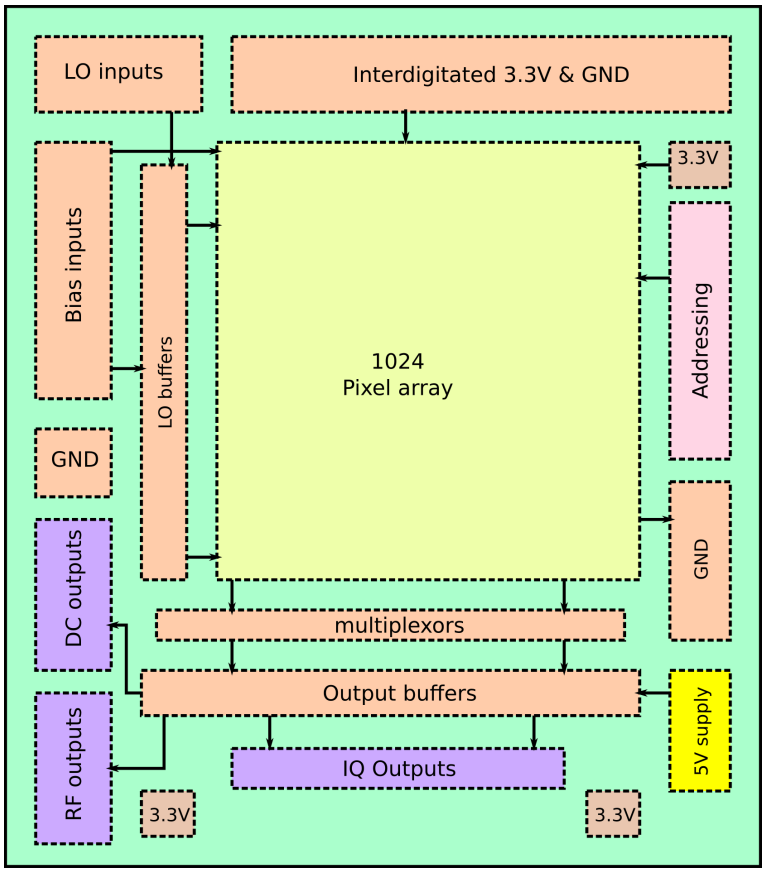

Figure 5.30: Layout plan for the LIDAR1 chip

the pixels farthest away from the LO input pads had a bandwidth of only 4 MHz compared to a bandwidth of 60 MHz at the pixel nearest to the point at which the LOs are introduced. In LIDAR1, 32 unity gain buffers are introduced. These buffers drive the LO signal row by row, reducing the maximum wire length to 3.68 mm. The layout for these buffers is shown in Figure 5.31.

Another major change between MLCv6 and LIDAR1 is the power distribution net. As shown by the bonding diagram of MLCv6 (Figure 4.28), the power supply to the array was from only one corner of the chip. This results in an uneven power distribution around the chip (Figure 4.30). With LIDAR1, the power supply pads are distributed all around the chip. This greatly reduces the maximum voltage drop.

Similar to MLCv6, Bypass capacitance from the gate capacitance of PMOS

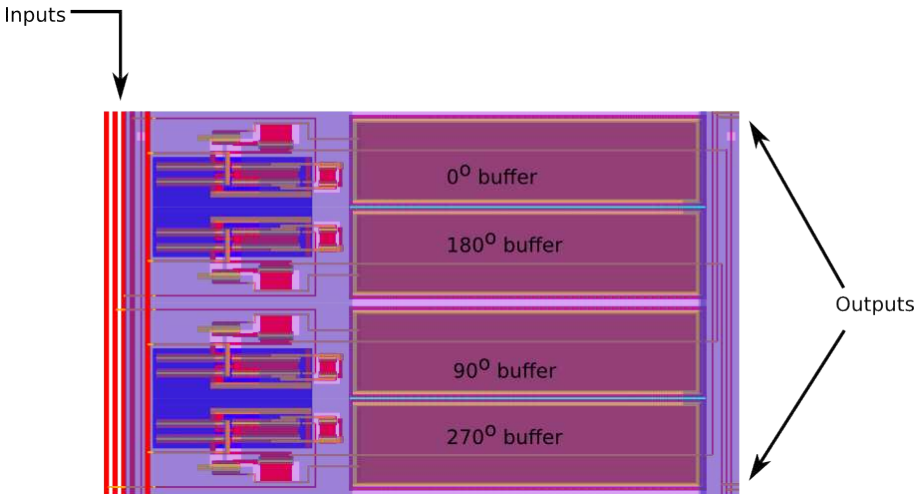

Figure 5.31: LIDAR1 local oscillator buffers for driving LO signals across a row. The 4 buffers drive the 0, 90, 180 and 270 degree reference signals into the array.

transistors is used on all bias lines to reduce switching noise and decouple power supply noise. In LIDAR1, improved layout technique leads to a greater decoupling capacitance.

Analysis of the voltage distribution is performed using a Cadence tool, Voltage Storm. Figure 5.32 shows a summary of the IR Voltage Storm analysis of the chip. It shows the variation in the 3.3 V supply to the array, showing a maximum of approximately 6 mV. This compares very favourably with MLCv6, which had a maximum drop of 66 mV. The ground bounce is approximately 3 mV, compared with MLCv6's ground bounce of 16 mV.

Figure 5.32 shows an improvement of about 10 times in LIDAR1 compared with MLCv6 in the power supply (Figure 4.30. This was achieved by moving the supply points all round the chip, instead of congregating them together at one place.

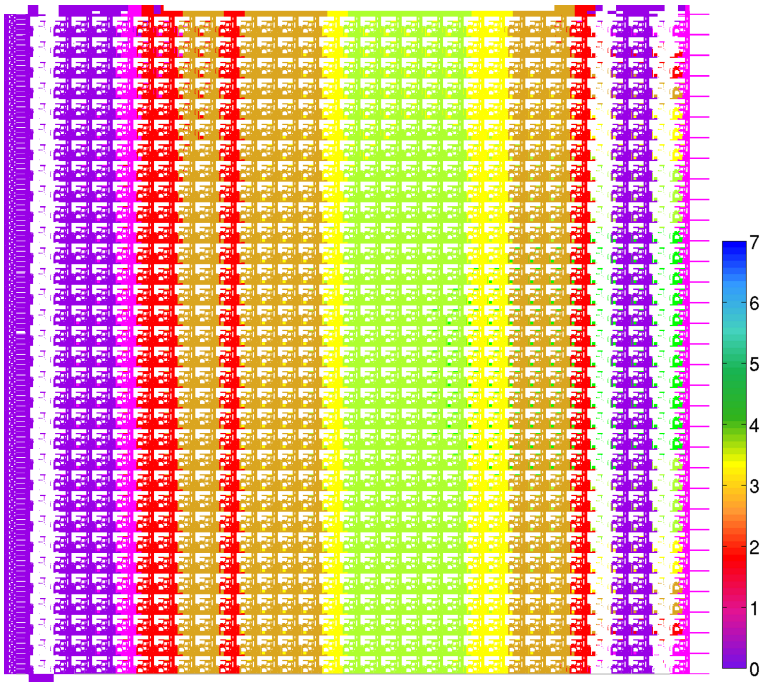

Figure 5.32: Voltage Drop analysis of LIDAR1, showing the IR drop in VDD across 1024 pixels. The supply is from pads at every corner, as shown in the bonding diagram in Figure 5.29. The maximum drop is approximately 7 mV, and the maximum bounce is 2 mV (not shown).

5.2.3 Corners Analysis

It is important to model the response of the circuit accounting for process variations using Corners Analysis. The analysis is combined with Monte Carlo experiment to repeatedly generate random samples. Thus a probabilistic result of the performance of the chip may be determined.

Worst speed and worst power corners were simulated on a row of pixels of LIDAR. Two pixel in the row have photocurrents which simulate light with different modulation frequencies. One of those pixels is selected and the outputs are observed. This was done to double check any output-shorting problems, a test which was not performed on MLCv6. This test would have resulted in the row address selection problem being found. The results of the anaylsis are summarised in Table 5.1. 100 points were specified for in a Monte Carlo run and the conditions

observed were Bandwidth, Gain and RMS Input Noise at 10MHz. The yield estimate is 75% with the given conditions. The simulation temperature is 90 °C, and a noise equivalent bandwidth of 5kHz is used.

The results suggest that 25% of the cameras could be expected to fall outside of the desired parameters because they exceed the maximum noise target. This is in contrast to MLCv6, where 62% of the cameras were not expected to meet the same bandwidth requirements, and 10% were not expected to meet the noise requirement.

Table 5.1: LIDAR1 Corners analysis

Test Name	Yield(%)	Min	Target	Max	Mean	σ(STD)
Bandwidth (Hz)	100	36.41M		39.66M	37.28M	0
*Nominal	100	36.41M	>30M	36.41M	36.41M	0
*Worst Power	100	36.63M	>30M	39.66M	39.04M	426.1k
*Worst Speed	100	36.41M	>30M	36.41M	36.41M	0
Gain (V/A)	100	5.641M		6.529M	6.529M	0
*Nominal	100	6.529M	>4M	6.529M	4.549M	0
*Worst Power	100	5.641M	>4M	6.466M	5.962M	316.1k
*Worst Speed	100	6.529M	>4M	6.529M	6.529M	0
Noise (A)	75	41.09p		62.46p	44.76p	nan
*Nominal	100	41.09p	<60p	41.09p	41.09p	nan
*Worst Power	100	44.98p	<60p	62.6p	52.111p	7.251p
*Worst Speed	100	41.09p	<60p	41.09p	41.09p	nan

Comparing the results with MLCv6 (Table 4.1), the bandwidth now meets and exceeds the revised target of 30 MHz. This has been achieved by a more robust design and layout that has resulted in a higher and more consistent bandwidth across the process corners. The same is true for the gain, in that the minimum gains well exceeds the target. Although at first glance the noise performance is reduced for LIDAR1, the mean noise is reduced compared to MLCv6.

5.3 Characterisation

Figure 5.33 shows the basic experimental setup that is used in initial characterisation of LIDAR1. It is important to find out that how closely it achieves the design objectives.

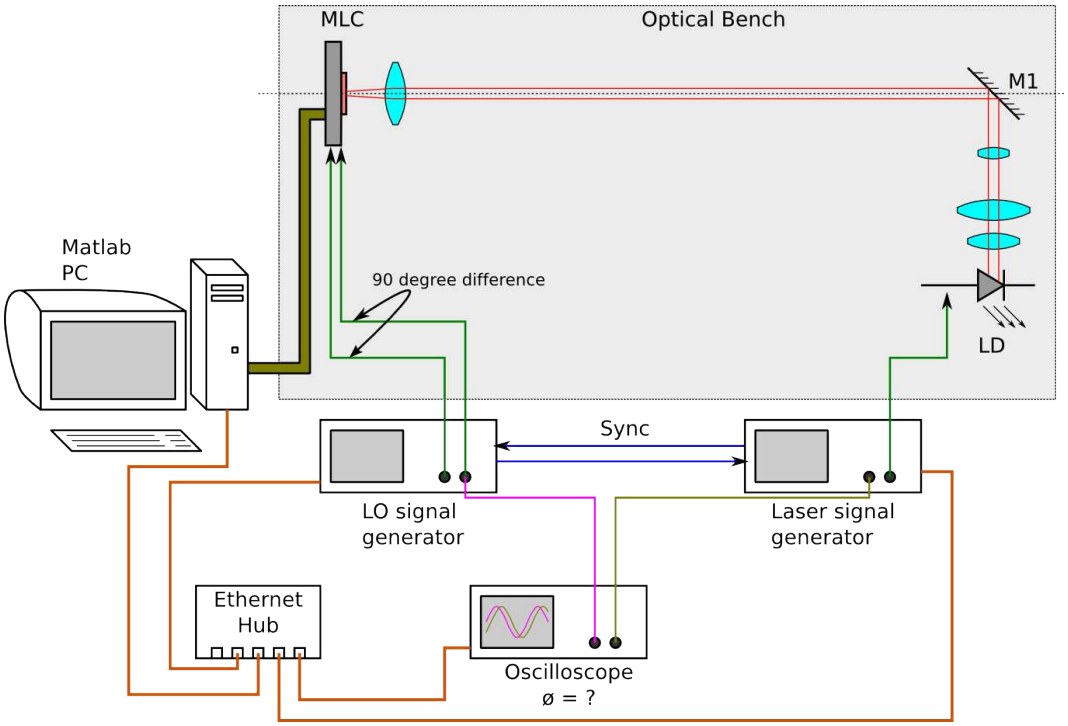

Figure 5.33: The experimental setup used in characterising LIDAR1.

5.3.1 Hardware

A printed circuit board (PCB) was designed for testing LIDAR1. It is made up of a single PCB with all the necessary components for proper operation. It contains the power supply regulators for the 3.3 V and 5 V supplies to the chip and other ancillary circuits on the PCB. The power supplies are conditioned by the use of bypass capacitors. The digital and analogue power supplies are kept separate. A schematic for the PCB is shown in Figure 5.34

The PCB performs the phase splitting necessary to generate the reference

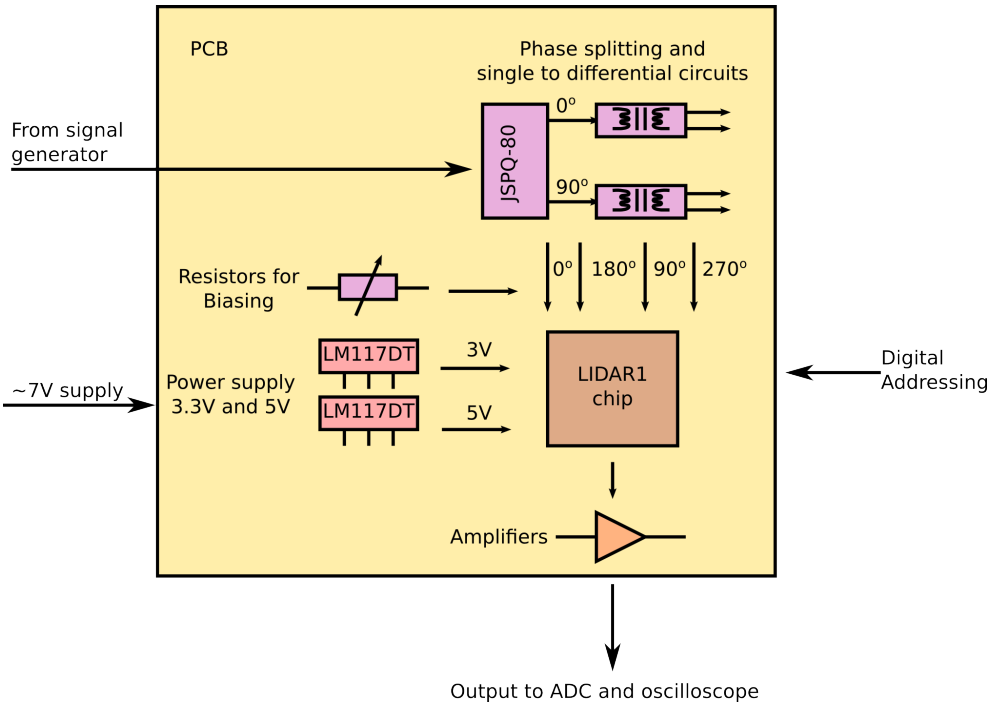

Figure 5.34: LIDAR1 PCB schematic

oscillation and its quadrature component. Phase splitting is achieved with a Mini Circuits JSPQ-80. It has a bandwidth of 3 MHz to 80 MHz, and generates a 90° signal given a sinusoidal input signal. Later it was decided to use a Tektronix signal generator to provide the 0 and 90 degree signals because there was large variation in the phase splitter's response with frequency.

The resistors necessary for the bias currents are also on the PCB. The values of the bias currents, and the resistances used are listed in Table B.2.

With bias resistances set to these values, the chip consumes approximately 420 mA, as expected from DC simulation. The pixel array consumes 183 mA (approximately 180 μA per pixel), and each output buffer consumes 10 mA. Since there are 22 buffers, they consume the majority of the current. A separate 5 V supply supplies this current.

The data from the camera is captured by a 16 bit, 16 channel NI PCI 6251. The

ADC is capable of 1 Ms/s (multichannel) acquisition rate.

5.3.2 Acquisition Software

The software for acquisition of data from LIDAR1 is written in C and C++, with a Matlab script driving the whole experiment. Comedi v0.8 [45] is used for the communication with the DAQ system. The digital controls to the experiment are also provided by the DAQ card. An ethernet network was set up to co-ordinate the signal generators and the oscilloscope.

5.3.3 Local (reference) oscillator generation and DC offsets

As explained in section 3.8.1, a good knowledge of the noise sources is required in order to correctly interpret measured results. This section will discuss them briefly, as encountered from an instrumentation perspective.

Because of the use of a continuous-time front-end, there is a fixed DC offset on the signal. With no light on the pixel, the DC output of a pixel is about 1.8 V, which decreases exponentially to about 1.1 V with increasing light level. This is different from most APS pixels, where the full power supply range is utilised, i.e. 0 to 3.3 V.

Figure 5.26 shows that even with no-illumination, there is still a non-zero (and significant) offset voltage on the outputs of a pixel. This must be considered when measuring the illumination, since the illumination is independent of this.

Another significant point to note is that the IQ outputs have an offset voltage that is slightly dependent on the LO conditions. It was observed during experimentation that the LO source (a Tektronix AFG 3252 signal generator) varied in amplitude and DC offset with varying frequency. A Marconi Instruments

2382 spectrum analyser was used to determine the frequency response. The variation in amplitude is shown in Figure 5.35. The figure shows that the amplitude must be compensated for in order to determine the phase correctly.

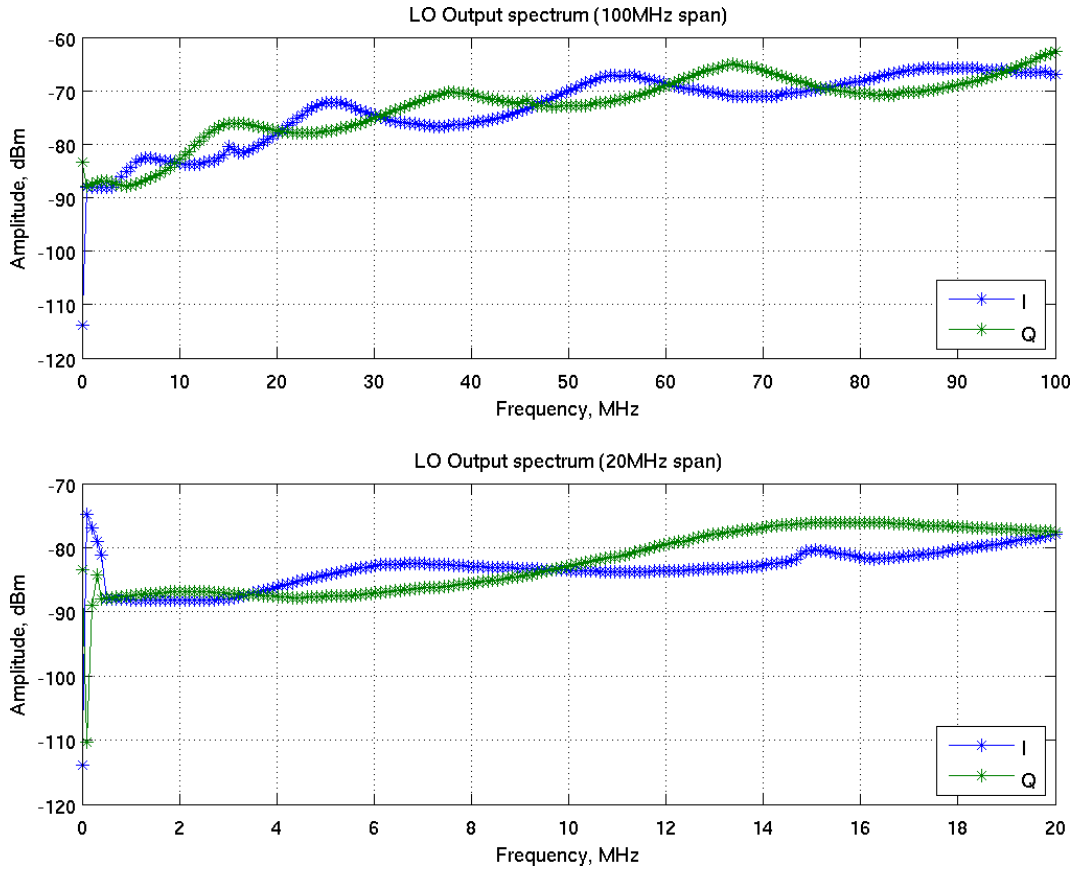

Figure 5.35: Reference Oscillator variation with frequency.

Identical cables are used, and also interchanged to make sure they were not responsible for this response. The cables provided acceptable responses up to frequencies in excess of 200 MHz.

Determining phase is difficult under these circumstances, because the offset must be accounted for in calculating the phase. Figure 5.36 shows how the calculated phase must account for the DC variation with varying amplitude and DC offset, both of which vary also with frequency because of the experimental tools. For example, it is seen that the offsets could vary with frequency (brown curve - shift in $(I_{\text{offset}}, Q_{\text{offset}})$, ie from circle to ellipse).

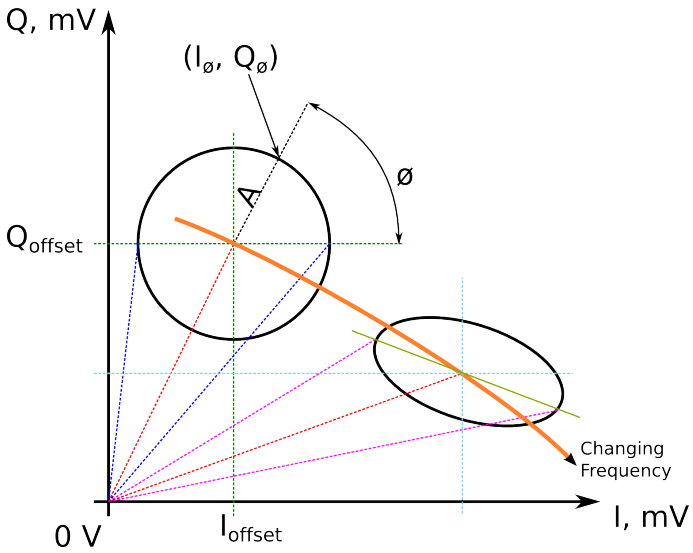

Figure 5.36: Determining phase, accounting for DC offset.

The phase can be determined using Equation 5.1. Q_{offset} and I_{offset} vary with the LO conditions (such as modulation frequency, amplitude and phase difference) and very slightly with the DC light level as shown in Figure 5.26. To determine the correct phase, the offsets must be accounted for before the centre of the circle is determined. One way of doing this is simply taking phase measurements with 0, 90, 180 and 270 degree shifts in the phase of the illumination, which gives 4 points of the circle, from which the centre may be determined to give correct phase measurement.

$$\Phi = \tan^{-1}\left(\frac{I_\Phi - I_{\text{offset}}}{Q_\Phi - Q_{\text{offset}}}\right) \tag{5.1}$$

Any difference in the gain of the I channel relative to the Q channel manifests in an elliptical shape, instead of a circular shape. This is also seen if the LO signals have different amplitudes going into the chip. An ellipse with foci at a non-zero angle (as shown in Figure 5.36) suggests a non-quadrature shift between the reference LO signals.

5.4 Experimental Results

This section presents some of the key results obtained from the experiments. It starts by presenting the response of single pixel to DC and AC illumination, and then images received using the whole array.

5.4.1 Single Pixel

The first experiment conducted was to determine the response of a single pixel to light. To this end, the DC and RFout channels of pixel (15, 16) near the middle of the chip were probed. A Newport 842-PE light power meter is used as a reference meter to determine the light power in all cases.

Figure 5.37 shows the response of the IQ outputs of chip. A sweep of the relative phase between the incoming light and the reference oscillator is made from -180° to 180° at 1 MHz. The voltage measured at the IQ output (after removing the DC offset) is shown in Figure 5.37a. I is plotted against Q in Figure 5.37b. This would ideally give a circle. It is elliptical because of a difference in the amplitude of the quadrature LO signals from the phase splitter. The off-axis shape also suggested a non-quadrature split (i.e. not 90 degrees difference). Using the calibrated signal generator for the LO resolves the elliptical shape into a circular shape, solving both problems.

The calculated phase is shown wrapped in Figure 5.37c. After unwrapping and subtracting the error in measured phase is shown in Figure 5.37d.

5.4.1.1 Frequency response - Amplitude and Phase

The first part of this experiment was to determine the amplitude response. The amplitude of the modulation component of the light is measured from the I and

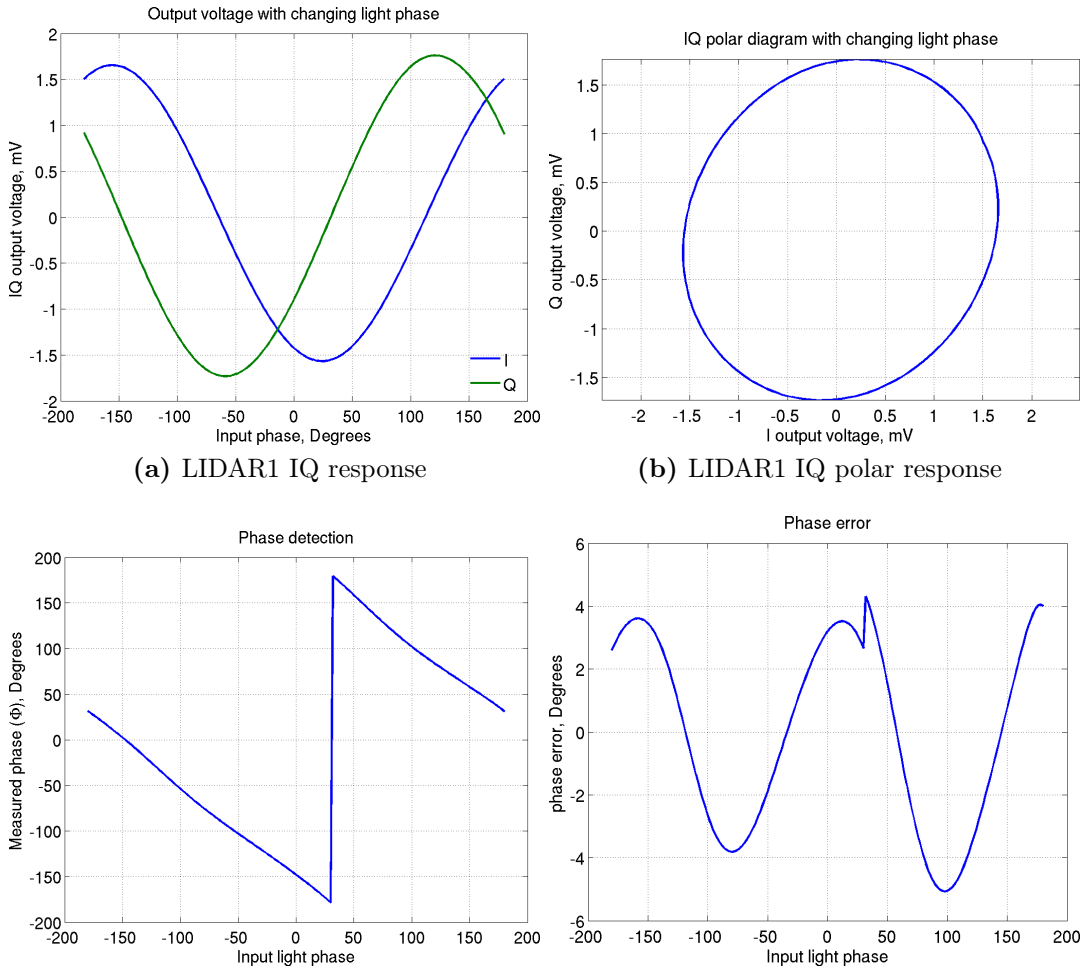

(a) LIDAR1 IQ response **(b)** LIDAR1 IQ polar response

(c) LIDAR1 IQ phase **(d)** LIDAR1 IQ phase error

Figure 5.37: LIDAR1 output IQ voltages, calculated phase, and phase error

Q outputs (after compensating for the offsets as discussed in section 5.3.3). The frequency is scanned from 100 kHz to 40 MHz. After each frequency scan, tunebias is increased. The light per pixel is 10 nW modulated to a depth of 50%.

The amplitude of the modulation component is calculated using Equation 5.2. Because the AC photocurrent (5 nA) is known, it is possible to calculate the transimpedance gain after the amplitude has been determined. The transimpedance gain is given by Equation 5.3, where I_{ph} is the AC photocurrent.

$$V(f, I_T) = \sqrt{(I_p - I_n)^2 + (Q_p - Q_n)^2} \tag{5.2}$$

$$Z(f, I_T) = \frac{\sqrt{(Q_p - I_n)^2 + (Q_p - I_n)^2}}{I_{ph}} \tag{5.3}$$

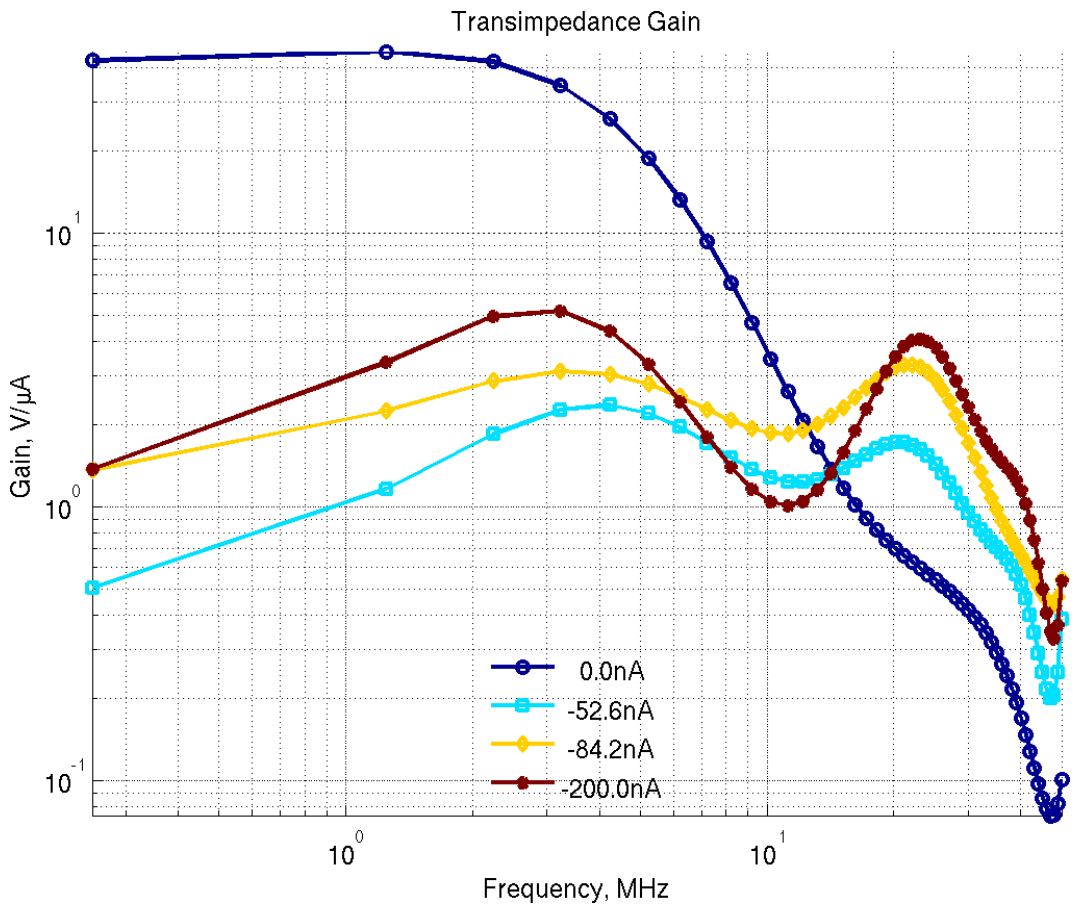

Figure 5.38: LIDAR1 pixel conversion gain with varying tunebias.

Figure 5.38 shows that at low frequencies, using tunebias = 0 nA (blue characteristic) gives a higher gain. This falls off faster with increasing frequency, and increasing tunebias enables an increase in bandwidth.

The next part was to determine the phase response. The IQ outputs are sampled, whilst the frequency is scanned to provide an idea of the operating range of LIDAR1. At the same time, tunebias is incremented to determine the impact on the phase and amplitude response.

Scanning the phase and frequency experimentally proved to be rather challenging. After a frequency change, the phase between the LOs and the light modulation signal varies randomly at the signal generator. A compensation mechanism was designed to help solve this, using a digital oscilloscope to determine the phase difference. The waveforms are acquired from the oscilloscope, and the phase

difference determined in Matlab. The Matlab code used for the acquisition sends a signal to the signal generators that provide the modulation signals to the experiment to compensate for the difference. The schematic showing experimental setup is shown in Figure 5.33.

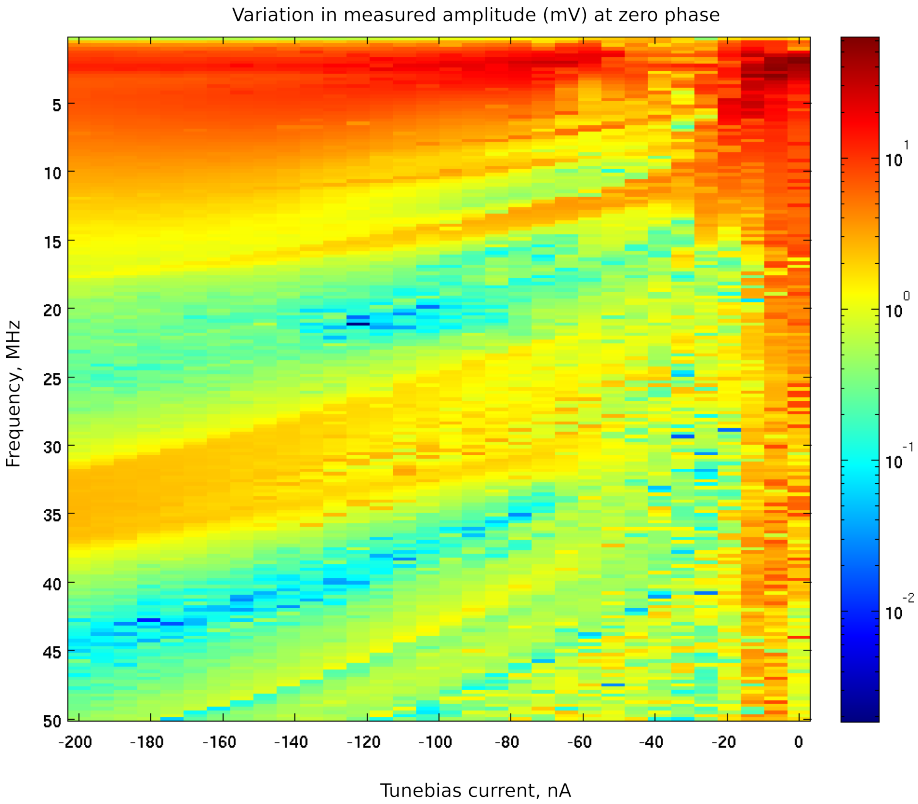

Figure 5.39: LIDAR1 Amplitude response with tunebias varied from 0 to 200 nA.

Figure 5.39 shows the amplitude response as the frequency and tunebias are varied. Figure 5.40 to Figure 5.44 show the phase response.

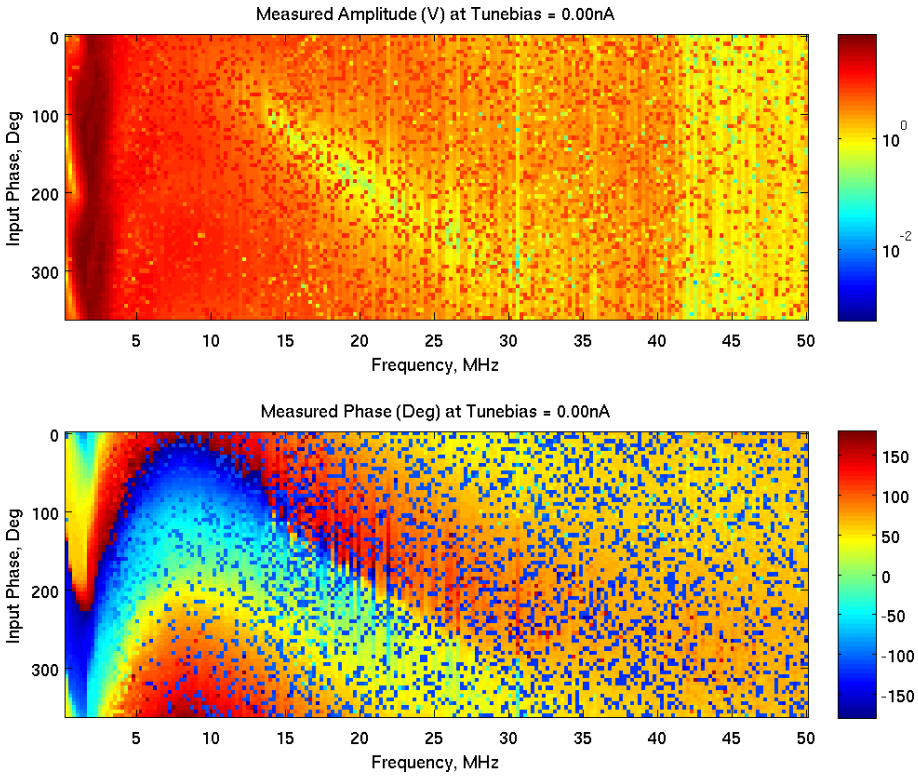

Figure 5.40: LIDAR1 amplitude and phase response. Tunebias $\approx 0\,\mathrm{nA}$.

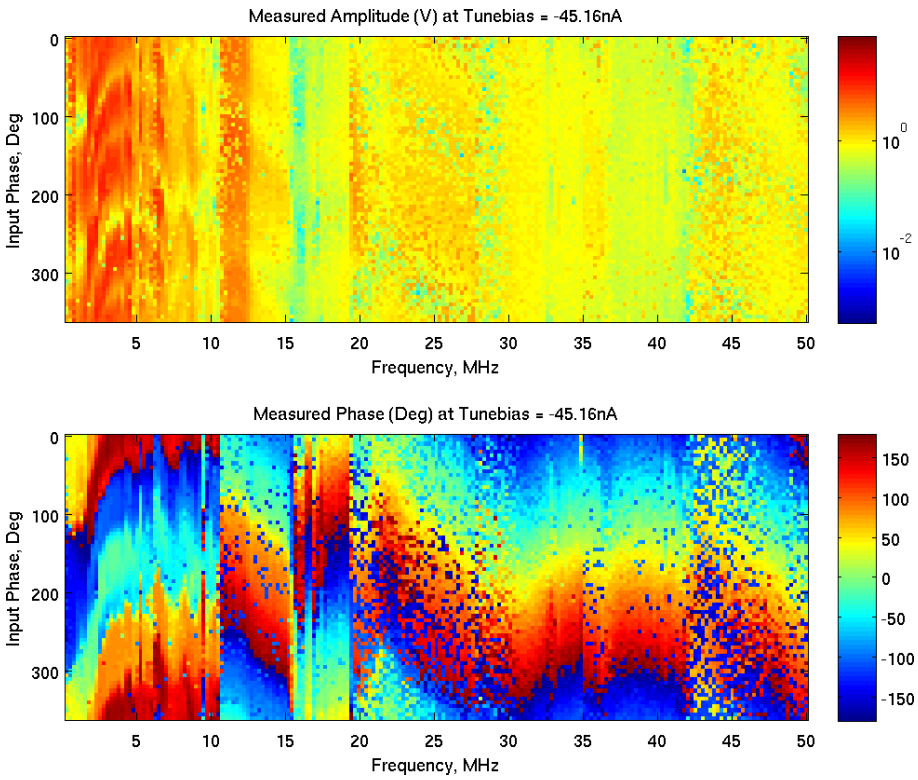

Figure 5.41: LIDAR1 amplitude and phase response. Tunebias $\approx 45\,\mathrm{nA}$.

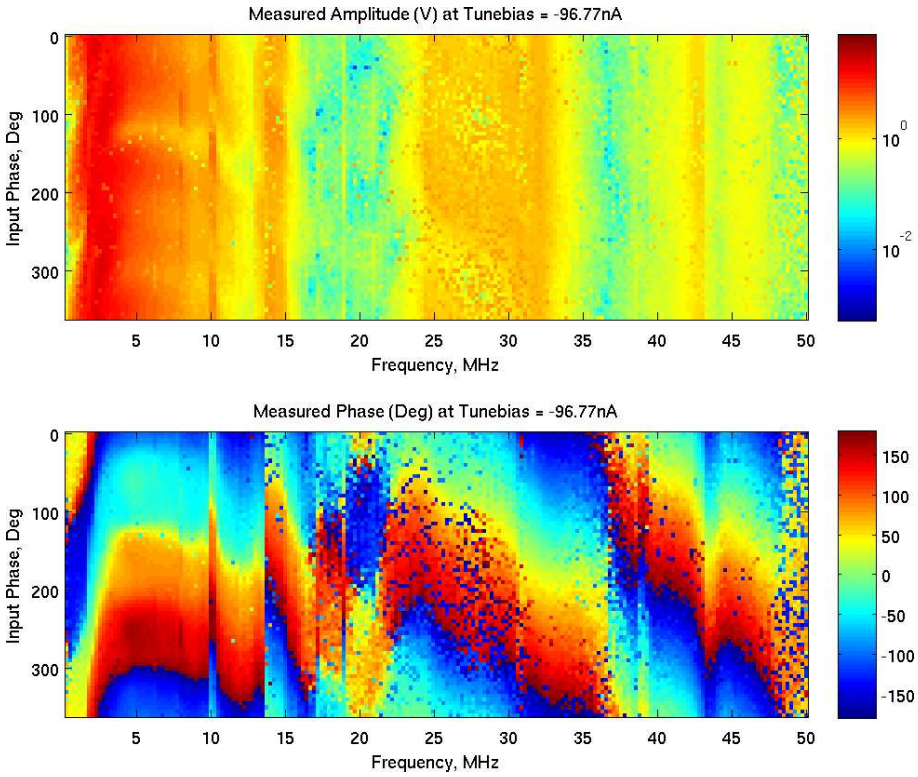

Figure 5.42: LIDAR1 amplitude and phase response. Tunebias ≈ 95 nA.

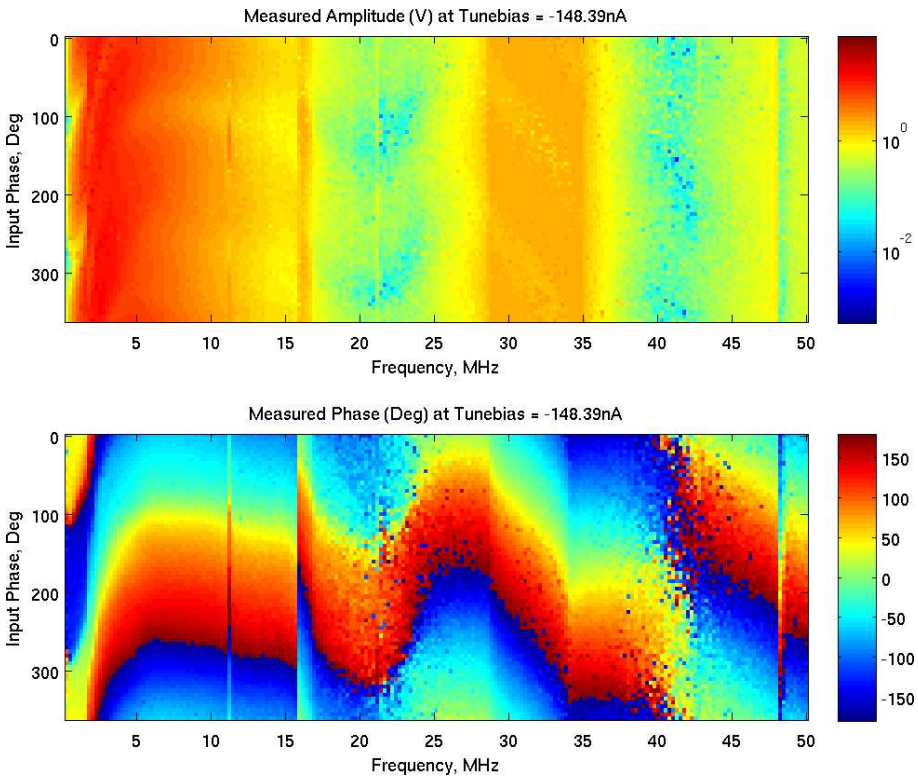

Figure 5.43: LIDAR1 amplitude and phase response. Tunebias ≈ 149 nA.

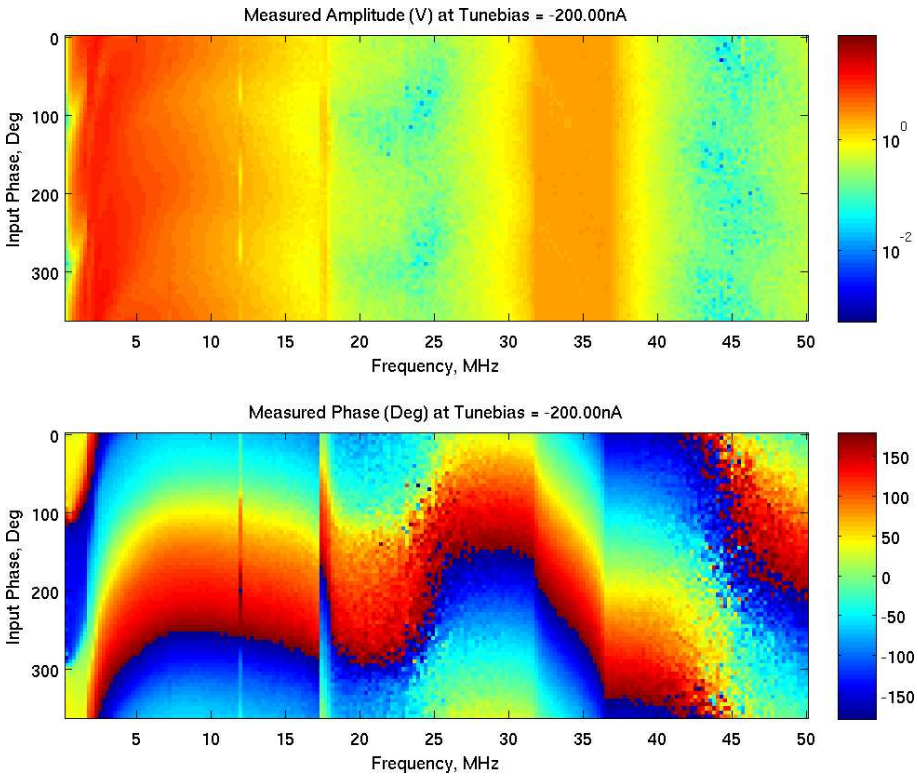

Figure 5.44: LIDAR1 amplitude and phase response. Tunebias $\approx 200\,\mathrm{nA}$.

5.4.1.2 Discussion

It is observed in Figure 5.39 that the bandwidth increases with increasing tunebias. It is also observed that there appears to be a trough in the amplitude response at about 10 MHz. This was rigorously investigated after the experiment and was shown to be caused by parasitic elements from the layout of the pixel. During the design, the pixel was laid out in blocks to reduce the computational demands of simulating the contribution of parasitics. The trough did not show in AC and PSS simulations used to simulate the whole pixel pre-fabrication. Using very long post-layout transient simulations which require significantly more computation resources and time identified the problem. This simulated response is shown in Figure 5.45.

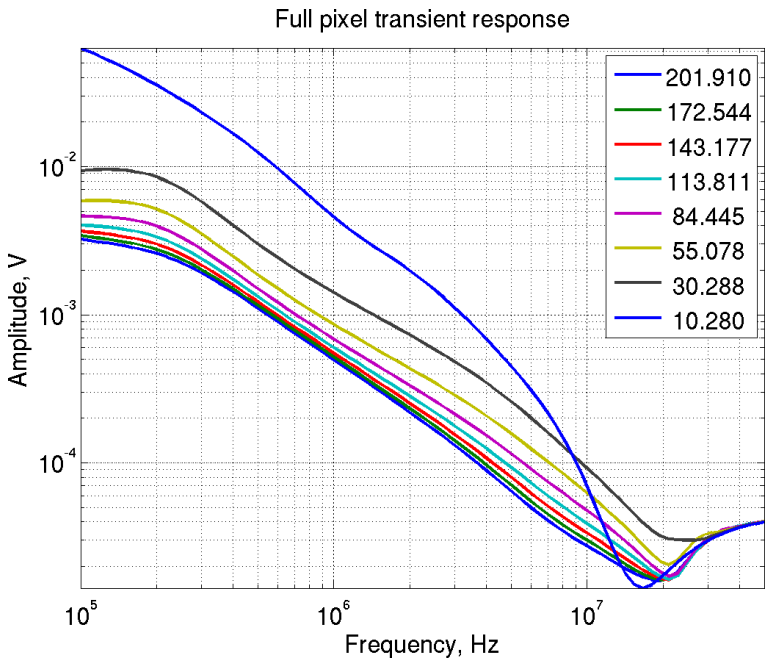

Figure 5.45: LIDAR1 amplitude response using transient simulation to probe source of trough observed at 10 MHz in Figure 5.38

The phase response is also observed to improve with tunebias. It is also flattening, as expected. The jumps in the phase response that are observed along the frequency axes are due to a glitch that caused the phase determination algorithm to incorrectly determine the zero phase.

The error in the phase response is investigated next. From this set of results (θ, I_T, f_{mod}) shown in Figure 5.40 to Figure 5.44, sections can be taken to look at the phase response in more detail. The error is determined by subtracting the expected phase from the measured phase. Where the signal is too low, the arctan function returns a value close to 0 or 180°. The error in the measured phase is shown in Figure 5.46 to Figure 5.48 for various values of tunebias. Each figure shows the phase response and the correspondence at a specific frequency.

It is also observed that there is significant wiggle in the response at low frequencies. This wiggle is due to poor reference signal quadrature split creating an elliptical response in the polar plot, as discussed earlier in section 5.4.1. The phase splitter used in this experiment was actually designed to operate from 8 to 80MHz, hence the poor performance at this frequency. When the signal generator was used to improve on the response, it also showed significant difference in the amplitude of the I and Q signals, as shown in Figure 5.35. This error can however be calibrated for, since it is repeatable at any chosen frequency.

The variation in the phase error with frequency is shown Figure 5.49. Subfigure 5.49a shows the data for the whole frequency range, and Subfigure 5.49b shows the higher tunebias data. The lower frequencies (under 2 MHz) in Subfigure 5.49a show a high error but this is due to the wiggle as observed earlier.

Figure 5.49b shows that a phase error of 8° can be expected at 15 MHz with tunebias on. This experiment was performed with 10 samples average to get one phase measurement and 5 nW of light modulated to a depth of 50%.

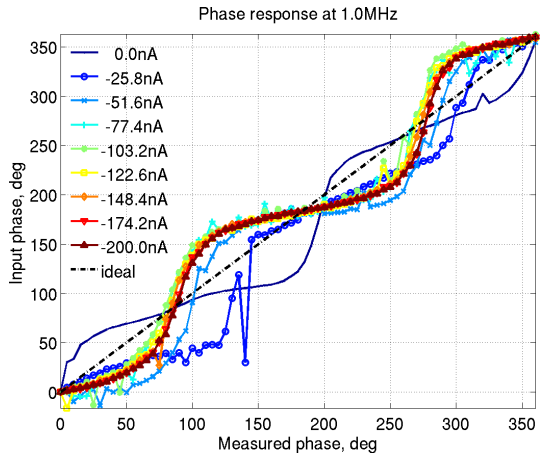

(a) Phase response at 1 MHz

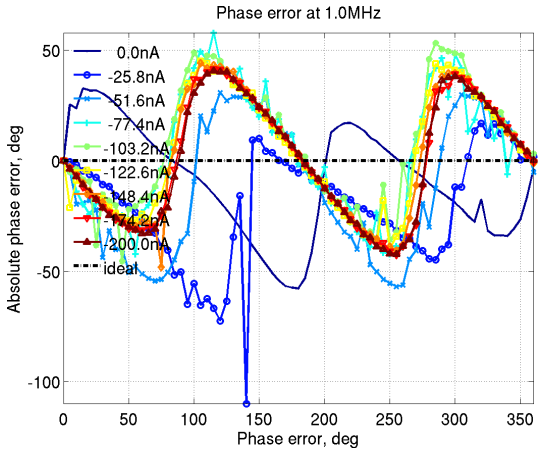

(b) Phase error at 1 MHz

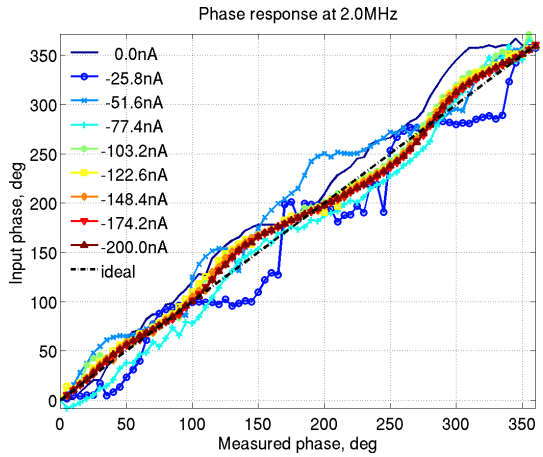

(c) Phase response at 2 MHz

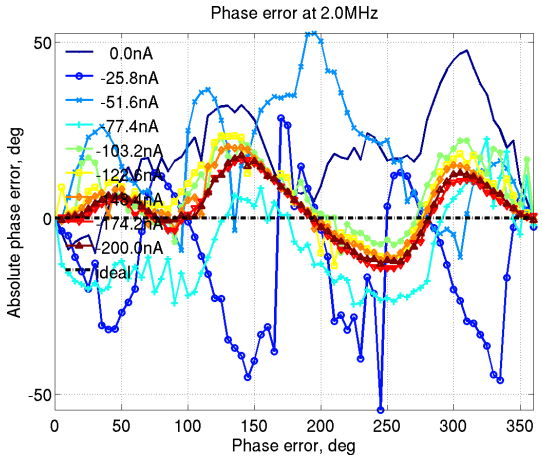

(d) Phase error at 2 MHz

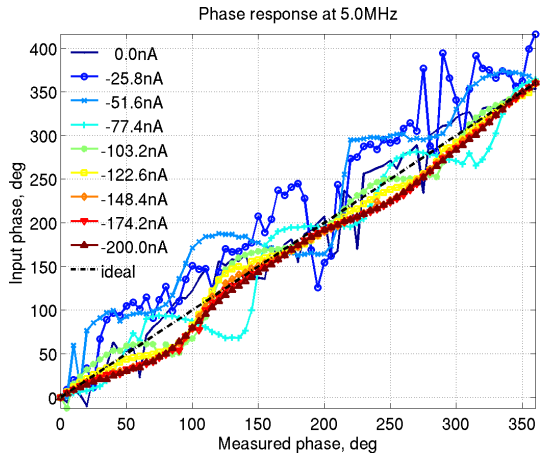

(e) Phase response at 5 MHz

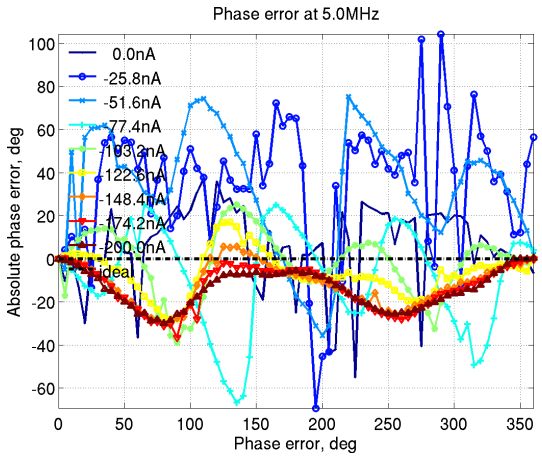

(f) Phase error at 5 MHz

Figure 5.46: LIDAR1 phase response and error at 1, 2 and 5 MHz for various values of tunebias.

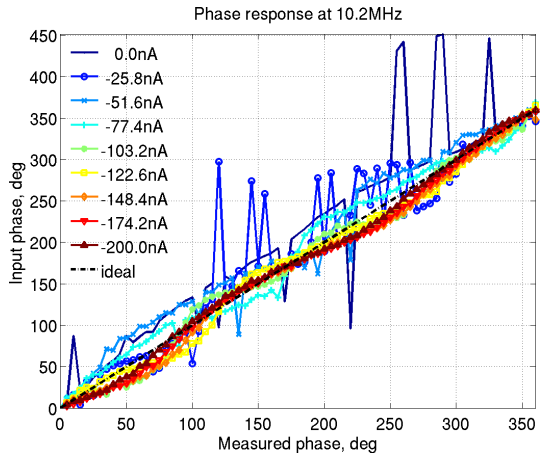

(a) Phase response at 10.2 MHz

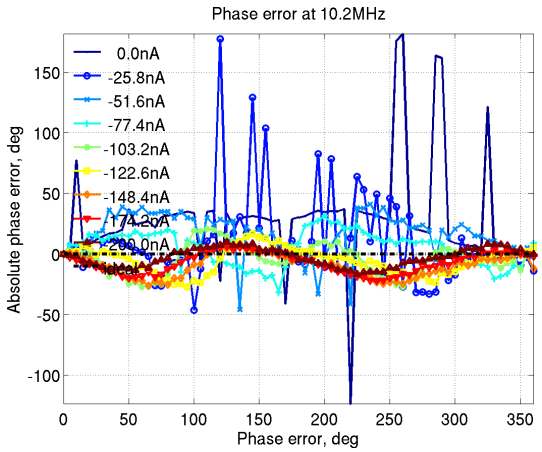

(b) Phase error at 10.2 MHz

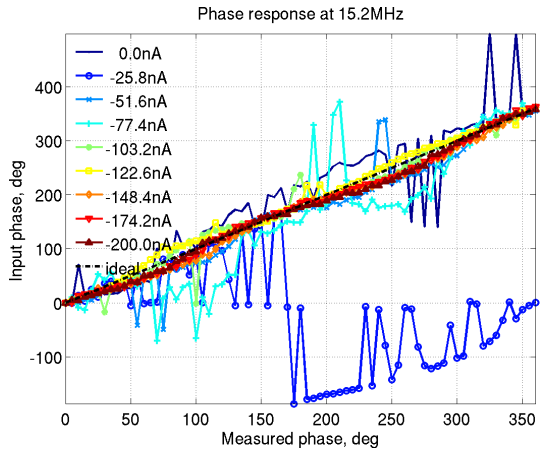

(c) Phase response at 15.2 MHz

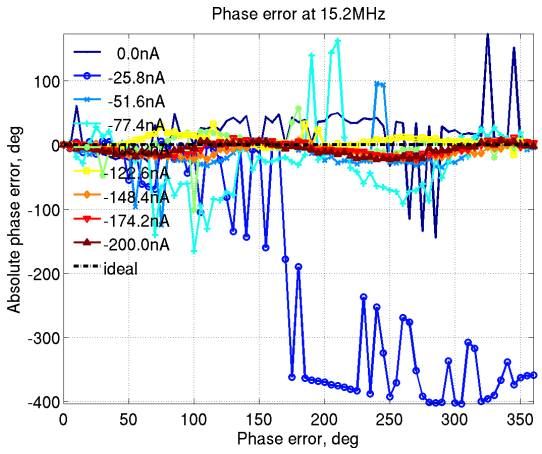

(d) Phase error at 15.2 MHz

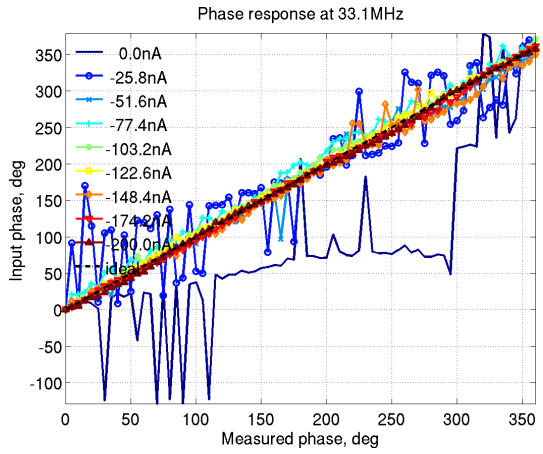

(e) Phase response at 33.1 MHz

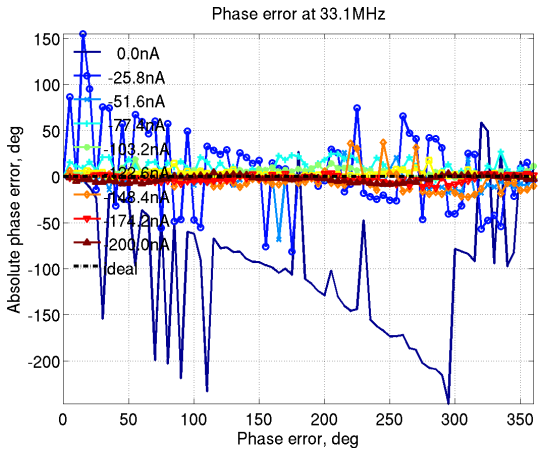

(f) Phase error at 33.1 MHz

Figure 5.47: LIDAR1 phase response and error at 10.2, 15.2 and 33.1 MHz for various values of tunebias.

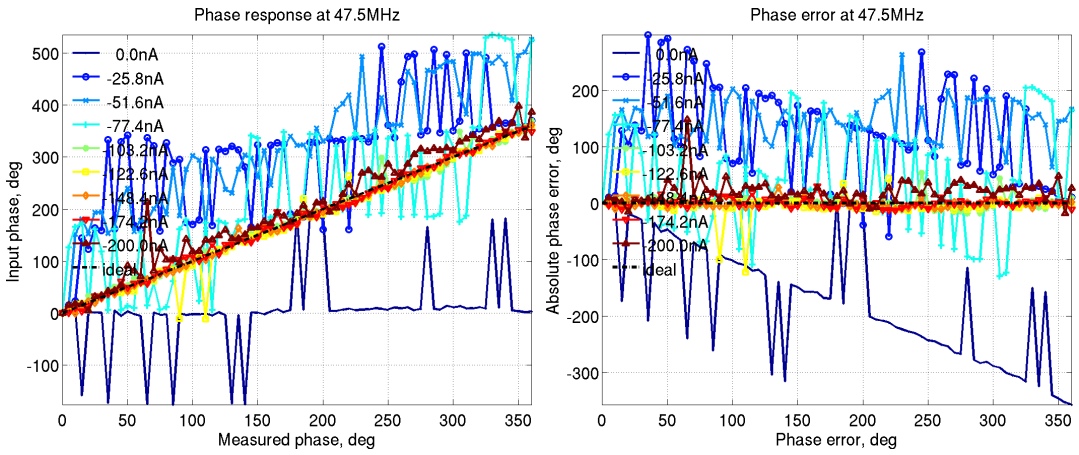

(a) Phase response at 47.5 MHz **(b)** Phase error at 47.5 MHz

Figure 5.48: LIDAR1 phase response and error at 47.5 MHz for various values of tunebias.

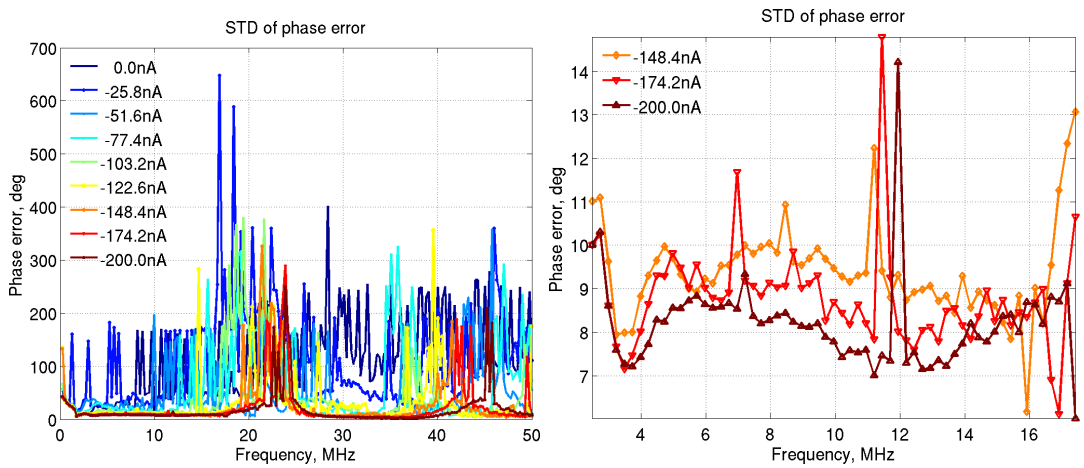

(a) Phase error with frequency **(b)** Phase error with frequency (subset)

Figure 5.49: Phase error for LIDAR1, for various values of tunebias. Subfigure 5.49b shows a subset of the same data in more detail.

5.4.1.3 SNR and phase error

It is important to note that the phase error is very closely tied to the signal present. The noise floor is approximately 200 pA, and since in section 5.4.1.2 there is approximately 2.5 nA of modulation signal per pixel, this is equivalent to an SNR of 12.5 (21.9 dB).

In this experiment 10 samples are taken per phase measurement and averaged, thus increasing the SNR to $12.5 \times \sqrt{10} = 39.5$. Thus using $\frac{360°}{39.5} = 9.1°$ the phase error of approximately 8 degrees is to be expected at this signal level.

5.4.2 Multiple pixel phase response

An experiment was also performed to determine the response of several pixels simultaneously. The light per pixel is approximately 50 nW DC background (40% modulation depth). The modulation frequency is 1 MHz, and tunebias is 100 nA.

The results shown in figure 5.50a show the response of a subset of the array when the phase is measured. The error in the measured phase is shown in figure 5.50b.

The typical phase error measured from Figure 5.50 was calculated to be 5 degrees.

5.4.3 Widefield Images

As shown in Figure 5.51, the image of a crosshair was obtained by shining light from a laser through a crosshair (which had been cut into a piece of card) onto the camera. The light per illuminated pixel is estimated to be 10 nW modulated at 10 MHz to a depth of 50%. The crosshair was inclined at an angle to spot any errors due to any addressing fault which would display a symmetric image correctly. It also provided a template upon which to physically orient the camera

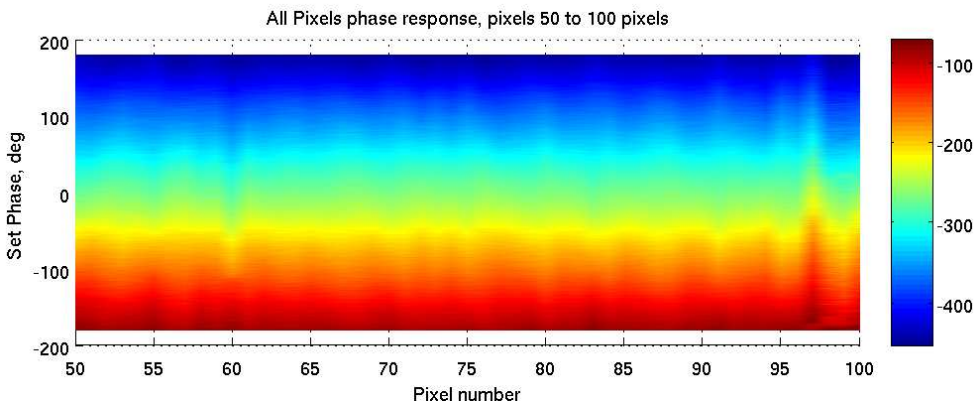

(a) Phase response

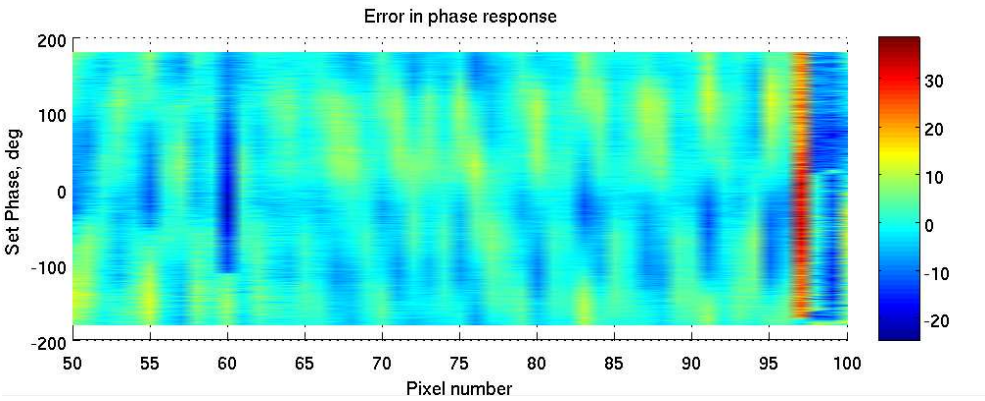

(b) Phase error

Figure 5.50: Phase response for a subset of the pixel array, showing 100 results pixels from 4 adjacent rows of 32 pixels. The error in the measurement is also shown in the lower subfigure.

correctly.

Figure 5.52 shows a DC image captured using LIDAR1. This is a picture of a hand. Illumination is from room lighting.

5.4.4 Output filter response

The response of the filter is important in determining the noise of the pixel, as it sets the selectivity of the system and affects the noise equivalent bandwidth. A single pixel is observed with the modulation set to 10 MHz. A difference is introduced (incremented in 100 Hz steps) between the modulation frequencies of the light source and the local oscillator. This creates a beat frequency, and the

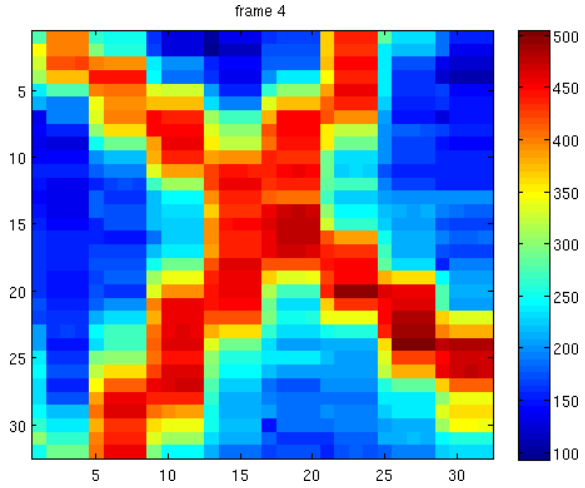

Figure 5.51: IQ Amplitude image obtained at 10MHz with LIDAR1 with 100 nA Tunebias. The units are arbitrary.

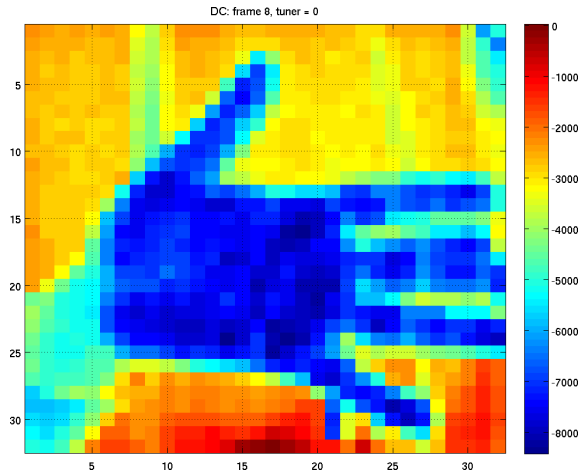

Figure 5.52: DC image obtained with LIDAR1. Tunebias = 0 nA. Room illumination only, at a rate of 30 fps. The units are arbitrary.

amplitude of this beat signal is observed on the IQ outputs. The analysis shows that the bandwidth is 2 kHz with bias resistance of 300 kΩ (bias current of 500 fA), which compares perfectly with the simulation results. The response is shown in Figure 5.53.

5.4.4.1 Dark Noise and Fixed Pattern Noise

The acquisition system uses an NI PCI ADC with a noise of 15 μV with an input range of 200 mV. It has a slew rate of 20 V/μs. These parameters are better than

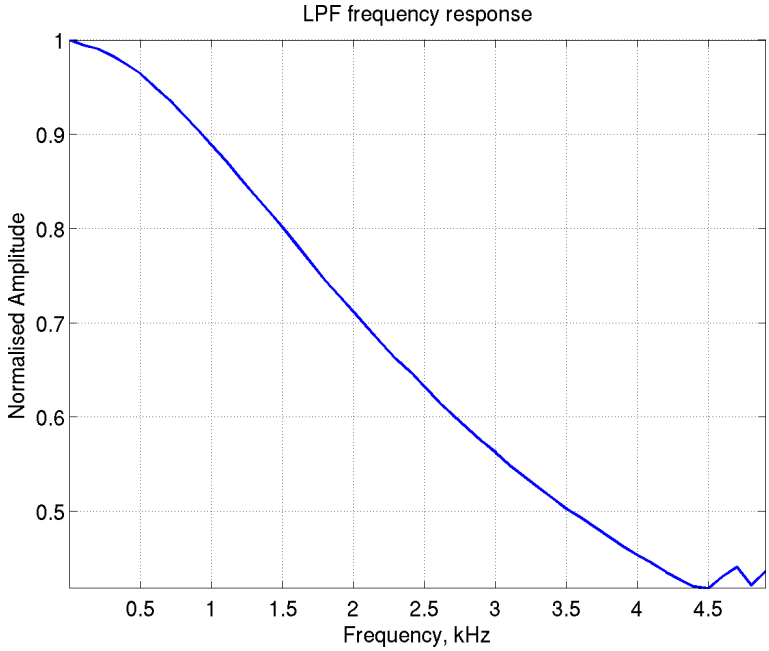

Figure 5.53: Experimental results shown the response of the low pass filter. Performed at 10 MHz with 500 pA bias current to filter.

noise of the MLC, so they are not included in the analysis.

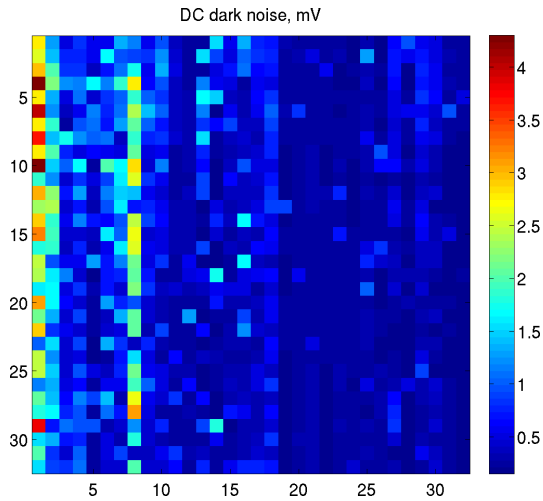

Figure 5.54: LIDAR1 dark noise. The units are mV.

The dark noise image is shown in Figure 5.54. It shows that in the absence of light, the variation at the outputs is approximately 280 μV from pixel to pixel across the whole array. This compares quite closely with the simulation results. Figure 5.55 shows the fixed pattern noise in the DC image. This shows a standard variation of approximately 2 mV, which also compares closely with simulation results. It is

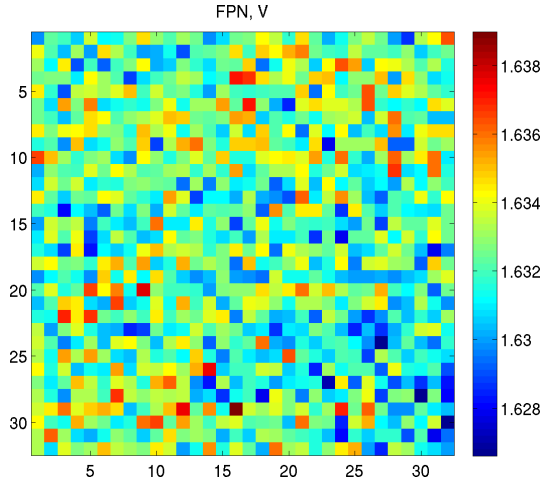

Figure 5.55: LIDAR1 fpn image. Acquired in the absence of light. The units are mV.

important to remember that an FPN image must be taken to determine the DC offsets of the camera before the actual image in all experiments.

5.5 Phase/DC light Dependence

A primary objective of this project was to reduce the relationship between the DC light and the phase response. As discussed in section 3.7.3, the logarithmic pixel suffers from varying phase response with DC light. This complicates accurate phase measurement especially in the widefield, but the innovative use of the tuning current linearises the response and provides a common operating point for the determination of the phase of the received light.

An experiment to measure how tunebias mitigates the Phase-DC light correlation was performed. The experiment is performed at 10 MHz with 10 nW of light modulated to a depth of 50%. A 635 nm LED used to provide the DC light and this is increased from 0 (off) to the equivalent of 5 μW per pixel, and tunebias from 0 to 100 nA. The phase was measured with increasing DC light. Figure 5.56 shows the results.

The dependance of the measured phase on DC light conditions can be immediately seen. The gradient of each line (Δ indicates phase change in degrees per μW of light per pixel) is provided. It is observed that higher values of tunebias give a lower gradient, confirming that tunebias reduces the dependence of the phase measurement on the DC light conditions, as expected.

The standard deviation from the line of fit is also provided as (δ in degrees per μW of light per pixel) and shows that using higher values of tunebias gives more accurate results.

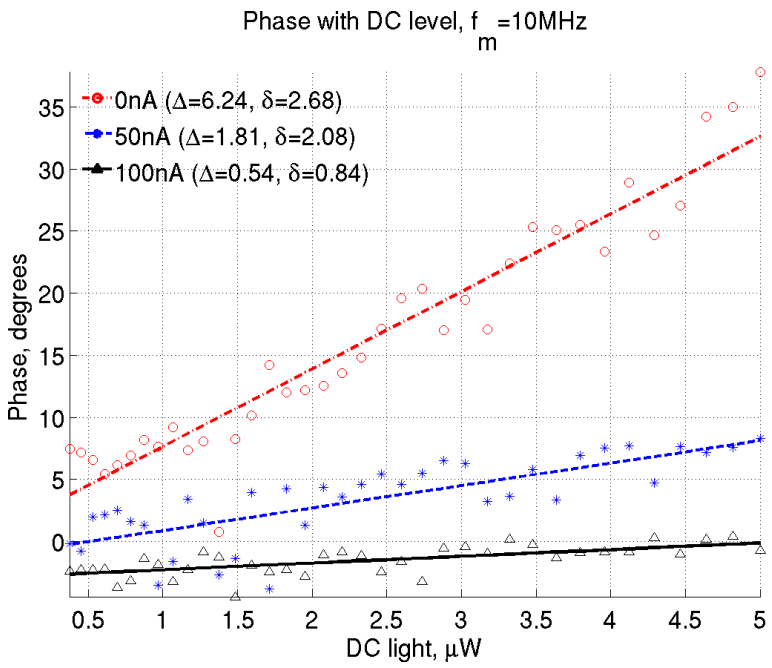

Figure 5.56: LIDAR1 Phase/DC light dependence. The figure shows the phase response at fixed input phase for various light levels and tuning currents is shown. The gradient of each characteristic gives the phase change with light in $^\circ/\mu$W.

The experiment is analogous to varying the modulation depth from 50%(LED off) to 0.1% (5 μW from the LED).

5.6 Conclusion

This chapter has introduced LIDAR1, a camera that was designed to implement the thesis presented in section 3.5. It shows the simulation results for the different parts of the pixel. The whole camera is described in detail.

The camera is characterised. Some major challenges that were experienced in the characterisation process are briefly discussed and methods for circumventing or correcting them presented. Experiment results that show the amplitude and phase response are then presented, showing that the agree with the theory.

Some images that are acquired with the camera are then presented, showing that it is capable of detecting intensity (DC), as well as modulated light (AC) images. The noise response is also discussed.

The next chapter presents a few experiments performed to test the camera in some applications which motivated its design.

6 | Applications

In this chapter, some results from applications of LIDAR1 are presented. A discussion is then presented of future possible applications.

6.1 Widefield Time of Flight Imaging

Following the characterisation of LIDAR1, some experiments were carried out to apply it as an imaging LIDAR camera. This experiment uses the ability of the camera to measure phase to determine the time-of-flight of light from a source synchronised with the camera via its local reference oscillators.

6.1.1 Experiment Setup

A schematic showing the configuration is shown in Figure 6.1.

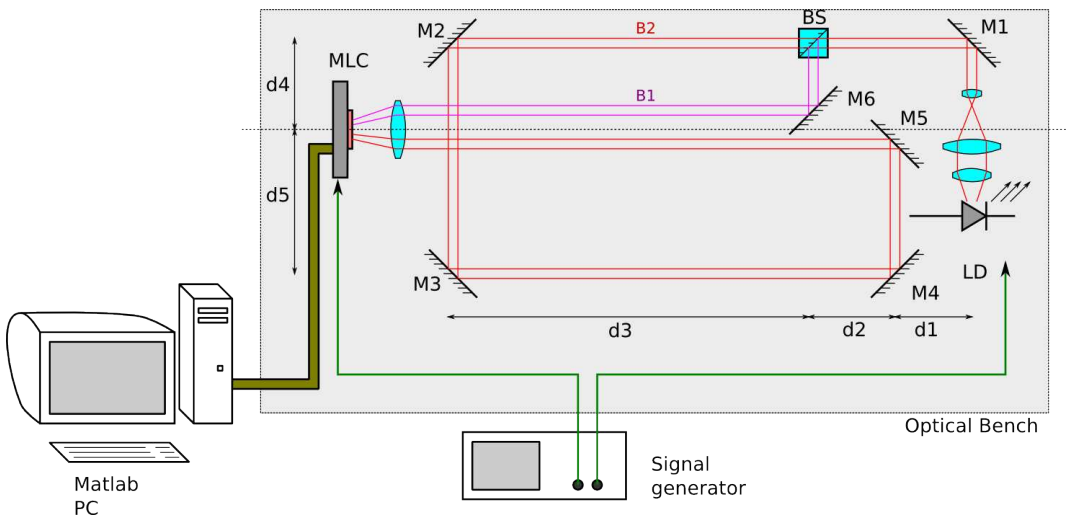

Figure 6.1: Experimental setup for imaging lidar experiment.

The modulated light camera is configured to work at $f_m = 20$ MHz. The gives a modulation wavelength $\lambda_m = c/f_m = 15$ m. A 625 nm 5 mW diode laser is used

to illuminate the scene. A lens arrangement is used to collimate the beam and a beam splitter arrangement is used to split the beam into two beams, B_1 and B_2. Measuring from M1, these two beams (B_1 is in purple and B_2 is in red) travel the lengths in Equation 6.1. The phase difference is determined by the optical path difference between the two beams, B_2 - B_1.

$$\begin{aligned} B_1 &\approx d_1 + d_2 + d_3 + d_4 \\ B_2 &\approx d_1 + d_2 + d_3 + d_4 + d_5 + d_3 + d_2 + d_5 + d_2 + d_3 \\ B_2 - B_1 &= d_5 + d_3 + d_2 + d_5 + d_2 + d_3 \\ &= 2(d_2 + d_3 + d_5) + d_4 \end{aligned} \tag{6.1}$$

The phase difference in degrees between the beams is given by

$$\phi = \frac{B_2 - B_1}{\lambda_m} \times 360 \tag{6.2}$$

where λ_m is the wavelength of the modulation. Since the light does not travel from light source to scene and back, it is not necessary to use $\frac{\Phi}{360}\Phi = \frac{\lambda_m}{2D}$. The measured lengths are d_1 = 20 cm, d_2 = 20 cm, d_3 = 100 cm, d_4 = 30 cm and d_5 = 50 cm. Using Equation 6.1, this gives an optical path length of approximately 3.4 m.

6.1.2 Results and Discussion

Figure 6.2 shows the results of the experiment. The DC image is taken with tunebias of 0 nA, measured in mV. Tunebias is then set to sink 100 nA. The amplitude and phase are measured using the I and Q data.

A threshold map is required because the noise on the I and Q data creates an image with a lot of random phase wherever there is low or noisy IQ voltage.

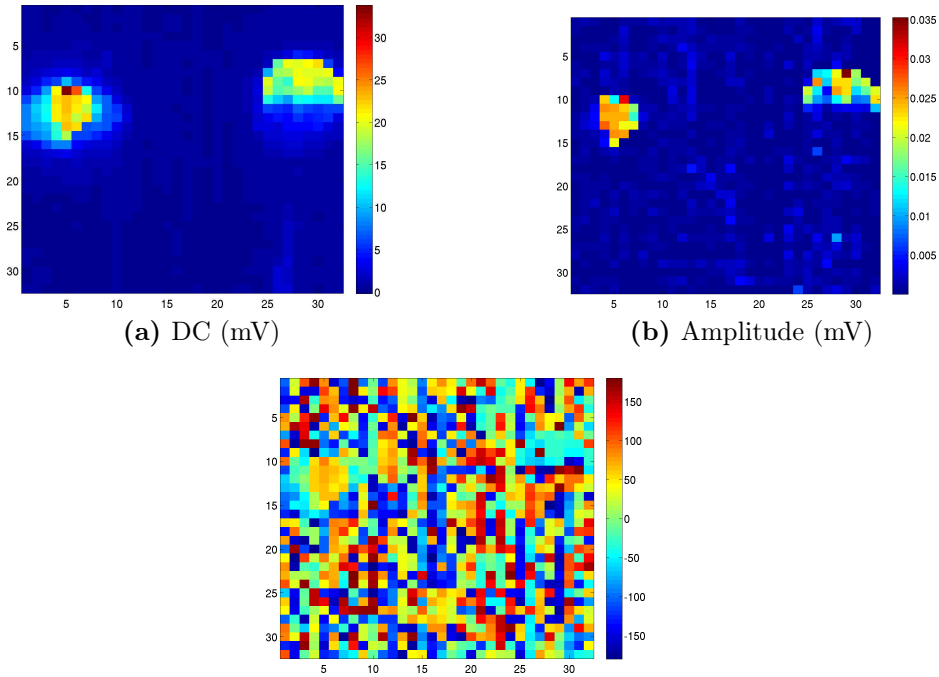

(a) DC (mV)

(b) Amplitude (mV)

(c) Phase (degrees)

Figure 6.2: LIDAR1 LIDAR experiment results. The DC image, as well as the amplitude and phase images

.

This is seen in Figure 6.2c. Therefore, the IQ amplitude is used to create a threshold map. The Matlab routine **graythresh** is used to determine a global image threshold using Otsu's method [49], and a binary intensity image created using **im2bw**. This binary map is shown in Figure 6.3a. After multiplying the phase image by this map, the areas with low (or no) IQ signal levels are mapped to a phase of -181 degrees (arbitrarily chosen).

It is observed in Figure 6.3b that there are two spots with phase of approximately 50 and -30 (or 290) degrees, a difference of 80 degrees. Using Equation 6.2 this equivalent to a path length difference (B2 - B1) of 3.4 m, as expected. Figure 6.3c shows the range image with the left spot (in yellow), offset to 0 m. The right spot is thus measured relative to the left spot and shows the correct distance. The colorbar corresponds to the entire measureable distance.

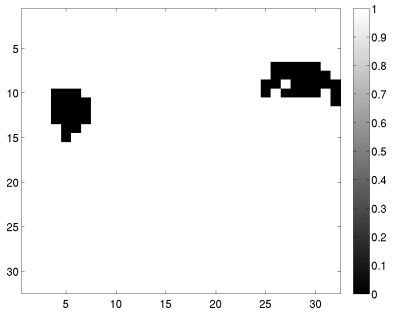

(a) Threshold map

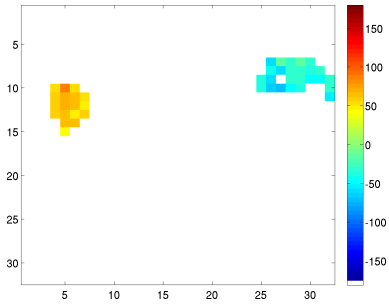

(b) Phase (degrees) - thresholded

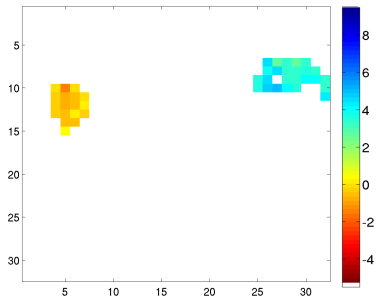

(c) Distance (m) - thresholded

Figure 6.3: Experimental results for the imaging LIDAR experiment. The phase image has the threshold applied to remove random noise values. The distance image is also shown.

6.2 Heterodyne Interferometry

Interferometry refers to the practice of interfering (combining or separating) a number of beams of coherent electromagnetic waves and the analysis of the produced pattern. It is an application of the principle of superposition to electromagnetic radiation, and the observed response is used as a diagnostic of the original state of the waves or of the path (length and refractive index) through which they travel from source to detector. The observed result is often a pattern referred to as a fringe. Figure 6.4 shows a basic schematic of a simple Michelson Interferometer, which is an example of an interferometer.

Homodyne interferometry refers to the practice of interfering two beams which have the same wavelength. This technique is the most common type of interferometry, and is found in interferometers such as the Michelson interferometer. A

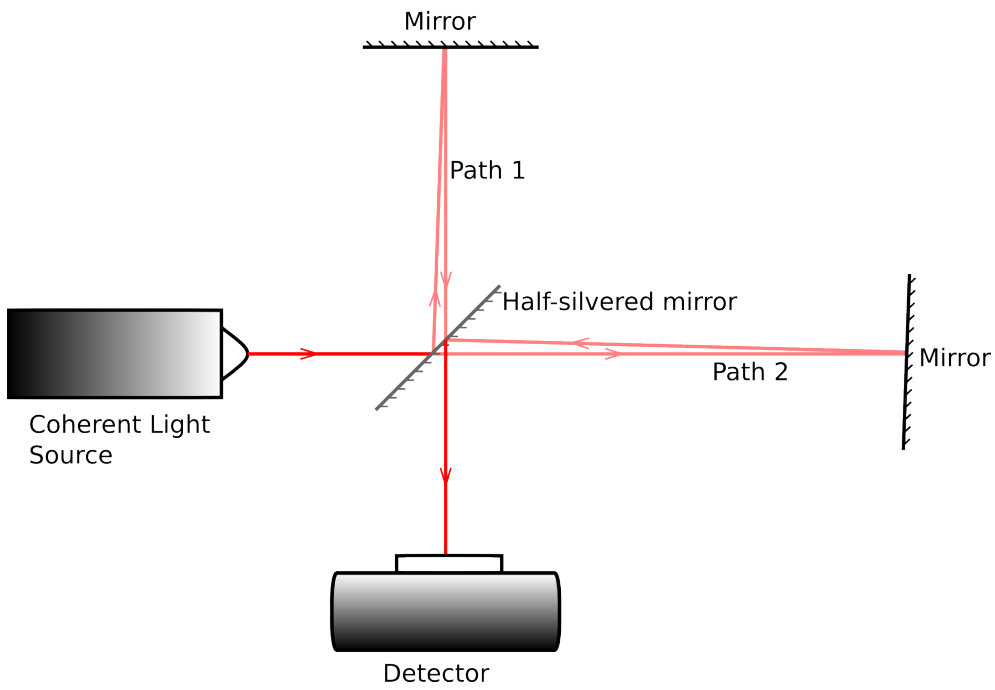

Figure 6.4: A schematic of a Michelson Interferometer.

schematic is shown in Figure 6.4. The interferometer creates interference patterns with intensity that are time-invariant, but depend on the spatial relationship of the two light beams. This factor is often referred to as the optical path length difference. Homodyne interferometry is however prone to noise, including background light, electrical noise and mechanical vibrations. This is particularly important when the noise sources exhibit a time varying nature much faster than the response of the detector used to observe the fringes.

Because the fringes are time-invariant intensity spatial patterns, a single detector can be used to scan the image. Alternatively, it is possible to use most non-specialised cameras (such as a webcam) to detect the DC image.

Heterodyne interferometry uses beams with different wavelengths. Similar to the mixing process discussed in Chapter 3, by introducing an optical frequency difference between the two beams in each arm of the interferometer (or using lasers with slightly different wavelengths), a beat frequency is synthesised when the two beams recombine at the detector. As with the lock-in demodulation

technique, two frequencies are synthesised: the sum and the difference of the optical frequencies of the beams.

If $E_R(x, y, t)$ and $E_I(x, y, t)$ are the real parts of the two interfering waves, which are a function of 2-dimensional space and time given by

$$\begin{aligned} E_R(x, y, t) &= a_r(x, y)\cos(2\pi f_r t + \phi_r(x, y)) \\ E_I(x, y, t) &= a_i(x, y)\cos(2\pi f_i t + \phi_i(x, y)) \end{aligned} \tag{6.3}$$

with f refers to the frequency, t is time, x and y are spatial coordinates, and ϕ is the phase difference between the two beams. a is the amplitude at any point (x, y). Using the substitution $\omega = 2\pi f$, the intensity image $I(x, y, t)$ at the point of detection may be written as

$$\begin{aligned} I(x, y, t) &= [E_R(x, y, t) + E_I(x, y, t)]^2 \\ &= \frac{1}{2}a_r(x, y)^2 + \frac{1}{2}a_i(x, y)^2 \\ &\quad + \frac{1}{2}(x, y)^2\cos(2\omega_r t + 2\phi_r(x, y)) \\ &\quad + \frac{1}{2}(x, y)^2\cos(2\omega_i t + 2\phi_i(x, y)) \\ &\quad + a_r(x, y)a_i(x, y)\cos((w_r + w_i)t + (\phi_r(x, y) + \phi_i(x, y))) \\ &\quad + a_r(x, y)a_i(x, y)\cos((w_r - w_i)t + (\phi_r(x, y) + \phi_i(x, y))) \end{aligned} \tag{6.4}$$

The first two terms of Equation 6.4 give the time-invariant or DC component, which may be written as $I_{DC}(x, y) = \frac{1}{2}(a_r(x, y)^2 + a_i(x, y)^2)$.

The remainder is the AC component is signified by I_{AC}. The detector is not capable of detecting the ω_r, ω_i and $\omega_r + w_i$ components, therefore only the term containing $\omega_r - \omega_i$ and DC terms are detected. This may be written as $I_{AC\star}$ (the modulated intensity term has frequency $f_r - f_i$). Writing $\omega_d = 2\pi(f_r - f_i)$, $\phi_d = \phi_r - \phi_i$ and $A(x, y) = a_r(x, y)a_i(x, y)$, the detected intensity may be written

as

$$I(x,y,t) = I_{DC}(x,y) + A(x,y)\cos(\omega_d(x,y)t + \phi_d(x,y)) \quad (6.5)$$

$$= I_{DC}(x,y) + I_{AC*} \quad (6.6)$$

I_{DC} is the normal intensity image seen by the human eye, and I_{AC*} is the modulation component that is detected by the MLC. The phase component ϕ_d depends on the optical path length, and remains constant as long as there is no relative motion between the arms of the interferometer. The phase changes by 2π for every difference of a wavelength (λ). The introduction of a medium with a different refractive index also changes the optical path length. Further information may be found in [50, 51].

Each pixel of the MLC detects I(x,y,t), i.e. I_{DC} and I_{AC*}. The DC component is made available as a DC intensity image by the DC outputs of the camera. More interesting is the AC component, which after conversion to an AC electrical signal $V_{AC} = k^{\cdot}A(x,y)\cos(\omega_d(x,y)t + \phi_d(x,y))$, is demodulated in-pixel, and low pass filtered. The demodulation occurs by mixing with a reference oscillator with the same frequency ω_d.

To give an example of the numbers involved, starting with a laser with a wavelength of 625 nm (red diode laser) and a Bragg cell with a shift of 10 MHz, the frequency of the light may be calculated from $c = f\lambda$ as $f = \frac{299.7\ \mathrm{MmS}^{-1}}{625\ \mathrm{nm}}$ =479.67 THz and 479.67 THz+10 MHz. After the frequency shift, the intensity image contains components that are amplitude modulated at frequencies at 10 MHz, approximately 479.67 THz and 959.34 THz. The high frequency component is not detected, but the MLC is able to simultaneously detect the DC component and the 10 MHz component. The 10 MHz frequency signal is still available via the RF outputs of the two pixels in the centre of the camera.

6.2.1 Experiment Setup

The interferometer setup used in this experiment is based on a Mach-Zehnder interferometer. Normally, a single beam is split up using a beam splitter (equivalent to a half silvered mirror). In this setup, however, one arm of the interferometer passes though an Acousto Optic Frequency Shifter (AOFS) (also referred to as an Acoustic Frequency Modulator or Bragg Cell). This cell uses the acousto-optic effect of a piezo-electric transducer to diffract and shift the frequency of light using ultrasonic waves. A Bragg Cell is shown in Figure 6.5. For further information about this device, see [52].

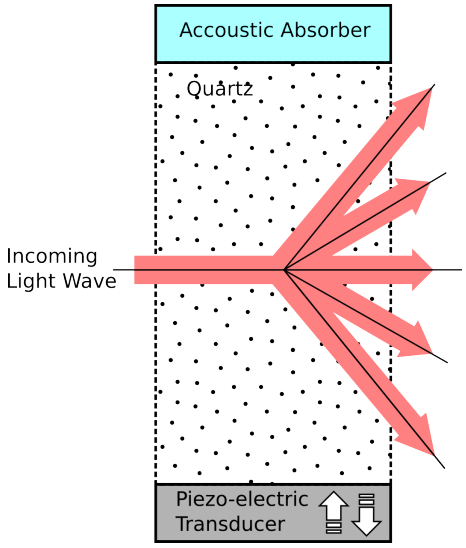

Figure 6.5: An Acousto-Optical Frequency Shifter (Bragg Cell)

The Bragg cell is configured to shift the frequency of the incoming light by 15 MHz. This light interferes with the main beam and is then demodulated by the MLC.

6.2.2 Results and Discussion

Figure 6.7 shows an interference fringe obtained from the experiment setup in Figure 6.6. Tunebias is set at a value of 100 nA, and this image captures the phase information captured in the modulation content. The image is captured at

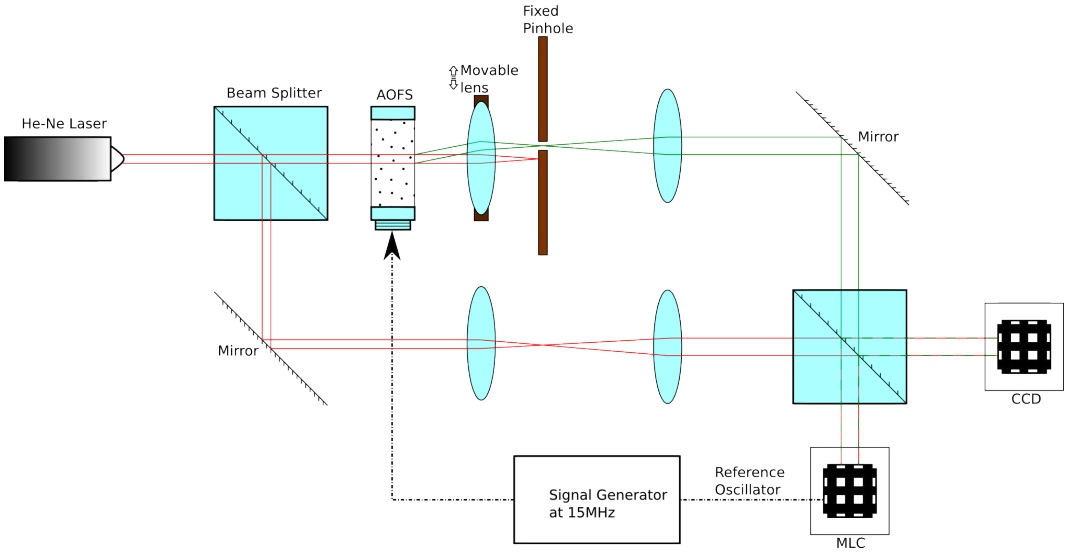

Figure 6.6: The experimental setup used in the heterodyne interferometry experiment

15 MHz with approximately 90 nW of light per pixel.

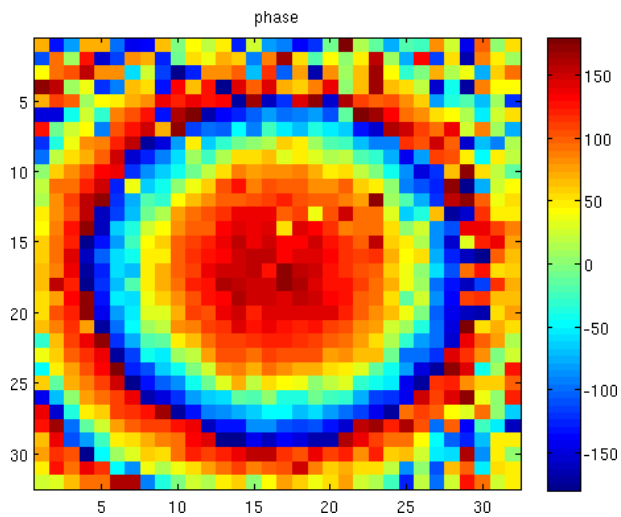

Figure 6.7: Heterodyne Interferometer phase image formed by interfering a uniform wave with a spherical wave producing a circular fringe pattern.

This system provides an improvement on previous systems, which report modulation frequencies from 10 to 25 kHz [53, 54]. For further information on this application, kindly refer to [55]. It also offers the prospect of even more stable detection, which is discussed in section 6.3.

6.3 Ultrastable Heterodyne Interferometry

Following the theory in section 6.2, it is possible to see that the time varying component I_{AC*} in Equation 6.4 still depends on the optical path length difference in the two beams. This difference can change due to temporal factors such as vibration. Normally, the modulated light is mixed with a local reference oscillator in the demodulation process, but by using a reference that is phase locked to the incoming light, it is possible to remove the temporal contribution to the measured phase.

To implement this, the high frequency output of one of the master pixels on the camera is connected to the local oscillator input. This means that any temporal disturbance to the phase affects both the incoming light and the local oscillator. That disturbance may thus be dismissed in the demodulation process, making this mode of operation very resistant to temporal noise from physical sources. This mode of self-demodulating the modulated light is referred to as Ultrastable Heterodyne interferometry.

6.3.1 Experimental Setup

A modified Mach-Zehnder interferometer is used for this experiment. It uses a fixed pinhole and a movable lens, making it possible to switch between homodyne and heterodyne modes. An audio speaker is attached to a mirror, and the vibration of this mirror is determined by a vibrometer.

The modulated light camera detects the modulated light, providing the IQ signals, and also the high frequency component. The high frequency component from one of the two RF outputs of the master pixel (section 5.2.2) is fed back as a reference oscillator. Any optical path length variation is common to both reference and

incoming light, which makes this highly immune to mechanical vibration.

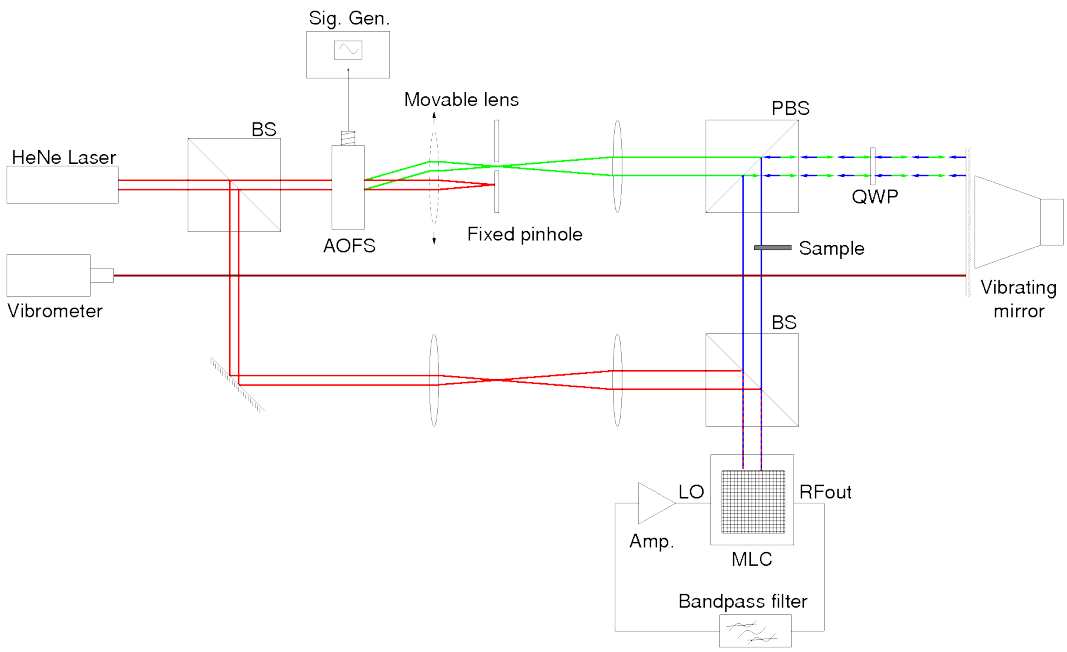

Figure 6.8: Experimental Setup for Ultrastable Heterodyne Interferometry experiment, showing modulated light camera, Signal Generator

6.3.2 Results and Discussion

The speaker in Figure 6.8 is configured to run at 1 and 62 Hz. This vibration causes a phase modulation in the fringe pattern observed. It is observed that the maximum measured vibration velocity in this setup is 85 mm/s (limited by mirror vibration). A standard interferometer may be able to work with 100 nm of displacement, but this system can tolerate displacements of 0.218 mm.

Figure 6.9 shows the vibration velocity measured by the vibrometer for various frequencies of vibration of the mirror mount.

Figure 6.10 shows the interferograms obtained when the experiment is configured to run using a signal generator as a reference (standard heterodyne interferometry). It can be observed that the obtained pattern is severely compromised by

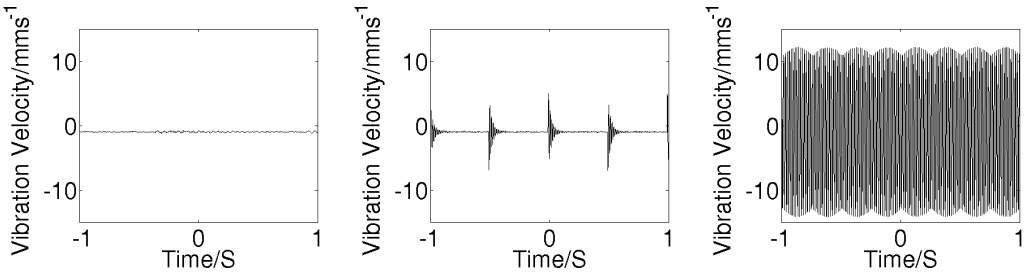

(a) No vibration **(b)** 1 Hz vibration **(c)** 62 Hz vibration

Figure 6.9: Mirror mount vibration velocity for various vibration frequencies

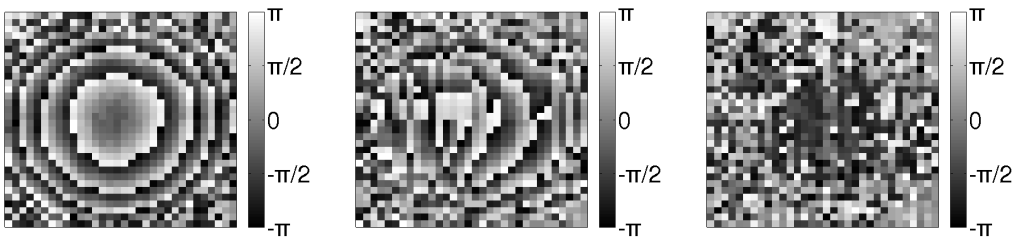

(a) No vibration **(b)** 1 Hz vibration **(c)** 62 Hz vibration

Figure 6.10: Standard heterodyne interferometry fringe for various mirror mount vibration frequencies

even the 1 Hz vibration, which has only a vibration velocity of 2 mm/s. At 62 Hz, the fringe pattern is almost completely obliterated.

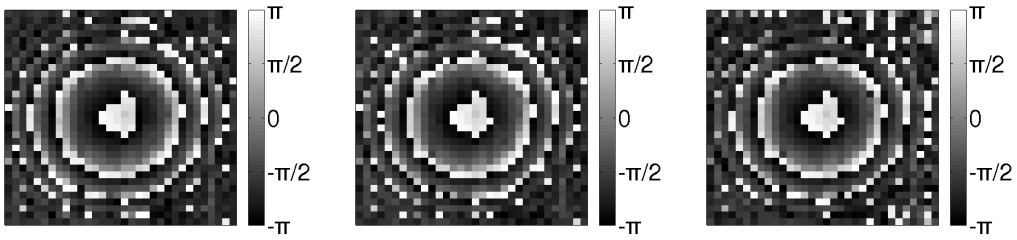

(a) No vibration **(b)** 1 Hz vibration **(c)** 62 Hz vibration

Figure 6.11: Ultrastable heterodyne interferogram images taken for various vibration frequencies.

The graphs shown in Figure 6.11 show the results of the ultra-stable experiment for various frequencies and levels of vibration. In this state, the RF output is used as reference, so that the system is self-referencing and phase shifts from the

varying optical lengths of the arms of the interferomter to do not contribute to the interferogram.

They show that the system is practically immune to most industrial environments not normally considered ideal for interferometers such as workshops, factories or operating theatres. For example, ISO2631 guidelines state maximum vibration amplitude should be 6.4 μm for an office [56]. The stabilisation offered by this setup allows makes it possible to use an interferometer quite easily in such an environment.

6.4 Practical Considerations

Having applied the camera under laboratory conditions, it is worthwhile to consider the practical usability of the camera for real life-applications.

As discussed in section 3.3, the phase accuracy is proportional to the signal to noise ratio. Since the noise is dominated by electronic noise in the pixels, it is therefore best to have as much modulated light as possible. This must be balanced with eye safety especially where lasers are used. It is also moderately challenging to design light sources which have high output power and low impedance so they can be modulated at high enough frequencies.

Consider the scenario shown in Figure 6.12. Assuming a point source co-axial with the camera and d metres away from the objects of interest in the scene. If the lenses are configured to image an area of interest A_{interest}, A_{beam} is the area illuminated by the beam from distance d, A_{array} is the area of the pixel array, and the area of interest has Lambertian reflection and an albedo (reflection coefficient) of 50% (at wavelength of illumination), the light received at the sensor P_{array} is

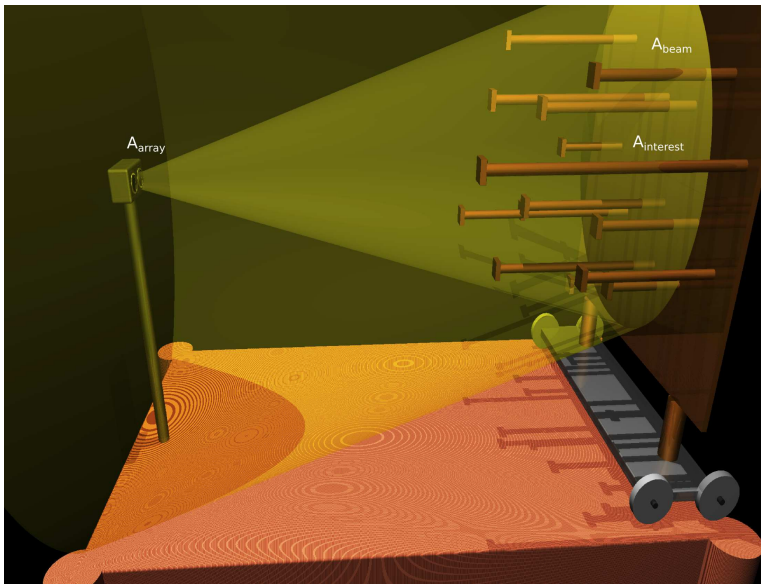

Figure 6.12: Imaging LIDAR practical scenario

$$P_{\text{array}} = \rho \cdot k_{loss} P_{\text{source}} \times \frac{A_{\text{interest}}}{A_{\text{beam}}} \times \frac{A_{\text{array}}}{A_{\text{reflected}}}$$
$$\therefore P_{\text{source}} = \frac{P_{\text{array}}}{\rho \cdot k_{loss}} \times \frac{A_{\text{beam}}}{A_{\text{interest}}} \times \frac{A_{\text{reflected}}}{A_{\text{array}}} \tag{6.7}$$

where P_{source} is the light power, k_{loss} is a unit-less measure of the transmission loss. The light source must be designed assuming that the objects to be ranged are at the maximum distance of $\lambda_m/2$. $\text{A}_{\text{reflected}}$ is thus half the surface of a sphere $= 2\pi(\lambda/2)^2$.

Working from Equation 6.7, the required optical power at the source may be calculated. For example, to obtain a distance resolution of 1 cm working at 30 MHz, this would require a phase error of 0.1%. A signal to noise ratio of 1000 is required. Since the rms noise floor at 30 MHz is approximately 0.2 nA, 200 nA of modulated photocurrent equivalent to 600 nW of light is required per pixel. Accounting for fill factor, this would require $P_{\text{array}} = 3.75\,\text{mW}$ over the array. Let the area of interest be 10 cm×10 cm, the illuminated area be 20 cm×20 cm, and the area of the optics be 2 cm×2 cm. If for the sake of simplicity, we ignore

transmission losses ($k_{loss} = 1$), the required optical power at the source can be calculated as

$$\begin{aligned} P_{\text{source}} &= \frac{3.75\,\text{mW}}{0.5}\frac{0.2^2}{0.1^2}\frac{2\pi \times 5^2}{0.02^2} \\ &= 3750\pi\,\text{W} \end{aligned}$$

which works out to approximately 11.7 kW of light. Averaging the frames and working at video rate (25fps instead of 1000fps) would greatly reduce the requirement by a factor of $\sqrt{40}$ which is approximately 1.86kW. Note this is a pessimistic scenario, especially with the use of lambertian surface.

With regards to heterodyne interferometry since this application uses a line of sight system, it is usually easy to provide enough light for a satisfactory SNR. It is also possible to enclose most of the system, making it eye-safe.

For imaging LIDAR use, there has to be a trade-off between maximum range and the range resolution (minimum distance), and this is directly related to the modulation frequency. At lower frequencies, a higher gain and range are available, but the resolution is quite poor. At higher frequencies, the reverse is true.

It is observed from section 5.4.1 that for general internal usage, a frequency of approximately 30 MHz is very attractive since it gives a good trade between the conversion gain, maximum range of 5 m and distance resolution for a given amount of light. The phase error is also relatively small as shown in subfigure 5.49b.

Since this design was to prove the concept, the 32×32 resolution is sufficient for lab experiments. Considering the LIDAR application, with this number of pixels, images in Figure 5.51 can be obtained. When used in the interferometer it is sufficient to show up to 16 spherical fringes, or up to 8 phase steps for 2 spherical

Figure 6.13: 64×64 pixel image printed at 72dpi

fingers. A greater pixel count would be very useful for this scenario.

The main limit to scaling the array size is the cost of silicon. The cost in the process used in this design was approximately 580 Euro per square millimetre (AMS 0.35μm CMOS C35B4C3 4M/2P/HR/5V IO discounted service [57]). With sufficient funding, it is very easy to scale up the pixel count. Power consumption is a smaller problem because instead of using 22 output buffers (which consume the majority of the power), 6 can be used. This would slow down the frame rate, but should still provide data at video rate or faster. It is also possible to configure the device to run with smaller current, although this will compromise the quality of operation.

For example, allowing for 1 mm for ancillary electronics aiding the array such as the pads and output buffers, the cost of silicon for the final design LIDAR1 is approximately given by 580Euro/mm^2 $\times$ (32 $\times$ 0.115mm + 1mm) $\times$ (32 $\times$ 0.115mm + 1mm) which is approximately 12,700 Euro. Similarly, a 64×64 array would cost approximately 40,500 Euro and consume 790 mA ($\approx$2.6 W) if only 6 output buffers were used. At the time of writing thermal properties of the chip package are not available from the fab-house, so it has been considered good practice to maintain a maximum power consumption of 3.3W (equivalent to current consumption of 1 A). Figure 6.13 shows that a 64 $\times$ 64 pixel picture provides enough resolution for recognising basic facial features.

Using a smaller feature size would reduce the power consumption and reduce silicon space so it is a very attractive option. It would also improve the fill factor,

which would make the light budget requirements less exacting.

7 | Discussion and Conclusion

This chapter presents a summary of the thesis and re-emphasises the important findings. It goes on to further discuss some of the results and then draws conclusions.

7.1 Thesis Summary

Chapter 1 introduces light detection. It starts with a brief introduction to electronic photo-detection by CCDs and CMOS devices. A number of photo-sensitive elements are presented and their performance parameters are discussed. The chapter also presents the idea of using modulated light as a marker in experiments and for ranging. The challenges of detecting low signals especially in the presence of high background light can be mitigated by modulation of some component of the light such as the intensity.

Chapter 2 presents some pixels and cameras designed for the capture of modulated light. There is a wide variety in the detection stage as well as the demodulation mechanism. One type of pixel uses either mechanical or electronic slits to integrate the light signal onto different capacitors with the slits synchronised to operate at a frequency which is a whole-number multiple of the modulation frequency. An example is the Povel pixel [6]. A second type of pixel continuously detects the light and uses a mixer or rectifier to demodulate it. An example is the Bourquin pixel, which uses a square-wave mixer for demodulation. The chapter also presents some devices that are not designed primarily for modulated light detection, but can be configured for use as such.

The theory of modulation and demodulation is presented in Chapter 3. This chapter discusses the various forms of modulation and then focuses on amplitude modulated light. There is a brief discussion of the light budget requirements for detecting modulated light and the requirements for the light source. This is followed by a discussion of noise and propagation of uncertainty in the detection system. The chapter then builds up a complete usable front-end, starting with a basic logarithmic pixel. At each stage of the development, an analysis of the various drawbacks is performed, and these are progressively improved, culminating in a final design. This final design forms the basis for the remainder of the thesis.

The first two designs are presented in Chapter 4. These are MLCv6FE and MLCv6. MLCv6FE is a prototype front end, comprising only a single pixel and two amplifiers. It served to check the theory as described in section 3.5. MLCv6 is a 32 by 32 array of pixels, each with full demodulation capability. The MLCv6 design contained an important error that crippled its full characterisation and use as a modulated light camera. It however provided valuable insight into other potential problems, leading to the design of the final camera.

Chapter 5 presents the final camera, LIDAR1. The details of the design and simulation results are presented in this chapter. Experimental results from the characterisation of the fabricated device are also presented and discussed. These experiments include measuring the RF output bandwidth, the IQ phase response and also the phase error at various frequencies and values of tunebias. The DC response is also presented. The characterisation results are then applied to various experiments, the major results of which are presented in Chapter 6.

Chapter 6 presents a number of scenarios in which a modulated light camera may be used. In the first scenario, LIDAR1 is applied to a time-of-flight experiment.

The detected phase gives an indication of the time of flight, thus the optical path length may be determined. In the second experiment, a heterodyne interferometer is set up, and used to detect fringes. Various configurations of the interferometer are used, and an ultrastable mode shows good resistance to vibrations. The chapter continues with a discussion of the practical use of the device.

7.2 Conclusions

This thesis has presented a modulated light pixel. It uses a logarithmic load in the front-end. The front-end is modified using a Regulated Cascode Circuit to extend the bandwidth. A bleed transistor is added to the front-end which sinks a variable current, **tunebias**. This current linearises the response and controls the light-gain-phase-amplitude relationship across the array.

The thesis has also presented a complete camera that uses this pixel. It is a 32 $\times$ 32 camera that detects unmodulated as well as modulated light components. It has been tested to work from 100 kHz to 50 MHz, and characterised from 1 to 40 MHz. The sensitivity of the camera is also very much improved as compared to previous work, with a minimum detectable signal of 500 pA at 10 MHz. The phase error (which also depends on the incident light level) has been determined to be 3 degrees at 40 MHz.

There is also very good characterisation information, which has allowed the camera to be utilized as time-of-flight camera as well as a heterodyne interferometer.

Comparing the experiment results with the aims and objectives as listed in section 1.5, it may be concluded that whilst not all of the design objectives have been fully met, they have served as good motivation for the development of the modulated light camera. For example, a pixel pitch of 100 μm was

set as an objective, but the achieved pitch is 115 μ, down from 130 μm in previous generations [28]. The pixel density has consequently improved. Another improvement is in the fill factor, which increased from 9% to 16%.

7.3 Future Research

Future research on the development of this camera would lead to even better results.

The noise may be reduced by the use of an alternative filter. The OTA filters used in LIDAR1 account for about 35% of the noise per pixel. Because they provide no gain of their own, this is a very high figure. Reduction of this noise contribution could reduce the noise at 10 MHz from 200 pA to 120 pA. This would greatly reduce the light power requirements as discussed in section 6.4

Secondly, the camera would greatly benefit from increased amplifier gain and bandwidth. The present amplifier has a bandwidth of approximately 38 MHz. Increasing this would greatly increase the bandwidth of the system, and thus the sensitivity. The amplifier is effectively the bottle-neck in the present profile. The gain is about 32 dB, and increasing this would reduce the post-amplifier noise contributions from the mixer and filters, increasing the sensitivity of the pixel.

Thirdly, a careful calibration of the sensor is required. Logarithmic pixels exhibit large pixel to pixel variation, and calibration for their gain and phase performance is required for optimum operation. The present detection assumes a uniform calibration across the array.

Another area of investigation is the trough in the amplitude response that is observed at about 10 MHz (Figure 5.38). As discussed in section 5.4.1.2, it is

possible to fix this by further improving the layout of the pixel. The specific problem has not been isolated, but this problem appears only in the post-layout simulations.

A final improvement to the camera would be reduction of the pixel pitch. Using a process with smaller minimum feature size would allow the use of smaller devices and hence a smaller circuitry area. This would lead to improvements in the fill factor and pixel density, allowing for more resolution in captured images.

The generation of reference oscillators has proved challenging particularly for wideband experiments. It is suggested that the oscillators/splitters be better characterised. This would lead to a reduction in the phase error as measured in section 5.4.1.2.

A | C35 Wafer cross-section

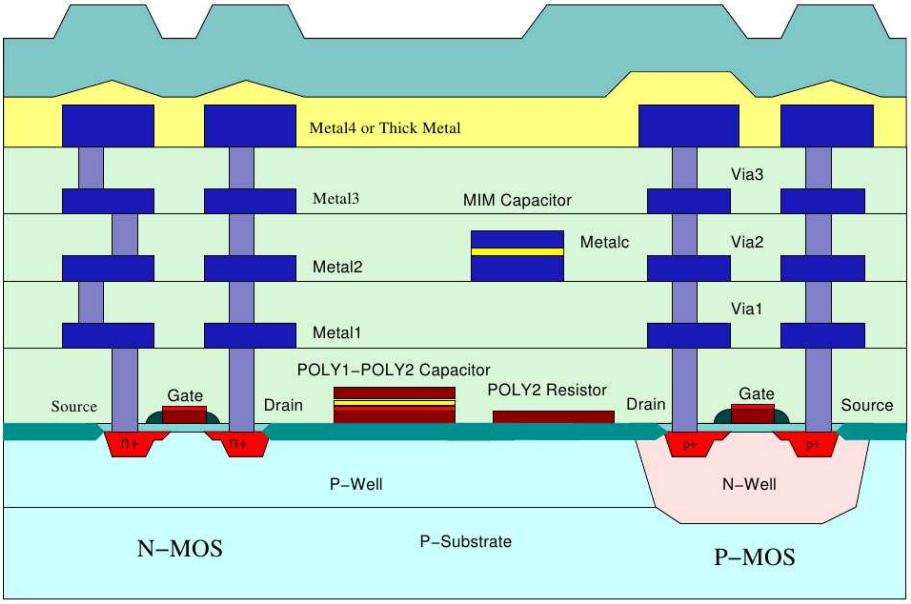

Figure A.1: CMOS C35 wafer cross-section

Figure A.1 shows a cross-section through the wafer for the process used in fabricating the devices presented in this thesis. The four metal layers are shown in blue, connected by vias.

B | Bias currents

B.1 MLCv6

Table B.1 is a list of the bias resistor configurations for MLCv6. The current values indicate bias currents at the pad level. An on-chip current mirror reduces these bias currents to appropriate levels for each pixel. It is ordered by bias current name.

Table B.1: MLCv6 bias currents

bias	Component	Pad (component) current	Resistance	Notes
ampbias	Amplifier	700 μA (10 μA)	1.8 kΩ	to V_{DD}
bufbias	Buffer	200 μA (10 μA)	7.8 kΩ	to GND
lpfbias	Filter	8.5 μA (500 pA)	300 kΩ	to V_{DD}
mixbias	Mixer	300 μA (20 μA)	5.8 kΩ	to V_{DD}
muxbias	Multiplexers	100 μA (10 μA)	21.9 kΩ	to GND
oabias	Output buffer	2 mA (2 mA)	1.2 kΩ	to V_{DD}
sfbias	Front-end	205μA (10 μA)	6.3 kΩ	to GND
tiabias	Front-end	700 μA (30 μA)	2.2 kΩ	to V_{DD}
tunebias	Front-end	91.5 μA (100 nA)	24.2 kΩ	to 5 V

B.2 LIDAR1

Table B.2 shows the bias resistor configurations for LIDAR1. The current values indicate bias currents at the pad level. An on-chip current mirror reduces these bias currents to appropriate levels for each pixel. It is ordered by bias current name. Figure B.1 shows them as laid out on the PCB.

Table B.2: LIDAR1 bias currents

bias	Component	Pad (component) current	Resistance	Notes
ampbias	Amplifier	700 μA (10 μA)	1.8 kΩ	to V_{DD}
bufbias	Buffer	200 μA (10 μA)	7.8 kΩ	to GND
lobias	LO buffers	100 μA (10 μA)	52 kΩ	to V_{DD}
lpfbias	Filter	8.5 μA (500 pA)	300 kΩ	to V_{DD}
mixbias	Mixer	300 μA (20 μA)	5.8 kΩ	to V_{DD}
muxbias	Multiplexers	100 μA (10 μA)	21.9 kΩ	to GND
oabias	Output buffer	2 mA (2 mA)	1.2 kΩ	to V_{DD}
sfbias	Front-end	205μA (10 μA)	6.3 kΩ	to GND
tiabias	Front-end	700 μA (30 μA)	2.2 kΩ	to V_{DD}
tunebias	Front-end	91.5 μA (100 nA)	10 kΩ	to 5 V

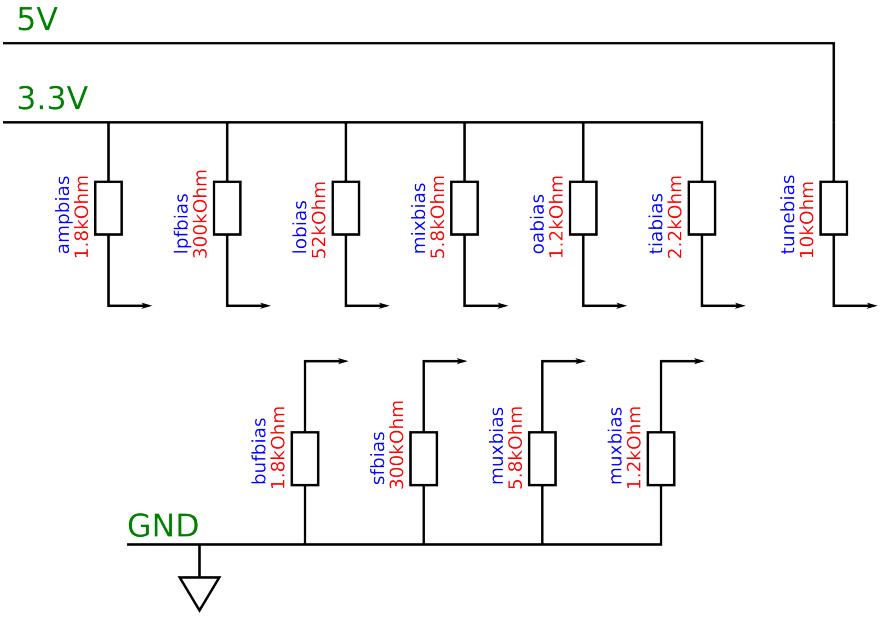

Figure B.1: LIDAR1 Biasing

C | Photomicrographs

This appendix shows photomicrographs of MLCv6 and LIDAR1.

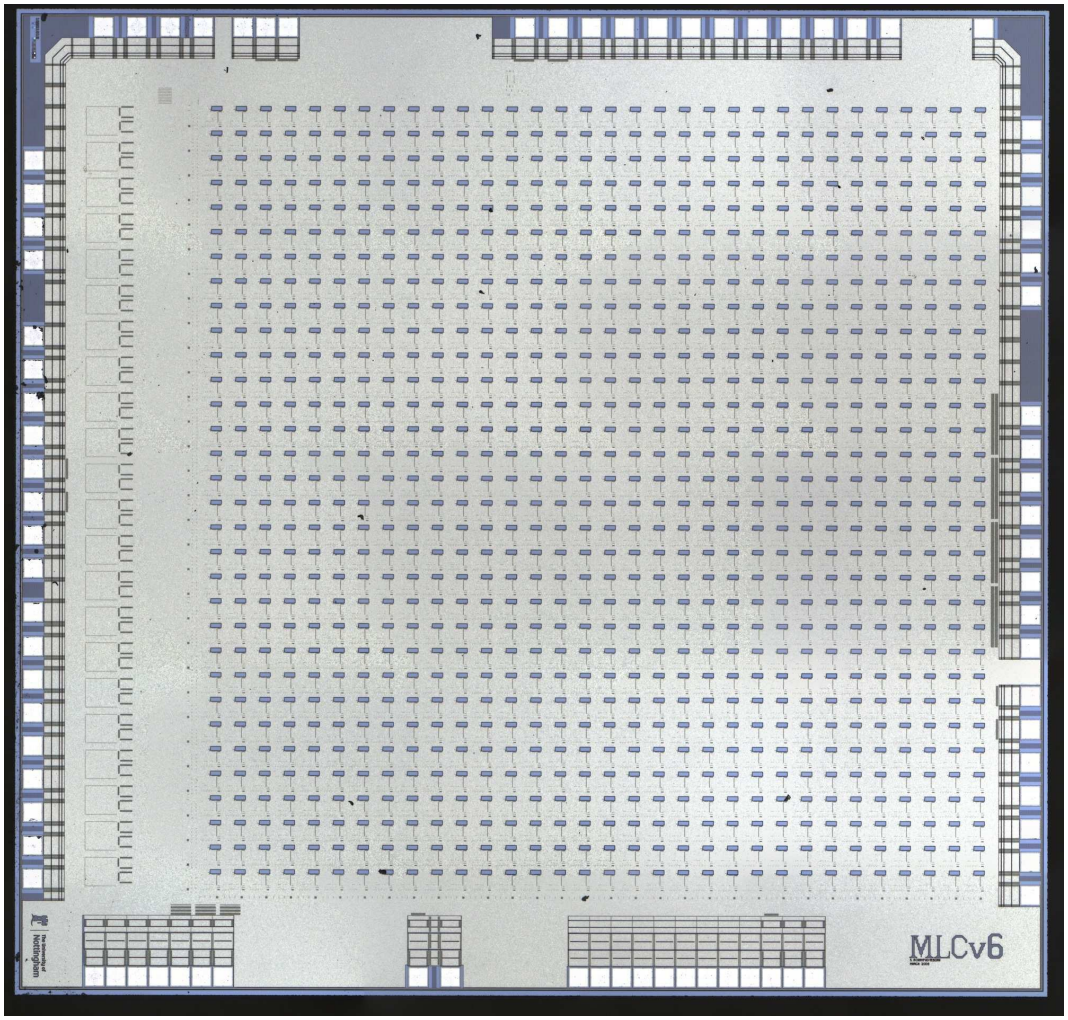

Figure C.1: Photomicrograph of MLCv6

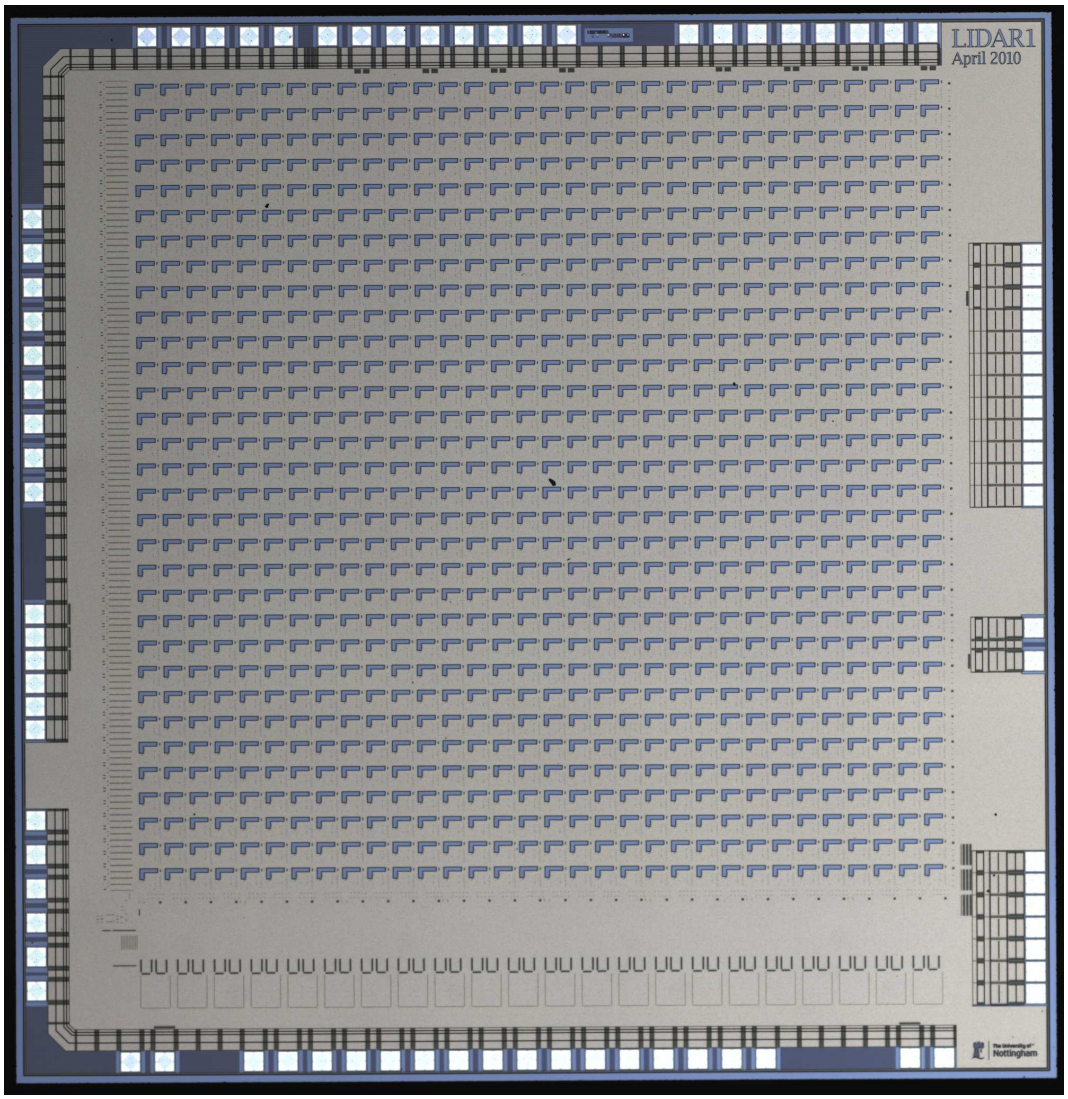

Figure C.2: Photomicrograph of LIDAR1

Bibliography

[1] G. Boyle, W.S.; Smith, "Charge coupled semiconductor devices," *Bell System Technical Journal*, vol. 49, pp. 587–593, April 1970.

[2] D. Li, S. Ameer-Beg, J. Arlt, D. Tyndall, R. Walker, D. Matthews, V. Visitkul, J. Richardson, and R. Henderson, "Time-domain fluorescence lifetime imaging techniques suitable for solid-state imaging sensor arrays.," *Sensors (Basel)*, vol. 12, no. 5, pp. 5650–69, 2012.

[3] B. UK, "Digital laser range-finder plr 25." `http://www.bosch-do-it.co.uk/boptocs2-uk/DIY/Tools/GB/en/hw/Rangefinders/95299/PLR+25/24115/3165140532464/index.htm`, 2012.

[4] N. A. Riza and M. A. Arain, "Angstrom-range optical path-length measurement with a high-speed scanning heterodyne optical interferometer," *Appl. Opt.*, vol. 42, pp. 2341–2345, May 2003.

[5] J. O. Stenflo and H. Povel, "Astronomical polarimeter with 2-d detector arrays," *Applied Optics*, vol. 24, pp. 3893–3989, November 1985.

[6] H. Povel, H. Aebersolf, and J. O. Stenflo, "Charge-coupled device image sensor as a demodulator in a 2-d polarimeter with a piezoelastic modulator," vol. 29, pp. 1186–1190, March 1990.

[7] T. Spirig, P. Seitz, O. Vietze, and F. Heitger, "The lock-in CCD - two-dimensional synchronous detection of light," vol. 31, pp. 1705–1708, September 1995.

[8] T. Spirig, M. Marley, and P. Seitz, "The multitap lock-in CCD with offset subtraction," *IEEE Transactions in Electron Devices*, vol. 44, pp. 1643–1647, October 1997.

[9] R. Lange, P. Seitz, A. Biber, and R. Schwarte, "Time-of-flight range imaging with a custom solid state image sensor," vol. 3823, pp. 180–191, SPIE, 1999.

[10] P. Gulden, M. Vossiek, P. Heide, and R. Schwarte, "Novel opportunities for optical level gauging and 3-D-imaging with the photoelectronic mixing device," *IEEE Transactions in Instrumentation and Measurement*, vol. 51, pp. 679–684, August 2002.

[11] S. Ando and A. Kimachi, "Time-domain correlation image sensor: First CMOS realization of demodulator pixels array," in *Proc. IEEE CCD/AIS*, pp. 33–36, 1999.

[12] S. Ando and A. Kimachi, "Correlation image sensor: Two-dimensional matched detection of amplitude-modulated light," *IEEE Transactions in Electron Devices*, vol. 50, pp. 2059–2066, October 2003.

[13] R. Schwarte, Z. Xu, J. Olk, R. Klein, B. Buxbaum, H. Fischer, and J. Schulte, "A new electro-optical mixing and correlating sensor: Facilities and applications of the photonic mixer device (PMD)," in *Sensors, Sensor Systems, and Data Processing*, vol. 3100 of *Proceedings of SPIE*, pp. 245–253, The International Society for Optical Engineering (SPIE), June 1997.

[14] R. Schwarte, "Phase and amplitude detector of electromagnetic waves from pixels operating in visible, UV and IR wavelengths." Patent, November 1999.

[15] P. Gulden, M. Vossiek, P. Heide, and R. Schwarte, "Novel opportunities for optical level gauging and 3-D-imaging with the photoelectronic mixing device," in *IEEE Instrumentation and Measurement Technology Conference*, May 2001.

[16] W. E. A. Shawkang M. Wu, Gary A. Ybarra, "A complex optimal signal-processing algorithm for frequency-stepped continuous wave data," *Circuits and Systems II: Analog and Digital Signal Processing, IEEE Transactions on*, vol. 45, pp. 754–757, June 1998.

[17] J. Ohta, K. Yamamoto, T. Hirai, K. Kagawa, M. Nunoshita, M. Yamada, Y. Yamasaki, S. Sugishita, and K. Watanabe, "An image sensor with an in-pixel demodulation function for detecting the intensity of a modulated light signal," *IEEE Transactions in Electron Devices*, vol. 50, pp. 166–172, January 2003.

[18] Y. Oike, M. Ikeda, and K. Asada, "High performance photodetector for modulated lighting," *IEEE Electronic Letters*, vol. 7, no. 5, pp. 640–645, 2001.

[19] D. Stoppa, N. Massari, L. Pancheri, M. Malfatti, M. Perenzoni, and L. Gonzo, "A range image sensor based on 10-um lock-in pixels in 0.18-um cmos imaging technology," vol. 46, pp. 248 – 258, January 2011.

[20] M. Roger Alan Light, *Design and Implementation of an Integrating Modulated Light Camera*. PhD thesis, The University of Nottingham, 2008.

[21] H. G. P. H. Benten, T. Routsalainen, A. J. MÃďkynen, T. E. Rahkonen, and H. K. Kopola, "Integrated synchronous receiver channel for optical instrumentation applications," in *Sensors, Sensor Systems, and Sensor Data Processing*, vol. 3100 of *Proceeding of SPIE EurOpto*, pp. 75–88, September 1997.

[22] S. Bourquin, P. Seitz, and R. Salathe, "Two-dimensional smart detector array for interferometric applications," *IEEE Sensors Journal*, vol. 37, pp. 975 – 976, July 2001.

[23] G. N. Lu, G. Guillaud, G. Sou, F. Devigny, M. Pitaval, and P. Morin, "Investigation of CMOS BDJ detector for flourescence detection in microarray analysis," in *IEEE-EMBS'2000*, pp. 381–396, 2000.

[24] G. Lu, P. Pittet, G. Carrillo, and A. El Mourabit, "On-chip synchronous detection for cmos photodetector," in *Electronics, Circuits and Systems, 2002. 9th International Conference on*, vol. 1, pp. 355 – 358, 2002.

[25] M. C. Pitter, J. Goh, M. G. Somekh, B. Hayes-Gill, M. Clark, and S. P. Morgan, "Phase-sensitive cmos photo-circuit array for modulated thermoreflectance measurements," *Electronics Letters*, vol. 39, pp. 1339 – 1340, sept. 2003.

[26] M. Pitter, R. Light, M. Somekh, M. Clark, and B. Hayes-Gill, "Dual-phase synchronous light detection with 64/spl times/64 CMOS modulated light camera," *IEEE Electronic Letters*, vol. 40, pp. 1404–1405, October 2004.

[27] P. Dmochowski, B. Hayes-Gill, M. Clark, J. Crowe, M. Somekh, and S. Morgan, "Camera pixel for coherent detection of modulated light," *Electronics Letters*, vol. 40, pp. 1403 – 1404, Oct. 2004.

[28] P. Dmochowski, *CMOS Modulated Light Cameras.* PhD thesis, The University of Nottingham, 2006.

[29] S.-Y. Ma and L.-G. Chen, "A single-chip CMOS APS camera with direct frame difference output," vol. 34, pp. 1415–1418, October 1999.

[30] S. Kleinfelder, S. Lim, X. Liu, and A. El Gamal, "A 10000 frames/s cmos digital pixel sensor," *Solid-State Circuits, IEEE Journal of*, vol. 36, pp. 2049 –2059, dec 2001.

[31] C. Niclass, A. Rochas, P. Besse, and E. Charbon, "A cmos single photon avalanche diode array for 3d imaging," in *Solid-State Circuits Conference,*

2004. Digest of Technical Papers. ISSCC. 2004 IEEE International, vol. 1, pp. 120 – 517, feb. 2004.

[32] C. Niclass, A. Rochas, P.-A. Besse, and E. Charbon, "Toward a 3-d camera based on single photon avalanche diodes," *Selected Topics in Quantum Electronics, IEEE Journal of*, vol. 10, pp. 796–802, july-aug. 2004.

[33] Y. Perelman and R. Ginosar, "A low-light-level sensor for medical diagnostic applications," *IEEE Journal of Solid-State Circuits*, vol. 36, no. 10, pp. 1553 – 1558, 2001.

[34] B. Freedman, A. Shpunt, M. Machline, and Y. Arieli, "Depth mapping using projected patterns," 05 2010.

[35] G. E. Nilsson, T. Tenland, and P. A. Oberg, "Evaluation of a laser doppler flowmeter for measurement of tissue blood flow," *Biomedical Engineering, IEEE Transactions on*, vol. BME-27, pp. 597 –604, oct. 1980.

[36] R. A. Rhode, "Solar spectrum." `http://en.wikipedia.org/wiki/File:Solar_Spectrum.png`, June 2007.

[37] G. Kopp, G. Lawrence, and G. Rottman, "The total irradiance monitor (tim): Science results," in *The Solar Radiation and Climate Experiment (SORCE)* (G. Rottman, T. Woods, and V. George, eds.), pp. 129–139, Springer New York, 2005. 10.1007/0-387-37625-9_8.

[38] J. B. Johnson, "Thermal agitation of electricity in conductors," *Phys. Rev.*, vol. 32, pp. 97–109, Jul 1928.

[39] R. J. Baker, *CMOS Circuit Design, Layout and Simulation.* IEEE Press, second ed., 2007.

[40] S. G. Chamberlain and J. P. Y. Lee, "A novel wide dynamic range silicon photodetector and linear imaging array," *IEEE Journal of Solid State devices*, vol. 19, pp. 41 – 48, February 1984.

[41] B. Razavi, *Design of analog CMOS integrated circuits.* McGraw-Hill series in electrical and computer engineering, McGraw-Hill, 2001.

[42] S. M. Park and C. Toumazou, "A packaged low-noise high-speed regulated cascode transimpedance amplifier using a 0.6um n-well cmos technology," in *Solid-State Circuits Conference, 2000. ESSCIRC '00. Proceedings of the 26rd European*, pp. 431 –434, sept. 2000.

[43] B. Hosticka, "Improvement of the gain of mos amplifiers," *Solid-State Circuits, IEEE Journal of*, vol. 14, pp. 1111 – 1114, dec 1979.

[44] A. Hastings, *The Art of Analog Layout.* Prentice Hall, Inc, 1 ed., July 2001.

[45] I. A. David Schleef, Frank Mori Hess, "Comedi - control and measurement interface." `www.comedi.org`, March 2009.

[46] K. Ollivier, "wxwidgets." `www.wxwidgets.org`, March 2009.

[47] H. O. P. Ltd., "Persistence of vision raytracer pty, ltd." `www.povray.org`, March 2009.

[48] J. Silva-Martinez and S. Solis-Busto, "Design considerations for high performance very low frequency filters," Proceedings of the IEEE International Symposium on Circuits and Systems, 1999.

[49] O. Nobuyuki, "A threshold selection method from gray-level histograms," *IEEE Transactions on Systems, Man, and Cybernetics*, vol. 9, pp. 62–66, 1979.

[50] S. Vergamota, L. Cupido, M. E. Manso, F. Eusebio, A. Silva, P. Varela, J. A. C. Cabral, F. Serra, and C. A. F. Varandas, "Microwave interferometer with a differential quadrature phase detection," *Review of Scientific Instruments*, vol. 66, pp. 2547 – 2551, March 1995.

[51] H.-K. Teng and K.-C. Lang, "Heterodyne interferometer for displacement measurement with amplitude quadrature and noise suppression," *Optics Communications*, vol. 280, no. 1, pp. 16 – 22, 2007.

[52] H. Eklund, A. Roos, and S. T. Eng, "Rotation of laser beam polarization in acousto-optic devices," *Optical and Quantum Electronics*, vol. 7, pp. 73–79, 1975. 10.1007/BF00631587.

[53] A. Kimachi, "Real-time heterodyne imaging interferometry: focal-plane amplitude and phase demodulation using a three-phase correlation image sensor," *Appl. Opt.*, vol. 46, pp. 87–94, Jan 2007.

[54] A. Kimachi, "Real-time heterodyne speckle pattern interferometry using the correlation image sensor," *Appl. Opt.*, vol. 49, pp. 6808–6815, Dec 2010.

[55] R. Patel, S. Achamfuo-Yeboah, R. Light, and M. Clark, "Widefield heterodyne interferometry using a custom cmos modulated light camera," *Optics Express*, vol. 19, pp. 24546–24556, Nov 2011.

[56] C. G. Gordon, "Vibration control in microelectronics, optics, and metrology," vol. 1619, pp. 71–85, February 1992.

[57] E. IC, "Europractice ic fabrication general prices." http://www.europractice-ic.com/general_prices.php, 2012.